Fretting wear of the stainless steel / stainless steel contact under elevated temperature conditions

Radoslaw Rybiak

2008LYSEC13 Année 2008

THESE EN COTUTELLE

Ecole Centrale de Lyon – Université Polytechnique de Lodz

présentée devant

L'ECOLE CENTRALE DE LYON

pour obtenir le titre de DOCTEUR

spécialité : Matériaux

par

Radosław RYBIAK

FRETTING WEAR OF THE STAINLESS STEEL/STAINLESS STEEL CONTACT UNDER ELEVATED TEMPERATURE CONDITIONS

USURE PAR FRETTING D'UN CONTACT ACIER INOX/ACIER INOX SOUS HAUTES TEMPERATURES

Soutenance prévue le 27 Juin 2008 devant la commission d'examen de

M.	Yves BERTHIER	Rapporteur
Mme.	Cécile LANGLADE-BOMBA	Rapporteur
M.	Léo VINCENT	Membre
M.	Siegfried FOUVRY	Directeur de thèse
M.	Bogdan WENDLER	Directeur de thèse
Mme.	Bénédicte BONNET	Membre

CONTENTS

INTRODUCTION

Fretting wear is perceived as a plague in many industrial fields (aeronautics, nuclear engineering etc.) as degradation of mated surfaces due to wear is one of the principal problems resulting in necessity of repairing or replacing mechanical components. It is defined as a small displacement amplitude oscillatory motion between two nominally stationary solid bodies in contact under normal load. This process is usually observed in assemblies subjected to vibrations.

Within the framework of the present dissertation the elevated temperature conditions are being investigated to reproduce working conditions of the trunnion vane/bushing joints in the Variable Stator Vane system of the high pressure compressor of the GE90-115B two-spool high bypass turbofan engine. By analyzing the character of wear processes occurring in the VSV system a stationary bushing contacted with making torsional movements a vane trunnion can be considered as a joint subjected to fretting torsion. In this dissertation, however, the alternating fretting experiments under normal load equivalent to the airflow-induced interaction force between bushing and vane are being studied as it is much easier to implement in laboratory set-ups than fretting torsion by remaining similar loading conditions (i.e. pressure and relative sliding).

This work focuses on a few aspects. The origin of the low friction and wear 'glaze' layer is profoundly investigated. The fretting wear mapping of the 'glaze' layer activation as a function of temperature, displacement amplitude and pressure is plotted and discussed. Finally, the 'composite' wear law is developed, which allows the prediction of wear volumes under variable temperature and mechanical loading conditions.

The present Ph.D. dissertation is divided into four chapters. In Chapter 1 a bibliographic survey of the fretting issue is made and the relevant industrial issues described. The influence of environmental conditions on the tribological behaviour of alloy steels and superalloys is extensively discussed.

In Chapter 2 the materials used in the experiments and the fretting apparatus are presented. The contact mechanics of the considered contact geometry as well as the method used for wear volume evaluation is described.

In Chapter 3 the results of the investigations conducted under invariable loading conditions are discussed. Particular attention is paid to the impact of the temperature

on the tribological behaviour of the considered tribo-system. In-depth analytical investigations of the evolution of the interface as a function of temperature are also discussed. Moreover, the effect of the pre-oxidation is studied.

In Chapter 4 the fretting wear behaviour under variable temperature (adequate to those occurring in the VSV system) and mechanical loading conditions is investigated. The dynamics of the third body evolution under variable temperature conditions during a single fretting test is discussed. Fretting wear mapping of the 'glaze' layer activation as a function of temperature, displacement amplitude and pressure is elaborated. By considering the additive properties of the dissipated energy, the 'composite' energy wear formulation is developed to capture wear kinetics under variable loading conditions. It integrates the energy wear coefficient as a function of imposed loadings.

CHAPTER 1

INDUSTRIAL ISSUES AND BIBLIOGRAPHY

CHAPTER 1: INDUSTRIAL ISSUES AND BIBLIOGRAPHY

1. FRETTING WEAR IN THE GE 90-115 B AERONAUTIC CIVIL ENGINE

1. 1. Working principle and structure of the GE 90-115 B turbofan engine

A jet engine is an engine that discharges a fast moving jet of gases to generate a tremendous thrust to drive the plane forward.
Working principle of the jet engine can be summarized into the following points:

1. The engine sucks air in at the front. The inlet and fan pull the air in;
2. Air successively flows through the low pressure compressor then through the high pressure compressor in order to increase the air pressure;
3. The compressed air flows into a combustion chamber and is mixed with the fuel. An electric spark is used to light the mixture;
4. Burning gases are subsequently release in the turbine, which drives the compressor. Finally, the burning gases expand and blast out through the back of the engine. As the jets of gas shoot backward, the nozzle releases the gases and the aircraft is thrust forward.

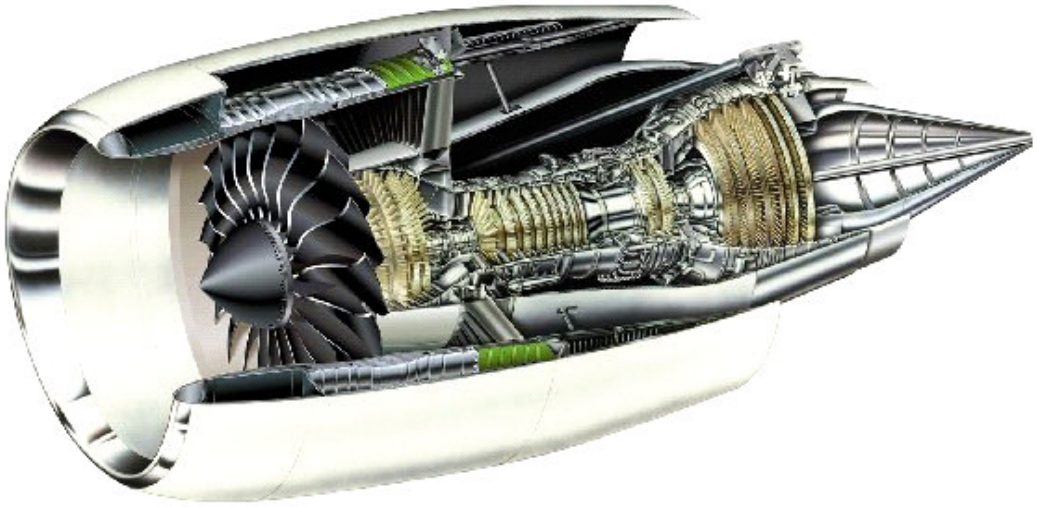

Figure 1: Image of the GE90-115B two-spool high bypass turbofan engine.

The GE90-115B civil engine (Figure 1) that some systems (e.g. low pressure compressor and part of the high pressure compressor) are designed and manufactured

by SNECMA is a two-spool high bypass turbofan engine (french ‘double-corps double-flux’) and is made up of 6 main components (Figure 2):

1. Fan;
2. Low Pressure Compressor (LPC);
3. High Pressure Compressor (HPC);
4. Combustion chamber;
5. Low Pressure Turbine (LPT);
6. High Pressure Turbine (HPT).

The turbofan engine generates dual airflow, the primary in the engine core, and the secondary in the bypass duct. To make it possible, a technology of a two-spool shaft is applied. It signifies that the engine is made up of two mechanically independent assemblies where the first is made up of the low pressure turbine driving the low pressure compressor and fan, however the second consists of the high pressure turbine, which drives the high pressure compressor. In this type of engine only some part of absorbed air participates in burning processes, giving so-called primary flow, which drives two-spool shaft system. The rest of absorbed airflow is accelerated in bypass duct by fan. The secondary flow produces around 80% of the thrust. The turbofan system is commonly used by airliners because it gives an exhaust speed that is better matched to subsonic airliner’s flight speed. A conventional turbojet engines generate an exhaust that ends up traveling very fast backwards, and this wastes energy. By emitting the exhaust so that it ends up traveling more slowly, better fuel consumption is achieved. In addition, the lower exhaust speed gives much lower noise. As regards dimensions, the fan of the GE90-115B engine measures more than 3 m of diameter and almost 5 m of length. The GE90-115B entered service in 2004 as the exclusive power plant for Boeing’s longer range 777-200LR and -300LR models.

The high pressure compressor, which cross-section is presented in Figure 3, is made up of rotor and stator. Rotor consists of several stages of rotor blades (RB) turning at high speed (more than 10000 revolutions per minute during take-off). That is exactly the rotor blades give a speed to airflow.

Stator of the GE90-115B two-spool high bypass turbofan engine is made up of stages of stator vanes placed between corresponding stages of rotor blades. Particular feature of its first 3 stages is that the vanes are of variable geometry. To be able to change and

control geometric settings of the vanes of these 3 stages as a function of working conditions of the engine, a complex VSV (variable stator vane) system is installed.

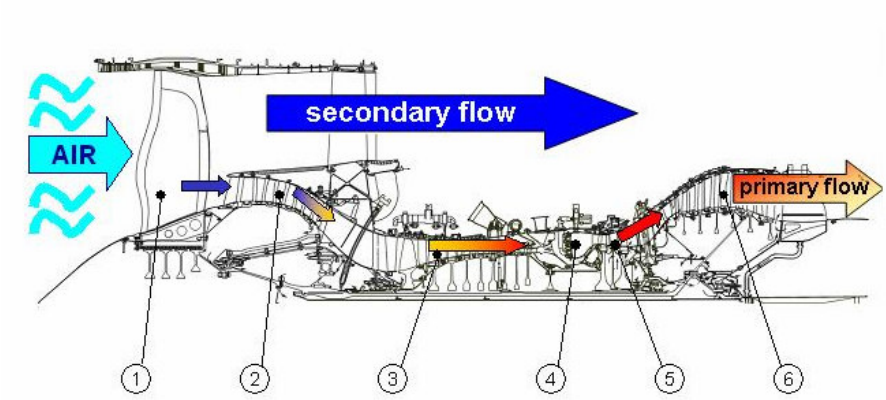

Figure 2: Cross-sectional view of the GE90-115B turbofan engine.

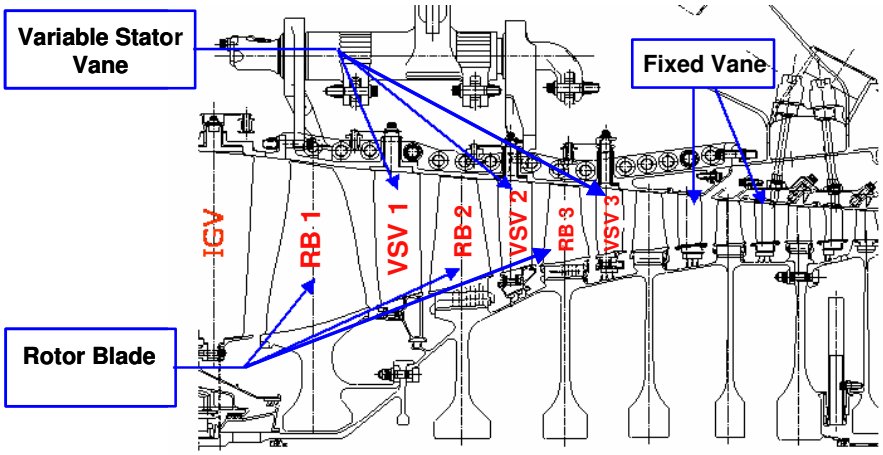

Figure 3: Cross-section of the high pressure compressor of the GE90-115B engine.

1. 2. Variable Stator Vane system – presentation, working conditions and loads

The function of the VSV system is to control the amount of air flowing through the compressor. To increase the operating capacity of the compressor the stator vane stages are designed with vanes that can rotate in around an axis that is in its longitudinal direction to adjust the angular orientation of the vane with respect to the airflow traveling through the compressor. The adjustment of the angular orientation allows changing the speed of airflow, thus optimizing the performance of the compressor. The VSV system is located approximately one third of the way back from the front of the engine. In case of the GE90-115B engine the VSV system

consists of an actuation system and 3 individual stages. Working temperature of the variable stator vanes at particular stages is different and fluctuates depending on the phase of the flight. At the first stage there is 114°C and 206°C, at the second 164°C and 274°C, and at the third 218°C and 350°C during the cruise and take-off, respectively. Movement of variable vanes is initiated by an actuator (fixed on the engine case), which induces turning of the actuation shaft. Subsequently, the latter transmits the movement to the actuation rings by means of adjustable turnbuckles. The levers, which are jointed to the actuation rings, turn around the axes of the vanes inducing their rotation. Figure 4 shows 3D view of the VSV system. The rest stages of stator (above 3rd stage) are consisted of fixed vanes. Besides, there is the other stage of variable settings, called Inlet Gas Vane (IGV), placed between the low pressure compressor and the high pressure compressor.

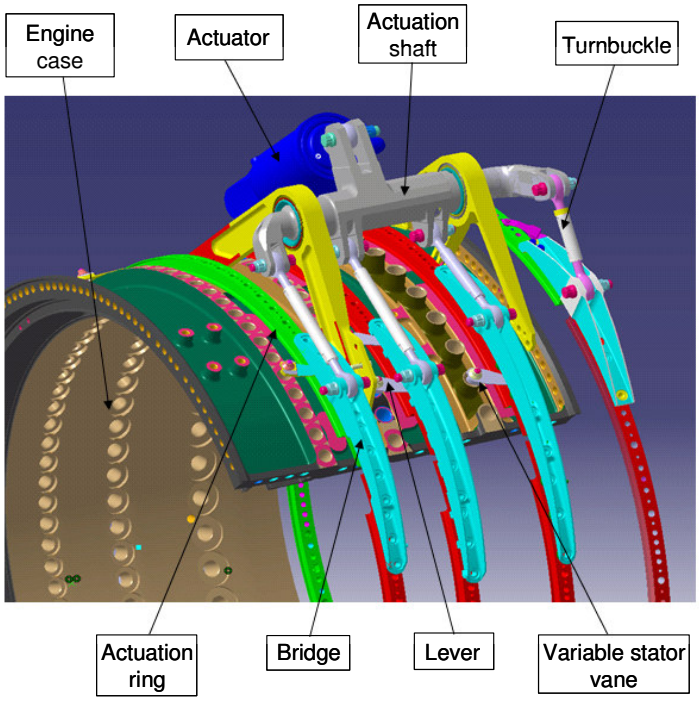

Figure 4: 3D view of the VSV system of the GE90-115B turbofan engine.

The variable stator vane structure includes an outer trunnion disposed in a complementary mounting boss in the stator case for allowing rotation of the vane relative to the case. A lever arm is fixedly jointed to a coaxial stem extending outwardly from the vane trunnion. The distal end of the lever arm is operatively jointed to an actuation ring that controls the angle of the vane. All of the vane lever

arms in a single stage are joined to a common actuation ring for ensuring that all of the vanes are positioned relatively to the airflow in the compressor stage at the same angular orientation.

Variable stator vane assembly includes a bushing and washer disposed between a trunnion attached to a variable vane and a case. The bushing and washer have the task of decreasing the coefficient of friction between the trunnion and the case and thereby of facilitating rotation of the vane through the trunnion. The bushing and washer also help prevent wear of the trunnion and case, which are expensive to repair and/or replace. The vanes are made from titanium alloy in case of 'colder' stages and from stainless steel for 'hotter' ones, however bushings are made from carbon-based or metallic materials. The vane/bushings assemblies can be different depending on the engine and particular stages, but generally it is always one or two external bushings in the engine case and one mounted in the internal ring in the base of the VSV system. The vane/bushings joint is presented schematically in Figure 5.

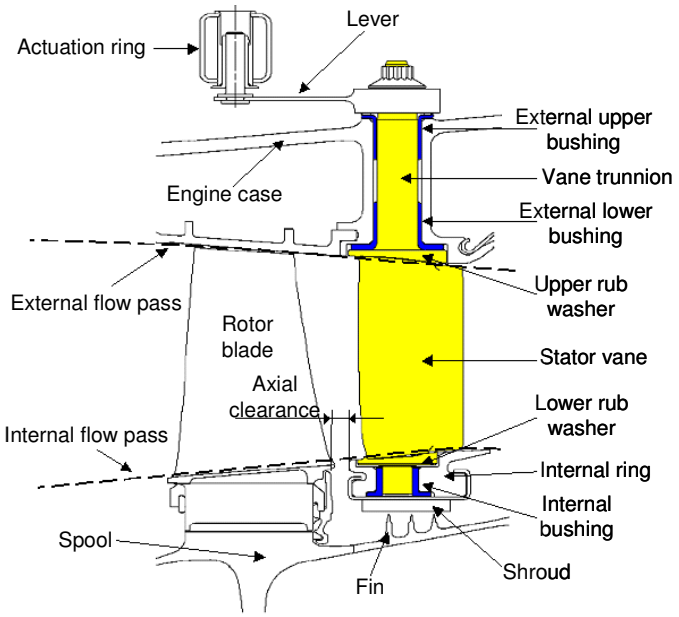

Figure 5: The vane/bushings joint in the VSV system.

Pressure present in the compressor increases with the stages and is always higher in the lower part of variable stator vanes than in the higher one. This compressed airflow exerts pressure on the vanes. Aerodynamic stresses (opposite to the airflow direction) are then induced in the vanes, which interact with the external bushings what results in wear in the vane trunnion/bushings contact. Another part of the VSV system

subjected to wear is the vane trunnion/internal bushing joint. Internal bushing is placed in the internal ring, freely mounted, which is positioned and maintained along the axis of the engine by the vane. This ring also participates in positioning the VSV. High pressure air present in the lower part of variable stator vanes causes pushing the internal ring towards the front direction of the engine, what consequently exerts pressure on the internal bushing and finally on the vane trunnion. Generated wear is of the same order as in the case of the external bushings.

When a bushing or washer system fails due to excessive wear, serious problems for the compressor may occur. The failure of the bushing and washer may create an increase in leakage of compressed air from the interior of the compressor through the variable stator vane assembly, which results in performance loss for the compressor. In addition, failure of the bushing and washer can result in contact between stator vane and the case, which causes wear and increases overhaul costs of the engine.

By analyzing the character of wear processes occurring in the VSV system a stationary either internal or external bushing contacted with making torsional movements a vane trunnion can be considered as a joint subjected to fretting torsion. In this dissertation, however, the alternating fretting experiments under normal load equivalent to the airflow-induced interaction force between bushing and vane are being studied as it is much easier to implement in laboratory set-ups than fretting torsion by remaining similar loading conditions (i.e. pressure and relative sliding).

2. TRIBOLOGICAL PROCESSES

Tribology is the science and technology of friction, lubrication, and wear. The name is derived from the Greek where *tribo* means 'I rub' or 'pertaining to friction' by rubbing and *logos* denotes 'science'. Tribology is an interdisciplinary subject, which to be understood well, necessities contributions from engineers, chemists, physicists, scientists, mathematicians as well as material and lubricant technologists. Tribology as a science was formally established slightly over 40 years ago. Previously, particular branches of Tribology were investigated by different scientific disciplines. And thus, issues of dry friction was a part of physics, boundary friction – physico-chemistry, lubrication – branch of petrol technology, wear – machine technology. The term 'Tribology' was introduced by British experts in 1966 in the report for Parliament

about state of lubricating technology [Jost (1966)]. It was defined as *the science and technology of interacting surfaces in relative motion and all practices related thereto.*

2. 1. Historical outline of Tribology

The world literature on lubrication, friction and wear has been growing steadily for over the past 100 years. And although the word Tribology was coined a short time ago, tribological knowledge and technology existed from the earliest time. Evidences of tribological issues could already be found in the third millennium BC. It is believed that lubricating materials were introduced in Egypt during the early civilizations period. In reference to Dowson (1998) it is possible to quote 3 main evidences of using lubricants in ancient Egypt. So, the first is that hydrated calcium sulphate (gypsum) was used to form the thin bed of viscid mortar to slide huge stone blocks for building of pyramids. The second indication is that water lubrication was used for transportation of heavy stone blocks. And lastly, the third proof, which demonstrates a chariot from about 1400 BC with traces of a lubricant (presumably, mutton or beef tallow) at its axle. Figure 6 shows the real painting preserved from around 2400 BC on which a man pouring water from a jar, presumably as a lubricant, in front of the sledge is presented.

Figure 6: A man pouring water from a jar, presumably as a lubricant, in front of the sledge with a statue of Ti in Saccara (Egypt), circa 2400 BC (after [Nosonovsky (2007)]).

Dowson, inspired by the painting from El-Bersheh that shows 172 men dragging a giant statue (Figure 7), performed simple calculation and got a remarkable result. According to him, assuming an average force of a slave as 800 N, it could be achieved

a total drag force of 172 x 800 N = 137.6 kN. Presupposing the weight of the colossus 600 kN, it was then calculated the coefficient of friction as $\mu = 60/137.6 = 0.23$, which was compared with that of wet wood-on-wood (μ=0.20). It allowed a conclusion that the sledge was indeed sliding over lubricated planks of wood.

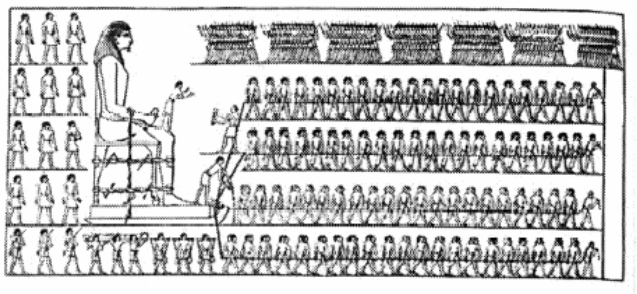

Figure 7: Painting from El-Bersheh, circa 1880 BC, showing transportation of a huge statue (after [Nosonovsky (2007)]).

Moreover, it was found that in Hebrew Bible the word oil appears very often (193 times) and is in conjunction with the verbs 'to smear' and 'to slip', indicating that it was utilized for tribological purposes [Nosonovsky (2007)].

Along with developing practical solutions within the scope of friction and lubrication, the first scientist studies were undertaken to write friction laws e.g. by Amonton (Amonton's law (1699)). However, it was not him who was named as a father of modern Tribology, but Leonardo da Vinci (1452-1519) who had studied incredibly manifold tribological subtopics (friction, bearing materials, plain bearings, lubrication systems, gears, screw-jacks and rolling-element bearings) already 150 years before Amonton's Law of Friction were introduced. Except Amonton, such names as Desanguliers, Euler and Coulomb should be mentioned. These pioneers brought Tribology into standards, and their laws are being still applied to many engineering problems even today.

Tribology is crucial to modern machinery which uses sliding and rolling surfaces. It has high economic importance. It was evaluated, in the report of Jost (1966), that around 515 billions pounds could have been saved by British industry if the correct use of tribological knowledge already existing had been made. It is generally believed that the economic losses resulting from ignorance of tribology reach around 6% of gross national product of the USA (and up to 4% of GNP in developed countries). It is approximately one third of world energy resources in present use appear as friction in

different forms. Thus, the main purpose of research in tribology is to minimize and eliminate losses caused by friction and wear at all levels of technology, where the rubbing of surfaces is involved.

2. 2. Destruction mechanisms involved in wear process

Wear is the result of material removal by physical separation due to micro-fracture, by chemical dissolution, or by melting at the contact interface [Bhushan (2001)]. Most machines fail due to wear of their components, losing their durability and reliability. Hence, wear control is still being grown to be engineers' challenge for the advanced and reliable technology of the future.

There are several classifications of wear, however they all are related to the classifications previously proposed by Burwell and Strang (1952) and Archard and Hirst (1956). The former distinguished seven types of wear, whilst the latter envisaged only two. The latter classification of mild (characterized by low contact resistance) and severe (characterized by high contact resistance) wear was subsequently developed by Quinn (1962, 1967, 1983a, 1983b), who introduced an oxidational theory of wear, where mild wear was recognized as that, which involves reaction with the environment, in particular with oxygen.

According to the classification introduced by Burwell and Strang (1952) the following types of wear can be distinguished: adhesive wear, abrasive wear, corrosive wear, fatigue wear, fretting, cavitation and erosion. Among them first four wear processes are generally recognized as fundamental and major ones.

Wear mechanisms are described by considering complex changes during friction. The dominant wear mechanism may change from one to another for reasons that include changes in surface material properties and dynamic surface responses caused by among others: frictional heating, chemical film formation, and wear. Generally, wear does not take place through a single wear mechanism, but is a complex process involving different destruction modes at the same time. Thus, recognition and comprehension of particular wear mechanisms is important. Schematic drawings of four main wear mechanisms are illustrated in Figure 8.

Severe wear and mild oxidational wear classified by Quinn (1980) are corresponding to adhesive wear and corrosive wear by Burwell and Strang (1952), respectively.

Wear induced by fretting is the subject of this dissertation, thus it is discussed extensively afterwards in this chapter.

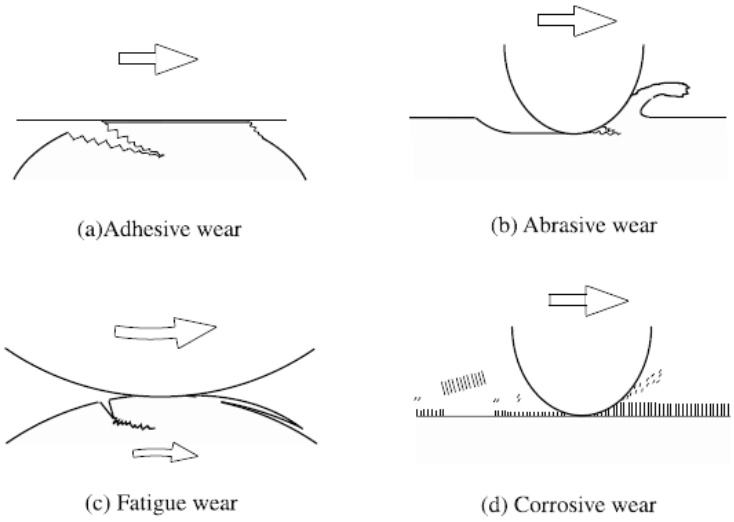

Figure 8: Schematic drawings of four main wear mechanisms: (a) adhesive, (b) abrasive, (c) fatigue and (d) corrosive wear (after [Bhushan (2001)]).

Adhesive wear consists in the formation of local adhesive nodes in the micro-areas of the surface layer deformation due to the molecular force interactions between asperity peaks, and their subsequent breaking associated with detachment and/or smearing of the particles on to the mated surfaces. The plastic deformation in the real contact area is a result of dislocations migration induced by high pressure and shearing. Due to such large deformation, a crack is initiated and propagated in the combined fracture process of tensile and shearing. When the cracks reach the contact interface, wear particles are formed and adhesive transfer is completed. Adhesive wear occurs especially in the contacts of metals characterized by high affinity. Elevated temperature intensifies the inclination for the formation of the adhesive junctions for the self-mated metals or for similar crystallographic structure metallic bodies being in contacts. Depending on the operating conditions and material properties, wear coefficient K_{ad} (defined in the further part of Chapter 1 – relation 5) in adhesive wear of metals varies between 10^{-7} and 10^{-2} [Archard (1953), Hirst (1957)].

Abrasive wear takes place when wear of material is a result of ploughing of the weaker material by stronger one. It occurs if the contact interface between two surfaces has interlocking of an inclined or curved contact. Abrasive grooves can be then observed onto the weaker body. Moreover, some detached loosely moving or

immobilized, in one or both of the interacting surfaces, hard particles can also act as abrasive bodies. Abrasive wear usually proceeds very fast, and wear coefficient K_{ab} for metals varies between 10^{-4} and 10^{-1} [Rabinowicz (1980)], depending on the contact conditions and material properties. Comparing K_{ab} and K_{ad} in adhesive wear, abrasive wear can be recognized as severe one.

Three different modes in abrasive wear, illustrated in Figure 9, can be distinguished: micro-cutting, wedge forming, and ploughing [Hokkirigawa et al. (1988)]. Generated wear particles form in different way and have different shapes depending on particular modes. In the micro-cutting mode, long and curled ribbon-like wear particles are formed (Figure 9a). This mode is characteristic of ductile materials. In the wedge-forming mode, a wedge-like wear particle is formed at the tip of the grooving asperity and stays there working as a kind of built-up wedge to continue grooving (Figure 9b). In the case of the ploughing mode, wear particles are generated as a result of repeated sliding passes and accumulation of plastic flow at the interface. Single pass of sliding produces only a shallow groove (Figure 9c).

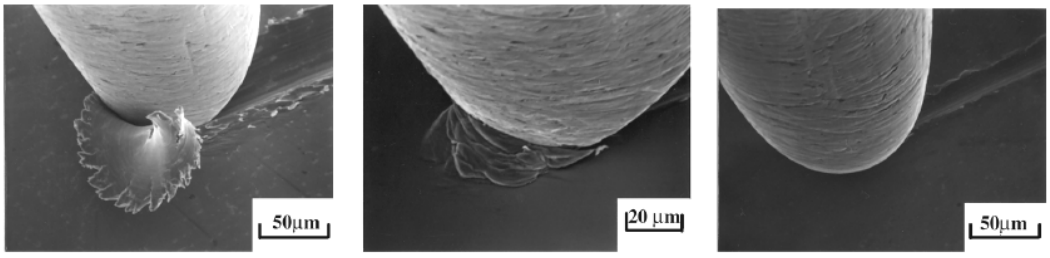

Figure 9: Different modes of abrasive wear observed by SEM: (a) micro-cutting, (b) wedge-forming and (c) ploughing (from [Hokkirigawa et al. (1988)]).

Corrosive wear is a tribochemical wear accelerated by corrosive media. It takes place when sliding proceeds in the environment of corrosive liquids or gases, where products of chemical or electrochemical reactions are formed on to the interacting surfaces. Such products may adhere strong to the surface and may exhibit different properties from the bulk material. If so, wear proceeds differently from that of the bulk material, and is mainly dominated by the reaction products formed by the interaction of solid materials with the corrosive environment. In this type of wear, tribochemical reaction produces a reaction layer on the surface. At the same time, such layer is removed by friction. Therefore, relative growth rate and removal rate

determine the wear rate of the reaction layers and, as a result, of the bulk material. The most representative mode of corrosive wear is oxidative wear of metals.

Fatigue wear can be defined as a wear of solid surfaces caused by fracture from material fatigue. This kind of wear is produced during friction under repeated cycles of loading contacts. It leads to micro-cracks formation and propagation that evolves to macro-cracks and result in separating of material particles. The latter phenomenon is called spalling. In fatigue wear, high-cycle fatigue and low-cycle fatigue mechanisms can be distinguished.

3. FRETTING DESTRUCTION PROCESS

Fretting is defined as a reciprocating micro-displacement amplitude oscillatory motion between two nominally stationary solid bodies in contact under normal load. Depending on the loading conditions (displacement amplitudes, normal loads) different types of fretting damage mechanisms can be distinguished.

3. 1. Introduction

Fretting phenomena were first observed by Eden et al. (1911) when they found iron oxide debris in the steel grips of their fatigue machine in contact with a steel specimen. However, a definition and term 'fretting corrosion' was established by Tomlinson (1927) who conducted the quantitative study and concluded that relative movement had to occur to cause fretting. The successive investigations on the fretting phenomena were carried out among others by Godfrey and Bailey (1952) as well as by Halliday and Hirst (1956). They all demonstrated the significant impact of oxide particles that are present in the wear scar. In the 60s of the last century Wayson (1964) and Hurricks (1970) advanced the knowledge about mechanisms of fretting wear in metals. The latter concluded that the process can be divided into three stages, those of initial adhesion and metal transfer, the production of debris in a normally oxidized state and, finally, the steady-state wear condition. Moreover, he observed that abrasion as a cause of fretting damage is favoured only as a minor factor. Vingsbo and Soderberg (1988) were first who proposed the fretting maps to describe the relationship between wear and displacement amplitude, later developed by Vincent et al. (1992) by introducing the fretting regimes. Significant contribution

about the fretting fundamentals was brought by Waterhouse (1972) in the book "Fretting Corrosion".

Many nominally stationary joints of components in mechanical systems are subjected to vibrations and complex variable loading conditions. As a result, damage caused by fretting may take place what leads to the failure of the elements. Fretting is perceived as a plague in many industrial fields (aeronautics, nuclear engineering, automotive issues etc.). The degradation by fretting can be encountered for example in blade/disc joints in jet engines, steam generator tubes in a nuclear power plants, rolling bearings, riveted or screw joints, steel ropes, electric contacts or medical implants. Fretting is indeed a complex process, whose all involved mechanisms and kinetics are not completely identified and formalized yet. It was defined more than 50 factors that affect fretting [Collins (1981)], however this issues is still open to be complemented by other parameters like, e.g. impact of the magnetic field [Sato et al. (2000)].

3. 2. Contact conditions

Complexity of industrial tribo-systems does not often allow the straightforward transposition of their contact geometries to the simplified ones studied in laboratory conditions. Hence, three basic reference configurations are proposed and investigated (Figure 10):

- plane/plane,
- cylinder/plane,
- sphere/plane.

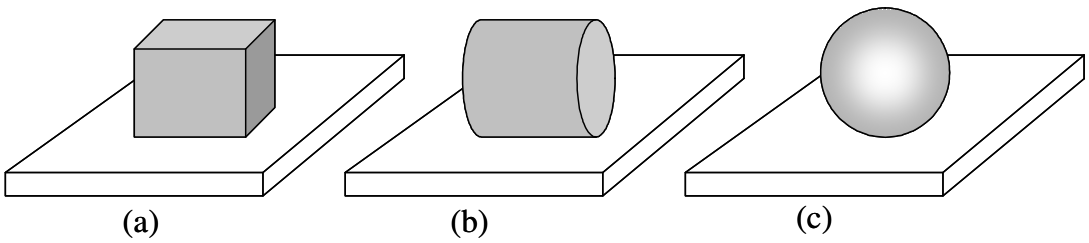

Figure 10: Three basic fretting contact geometries: (a) plane/plane, (b) cylinder/plane and (c) sphere/plane.

The linear cylinder/plane and point sphere/plane contact geometries are the most often used to investigate the fretting phenomena due to their simplicity of contact

mechanics and ease of implementation. The stress distribution and elastic deformation for these two geometries can be determined analytically according to the Hertz's theory [Hertz (1882)]. His work basically summarizes how two axi-symmetric objects placed in contact will behave under loading. The model bases upon the classical theory of elasticity and continuum mechanics. More complex and profound information on contact mechanics can be found in works of Johnson (1985) and Hills et al. (1993).

However, above-mentioned contact geometries are poorly corresponding to the real vane/bushing contact occurring in the VSV system of the turbofan engine that is closer to the plane/plane contact. Even though the plane/plane configuration requires a specific alignment to guarantee the flat/flat contact, it allows maintaining a constant geometry of the contacted surfaces independently of the degree of surface wear by contrast with a conventional sphere/plane configuration. However, mechanical analysis of such geometry reveals discontinuity in the pressure distribution on the borders of the contact. Different types of plane/plane contact configurations were developed by Snecma, where the border effect was significantly reduced, so that reproduce the pressure field distribution that occurs in the contact blade/disc in the fan of the jet engine. At the beginning an axi-symmetrical pin type specimen had been tested, then two different pin type specimens (2D scale reduced and 2D scale 1 pin) were studied to better reproduce the real contact [Paulin (2006)] (Figure 11). The pressure profiles generated under such conditions were investigated by Alexandrov et al. (1986).

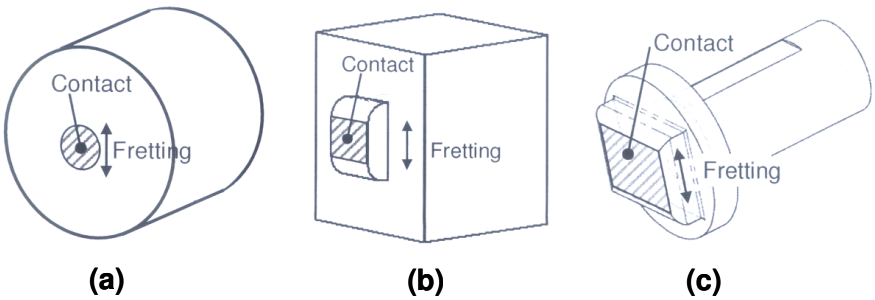

Figure 11: Different geometries to describe the plane/plane contact: (a) an axi-symmetrical, (b) 2D scale reduced and (c) 2D scale 1 pin type specimen.

Two main test configurations are developed (Figure 12):

- *Fretting Fatigue test* is derived from a classical fatigue experiment where two pads (plan, cylinder or sphere) are pressed on the fatigue specimen. The pads are put perpendicularly in relation to the axis of the fatigue specimen. This specimen is here subjected to the cyclic tension. As a result, relative displacement (δ) and cyclic tangential load (Q) are induced by the strain generated through the fatigue sample subjected to external loading (P). In this configuration cracks nucleates and subsequently propagates due to applied external loading. This type of experiments permits to quantify the influence of the contact and fretting on the specimen lifetime under fatigue by means of the Wöhler curve. In this type of test, fretting and fatigue loading are in phase;
- *Plain Fretting test* (also called fretting wear test) is equivalent to a classical reciprocating wear experiment, but sliding amplitude is here smaller than dimension of the contact. Micro-displacement is here generated by a relative motion between two bodies induced, for instance, by electro-dynamic shaker or hydraulic system. This type of configuration enables to analyze wear process and crack nucleation at the same time. Moreover, for this test, the influence of loading parameters is much easier to measure.

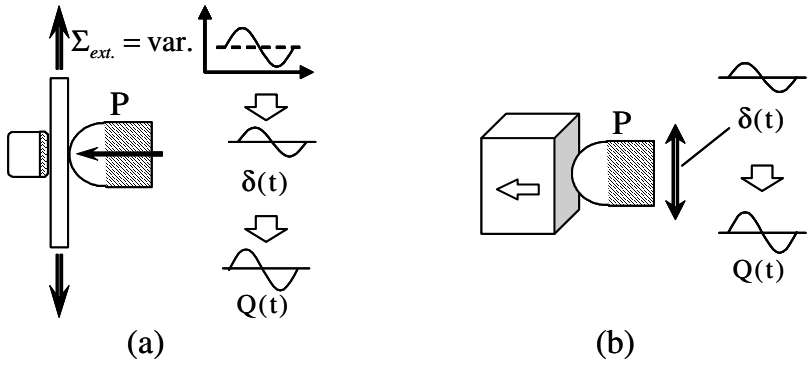

Figure 12: Fretting test configuration: (a) Fretting Fatigue and (b) Plain Fretting test.

The most commonly used fretting test configuration in the tribology is ball-on-flat one. Blanpain et al. (1995) defined three fretting modes for this geometry (Figure 13):

- linear displacement (mode I),

- radial displacement (mode II),
- circumferential displacement (mode III).

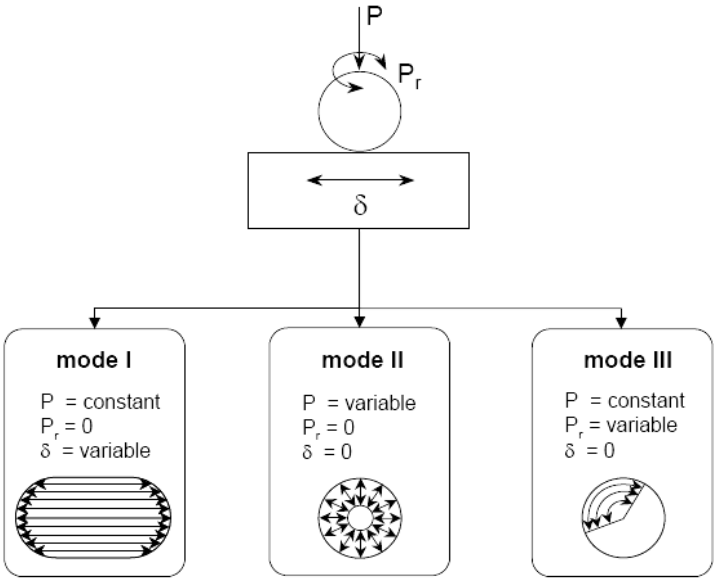

Figure 13: Presentation of the three fretting modes with representative wear tracks; P – normal load, P_r – rotation load, δ – displacement.

Due to the simplicity of its operation and of the contact mechanics, mode I is the fretting mode readily explored in laboratories. Moreover, it is the most representative for the majority of industrial contacts. Variable normal load testing (mode II), also known as 'false Brinelling', is investigated less frequently, although it is a common problem encountered in ball bearings. Torsional relative displacement fretting mode III can be observed in the nuclear or fuel industry (heat exchangers or steam generators).

3. 3. Sliding conditions

It is generally stated that fretting process (mode I) occurs under alternating micro-displacement. It was reported that even for displacement amplitude lower than 1 μm damage caused by fretting can take place [Kennedy et al. (1983)]. Threshold value of displacement amplitude for transition from fretting to reciprocating sliding was variously interpreted and found to occur within a wide range of amplitudes between 50 and 300 μm [Halliday et al. (1956), Vaessen et al. (1968-1969), Ohmae et al. (1974), Gordelier et al. (1979)]. This problem was later clarified by Fouvry et al.

(1996), who related this limit to the contact dimension. He introduced the e coefficient, which is defined as a sliding ratio (relation 1):

$$e = \delta_g / a \qquad (1),$$

with: δ_g - the sliding amplitude that is different from the displacement amplitude due to the contact and test apparatus compliance, a - the contact radius.

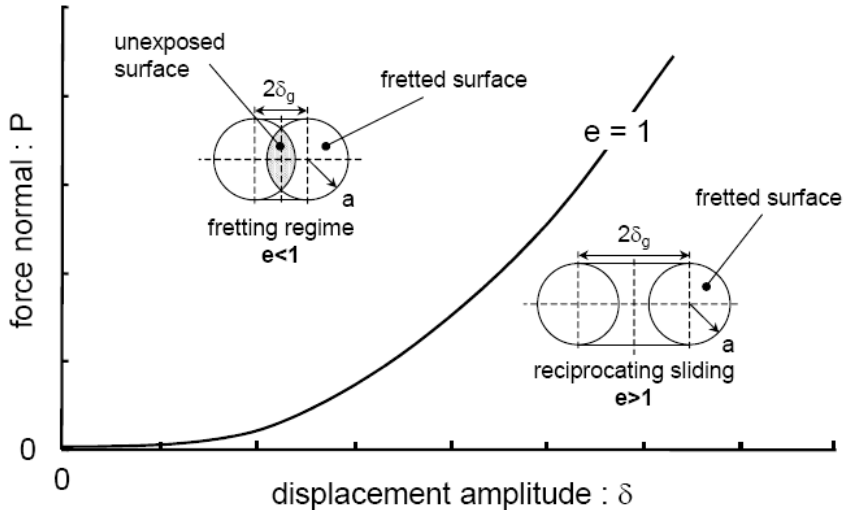

Figure 14: Definition of sliding parameter e and identification of transition between fretting conditions and reciprocating regime (sphere/sphere contact).

Figure 14 shows definition of sliding ratio and identification of transition between fretting regime and reciprocating sliding for the contact sphere/sphere. The boundary between fretting and reciprocating conditions is related to the limit value $e = 1$. When e remains lower than 1, an unexposed surface exists and fretting conditions take place whereas the system turns into the reciprocating regime when e is higher than 1 and all surface is exposed to the atmosphere. For a low value of tangential force, the micro-displacement between two bodies occurs. This displacement increases as the tangential force becomes higher what results in change of fretting contact conditions. Dynamic tangential force and displacement measurements during the fretting tests and some post-mortem metallographic examination allowed Vingsbo et al. (1988) to distinguish three different regimes of fretting:

- Stick regime: the interfacial sliding between two bodies does not occur as displacement is accommodated by elastic deformations. Stick domain is maintained

by locked asperities that can be plastically shared in the direction of micro-movement. In this case, low damage fretting by very limited oxidation and wear can be observed. For this regime the evolution Q=f(δ), called fretting loop or fretting cycle, takes form of closed linear relation (Figure 15a);

-Stick-slip regime: occurs when displacement amplitude is higher than that in the stick regime. In this case the sliding does take place, however the stick zone is a dominating area in the contact. Increase of the displacement amplitude makes the stick zone smaller. Surface degradation is here characterized by cracking as a result of contact fatigue. If rough surfaces are subjected to contact the stick zone can be spread for a number of local single contacts. This regime is characterized by the closed Q – δ fretting cycle, which takes a characteristic shape of elliptic hysteresis (Figure 15b). The elastic analysis of the sphere/plane and cylinder/plane contact [Mindlin (1949)] allows the explication of the pressure field and surface shearing. Considering the friction law of Coulomb it is $q(x,y) = \mu \cdot p(x,y)$ and $q(x,y) < \mu \cdot p(x,y)$ in the sliding and stick zone, respectively. For the elastic sphere/plane contact the size of the stick zone can be expressed by the sliding parameter (k):

$$k = \frac{c}{a} = \left(1 - \frac{Q^*}{\mu \cdot P}\right)^{1/3} \qquad (2),$$

with: c – the stick zone radius, a – the Hertzian contact radius, Q* - the tangential force amplitude, μ – the coefficient of friction operating within the sliding domain, P – the normal force.

-Gross slip regime: with still increasing displacement amplitude, the stick zone no longer occurs and entire contact area is subjected to sliding. Severe surface damage by wear, assisted by oxidation takes place. The Q – δ fretting loop characteristic of this regime is open and takes more quadratic shape (Figure 15c). Hence, the maximal tangential force Q* is here constant and do not depend on the sliding amplitude, what allows describing it by the classical Amonton's friction law: $Q^* = \mu \cdot P$ where μ – coefficient of friction and P – normal force.

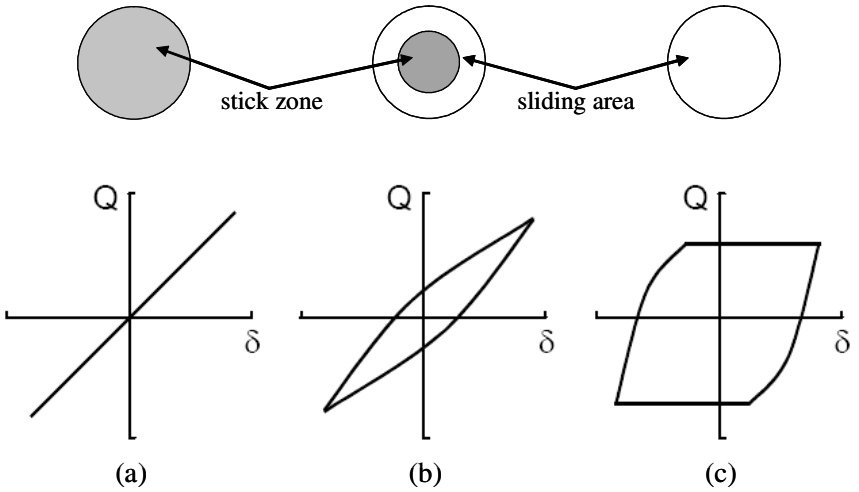

Figure 15: Contact definitions and corresponding fretting loops for different fretting regimes: (a) stick regime, (b) stick-slip regime and (c) gross slip regime.

3. 4. Fretting maps

The concept of the fretting map was primarily introduced by Vingsbo et al. (1988) for a sphere/sphere contact geometry. They mapped fretting sliding domains based on relation between three fretting parameters: normal force, displacement amplitude and frequency. This approach was later developed by Vincent et al. (1992), who defined three fretting regimes for the running conditions recorded during fretting test:

- *Partial Slip Regime (PSR)*: corresponding to the condition when stick-slip sliding regime is maintained during the test, observed for the lowest values of displacement amplitudes;
- *Gross Slip Regime (GSR)*: corresponding to the condition when gross slip sliding regime is maintained through the interface during running test, characteristic of the highest values of displacement amplitudes;
- *Mixed Fretting Regime (MFR)*: corresponding to the condition when gross slip and partial slip regimes are occurring during the single fretting test, observed for intermediate values of displacement amplitudes.

Based on the above classification the Running Condition Fretting Map (RCFM) was put forward [Vincent et al. (1992)], where particular fretting regimes are mapped as a function of normal force and displacement amplitude (Figure 16). However, that map was incomplete because did not take into account the material response and its degradation. This information was later supplemented by Blanchard et al. (1991) by

introducing the Material Response Fretting Map (MRFM) (Figure 16). Two main damage mechanisms: cracking and wear, were there mapped in the same way by depending on normal force and displacement amplitude. The RCFM maps are plotted from the direct analysis of the fretting loops whereas the MRFM maps cannot be made until after more profound metallographic analysis of the wear scars will carried out. The MRFM map is especially important as it can be used by engineers and designers to define the related wear mechanisms encountered in specific mechanical systems under different loading conditions.

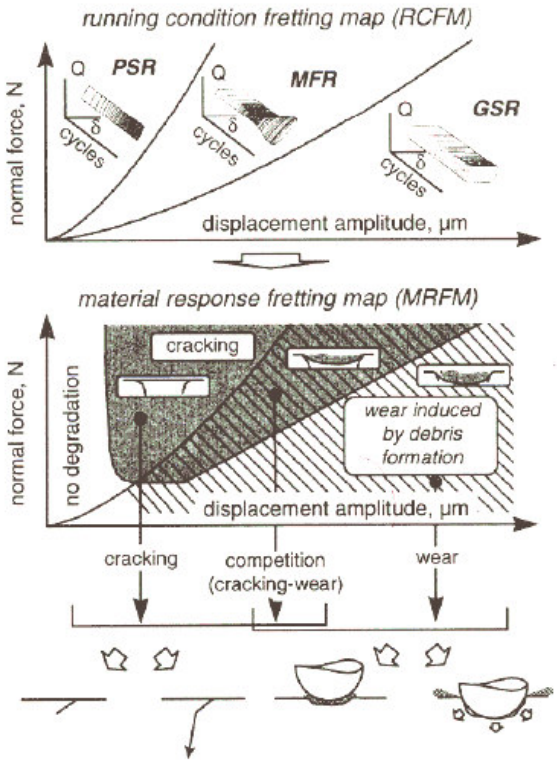

Figure 16: Fretting maps (RCFM and MRFM) representation (after [Fouvry et al. (2000)]).

3. 5. Transition criteria

Analyzing and verifying the single fretting cycle during the tests Fouvry et al. (1995a, 1996) introduced three criteria (Figure 17) that allowed a quantitative determination of the transition between partial and gross slip conditions for alternating loadings. These criteria were produced for the sphere/plane contact configuration assuming Mindlin's hypotheses. Therefore, in turn the energy ratio, aperture ratio (also called

sliding ratio) and system free ratio criteria characterized respectively by the coefficients A, B and C were proposed. The transition values of the coefficients were determined as $A_t = 0.2$, $B_t = 0.26$ and $C_t = 0.77$, below which partial slip conditions occur. The threshold values were found to be independent of the material properties. Nevertheless, computation of parameters A and B requires determination of the compliance of the system as they depend on the tangential accommodation of the fretting assembly. The aperture ration and system free criterion are highly dependent on the sliding aperture (δ_0) variation. Hence, it appears that the value of energy ratio A is the easiest to be accurately determined from among the above-mentioned criteria as dissipated energy for each cycle (E_d) is less dependant on the data scattering than the sliding aperture (δ_0) (also called sliding amplitude δ_g).

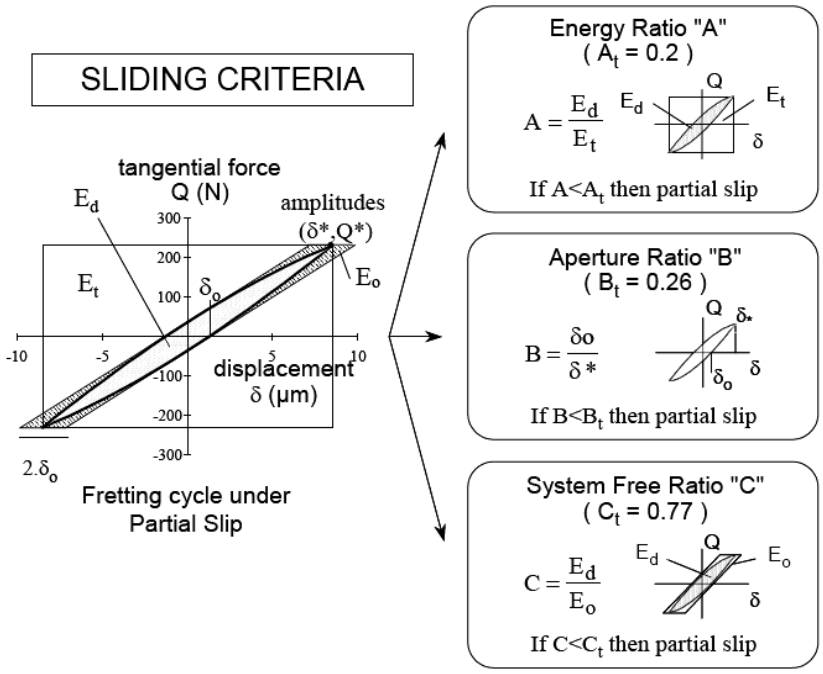

Figure 17: Fretting loop analysis by quantitative parameters A, B and C to define the sliding transition (after [Fouvry et al. (1996)]).

Transition between fretting and reciprocating sliding can be characterized throughout analyzing the changes of friction coefficient, wear coefficient, wear volume, wear scars profile or wear debris features before and after the boundary point. As an example, for a sphere/plane self-mated steel contact wear coefficient and wear volume

were observed to be the most appropriate parameters for identifying the transition criterion due to their quantitative values [Chen et al. (2001)].

3. 6. Fretting damage mechanisms

Fretting Wear (characteristic of Plain Fretting tests) and *Fretting Cracking* (characteristic of Fretting Fatigue tests) are two main damage mechanisms that can cause the catastrophic failure of the mated surfaces under fretting conditions.

Fretting Cracking is due to cyclic stresses resulting from the relative motion between interacting bodies, which are conducive to crack nucleation and their propagation. This type of damage appears as a consequence of local overstressing. The fretting cracking is not a subject of this dissertation, thus it is being discussed briefly.

Fretting Wear is due to the interfacial shear work resulting from the relative motion between interacting bodies and is related to the debris formation and loss of material of contacting bodies. Fretting wear can be comprehended as a response of the tribo-system to the global overstraining of the surface.

Fretting Cracking and Fretting Wear are usually considered separately, however it should be taken into account that under certain operating conditions they can be identified as two competing processes, what is illustrated on the Material Response Fretting Map in Figure 16. It accounts for why cracking can be observed under fretting wear conditions and debris formation under fretting cracking regime [Waterhouse (1981), Zhou et al. (1992)].

Fretting wear and fatigue concepts do not take into account the influence of the interacting environment. In fact, pure fretting, when the chemical reactions do not occur, is rather unusual rarely investigated process as the specific apparatus where inert gases or vacuum must be used to produce neutral surrounding atmosphere. Hence, the third mechanism of fretting damage – fretting corrosion – can be distinguished. Indeed, the term of 'fretting corrosion' was originally used to define destruction processes caused by fretting in air environment [Tomlinson (1927)], for years considered as a synonym of fretting damage later**.** Corrosion appears in case of oxidation process what can strongly affect the damage mechanisms. However, at present it is treated as a secondary process in relation to fretting wear and fretting fatigue. Fretting corrosion can be defined as a destruction process under fretting regime stimulated by corrosive impact of the ambient atmosphere. Generated wear

products take usually form of metal oxides detached from the surface or oxidized debris. In addition, fretting damage is here accelerated by stresses generated by interacting solids, which increase the chemical reactivity of surfaces.

3. 6. 1. Fretting Cracking (i.e. endurance under Fretting Fatigue loading conditions)

Fretting Cracking under Fretting Fatigue loading conditions is observed mainly in the areas of stress concentration, e.g. in splines, shaft keys or cables. It usually takes place within or at the edge of the contact area. Then, the subjected component can be easily damaged if the crack propagates.

Under Fretting Fatigue loading conditions, materials performance can be characterized by a S-N curve (commonly used in characterizing the classical fatigue tests), also known as a Wöhler curve, which relate the number of cycles to failure (N) with maximal amplitude of cyclic stresses (S) (Figure 18). Plotting the Wöhler's curves allow an establishment of the endurance limit of materials, i.e. the maximal tension value at which the specimen failure will not occur even after great number of cycles (i.e. from the range 10^8-10^9 cycles or greater). It was shown that conjoined action of fretting and fatigue causes a significant decrease (from 2 to 5 times) of lifetime of the studied specimen in comparison with the pure fatigue test [McDowell (1953), Waterhouse (1992)].

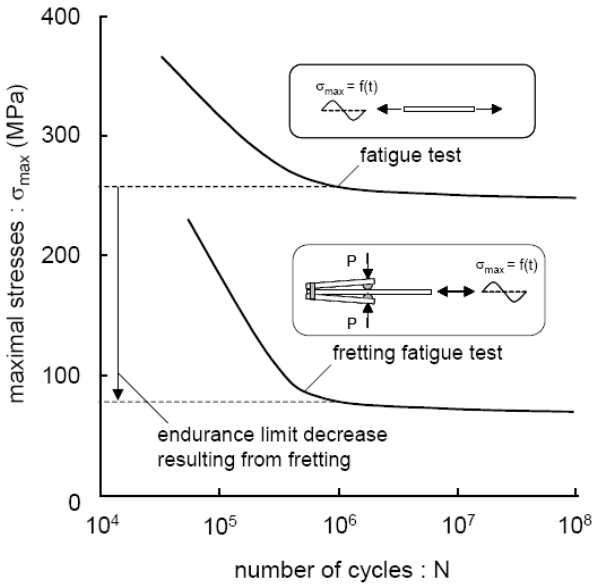

Figure 18: Comparison of Wöhler curves for Fatigue and Fretting Fatigue tests.

Apart from the tensile strain, the normal force and the displacement amplitude (induced by the specimen deformation under normal force and tangential stress) are two important parameters studied in fretting fatigue tests. Cracking behaviour of material is considered as a function of contact pressure and fatigue stresses. Thus, many authors showed that endurance limit diminished monotonously with increase of pressure in the contact [Endo (1976)]. On the other hand, Del Puglia et al. (1994) observed that the specimen lifetime reach some minimum for certain contact pressure. Waterhouse (1981) reported that the critical relative displacement amplitude for cracking phenomenon is comprised between 10 and 25 μm. Lower values of displacement were not sufficient to reduce specimen lifetime. In reverse, increase of displacement moves degradation process toward debris formation, where particles detachment eliminates the micro-cracks before they begin to propagate.

The point of first crack initiation and its direction are of great importance due to their industrial relevance. It was showed by Nakazawa et al. (1992), who investigated the plane/plane configuration that the point of crack nucleation within the contact area depends on the sliding conditions (Figure 19). Cracks are there expected to nucleate within the slip zone, most likely on the contact border as higher normal loading and smaller displacement amplitude conditions are imposed. With increase of slip zone in the contact some multi-cracks are observed.

The following four formulations can be applied to predict the crack initiation:

- Dang Van fatigue approach [Dang Van (1993)]: the crack nucleation process is a function of two macroscopic stresses: shear one and hydrostatic pressure. If these two variables reach the limit value then thee is a high risk of cracking on a critical grain;
- Crossland fatigue description [Crossland (1956)]: the macroscopic loading path is considered and crack nucleation risk is expressed as a combination of shear stress and hydrostatic pressure;
- McDiarmid fatigue formulation [McDiarmid (1991)]: identifies the maximal shear stress amplitude and indicates the critical plane where the crack is expected;
- Smith-Watson-Topper fatigue criterion [Smith et al. (1970)]: crack will initiate due to shear stress and will grow on a certain plane perpendicular to the direction of the principal stress.

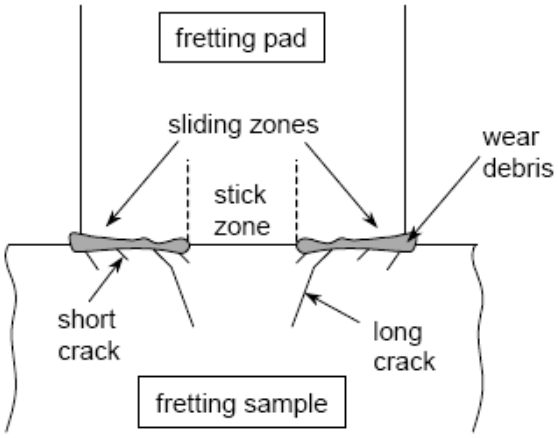

Figure 19: Fretting damage mechanisms for plane/plane contact geometry [Nakazawa et al. (1992)].

In Fretting Fatigue test there can be encountered two forms of cracks: short (of the length of some tens of micrometers) and long ones that have propagated.
Micro-cracks appear very early in the lives of components. It was originally demonstrated by Forsyth (1961) that in ductile materials fatigue cracks propagate in two distinct stages (illustrated in Figure 20):

- Stage I: short cracks are generated, which orientation to the surface is comprised within the angle limits from 10° to 60° corresponding to the maximum shearing plane. The length of the crack varies and depends on the mechanical properties of the studied tribo-system. Initiation and propagation of short cracks are mainly controlled by the loading conditions of fretting;
- Stage II: during this stage the general plane of the previously generated short crack propagates perpendicularly to the direction of the maximum tensile stress. The evolution of long cracks is characterized by uniaxial fatigue strains in the material.

The presence of short and long cracks in a studied specimen suggests a complex fatigue strain and fretting loading at a time. However, there can be some conditions under which crack initiated by fretting do not propagate into the long one when so-called ‘crack arrest’ takes place. Hills et al. (1988) showed that the specimen lifetime can approach infinity in the presence of short cracks. Hence, it is important to

find a loading transition between fatigue strain and fretting. This transition can be determined by using the Kitagawa-Takahashi diagram [Kitagawa et al (1976)].

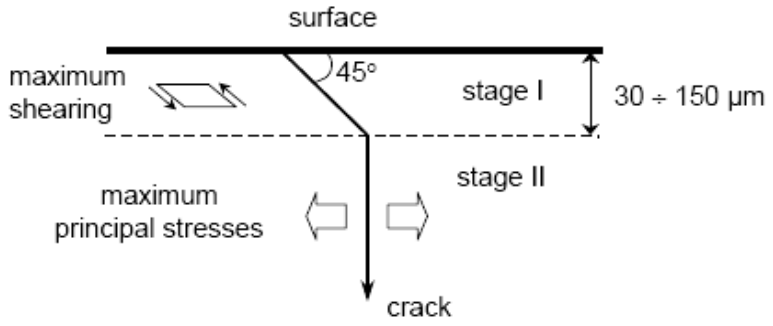

Figure 20: A two stage process of fatigue crack propagation [Forsyth (1961)].

3. 6. 2. Fretting Wear

By contrast with fretting fatigue damage where destruction by cracking takes place, the wear phenomenon under fretting conditions is hardly formalized because it involves mechanisms, which are considerably less quantifiable, such as:

- Material transfer;
- Modification of surface interface as a result of material removal;
- Flow of the wear debris within the interface;
- Mechanisms related to the impact of environmental conditions (oxidation, hydratation);
- Coupling between thermodynamic, mechanical and physico-chemical aspects.

There are different wear mechanisms and numerous factors affecting the tribological processes. Hence, no single predictive equation or group of limited equations could be found for general and practical use. Meng and Ludema. surveyed the journal *Wear* between 1957 and 1992 and associated *Wear of Materials* (WOM) conferences from 1977 to 1991. They found 182 wear equations allowing wear quantification for the many types of wear. Those models often had theoretical-empirical character, so many tests had to be performed to determine related coefficients. Moreover, many of the equations were deduced for specific tribo-systems. Consequently, their simple use is limited and employment to the industrial issues impossible.

Review conducted by the authors [Meng et al. (1995)] showed that between 1947 and 1992 three schools in wear modelling successively developed can be distinguish.

- Years 1947 – 1970: During this period empirical equations were widely used. They based directly on the experimental results obtained under various conditions. For example, Rhee (1970) investigated the impact of normal force (P), sliding speed ($\dot{S}$) and time (t) on the total wear of polymers. He proposed the following formulation:

$$\Delta m = K \cdot P^a \cdot \dot{S}^b \cdot t^c \quad (3),$$

with: Δm – the weight loss, K, a, b, c – the empirical constants.

Empirical models are applicable only within the range of parameters they are defined for, but are far more accurate than the theoretical relations developed under the same conditions.

- Years 1970 – 1980: Contact-mechanics-based equations were commonly developed within this time. The wear kinetics was then described by taking into account the real contact area and mechanical properties of the contacted materials as: Young's modulus or hardness.

The most representative formulation for this model group, nota bene commonly used in industrial application till these days, was elaborated by Archard (1953) (relation 4 and 5), who published well in advance of the later contact mechanics laws.

$$V = K \cdot S \cdot A \quad (4),$$

$$V = K \cdot S \cdot \frac{P}{H} \quad (5),$$

with: V – the total wear volume, K – the dimensionless wear coefficient, A – the real contact area, S – the sliding distance, P – the applied normal load, H – the hardness of the wearing material.

The wear coefficient K was interpreted by Archard as a probability to form a wear particle at each asperity encounter, however, the other authors proposed different interpretations of this coefficient [Shaw (1977), Hutchings (1992), Johansson (1993)]. Moreover, similar models were later proposed [Rabinowicz (1965), Moore (1980)].

- Years 1980 – 1992: Equations of wear kinetics based on the material failure mechanisms were evolved within this period. In this case, the wear resistance was no longer considered as an intrinsic property of materials, but was assumed to be closely related to the fatigue properties, shear failure defined by slip line analysis, dislocation mechanics brittle fracture properties or oxidation phenomena. In the last case, wear

was thought to be due to loss of oxide, e.g. the oxidational theory of wear [Quinn (1967)] that is discussed afterwards.

Quantification of wear rate in the case of Fretting is more complicated in comparison with, for example, sliding wear, because the former is strongly affected by debris trapping within the friction interface, what results in a significant modification of the interface as a result of debris flow and specific transfer of material.

Works concentrated on quantitative description of fretting problem were undertaken, among others, by Klaffke (1994) and by the group of prof. Celis [Blanpain et al. (1993)]. The first made a comparison of different surface treatments as function of relative humidity using similar wear coefficient to that in the classical Archard's model. The second related the wear resistance of different hard coatings to the sliding distance, normal force and number of cycles (Figure 21). Recently, Goryacheva et al. (2001) proposed to quantify the wear under partial slip regime by local formulation of the Archard's law. The evolution of wear was there correlated with the modification of the contact geometry during the fretting test followed by redistribution of the stress field and deformation took place. This was connected with the wear volume by the integration of the local Archard's law within the whole contact area.

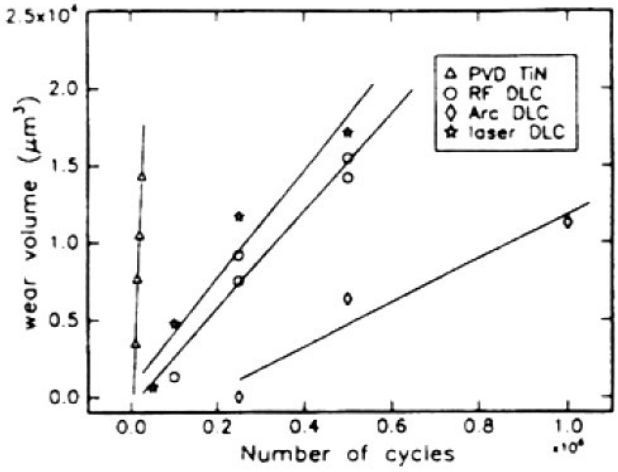

Figure 21: Wear volume evolution of different coatings as a function of applied number of fretting cycles [Blanpain et al. (1993)].

For recent 15 years an energy approach has been developed to describe fretting behaviour. The damaging processes, which take place in the contact, can be assumed to be driven by an increase in the contact temperature, material structure

transformations, debris generation or tribofilm formation. Indeed, all these processes involved in wear are activated and stimulated by frictional energy dissipated in the interface (Figure 22).

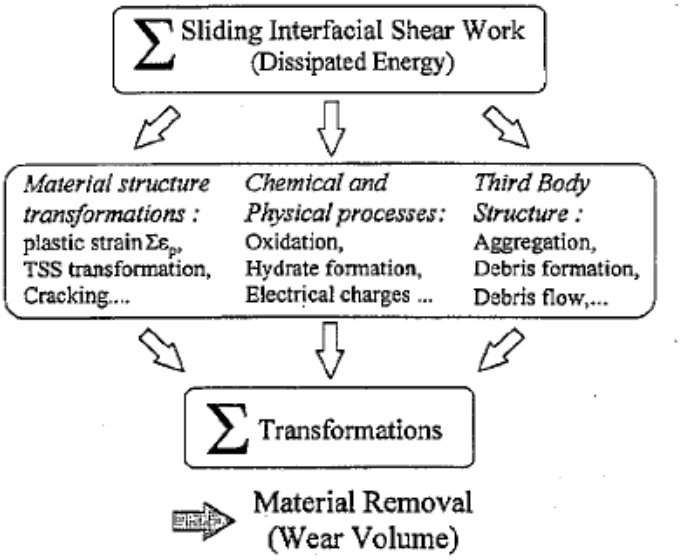

Figure 22: Dissipated energy concept as activating factor of wear (after [Fouvry et al. (1996)]).

First attempt to provide a quantitative description of dissipated energy was carried out by Matveesky (1965). He put forward the concept of 'Friction Power Intensity' (Q_F) to evaluate a degree of frictional heating occurring in the contact zones of rubbing surfaces:

$$Q_F = \frac{\mu \cdot P \cdot \upsilon_S}{A} \qquad (6),$$

with: μ – the coefficient of friction, P – the applied normal force, υ_S – the relative sliding velocity and A – the real area of contact.

This concept expresses the rate at which energy is generated by friction in the contact zone, but does not take into account the duration over which the energy is released to the mated bodies. Thirty years later, Plint (1995) developed the model of Matveesky and introduced the notion of 'Energy Pulse' (EP) as the product of the friction power intensity and the time for a point on the rubbing surfaces to transit through the contact zone:

$$EP = \frac{Q_F \cdot t_t}{2} = \frac{\mu \cdot P \cdot \upsilon_S \cdot t_t}{2A} \quad (7),$$

with: t_t – the time of transit in the contact zone. In his model, author suggested that the amount of energy per unit of contact area dissipated at each encounter of the rubbing surfaces is closely related to the severity of contact conditions. This formulation was put forward for the case when two mated bodies are in motion and the energy generated in the contact zone flows at an equal instantaneous rate into the two contacting objects.

In the same year Fouvry et al. (1995b) and Mohrbacher et al. (1995) introduced the approach of accumulated dissipated energy for bidirectional sliding, appropriate for fretting phenomenon description. Dissipated energy (Ed) was formulated as a product of relative displacement (δ) of two bodies in the contact and value of the tangential force (Q) taken from on-line recorded fretting loop (relation 8).

$$Ed = \sum Q \cdot \delta \approx 4 \cdot Q \cdot \delta^* \quad (8).$$

Recently, Huq and Celis [Huq et al. (2002)] used this concept to express the wear rate as a volumetric material loss per unit of dissipated energy in ball-on-disc unidirectional sliding. The following equation for dissipated energy was there presented:

$$Ed = \mu \cdot P \cdot \upsilon_S \cdot t \quad (9),$$

with: t – the duration of sliding test.

Numerous studies [Liskiewicz et al. (2006), Huq et al. (2002), Fouvry et al. (1997), Mohrbacher et al. (1995a), Wei et al. (1997)] showed that linear relationships between the wear volume and the accumulated dissipated energy calculated from the relation 8 can be plotted (Figure 23) and, from the slope of such evolutions, the so-called energy wear coefficient (α) (relation 10) can be identified, what allows a comparison of wear resistance of different bulk materials and surface treatments.

$$\alpha = \frac{V}{\sum Ed} \quad (10).$$

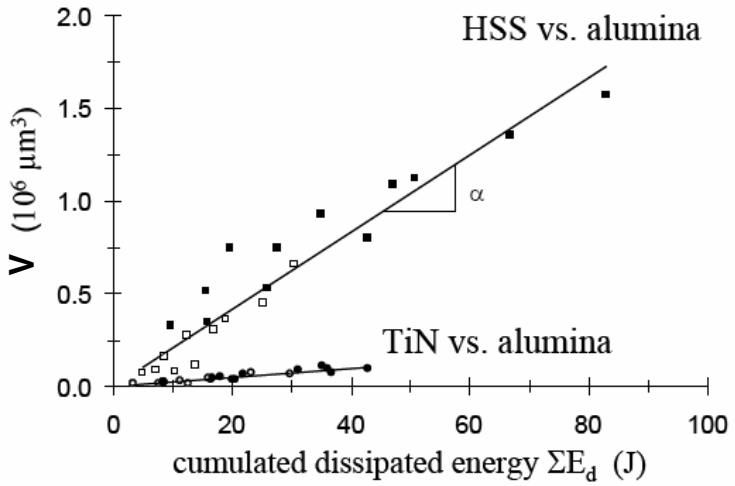

Figure 23: Correlation between wear volume and the accumulated dissipated energy (after [Fouvry et al. (1996)]).

The energy approach, extensively validated for different couples of materials (TiN, steel) [Fouvry et al. (1997) and (2003), Liskiewicz et al. (2005)] was however found to be poorly applicable to describe the behaviour of the tribo-systems characterized by severe adhesion. For brittle materials like hard coatings or hardened steels, debris is obtained and easily ejected from the interface. Thus, the wear kinetics is linked to the input energy provided by the friction work and, linear evolutions between the accumulated dissipated energy and the wear volume extension are observed. When ductile materials like titanium or aluminium alloys are considered, in addition to the energy required to generate the debris, a given quantity of the friction energy is consumed in eliminating the debris from the interface. The higher the sliding amplitude, the faster the debris is ejected, and consequently the higher the energy wear coefficient. The relative impact of sliding on the energy efficiency of wear is therefore explained by the necessity to generate debris and successively eliminate it from the contact interface. The problem of the fretting behaviour of titanium alloys was undertaken and in-depth studied by the group of Fouvry [Fouvry et al. (2004), Paulin et al. (2005)]. They defined a unified fretting wear parameter (FW) (relation 11), expressed in Joules, which controls the wear kinetics of the Ti-6Al-4V alloy

under fretting loadings by weighting the accumulated dissipated energy (E_d) by a normalized sliding amplitude ($\frac{\overline{\delta}_g}{\delta_{g\_ref}}$).

$$FW = \frac{\overline{\delta}_g}{\delta_{g\_ref}} \cdot \sum Ed \quad (11),$$

with: $\overline{\delta}_g$ – the mean sliding distance of the test, δ_{g_ref} – the reference sliding amplitude.

The wear volume (V) can be therefore written:

$$V = \alpha_S \cdot FW \quad (12),$$

with: α_S – the sliding reduced energy wear coefficient.

A linear evolution between wear volume (V) and fretting wear parameter (FW) was then observed for the invariable amplitude conditions for materials that are sensitive to the adhesion phenomenon. By modifying the equation 11, a new formulation of the sliding reduced energy wear factor was introduced (ΣEd_S):

$$\Sigma Ed_S = \sum_{i=1}^{N} \frac{\delta_{g(i)}}{\delta_{g\_ref}} \cdot Ed_{(i)} \quad (13),$$

with: $\delta_{g(i)}$ and $Ed_{(i)}$ – the sliding amplitude and the dissipated energy at the i th cycle.

Then, by using this modified fretting wear parameter it was possible to capture the wear kinetics for variable sequential tests conditions:

$$V = \alpha_S \cdot \Sigma Ed_S \quad (14).$$

The global energy analysis allows the wear coefficients to be determined more or less independent of test conditions, thus a comparison of different palliatives can be performed. Nevertheless, a change toward another contact configuration modifies the established test conditions, what is a great obstacle to develop a general model. The quantitative variables are defined globally while the wear volume related to the accumulated dissipated energy does not consider the local aspects of degradation. Hence, local energy approach put forward by Fouvry S. et al. (1997), appears to be a reliable formulation to relate the local wear to the energy dissipated in the interface of the contact area. Later, this concept was applied and developed by Liskiewicz and co-authors [Liskiewicz et al. (2005a), (2005b) and (2005c)] to determine durability of the hard coatings, which is classically related to the substrate reaching condition. Hence,

compared to a conventional wear volume analysis, wear depth quantification appears more suitable to predict the coating lifetime. By considering the dissipated energy as the controlling parameter of wear, it was assumed that the wear depth (h) is related to the cumulated dissipated energy density ($\sum Ed_h$) (i.e. energy per unit area). The wear depth extension can be therefore formalized through the following simple linear relationship:

$$h = \beta \cdot \sum Ed_h \qquad (15),$$

with: β – the energy wear coefficient defined from the energy wear depth analysis.

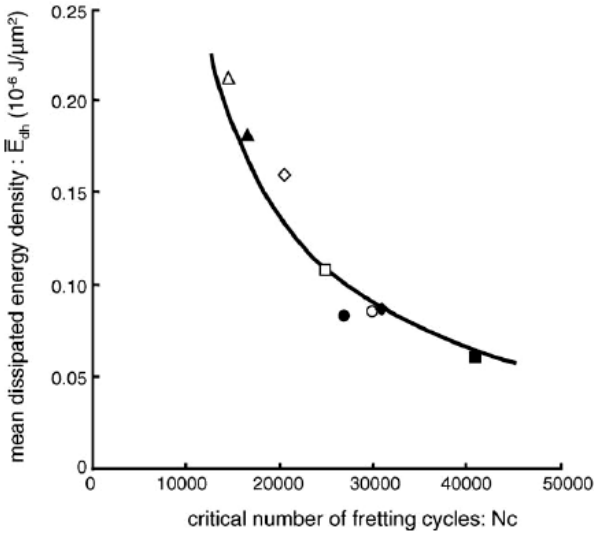

Figure 24: TiC coating endurance for different sliding amplitudes: constant ones and variable; Fretting test conditions: RH= 50%, f = 5 Hz, P = 100N (after [Liskiewicz et al. (2005a)]).

Hence, for a given coating thickness (e), it can be identified the critical dissipated energy density (Ed_{hc}) related to the moment when the substrate is reached:

$$Ed_{hc} = \frac{e}{\beta} \qquad (16).$$

One fundamental conclusion from this relationship can be drawn, namely that the coating endurance is simply related to a critical energy density delivered to the tribo-system. Thus, it can be determined the critical number of cycles N_C to reach the substrate:

$$N_C = \frac{Ed_{hc}}{\overline{Ed}_h} \quad (17),$$

with: $\overline{Ed}_h$ – the averaged energy density through the test.

An energy density-coating endurance chart (i.e. $\overline{Ed}_h - N$ curve) equivalent to the S-N fatigue Wöhler's representation was introduced. The coating endurance is then formalized as a function of the imposed mean energy density (Figure 24).

3. 7. Third body formation and transport

3. 7. 1. Third body approach

The third body approach was developed in the early 70s by Godet and his research group [Godet (1984), Colombie et al. (1984), Berthier et al. (1988), Vincent et al. (1992)]. This concept does not consider the dry contact through volumes of mated bodies, but through the interface notion. Indeed, from the standpoint of volumes or bulk solids, friction and wear are intrinsic properties of materials, whereas, from the standpoint of tribology of interface, friction and wear depend on the chemical composition and rheological properties of the interfaces. Thus, third body approach is based on the assumption that rather the quantity of the debris ejected outside the contact interface is as a factor that controls wear than quantitative determination of the total wear volume of the first bodies. Wear debris remaining in the contact is an operator that separates the first bodies protecting them against direct contact and participates in the process of loads transmission between the first bodies accommodating the greater part of their difference in speed. The third body can be introduced to the interface voluntary (grease, oil, nano-partices, etc.), or can results from wear process of the first bodies – debris film maintained within the contact area.
Third body load-carrying capacities under fretting conditions for steel-steel and chalk-glass contacts were studied by Colombie et al. (1984). They found that wear-protective third body formed from particles can develop even in the latter case (compacted chalk powder bed was formed between contacting bodies). Moreover, analytical characterization of wear debris and interfaces permitted them to propose theory of the third body formation that can be summarized in the following points:

1. Wear particles are formed following surface plastic deformation. Subsequently they are fragmented followed by their strong oxidation (Figure 26);

2. First body wear is governed by the formation and maintenance of the third body and by its abrasiveness;
3. Third body ejection depends on test machine dynamics and specimen shapes;
4. Identical behaviours are noted independently of the used first body material when the third body is formed.

Different aspects of the role of oxide wear debris were investigated by Varenberg et al (2002). They found that the role of oxide wear debris depends on the dominant wear mechanism of fretting wear. When adhesive wear mechanism is dominant the oxide wear particles act like a solid lubricant to reduce the damage caused by fretting. However, when the abrasive mechanism is prevailing the oxide wear particles facilitate the wear rather than protect against it. These results support the work of Colombie et al. (1984). It was shown by Iwabuchi (1991) that depending on normal load and slip amplitude artificially supplied particles of Fe_2O_3 can have either a beneficial effect, reducing wear, or a harmful one, facilitating wear. The former is caused by the quick formation of the compacted oxide layer, which acts as the third body load-carrying structure. It was also demonstrated that removing in-situ-formed wear debris from the interface prevents the severe to mild wear transition [Hiratsuka et al. (2005)].

Subsequent study on the friction interface allowed the third body concept to be progressively extended to the notion of velocity accommodation mechanisms [Berthier et al. (1989), Berthier (1990)]. Authors proposed formalism, which defines different sites and processes occurring at the interface (Figure 25). Contact is here defined by five sites (S_i) and four accommodation modes (M_j). The five identified sites are: two first bodies, a "bulk" third body and two third body films separating rubbing solids and bulk third body. However, four accommodation modes are represented by the elastic, breaking, shearing and rolling ones. The accommodation mechanism is defined by the couple of site and mode (S_iM_j) and 20 different configurations can be distinguished. It was shown by Vincent [Vincent et al. (1992)] that third body tribo-films (S_2 and S_4) are also activated under fretting conditions.

Thus, wear of the mated materials is defined by the quantity of wear particles ejected from the interface and can be calculated based on the determination of the flow of debris (w). For the case of a unidirectional contact this can be expressed by the following relation (18):

$$w = l \cdot \int_0^{h_d} u(y)dy \qquad (18),$$

with: l – the length of contact, h_d – the thickness of the debris film and u – the debris ejecting velocity distribution.

This model well describes real mechanisms of accommodation and damage, nevertheless it is difficult to formalize and does not allow a simple comparison of different tribo-systems. Analysis by means of this model allows an interpretation of the complex tribological phenomena related to impact of third body on decrease of the friction coefficient or its beneficial influence on wear kinetics. The third body and velocity accommodation notions permit also to better account for a big difference of wear kinetics observed for the contacts where debris is relatively easily trapped within the contact area (e.g. fretting) by contrast with the ones where wear particles are rapidly ejected from the interface (e.g. reciprocating sliding). Moreover, presented approach facilitates an analysis of the sliding regimes recognized in fretting. Thus, modification of accommodation site or mode can affect friction evolution and consequently transition from partial to gross slip regime.

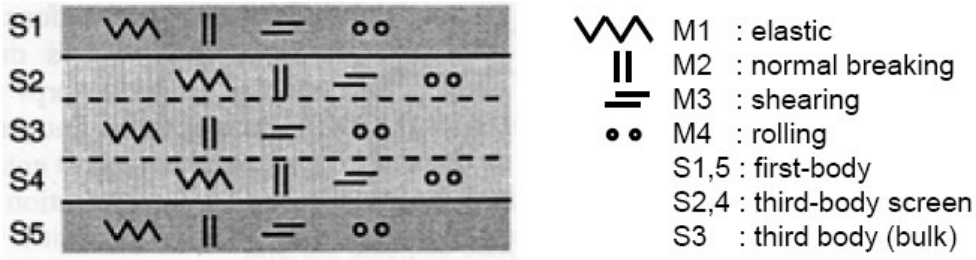

Figure 25: Accommodation mechanisms at the interface [Berthier et al. (1990)].

3. 7. 2. Tribologically transformed structure

Further in-depth study on determination of phenomena related to debris formation in the friction interface permitted a development of third body generation law. Moreover, it was shown that metallic contacts subjected to fretting wear tend to generate a specific transformed layer underneath the surface interface [Blanchard et al. (1991), Zhou et al. (1997), Sauger et al. (2000)]. This specific layer is called the tribologically transformed structure (TTS) and forms following plastic deformations induced by a relative movement of two solid bodies under normal load during the

very first fretting cycles. Authors proposed two-stage wear mechanism where first accumulation of plastic deformation (without wear and TTS) takes place, after which rapid formation of TTS (its formation is finished) and wear by removal of material resulting in formation of wear debris occurs (Figure 26). Thickness of the formed TTS remains constant, while total thickness of worn surface increases (Figure 27). Tribologically transformed structure appears as a nanocrystalline structure, corresponding to the chemical composition of the initial material and made of the more stable structure according to the equilibrium diagram. Its Young modulus is like that of the original metallic structure, but its hardness is significantly higher. By contrast with the compacted debris layer, the TTS contains a very small amount of oxygen, similar to that observed in the bulk material what permits a conclusion that oxygen is not the controlling factor for TTS generation.

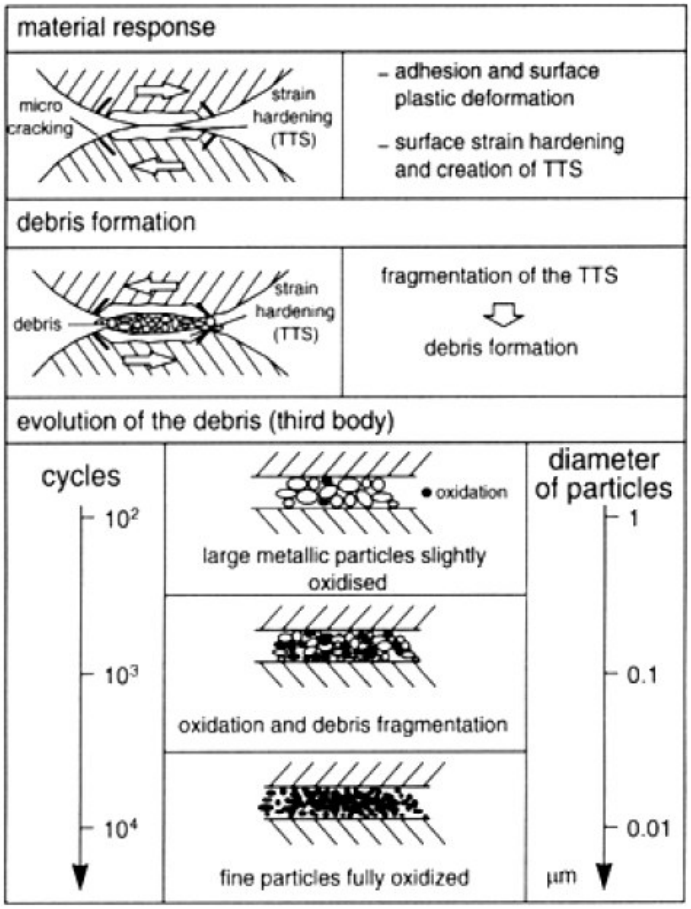

Figure 26: Formation and evolution of the third-body through the contact interface [Blanchard et al. (1991)].

Evidence in favour of TTS existence was presented based on investigations on the self-mated contacts. However, Rigney et al. (1984) investigated heterogeneous materials in the contact. They put forward a theory of mechanically mixed layer (MML). It was shown that local contacts cause large plastic strains in either or both solid components. The plastic deformation changes the near-surface microstructure and makes the material unstable to local shear. As a result, transfer of particles that are further deformed and mixed with counter-face material and/or environmental components is produced and ultrafine-grained material called MML is generated. The very fine microstructure in this transfer material is stabilized by the mixing in (mechanical alloying) of a second phase.

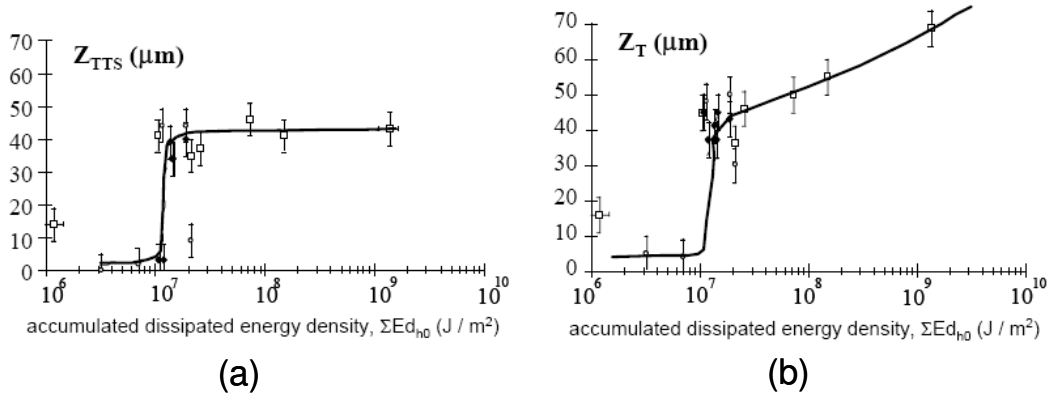

Figure 27: Thickness evolution versus accumulated local dissipated energy: (a) TTS; (b) total worn surface [Sauger et al. (2000)].

Transformations of these superficial layers (TTS and MML) modify the initial properties and thereby behaviour of the contacted materials. Thus these phenomena have to be considered in analyses of debris formation. However, even if we realize that the surface processes induced by the plastic deformation play a crucial role in comprehension of the third body approach, it is still very complicated to integrate this factor into a quantitative model.

3. 7. 3. Flows and rheology notions

Flows and rheology concepts are used for analyzing and structuring dynamic phenomena created by contacts and their interaction with the environment, in the physico-chemical and mechanical sense [Descartes et al. (2002)]. These notions

enable the progression and evolution of solid third bodies (properties, localisation, etc.) to be formalized during their migrations in and outside the contact. The flows of the third body represent the tribological circuit approach (Figure 28). This approach was introduced by Berthier (1990) and defines the different flows of the third body activated in the contact. This is a mechanical approach similar to that used in 'lubrication', i.e. with fluid third bodies, which leads to correlating the changes in friction to the rheology and flows of the solid third bodies circulating in the contact.

The possible flows of the third body that can be activated in an elementary two-dimensional contact are illustrated in Figure 28.

The internal source flow (Q_i) corresponds to the detachment of particles due to TTS, cracking, adhesion, etc. It leads to the formation of the natural third body. The external source (Q_e) flow stems from the introduction of the artificial third body between first bodies. The internal flow is the flow of the third body that circulates between the first bodies (trapped particles). The external flow is the flow of the third body that escapes from the contact. It splits into a recirculation flow (Q_r) and a wear flow (Q_w). The re-circulation flow is composed of the third body re-introduced into the contact. However, wear flow is composed of the third body that has been definitively ejected from the contact and can no longer participate in velocity accommodation.

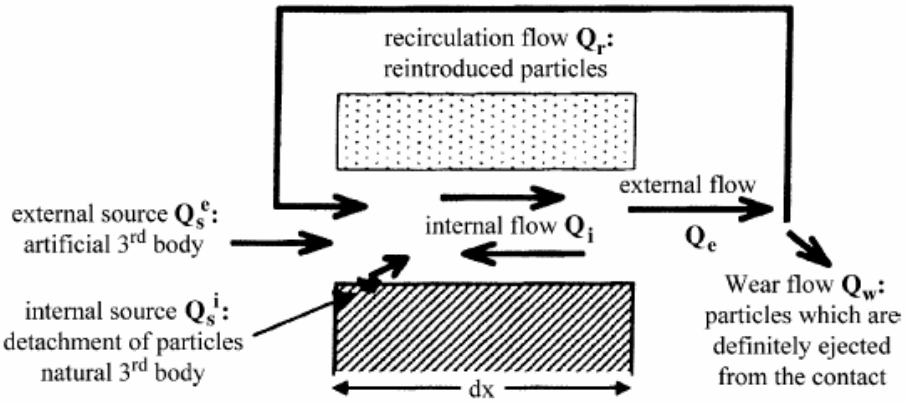

Figure 28: Tribological circuit for an elementary two-dimensional contact (from [Descartes et al. (2002)]).

Rheology notion of solid third body permits, among others, a relative characterization on the basis of their 'cohesion' and 'ductility'. These two properties are determined

by observations of the third body and are related to its morphologies and texture. In this case the word texture is not used in the metallurgical sense but more classically refers to the orientation of the third body layers or the third body particles, their size, shape and arrangement. The term cohesion is chosen by analogy with cohesion of powder mixture. The qualitative comparison of different third body cohesions for the scale of observation chosen is depicted in Figure 29. Third body of very low cohesion is very powdery and composed of small particles (Figure 29a) by contrast with highly cohesive third body that is very compact and appears to be more compressed (Figure 29c).

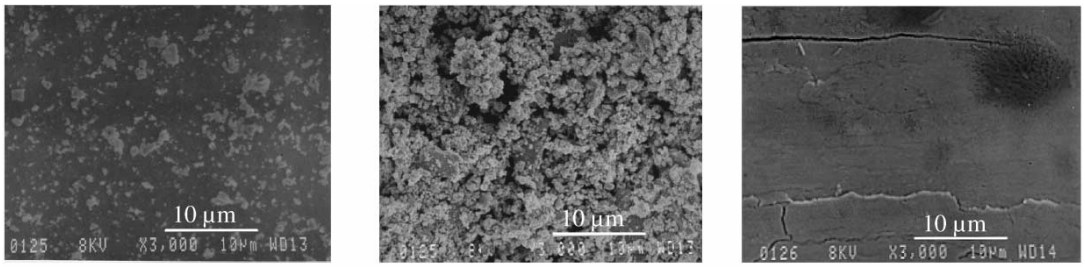

Figure 29: Relative cohesion of the solid third body (SEM images): (a) very low; (b) low; (c) high (from [Descartes et al. (2002)]).

The term ductility chosen by analogy with plastic flow characteristics of metals and it expresses the ease with which third body spreads and extrudes in the contact. Low ductility means that the third body spreads little and only covers a small area of the contact (Figure 30a). On the contrary, high ductility means that third body spreads easily and covers a large part of the contact are (Figure 30c).

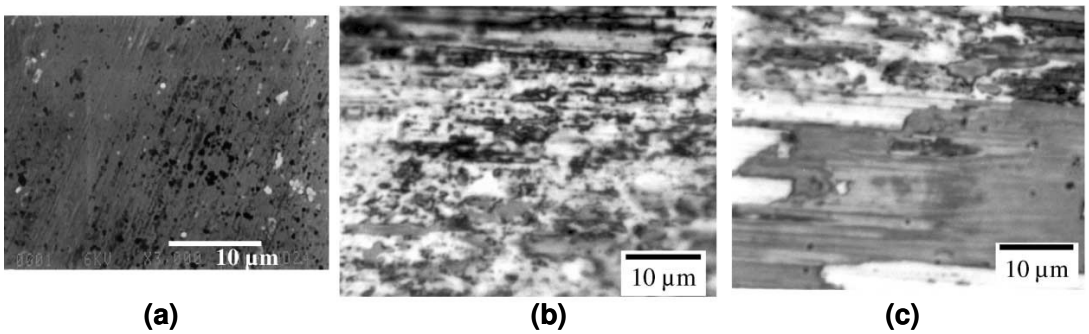

Figure 30: Relative ductility of the solid third body (SEM images): (a) low; (b) not very high; (c) high (from [Descartes et al. (2002)]).

3. 8. Fretting damage methodology

Fretting can have dangerous repercussions for the operation of mechanical systems. Particularly perilous is damage caused by cracking as it often cannot be detected before the subjected component ruptures completely. Hence, it is of great importance to predict dominating mechanism of fretting damage and determine the risk of the component failure.

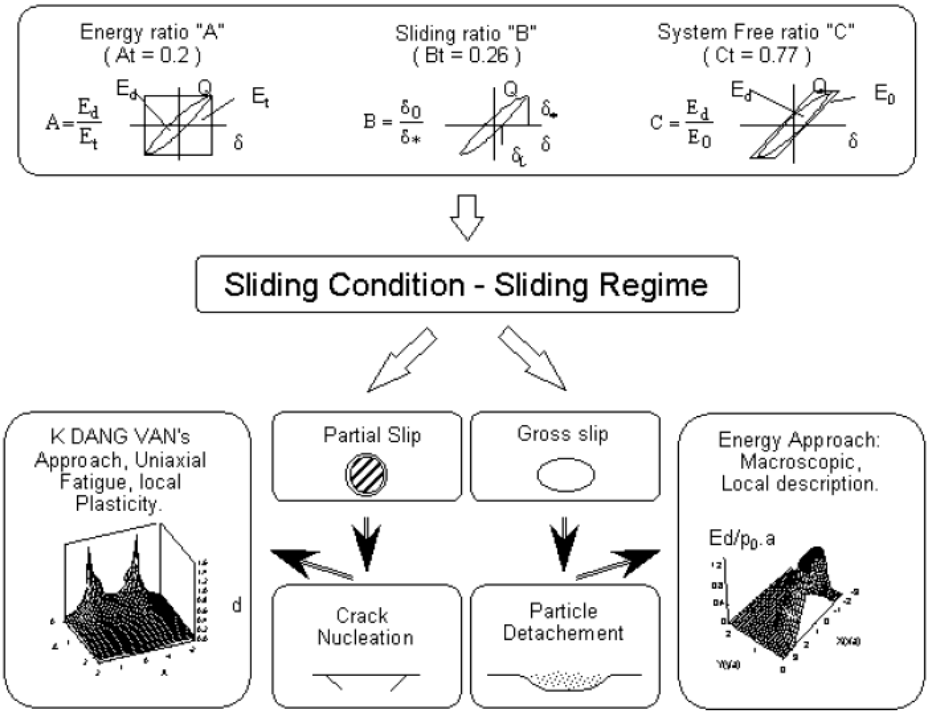

Figure 31: Illustration of the methodology developed for the fretting damage analysis (after [Fouvry et al. (1996)]).

In order to predict the fretting damage the methodology elaborated by Fouvry et al. (1996) was proposed (Figure 31). It consists in an identification of sliding condition through the quantitative parameters A, B, C, which define the transition between partial and gross slip regimes. When the fretting regime is defined the main mechanism responsible for surface process degradation can be indicated. If it is the partial slip, the cracking phenomenon is expected and nucleation condition can be precisely determined and quantified by one of the fatigue approaches, e.g. by means of multiaxial fatigue analysis of Dang Van [Dang Van (1993)]. However, gross slip conditions favour material removal and debris formation as a principle material

surface degradation process. In this case damage can be quantitatively described by referring the loss of material to the energy dissipated in the contact (e.g. as in Figure 23).

3. 9. Palliatives in fretting

Considering the economical and social losses that may be caused under fretting loadings, some appropriate steps should be taken in order to eliminate or at least to limit the adverse effects of fretting. The overview of various palliative strategies including different treatments such as lubricants, low friction coatings, soft thick coatings, shot peening and hard ceramics were performed by Fouvry et al. [2006].

Protection against fretting has to be taken into account already during design stage of the fretting couple. By designing the appropriate contact geometry of nominally stationary junction, the concentration of the stresses and consequently cracking by fretting fatigue can be avoided. Construction treatment can also contribute to reduction of reciprocal displacement amplitude [Guzowski (1998)]. Nevertheless, damage by fretting cannot be completely avoided as this kind of destruction process was reported to take place even under displacement amplitude lower than 1 μm [Kennedy et al. (1983)].

Another very important aspect allowing fretting damage to be reduced is adequate material selection for mated components. In general, tribo-systems with polymers are characterized by higher fretting resistance compared to e.g. steel/steel ones, and hard steel has higher resistance than the soft one. Polymers display lower Young modulus, thus under fretting loadings most of the displacement is accommodated by elastic deformation rather than by sliding. This can explain why with polymers smaller wear is observed. Of course, there are always some exceptions like high chromium steel where brittle and hard oxides formed on its surface contribute to increase of wear rate [Varenberg et al. (2002)].

Appropriate surface engineering treatments can provide an effective protection against fretting. Thus, the following methods with adequate processes increasing fretting resistance can be enumerated [Harris et al. (1985), Labedz (1988), Waterhouse (1988), Fu et al. (2000)]:

- *Induce a residual compressive stresses*: one of the most effective way to decrease damage caused by fretting fatigue (e.g. by shot-peening, nitriding,

carburizing, ion implantation, etc.). Fridrici et al. (2001) showed that compressive residual stresses have an important effect by limiting crack propagation. By contrast, Kubiak et al. (2005) observed only negligible impact of shoot-peening on crack behaviour. Indeed, influence of shoot-peening on crack initiation and its propagation is directly related to the imposed contact loadings. Thus, large sliding can relax the compressive stresses very fast diminishing significantly the positive effect of that kind of surface treatment;

- *Decrease of coefficient of friction:* lower value of friction forces leads to lower shear stresses and related destruction response. This effect can be produced by introducing solid lubricants or applying different surface treatment techniques PVD, CVD, nitriding, carburizing, etc.;
- *Increase of the surface hardness*: this action prevents the adhesive and abrasive wear in fretting (e.g. by nitriding, shot-peening, PVD and CVD techniques, etc.);
- *Control of surface chemistry*: tribochemical reactions that proceed onto the interacting surfaces can produce lubricating layers (e.g. oxide or nitride layers) and significantly improve fretting resistance.

An effective method to decrease the coefficient of friction and wear rate is to apply lubricants [Kalin et al. (1997), Zhou et al. (1999)]. However, on certain conditions such as low sliding speed, low sliding amplitude or high pressure, lubricating does not always bring desirable effects. Shima et al. (1997) reported that for small strokes, i.e. for conditions approaching almost complete 'stick' regime, values of the coefficient of friction values under oil lubrication were well in excess of double those observed without it. These high values were accounted for by the fact that the oil was unable to penetrate into the fretting contact region, but did maintain a shield around it, so that metal-on-metal contact was maintained under oxygen deprived conditions. Thus, an effective lubricating is possible in case of fretting only if constant inflow of grease or oil can be maintained within the contact area. Moreover, it should be noticed that for certain mechanical systems an application of liquid oils is not possible, e.g. at elevated temperature working conditions, and then other palliative solutions has to be introduced e.g. solid lubricating coatings.

4. INFLUENCE OF ENVIRONMENTAL CONDITIONS

Apart from mechanical loadings the environmental factors: temperature and relative humidity can strongly affect the tribological behaviour of contacted components, so their influence has to be taken into account with particular care as well. Many industrial tribo-systems have to withstand elevated temperature conditions or frequent changes in ambient humidity for long hours without failure. For example, stator vane/bushing joints in turbofan engines, electrical contacts in car engines or nuclear power plants are exposed to the elevated temperature conditions. Hence, comprehension of the effect of the environmental factors is a crucial issue for engineers and researchers, who put a lot of effort into finding adequate material treatment solutions to upgrade the resistance to wear of machine components working even under very high temperatures.

In the present dissertation dry contacts subjected to fretting wear under elevated temperature conditions are being studied, thus effect of temperature is discussed extensively whereas of humidity only briefly.

4. 1. Effect of elevated temperature

The elevated temperature in the contact area of interacting bodies can be induced either by frictional heat during room temperature tests (e.g. for unidirectional sliding) or by external heat (typically for reciprocating sliding). External heat is important in high-temperature sliding, such as can be encountered in jet engines. Elevated temperature conditions promote oxidation process that may drastically change tribological response of the systems. Thus, static oxidation and tribo-oxidation processes of metals and alloys are precisely described below.

4. 1. 1. Oxidation of metals and alloys

The type of oxides formed as a result of tribochemical processes that takes place in the interface of contacting bodies cannot be deduced without considering the aspect of static oxidation of metals. This, in turn, cannot be studied without employing thermodynamic and kinetic bases of the possible reactions. Thermodynamics and kinetics provide a good background for the prediction and comprehension of the static oxidation results. During oxidation process metals may react with oxygen to produce

an oxide at the surface. There is interest in three aspects of this reaction: the ease with which the metal oxidizes, the nature of the oxide film that forms, and the rate at which oxidation occurs [Askeland (1998)].

The ease with which oxidation may occurs is given by the Gibbs free energy of formation of the oxide. The overall equation for oxidation of a metal (Me) may be represented as follows:

$$xMe(s) + \frac{1}{2} yO_2(g) \leftrightarrow Me_x O_y(s) \qquad (19).$$

The driving force for this reaction is the Gibbs free energy change ($\Delta G(T)$) associated with the formation of oxide from the reactants at the temperature T and it can be written as:

$$\Delta G(T) = \Delta G^0(T) + R \cdot T \cdot \ln Q \qquad (20),$$

with: $\Delta G^0(T)$ – the standard Gibbs free energy, R – the universal gas constant, T – the temperature in Kelvin and Q – the reaction quotient.

The standard Gibbs free energy of formation of a compound is the change of Gibbs free energy that accompanies the formation of 1 mole of that substance from its component elements, at their standard states (the most stable form of the element at 25°C and 1 bar). At equilibrium, when $\Delta G(T) = 0$ the equation 20 becomes:

$$\Delta G^0(T) = -R \cdot T \cdot \ln K \qquad (21),$$

with: K – the equilibrium constant for any reversible reaction at equilibrium.

The ease with which different metals tend to form oxides can be read off the Ellingham diagram (Figure 32 [Ellingham (1944)]), which depicts standard Gibbs free energy change (ΔG^0) for the oxidation reaction as a function of the temperature. The higher is the negative ΔG^0 the higher is the tendency of a metal to spontaneous formation of an oxide in alloy. Thus, the noble metals, which are easily reduced, occur at the top of the diagram, while the more reactive metals are at the bottom. However, some of the metals with high tendencies to oxidation (Al, Ti) resist oxidation from room temperature up to certain elevated temperatures due to the impermeability of the coherent compact oxide film that forms first. The protective nature of formed oxide layers can be qualitatively assessed by using Pilling-Bedworth law [Askeland (1998)]. The related parameter, so-called Pilling-Bedworth ratio defined as a ratio of oxide volume grown to unoxidized material consumed in oxidation, can be determined. And thus, if the Pilling-Bedworth ratio is less than one,

the oxide occupies a smaller volume than the metal from which it formed. The oxide coating is therefore porous and oxidation continues rapidly – typical of metals such as magnesium. If the ratio is one or two, the volumes of the oxide and metal are similar, and an adherent, nonporous, protective film forms – typical of, above mentioned aluminium and titanium. If the ratio exceeds two, the oxide occupies a large volume and may flake off the surface, exposing fresh metal that continues to oxidise – typical of iron.

Oxide layer or scale on the surface of metal or alloy can give protection by acting as a barrier between metal and reactive gas (oxygen). However, effectiveness of such barrier is, among others, a function of temperature-dependent diffusion rate of the reactants across the barrier and defect nature of the barrier. Typical oxides in metals are Al_2O_3, NiO, Cr_2O_3, SiO_2, MgO, FeO, Fe_2O_3. However, oxide scale formed on metal is not often uniform, but consists of different type of oxides of the same element within thickness. For example, in case of pure iron there is thin inner layer of Fe_2O_3 on the surface above which there grows outer more defective layer of Fe_3O_4 and at higher temperature (above 570°C) FeO phase that is very defective poor barrier to diffusion becomes stable [Dobrzanski (1999)]. As it can be got from Ellingham diagram (Figure 32) Fe_3O_4 has the lowest standard Gibs free energy, so it tends to form easier than Fe_2O_3. In order to predict the oxidation results the stability of particular oxides at given temperature has to be taken into account as well. And thus, magnetite (Fe_3O_4) is known to undergo the following phase transformation with temperature increase [De Boer et al. (1954), Goto (1964),]:

$$Fe_3O_4(\text{magnetite}) \overset{200^\circ C}{\rightarrow} \gamma - Fe_2O_3(\text{maghemite}) \overset{400^\circ C}{\rightarrow} \alpha - Fe_2O_3(\text{hematite}) \quad (22).$$

In case of alloys, there may take place selective oxidation. It means that some alloying elements (Cr, Ti, Al, Si etc.) of an alloy, have a higher affinity for oxygen than other alloying elements (Ni, Fe, Co, Cu etc.), and consequently, may oxidize earlier (according to thermodynamic aspect, see Ellingham diagram (Figure 32)) and more rapidly. Thermodynamics allows prediction of the final equilibrium state for a reaction, but gives no information about reaction rate. Kinetics expresses the speed of the oxidation process. Reaction rates depend on a number of factors, such as temperature, oxygen pressure, dwell time, surface area or surface pre-treatment. The corresponding kinetics equations can be written assuming an adequate oxidation law

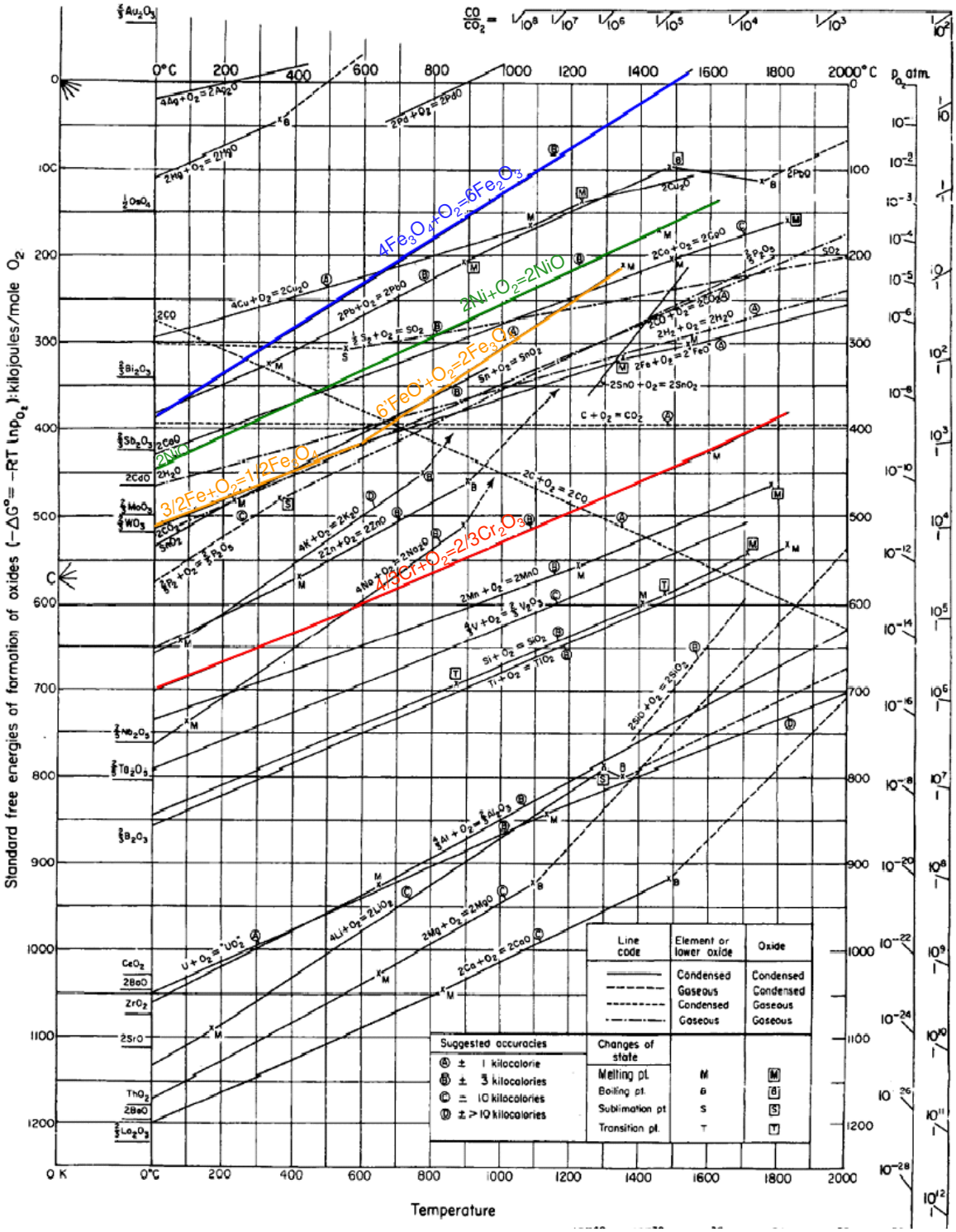

Figure 32: Ellingham diagram (after [Ellingham (1944)]); Alloying elements, which are the components of the investigated in the present dissertation alloys, are presented in colours.

(i.e. parabolic, logarithmic etc.). As regards the effect of alloying elements on oxidation rate, Al, Si and Cr form stable oxides with low diffusion coefficients for oxygen. Even though, they all have high affinity with oxygen, when formed, the thin compact oxide layer resists oxygen diffusion and limits further oxidation of the alloy. Some other metals such as Ni, Fe, Co, W, Ti do not form protective oxide layers and their oxidation rate is high. For example, in case of high temperature oxidation in air of Ni-20%Cr alloy (typical gas turbine alloy) complex oxides are formed, i.e. thin protective barrier layer of Cr_2O_3 at the base of the NiO-rich scale, containing spinel-type $NiCr_2O_4$ oxide [Stott (1998)].

4. 1. 2. Tribological behaviour of metals and alloys

Although there is good understanding of static oxidation of metals and alloys as well as mechanisms of oxide formation, this is not entirely clear (e.g. kinetics of oxidation) in situations when relative motion under load occurs between contacting bodies. The oxides can be considered as in-situ solid coatings for applications that involve high temperature conditions or where the application of engineered solid coatings is either difficult or impossible. It was shown that even at room temperature, the development of oxides within the area of the contact may lead to the reduction to some extent metal-to-metal interactions and, hence wear rate, giving mild wear conditions. Higher temperature of the contact area promotes higher oxidation rate what may support the development of wear-protective oxide layers onto contacting surfaces as a result of tribo-sintering of oxide particles. However, these oxides are not always effective in reducing the wear of metals. The beneficial effect of in-situ formed oxides depends on their chemistry and structure.

4. 1. 2. 1. Flash temperature

Transformation of a part of frictional energy to heat is responsible for increase in the temperature of sliding bodies, especially in real contact regions (at the peaks of contacting asperities). Calculation of this temperature and prediction of its distribution is very difficult due to a complexity of the problem where a number of interfacial properties, usually undetermined in details, affect the generation of frictional heat in tribo-contact. For example, in fretting wear, the mechanical and thermal properties of

interface are constantly changing due to its tribochemical transformations what makes them impossible to determine exactly.

The review of different models for calculating temperature rise (called flash temperature) for dry ball (silicon nitride)-on-flat (steel) contact under fretting conditions was performed by Kalin et al. (2001). The authors showed significant discrepancies between the results that can be obtained for the same contact and loadings using different models. Figure 33 shows the average and maximum temperature rise obtained according to different models at 88 N normal load, 50 μm displacement amplitude and 210 Hz frequency of oscillation where no variation of influencing factors was employed. It can be observed that the temperatures calculated using the same input parameters vary quite significantly, by about a factor of 3. Moreover, the temperature of contact area was shown to increase with displacement amplitude due to increasing sliding speed. By using different methods for determination of the real contact area or different input values for the thermal conductivity the calculated flash temperature during dry fretting can vary by as much as dozen hundreds of degrees Celsius. Such large mismatch suggests that severe limitations in accuracy must be considered and care in the interpretation of results taken. Notwithstanding, it must be noticed that in this consideration [Kalin et al. (2001)] tests were performed under very high frequency of oscillation (210 Hz), which results in fast heat generation and accumulation in small contact dimension.

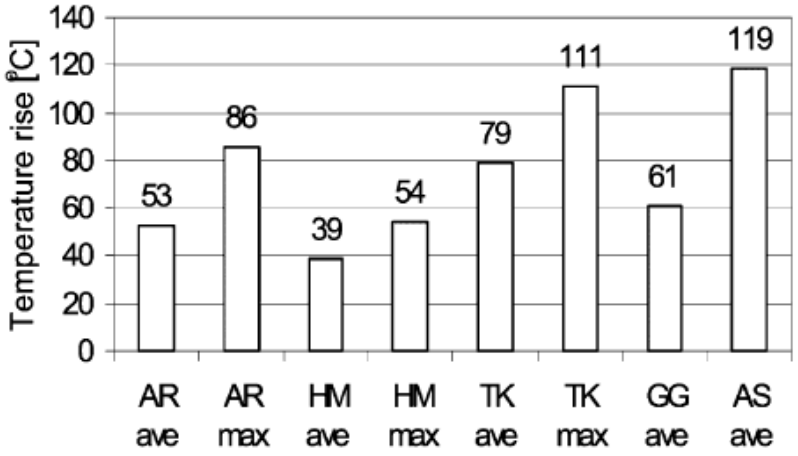

Figure 33: Results of various models for the average and maximum temperature rise under unlubricated fretting at 50 μm displacement amplitude (from [Kalin et al. (2001)]); Symbols: AR=Archard, HM=Holm, TK=Tian–Kennedy, GG=Greenwood–Greiner, AS=Ashby–Abulawi–Kong.

Low frequency (10 Hz) fretting experiments for unlubricated ball-on-flat steel (AISI 52100) self-mated contact was studied by Kolodziejczyk et al. (2007). Authors calculated that the flash temperature for the most severe test conditions investigated (2 GPa maximal Herzian pressure and 150 μm displacement amplitude) did not exceed the value of 30 K above the test temperature. Thus, the structural changes of the material in the contact were there interpreted to be hardly probable due to frictional heat, but more likely due to mechanical transformations [Sauger et al. (2000)].

Another authors [Glascott et al. (1985)] investigated the low-speed reciprocating sliding (peak-to-peak amplitude 2.5 mm) of dry Jethete M152 self-mated contact under a load of 1.5 kg. They demonstrated that a relatively high number of load-carrying junctions occur in the interface between plastically deformed, wear-protective oxide layers, so load supported by any one junction is quite small. Hence, the mean, surface, flash temperature rise during sliding would be expected to be relatively small. That was confirmed by their computation (using Archard's model), which gave a value of mean temperature rise at a typical oxide-oxide junction as low as 2°C.

In the present dissertation low frequency fretting experiments are being investigated. Thus, by taking into account above discussion on the flash temperature aspect the effect of the frictional heat on the temperature rise in the studied contacts can be assumed to be negligible.

4. 1. 2. 2. Generation of oxides during sliding wear

The mechanisms of oxide generation under low-speed reciprocating sliding at elevated ambient temperatures were investigated extensively by the group of prof. Stott [Glascott et al. (1985), Stott (1998), Jiang et al. (1998)]. Three limiting cases for the generation of oxide were identified [Stott (1998)]:

1. Oxides may be formed by oxidation of the metal asperities while in contact. At the same time, more general oxidation of all the apparent area of contact occurs. Oxides from both sources may be removed completely during subsequent traversals, exposing clean metal to the environment that is reoxidized in the next traversal. This is similar to the mild oxidational wear model [Quinn (1967, 1983a, 1983b)]. The resulting wear debris may be ejected from the contact or cause abrasion of the metal substrate,

increasing wear, or may be compacted between the sliding surfaces to give wear-protection. This was termed an 'oxidation-scrape-reoxidation' mechanism.

2. Some particular conditions like high ambient temperature may lead to the following scenario. The oxides developed during sliding (or present on the surface prior to sliding) may be removed only partially or not at all by the sliding action and continue to thicken with time. This wear situation was termed a 'total oxide' mechanism. Such mechanism associated with deformation of the oxides can give protection against further wear.

3. Another possible source of oxides during sliding is oxidation of metallic debris. Such wear debris particles, produced in the early stages of the test, may be broken up and fragmented under sliding action, thereby exposing fresh areas of clean metal for further oxidation. This wear situation was termed 'metal debris' mechanism. During sliding, the oxidation process is promoted by the heat of deformation and the increased energy of the particles due to the increased defect density and surface energy. Moreover, if the heat of oxidation released is taken into account, fine metallic particles may be oxidized spontaneously and completely. Hence, a significant amount of oxides can be generated during low-speed sliding, even at low temperatures. The resulting oxide debris can develop into a wear-protective layer, as considered later.

4. 1. 2. 3. Establishment of wear-protective layers

It was already mentioned that wear particles generated in the interface can strongly affect tribological behaviour of metals. In case of reciprocating sliding or alternating fretting the wear debris can be retained on the contacting surfaces as shown schematically in Figure 34 [Stott (1998)]]. Although, some are lost, resulting in wear, others are maintained within the scars where they are comminuted by repeated plastic deformation and fracture while moving freely between the sliding surfaces. However, once they are reduced to a sufficiently small size, they can be agglomerated at certain locations, particularly in grooves, due to adhesion forces between solid surfaces arising from surface energy, and develop compact layers that eventually become load-carrying (Figure 34c). An adhesion between solids can be represented by a nominal tensile stress parameter (σ_a). To break the N pairs of particle contacts adhered together the σ_a can be expressed by the following relation [Jiang et al. (1998)]:

$$\sigma_a = k \cdot D^{-1} \cdot \gamma \qquad (23),$$

with: k – the constant of proportionality, D – the particle diameter, γ - the surface energy between two solid surfaces.

According to the relation 23, the adhesion strength of particle agglomerates increases with decrease in particle size. The rise of temperature leads to increase of surface energy between solids, thus of adhesion as well. Consequently, fine particles are sintered together to some extent to form more solid layers. The sintering process of fine particles was reported to occur at temperatures only slightly above 20°C [Zhou et al. (1989)], but of course is more significant at higher temperatures. This reduces

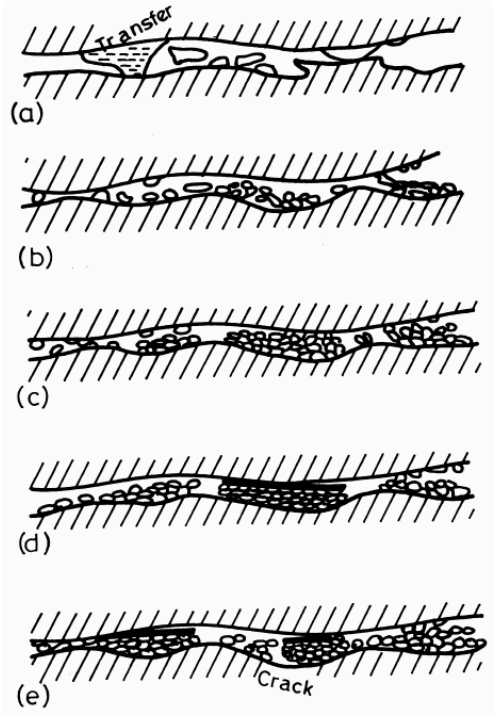

Figure 34: Schematic diagram showing the processes of development of wear debris particle layers and 'glaze' layers during dry sliding wear (after [Stott (1998)]); (a) Generation of metallic wear debris; (b) Comminution, oxidation and agglomeration of debris particles; (c) Compaction of agglomerated debris particles; (d) development of 'glaze' layer over compacted particle layer under some conditions; (e) Breakdown of wear-protective layers and development of new protective layers in other areas.

material loss since newly formed debris particles are recycled into the layers while, as the particles are heavily deformed and oxidized, the layers are hard and give protection against wear damage. As sliding progress, two competitive processes take place: break-down of the layers (Figure 34e) and sintering between particles, which consolidate the layer (Figure 34d). The latter process is accelerated as temperature in the contact area elevates. When the surface becomes solid before break-down occurs, wear is low due to formation of so-called 'glaze' layer on top of the compacted debris particles. On the other hand, if there are weak sintering bondings in particles layers, the loose hard oxide particles are removed more easily resulting in higher wear.

The conclusion from above discussion is that the elevated temperature conditions promote formation of the wear-protective glaze layers. It was reported that there is a certain critical value of temperature required to establish a 'glaze' surface under a given set of conditions [Stott (1998)], depending also on investigated materials [Glascott et al. (1985)]. Summarizing, the sliding wear process at different temperatures can be depicted schematically as in Figure 35.

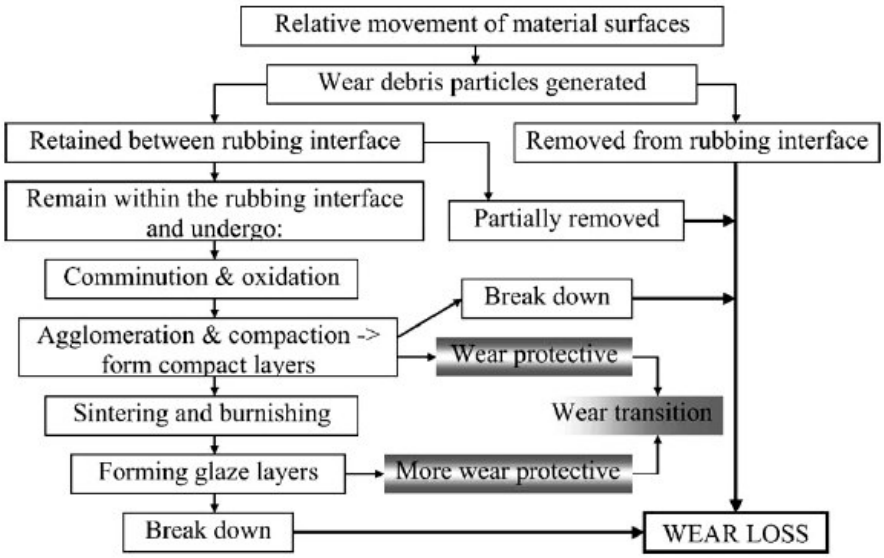

Figure 35: A diagram showing the wear model for dry sliding wear of metals at various temperatures (from [Jiang et al. (2004)]).

On the basis of the above description of a wear process, a mathematical model accounting for the establishment of such wear-protective layers was developed [Jiang et al. (1995)]. In the model it was assumed that the wear rate of the wear-reducing

layers is negligible compared to that of other areas and wear debris particles are only produced from unprotected zones. Thus, the wear volume after sliding time (t) is expressed by the following equation:

$$V(t) = \frac{\pi}{6}\int_0^t \left\{ A(t) \cdot N(t) \cdot [1 - C_e(t)] \int_0^\infty [D^3 \cdot f(D) \cdot P_r(D)] dD \right\} dt \qquad (24),$$

with: $N(t)$ – the number of wear debris particles formed per unit time at time t, $A(t)$ – the apparent area of the wear scar at time t, $C_e(t)$ – the effective coverage by wear-protective layers at time t, $f(D)dD$ – the percentage of newly generated particles that fall in the diameter range of D to $(D + dD)$, and $P_r(D)$ – the probability that a wear particle of diameter D is removed from the wear track.

The volume of wear debris particles retained within the rubbing surfaces at time t ($V_{retained}(t)$) is as follows:

$$V_{retained}(t) = \frac{\pi}{6}\int_0^t \left\{ A(t) \cdot N(t) \cdot [1 - C_e(t)] \int_0^\infty D^3 \cdot f(D) \cdot [1 - P_r(D)] dD \right\} dt \qquad (25),$$

with: $[1 - P_r(D)]$ – the probability that a wear particle of diameter D will be retained in the interface.

If all particles retained within the rubbing surfaces are assumed to be compacted eventually to form wear protective layers and the average thickness of these layers is δ, then the coverage of the wear surface by such compact wear particle layers ($C_{compact}$) is related to the volume of the retained particles ($V_{retained}(t)$), as follows:

$$C_{compact} = \frac{V_{retained}(t)}{A \cdot \delta} \qquad (26).$$

These layers are particularly effective if a 'glaze' oxide of critical thickness ($\delta(c)$) can be established on their surfaces. The oxidation kinetics of the wear debris can be expressed in terms of a scale thickness (x) as:

$$x = g(t) \qquad (27),$$

with: $g(t)$ – the relevant function of time.

Hence, the critical time ($t(c)$) for a 'glaze' of critical thickness ($\delta(c)$) to develop on the compacted debris is:

$$t(c) = g^{-1}(\delta(c)) \qquad (28),$$

with: $g^{-1}(\delta(c))$ – the inverse function of $g\ (t(c))$.

If an area of compacted particle layer $dA_c(\tau)$ is established at time τ, then an area of 'glaze' equal to $dA_c(\tau)$ should have developed after a further period ($t(c)$), i.e. at a time $(\tau + t(c))$. Thus, the coverage of the apparent wear surface by 'glaze' layers (C_{glaze}) at time t is [Jiang et al. (2004)]:

$$C_{glaze}(t) = \int_0^{t-t_c} \frac{dA_c(\tau)}{A(t)} \qquad (29).$$

Thus, it is obvious that both a compacted particle layer and a 'glaze' layer may coexist. They are both protective but the latter is more effective. The fractional coverage of the wear surface by 'glaze' layer needed to cause the severe to mild wear transition is much less than that by non-'glaze' compact particle layer.

When both types of wear protective layers are present, the concept of an equivalent protective coverage of the wear surface (C_e) can be introduced (relation 30).

$$C_e = \frac{C_{compact}}{C_{compact\_limit}} + \frac{C_{glaze}}{C_{glaze\_limit}} \qquad (30),$$

with: C_{glaze} – the surface coverage of glaze layers, $C_{compact\_limit}$ (found to be 0.4-0.6) and C_{glaze_limit} (found to be 0.2) – the critical coverage of compact and glaze layers, respectively, beyond which the wear surfaces become completely protected and wear transitions from a high rate to a low one occur.

The model discussed above was successfully implemented to predict the wear and surface coverage of wear protective layers formed on Nimonic 80A alloy under various loads at 20°C and 400°C (Figure 36).Wide agreement between calculated results and reported experimental observations was obtained. Later, the model was developed to study the effect of partial pressure of oxygen on the generation rate of wear debris particles [Jiang et al. (2004)]. This effect was found to be in two ways. On the one hand, an increase in partial pressure of oxygen leads to a decrease in particle size, which facilitates the development of compact wear-protective layers, therefore reduces wear. On the other hand, the generation of rate of wear debris increases with increase in partial pressure of oxygen, which promotes wear. Also there, a reasonable agreement between calculated results and experimental investigations was achieved.

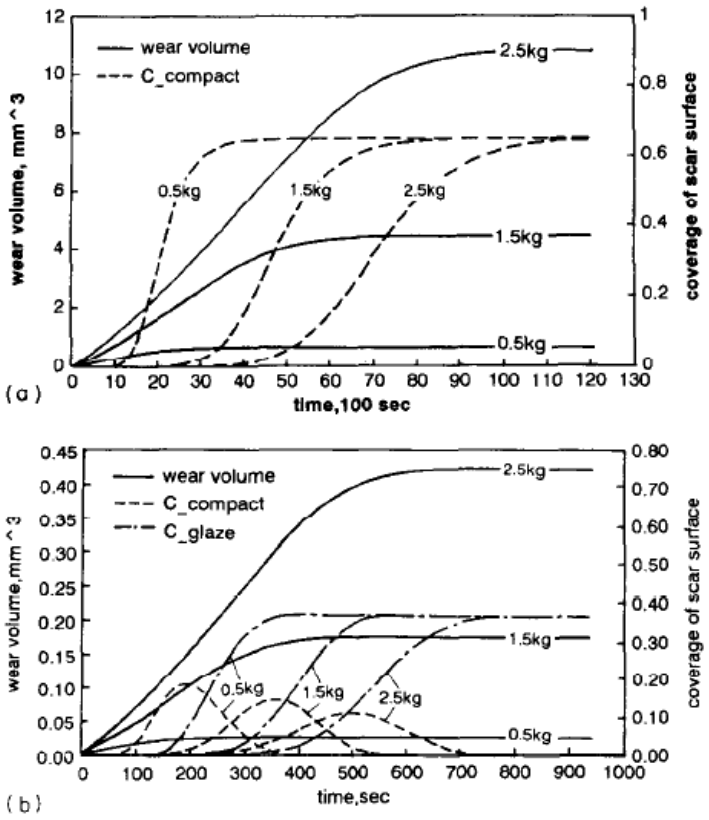

Figure 36: The calculated plots of wear versus sliding time under different loads at (a) 20°C and (b) 400°C (from [Jiang et al. (1995)]).

A 'glaze' layer formation was also reported by Inman et al. [Inman et al. (2005), Inman et al. (2006)]. The authors studied profoundly the impact of temperature and sliding speed on wear behaviour of supperalloys (the Nimonic 80A/Stellite 6 contact). They showed that low speed (0.314 m/s) sliding conditions accompanied by the high temperature (between 510°C and 750°C) favour compaction of particles and their sintering to form a wear protective nano-structured 'glaze' layer. The rapid formation of this glaze layer from primarily cobalt-chromium debris transferred from (and also back to) the surface of the Stellite 6, kept wear of both the Nimonic 80A and Stellite 6 to very low levels. However, increasing the sliding speed to 0.905 m/s suppressed glaze formation with only a patchy, unstable glaze forming on the Stellite 6 counter-face and an absence of glaze development on the Nimonic 80A sample. The high amount of oxide debris generated at 0.905 m/s instead acted as a loose abrasive assisting wear of especially the Nimonic 80A. This behaviour was attributed to a change in oxide chemistry (due to the dominance of nickel and chromium oxides

generated from the Nimonic 80A) resulting in poor oxide sintering characteristics, in combination with increased mobility and reduced residency of the oxide debris at 0.905 m/s. The obtained results allowed the authors to compose a simple wear map (Figure 37) detailing the effects of sliding speed and temperature on the wear of the investigated contact [Inman et al. (2006)].

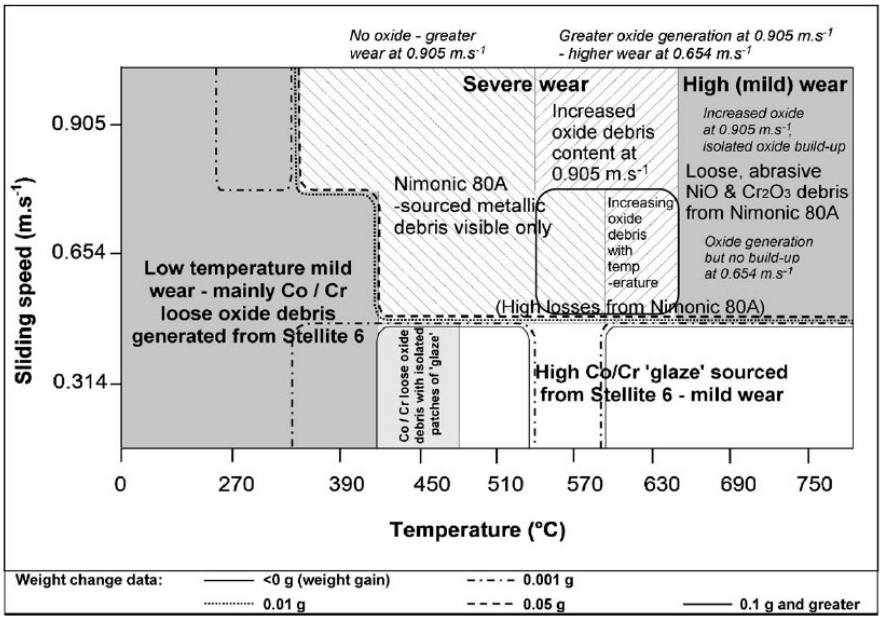

Figure 37: Sliding speed versus temperature wear map for the Nimonic 80A/Stellite 6 contact (after [Inman et al. (2006)].

4. 1. 2. 4. Kinetics of in-situ oxidation

In the beginning parabolic oxidation rate characteristic of static oxidation was assumed to take place at the contact area during sliding, e.g. in the oxidational theory of wear [Quinn (1967)]. This is controlled by the diffusion of metal or oxygen ions through the oxides. In the oxidational theory of wear, Quinn (1967) produced an expression for the wear rate under mild wear conditions, based on the equation. He modified Archard's interpretation by assuming that $(1/K)$ encounters are necessary to produce a critical oxide thickness (ξ) at the real area of contact (A) and obtained the following expression for the wear rate under mild conditions:

$$W_{theory} = \left[\frac{d \cdot A_p \cdot e^{-Q_p / RT_f}}{\xi^2 \cdot \rho_0{}^2 \cdot f_0{}^2 \cdot v} \right] \cdot A \qquad (31),$$

where: W_{theory} – the wear rate predicted by oxidational wear theory, d – the distance of sliding contact at an asperity, A_p – the Arrhenius constant for parabolic oxidation, Q – the oxidational activation energy for parabolic oxidation, R – the molar gas constant, T_f – the temperature of the real area of contact between the pin and the disc, ρ_0 - the average density of the oxides formed at the real areas of contact, f_0 - the mass fraction of oxide film which is oxygen, v - the speed of sliding at the contact zone.

He showed that if the sliding speed is comparatively slow or the loads are light the frictional heating is negligible and then the development of the contacting plateau of oxides is not sufficiently large for it to be the preferred contact region. This is describing a mechanism of severe wear. When temperature of the real area of the contact is high enough (under high speed or loads conditions) to provide sufficient amount of frictional heating, then the contacting plateau is oxidized preferentially to the other plateaux and the remainder of the surface. When the plateau reaches a critical oxide film thickness, the film becomes unstable and breaks up to form flakes, and eventually, wear debris. Afterwards the contact is displaced to the other plateau, and the virgin surface revealed is oxidized again to form another oxide film. Therefore, in this case the wear rate is related to the rate of oxidation.

Notwithstanding, the feasibility of using parabolic oxidation was questioned later by some researchers [Krause (1971), Childs (1980)]. Indeed, relative motion between interacting bodies results in oxide cracking what provides more rapid transport of metal and oxygen ions. Hence, it was suggested that linear oxidation is more appropriate during sliding [Childs (1980)]. Oxide cracking phenomenon supports the linear oxidation theory. Hong et al. [Hong et al. (1988)] proposed that linear oxidation, which results from cracking and detachment of the oxide layer, better describes tribo-oxidation. Figure 38 [Hong (2002)] depicts quantitative models of static-oxidative and tribo-oxidative scale growth and removal from substrate. Curve 3 represents mild tribo-oxidative kinetics under which the oxide layer is protective.

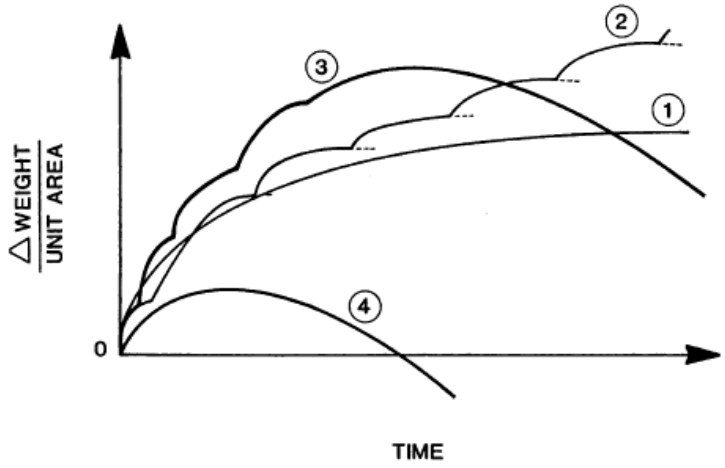

Figure 38: Quantitative models of static-oxidative and tribo-oxidative scale growth and removal from suitable substrates based on: (1) static-parabolic oxidation; (2) static-paralinear oxidation; (3) mild tribo-oxidative, and (4) severe tribo-oxidative kinetics (from [Hong (2002)]).

Quinn's linear oxidational wear model for pin-on-disc can be expressed as follows:

$$V = \frac{A[A_p \exp(-Q/RT_f)}{f_0 \cdot \rho_0} \cdot t \qquad (32),$$

with: V – the total wear volume, Q – the oxidational activation energy for linear oxidation, t – the sliding time.

A modified version of relation 32, as a function of dissipated energy (Ed) for the ball-on-flat configuration was proposed by Huq et al. (2002). So, the total wear volume (V) can be expressed by the following relation:

$$V = \frac{A}{f_0 \cdot \rho_0} \cdot Ed \qquad (33).$$

The above equation expresses the wear volume is linearly related to dissipated energy, but changes of tribochemistry in the contact results in a modification in the wear rate. It was shown that volumetric wear loss versus dissipated energy gives a good estimation about wear rate in comparison to wear rate expressed in terms of wear loss per unit time.

Friction causes chemical reactions to proceed much faster than they would otherwise. Formation of the material defects in the plastic zones under complex stress-strain loadings is, apart from flash temperature, one of the mechanisms by which friction

increases chemical reactivity on the interface. Hong et al. (1988) showed the reduction of activation energy during wear assuming linear kinetics and oxide-oxide contact. The tribo-oxidation energy of 316 stainless steel was there reported to be significantly lower (19.1 kJ/mole) compared to static activation energy (160 kJ/mole).

4. 1. 2. 5. Oxide chemistry and structure

Oxides formed at the contact area under sliding conditions are then removed as a result of repeated contacts. Due to the stress build-up between the oxides and substrates, the oxides become unstable when the oxides reach a certain thickness, especially if the Pillings-Bedworth ratio is high (> 2) [Askeland (1998)]. The type of oxides formed during tribo-oxidation has a substantial effect in producing wear- and friction-reducing oxide layers. Relatively soft and deformable oxides would facilitate development of such wear-protective surfaces. Next very influential factors are oxide cohesion and oxide/substrate adhesion. When the cohesion and adhesion are strong enough the retention of such protective layers can be facilitated. However, low friction and wear necessitate reasonably easy fracture of oxide-oxide asperity junctions between the surface oxide layers, resulting in an optimum ductility for an effective wear-protective oxide [Glascott et al. (1985)].

Relatively more ductile rather than very brittle oxides should be more amenable to plastic deformation, which suggests that Co_3O_4 or NiO should more readily form wear-protective oxide surfaces than Cr_2O_3, as was found at low ambient temperatures. Hence, if it could be possible to control the growth of oxides the development of NiO rather than Cr_2O_3 on Ni-Cr alloys or of FeO or Fe_3O_4 rather on Fe-Cr alloys would be expected to be more conducive to formation of a wear-protective oxide surface during wear [Glascott et al. (1985)].

Elevated temperature fretting behaviour of mild steels was studied by Hurricks (1972, 1974). Changes in the oxide structure was there thought to be responsible for an abrupt decrease in wear rate once the temperature was raised beyond 200°C [Hurricks (1974)]. According to the author the observed decrease of wear rate is believed to be due to the transformation in oxide structure, where a spinel Fe_3O_4 (magnetite) becomes more thermodynamically stable above 200°C than a rhombohedral α-Fe_2O_3 (hematite). It is generally known that the former is porous and can be easily sheared off, however the latter is hard and has an abrasive character [Buckley (1981)]. Hence,

Fe_3O_4 seems to reduce friction and wear more effectively than α-Fe_2O_3. Crystallographic structures of both oxides are shown in Figure 39.

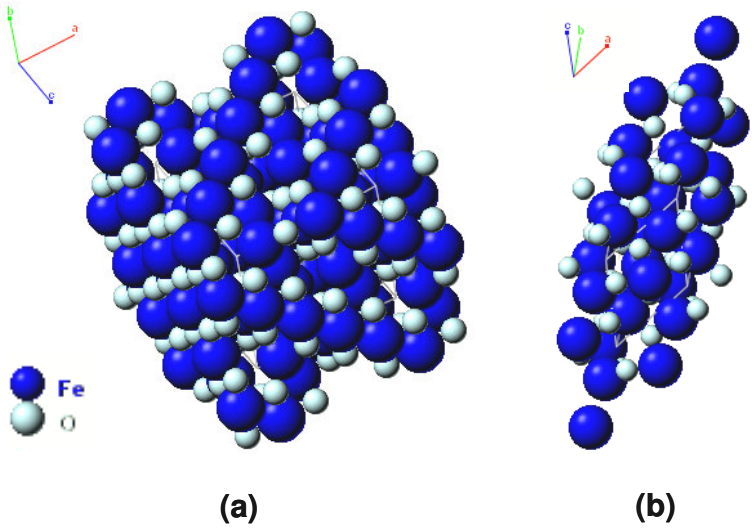

Figure 39: Crystallographic structure of (a) magnetite (Fe_3O_4) (after [Haavik et al. (2000)]) and (b) hematite (α-Fe_2O_3) (after [Pauling et al. (1925)]).

Structural impact of the third body and the associated oxide nature on the friction and wear behaviour was also shown by Kato [Kato (2003), Kato et al. (2007)] to be very influential who explored the effect of artificially supplied particles. He found that mild wear transition can be explained by the sintering rate of the supplied oxide particles. When the supplied oxide was highly diffusive (Fe_2O_3, SnO_2 or CuO), the tribofilm formation rate was high and the mild wear transition occurred after a shorter sliding distance. By contrast, no severe to mild wear transition was observed for poorly diffusive particles like Al_2O_3, TiO_2 or SiO_2. In the case of Fe_2O_3 particles, the sliding distance from the severe to mild wear transition was decreased when finer particles were supplied.

4. 2. Effect of relative humidity

The effect of relative humidity on the unlubricated wear of steel was studied extensively by many authors. Liew (2006) showed that wear increased nearly 1.5 orders of magnitude for steel/steel contact when relative humidity of the surrounding air decreased from 80 to 28% (Figure 40). The low humidity conditions promoted both delamination and adhesive wear, while the mild wear occurring at high humidity

levels was due to inhibition of these wear mechanisms by the formation of interfacial layers such as iron hydroxide and ferri-oxide-hydrates, and the adsorption of water on the worn surface in addition to the normal atmospheric oxidation.

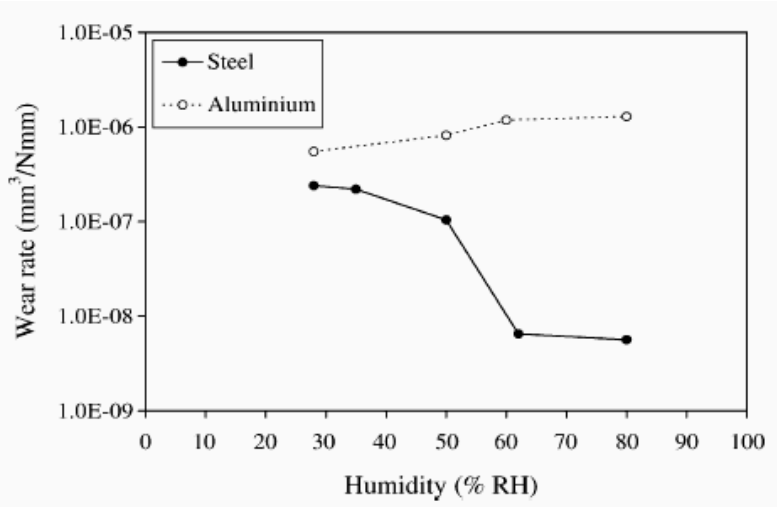

Figure 40: The effect of humidity on the wear rate of steel and aluminium pins (pin-on-disc test) (from [Liew (2006)]). Test conditions were as follows: velocity of 6 m/min, nominal load of 5N and sliding distance of 500 m.

Besides, it was reported that the sliding speed had significant influence on the effect of humidity on wear of steel [Tsuji et al. (1975)]. At low speed, the wear increased with a decrease in humidity. By contrast, high sliding speed results in an increase of wear with humidity. The impact of normal load was investigated by Bregliozzi et al. (2003, 2004). Wear and coefficient of friction of stainless steel were there found to increase when relative humidity decreased for loads higher than 2 N, while under lower normal load the effect of humidity was contrary and higher coefficient of friction with the humidity increase was observed.

5. OBJECTIVES OF THE WORK

Within the framework of the present dissertation the elevated temperature investigations are being undertaken to reproduce the working conditions of the trunnion vane/bushing joints in the Variable Stator Vane system. It has been shown in the bibliographic survey that environmental conditions may significantly affect tribological behaviour of alloy steels and superalloys. This has been associated to the significant modification of the interface. It has also been demonstrated that using

energy approach and assuming constant interface structure (i.e. given wear mechanism) the energy approach is able to predict the wear kinetics by a single energy wear coefficient independently of mechanical loadings (test duration, displacement, normal force) and even under variable loading conditions. Moreover, defining the objectives of the present work it must be taken into account an aspect that VSV system is subjected to variable temperature conditions during a flight of a plane.

Hence, the two main research objectives of this dissertation are:

1. Profound characterization of the tribological behaviour of the considered tribo-system under invariable and variable loading conditions using energy approach, allowing the fretting wear mapping of wear regimes as a function of temperature, displacement amplitude and pressure to be plotted;
2. Development of a 'composite' wear formulation allowing a prediction of wear volume under variable loading conditions.

To fulfill the objectives the following question have to be answered:

- What is the impact of temperature on the evolution of the energy coefficient of friction and energy wear coefficient?
- What is the evolution of the interface versus temperature; What is the change of its tribo-chemical and rheological properties?
- Is there any influence of pre-oxidation on the tribological behaviour?
- What is the dynamics of third body evolution under variable temperature test conditions corresponding to the real ones occurring in VSV system?
- Is it possible to make a map of wear regimes using an innovative variable loading conditions methodology?
- What is the impact of the mechanical loading conditions on the tribological behaviour and the associated interface?
- How energy wear approach can be transposed to capture wear volume under variable loading conditions?

CHAPTER 2

STUDIED MATERIALS
AND FRETTING EXPERIMENTS

CHAPTER 2: STUDIED MATERIALS AND FRETTING EXPERIMENTS

1. MATERIALS UNDER INVESTIGATION

The Jethete M152/A-286 tribo-system is being explored within the framework of the present dissertation. The characterization of the materials is presented below using information obtained from SNECMA.

Jethete M152 (UNS-S64152, AIR-Z12CNDV12) is a member of the Fe-12 Cr family alloys, with the additions of Ni and Mo. This alloy belongs to the class of martensitic stainless steels (morphology of the structure is shown in Figure 41a) and has a combination of properties, which include good ductility at high strength levels, uniform properties throughout thick sections and favourable strength at elevated temperatures. It also features outstanding fracture toughness and good oxidation resistance up to approximately 550°C. These all features, together with its favourable coefficient of thermal expansion (see Table III), make the alloy attractive for use for steam turbine components and compressor parts in gas turbine applications.

A-286 (UNS-S66286, AIR-EZ6NCT25) is an iron-base austenitic precipitation-hardened superalloy (classified as a stainless steel by SNECMA) with high content of Ni and Cr. Its structural morphology is shown in Figure 41b. It is used in situations when high strength up to 700°C is required as well as for cryogenic applications. Invoking the data provided by steel manufacturers [ATI Allvac (2001), Special Metals (2004)], the tensile strength of A-286 alloy decreases only by 90 MPa between room temperature and 400°C. A-286 alloy has an excellent oxidation resistance up to 982°C. Its corrosion resistance in many environments is similar to that characteristic of austenitic stainless steels. Moreover, it has superior corrosion resistance to nickel-base alloys when expose to sulphurous atmospheres at elevated temperatures. Applications of A-286 include jet engines, supercharger, and missile components comprising: wheels and blades, casings, afterburner and sound suppressor parts, fuel nozzles, fasteners, extraction tooling, miscellaneous hardware.

The main precipitating phases identified in A-286 alloy are γ' [$Ni_3(Ti,Al)$] and η (Ni_3Ti). The γ' is the major hardening phase in A-286, and is the most important intermetallic compound due to its natural morphology with small interparticle distance, preference for general precipitation and large volume percent. Other

favourable factors include the high ductility of the phase compared with minor precipitates and the coherency with the austenitic matrix because of close lattice matching. It forms as spherical precipitates that have a low surface energy. In the approach to equilibrium, the γ' transition phase is replaced by hexagonal η phase. As a cellular precipitate, forming in the range of 399°-982°C, it is nucleated at grain boundaries and can be detrimental to notched stress-rupture strength. Precipitation may also occur as Windmanstatten intergranular η which reduces hardness, strength, and physical properties, but not ductility. The presence of boron and aluminium in A-286 retards both modes of formation. The alloying elements such as: Mo, Cr and B are solid-solution strengtheners, at the same time the last is extremely potent and markedly improves stress-rupture properties [Muraca et al. (1972)].

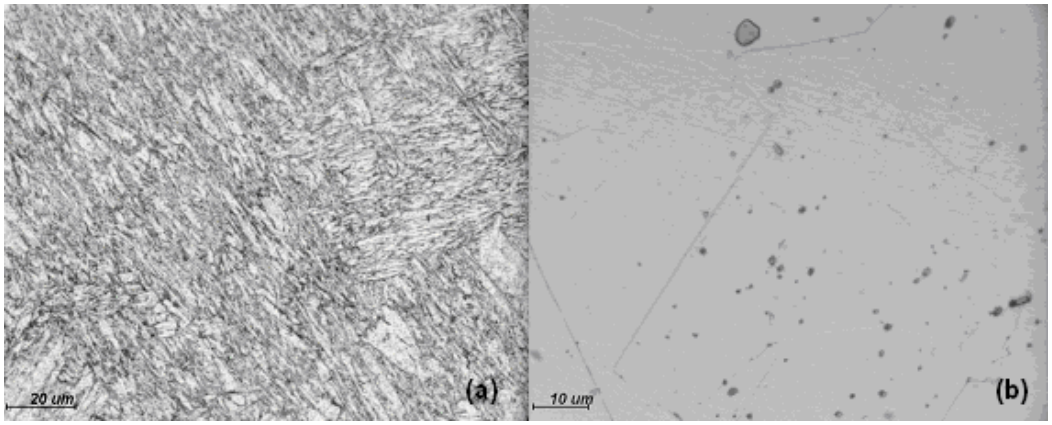

Figure 41: Morphology of the studied materials: (a) tempered martensite of Jethete M152 stainless steel and (b) spherical precipitations of γ' phase in austenitic matrix of A-286 superalloy; Royal water etching solution (mixture of concentrated nitric and hydrochloric acids in the ratio of one to three) was used to reveal morphology of the studied alloys.

The mechanical properties of the studied alloys are listed in Table I, the physical and surface ones in Table II, and their chemical compositions in Table III.

Materials	**Hardness**	**Young's Modulus [GPa]**	**Tensile Strength [MPa]**	**0.2% Yield Strength [MPa]**	**Poisson's ratio**
Jethete M152	344 HB	216	1150	900	0.30
A-286	311 HB	201	1035	698	0.30

Table I: The mechanical properties of the studied materials.

Materials	Average Surface Roughness: R_a [µm]	Density [g*cm^3]	Thermal Expansion^x [10^{-6}*m/(m*°C)]	Thermal Conductivity [W/(m*°C]
Jethete M152	0.40	7.75	12.0	30.0
A-286	0.40	7.94	17.2	12.7
x – between 20° and 400°C at 400°C				

Table II: The physical and surface properties of the studied materials.

Material	Compound average nominal wt. %						
Jethete M152	**C**	**Cr**	**Ni**	**Mo**	**Si**	**Mn**	**-**
	0.12	11.70	2.70	1.70	0.20	0.80	-
	V	**N**	**P**	**S**	**Fe**	**-**	**-**
	0.30	0.04	0.013	0.013	Remainder	-	-
A-286	**C**	**Cr**	**Ni**	**Mo**	**Si**	**Mn**	**Ti**
	0.04	14.80	25.50	1.25	0.50	1.50	2.10
	V	**Al**	**B**	**P**	**S**	**Fe**	**-**
	0.30	0.20	0.006	0.015	0.015	Remainder	-

Table III: The chemical compositions of the studied alloys: Jethete M152 and A-286.

2. DEFINITION OF THE FRETTING PARAMETERS

Quantifying the fretting process is possible owing to an on-line recording of fretting cycles (also called fretting loops) during the test. The fretting loop is defined as a representation of the tangential loading as a function of displacement (Figure 42). Several parameters can be derived from the recorded fretting cycle. They are described below.

The displacement amplitude (δ^*), maintained by the control system, corresponds to the maximum displacement amplitude imposed. The value of this parameter differs from the maximum amplitude achieved by the relative displacement of the two contacted bodies what is a consequence of the test assembly compliance.

The sliding amplitude (δ_g) is defined as a residual displacement when the tangential force is equal to 0. Applying this parameter any interactions induced by the tangential accommodation of the system on the displacement value (δ^*) can be controlled.

The maximum tangential force amplitude (Q^*) represents the maximum recorded value of the tangential effort transmitted by the contact. It is representative of the conventional coefficient of friction ($\mu = Q^*/P$) of the two contacted bodies under gross slip fretting conditions.

The dissipated energy of cycle (Ed) is characterized by the area of the fretting loop. The value of this parameter can be approximately quantified as a product of the maximal tangential force (Q^*) and sliding distance ($4 \cdot \delta_g$) during the cycle of the alternating fretting (relation 34):

$$Ed = 4 \cdot \delta_g \cdot Q^* \qquad (34).$$

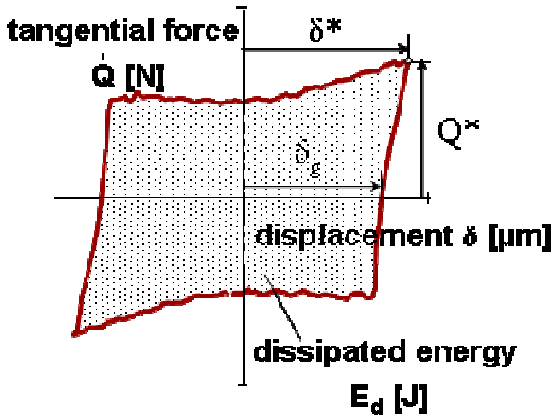

Figure 42: The fretting loop recorded during fretting test.

3. FRETTING WEAR EXPERIMENTS

3. 1. Fretting apparatus

Tests were carried out using an electrodynamic shaker activating a specific fretting rig manufactured by *DeltaLab* (United Kingdom) and upgraded in LTDS (Laboratory of Tribology and Dynamics of Systems) (France) illustrated in Figure 43.

Data acquisition platform created under LabView software was used for on-line collection and control of fretting parameters. The required value of the normal force (P) was maintained during fretting tests by a precise brushless engine, while the tangential force (Q) and displacement (δ) were recorded. Thus, the fretting loop $Q - \delta$ (Figure 41) could be drawn to extract quantitative variables, including the dissipated energy (Ed), the sliding amplitude (δ_g), the tangential force amplitude

(Q*) and the displacement amplitude (δ*). A developed acquisition module allowed also conducting the tests at constant sliding amplitude owing to automatic adjusting the displacement amplitude at maintaining a demanded value of the normal force. The relative displacement was determined by optical sensors, the tangential force by a piezoelectric sensor and the normal force by a strain gauge sensor. A reciprocating movement with a constant frequency was always imposed. All fretting tests were carried out in a closed chamber where the relative humidity was controlled as close as possible to the contact using a humidity sensor. The elevated temperature conditions were reached using heating elements placed into the lower holder. The temperature was measured by means of a thin thermocouple placed at top of the flank surface of the lower specimen as close as possible to the fretting contact. The rubbing surface of the upper specimen was heated by the lower specimen as a result of thermal conductivity. In order to maintain the required temperature in the contact, it was surrounded by a thermo-insulating fabric limiting the dissipation of heat and homogenizing the temperature.

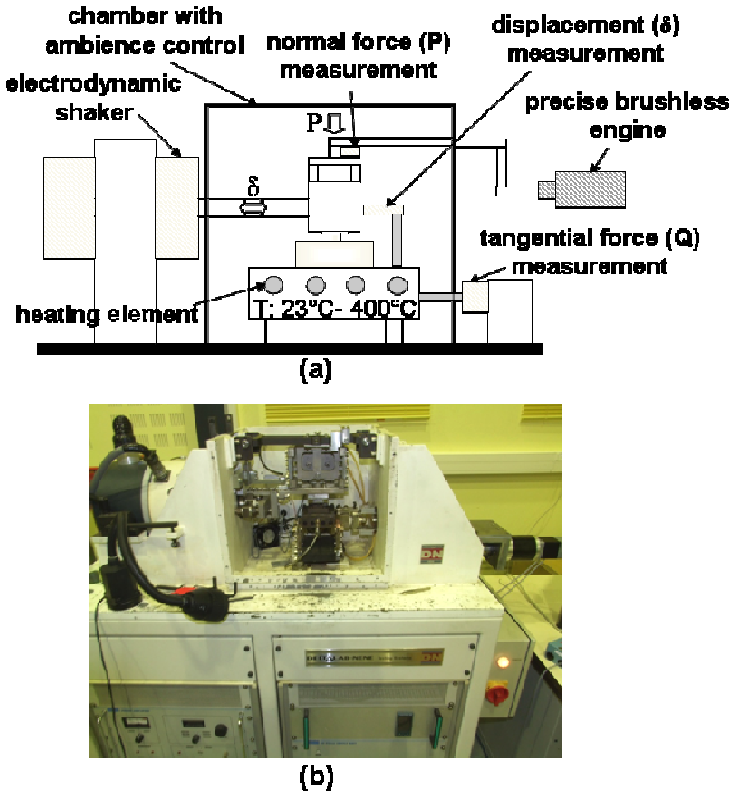

Figure 43: (a) Diagram and (b) photograph of the specific fretting apparatus.

3. 2. Contact geometry

The contact geometry used in the study was a plane/plane configuration. The upper axi-symetrical pin type Jethete M152 specimen with 3 mm diameter of the contact surface rubbed against the lower rigidly fixed cylindrical A-286 sample (Figure 44). The pin type specimen had a chamfer machined at a 45° angle between circular surface of the contact and cylinder that it was turned from. The applied contact geometry corresponded to about 7 mm^2 of flat apparent area of the contact (A_{ap}) that allowed low pressure conditions to be investigated. By contrast with a conventional sphere/plane configuration, it required a specific alignment to guarantee the flat/flat contact, but permitted practically constant pressure conditions independently of the surface wear. Illustrations of the contact configuration and specimens used in the study are presented in Figure 45.

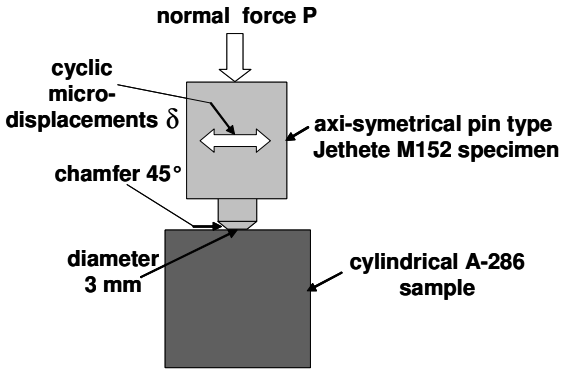

Figure 44: Diagram of the fretting contact geometry used in the study.

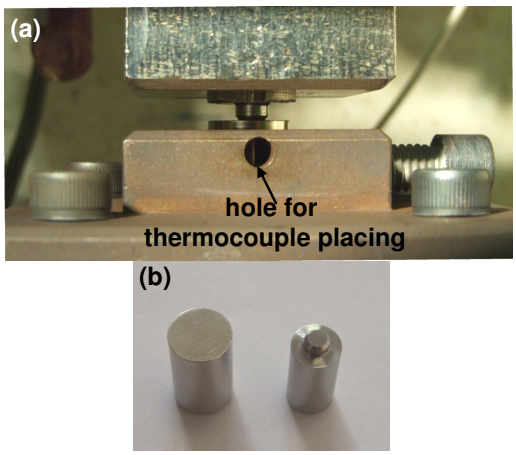

Figure 45: (a) Picture of the contact geometry applied in the study, (b) The specimens used in the tests: cylindrical A-286 and axi-symetrical pin type Jethete M152 sample.

3. 3. Contact mechanics of the studied plane/plane configuration

It was mentioned previously (i.e. in Chapter 1) that the plane/plane contact configuration produces discontinuities in the pressure distribution on the borders of the contact. Finite element analysis based on the created elastic finite element 2D axi-symetric model was used in order to quantify pressure distribution of the studied contact configuration of the Jethete M152/A-286 tribo-system. Figure 46 illustrates the developed model and mesh of 10 µm elements. The computation of the pressure distribution was performed for three values of the normal force: 88, 176 and 352 N. The pressure distribution profiles obtained at 88 and 352 N, where the maximum pressure peaks can be observed on the borders of the contact, are shown in Figure 47. However, it was demonstrated by Mary et al. (2007) and Paulin et al. (2008) that due to wear processes, the surfaces in the contact are modified in such a way that the pressure peaks yield to the flattening effect (related to the increase of the surface conformity) and the pressure profile evolves towards a homogeneous distribution. It can therefore be assumed that after a few cycles of fretting test the contact depicts a quasi flat constant pressure distribution that will promote a homogeneous evolution of the wear damage.

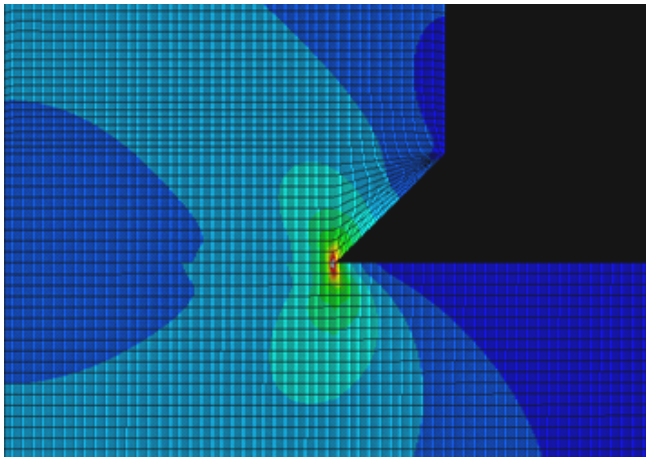

Figure 46: Developed 2D axi-symetric model with mesh of 10 µm elements.

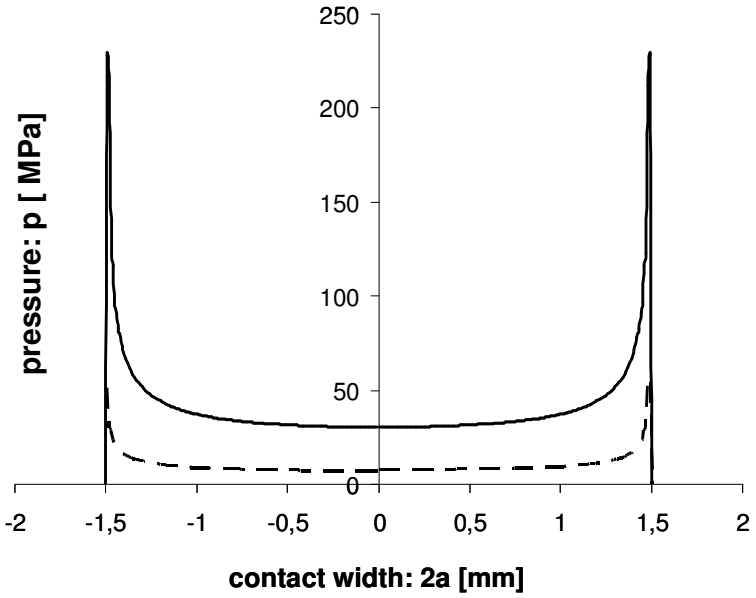

Figure 47: Pressure distribution characteristic of the studied contact configuration computed for the investigated Jethete M152/A-286 tribo-system under two values of the normal force: 88N (— —) and 352 N (———).

The computed values of maximum pressures (p_0) as well as of mean pressures (p_m) (defined as a ratio of the applied normal force (P) to the apparent initial contact area (A_{ap})) in the contact are given in Table IV.

Tribo-couple	**Normal force P [N]**	**Maximum pressure in the contact p_0 [MPa]**	**Mean pressure in the contact $p_m=P/A_{ap}$ [MPa]**	**½ width of the contact a [mm]**
Jethete M152/ A-286	88	57	12.5	1.5
	176	113	25	1.5
	352	227	50	1.5

Table IV: Maximum pressure (p_0) (obtained from finite element analysis), mean pressure (p_m) and semi-width of the contact (a) obtained under three considered normal forces for the applied plane/plane contact configuration for the Jethete M152/A-286 tribo-system.

3. 4. Experimental conditions

All fretting wear experiments were carried out under reciprocating sliding motion (alternating fretting) at a frequency (f) of 13 Hz and 10 ± 2% relative humidity (RH). Dry conditions without externally added lubricant are being investigated within the framework of the present dissertation. All applied loadings promoted gross slip conditions. The constant heating speed equal to 20ºC/min was always applied in order to achieve the required value of the elevated temperature.

Within the framework of the present dissertation both invariable and variable, during a single fretting test, loading conditions are being investigated. They are described in details in the relevant Chapters (i.e. invariable conditions in Chapter 3, variable in Chapter 4).

4. WEAR VOLUME EVALUATION

Specimens from the Jethete M152/A-286 contact were ultrasonically cleaned in acetone for a time period of 10 min each before and after tests in order to remove surface contamination and loose debris particles, respectively.

The wear volume of the studied tribo-couple was determined indirectly by converting the mass loss of the specimens, measured by means of precise laboratory balance equipment (measurement accuracy: ±0.01 mg), and assuming the densities of each material as in Table II.

In the present dissertation, the wear analysis is limited to the total wear volume (V) of the studied tribo-system defined as the sum of the upper (V_{upper}) and lower (V_{lower}) wear volumes (relation 35).

$$V = V_{upper} + V_{lower} \quad (35).$$

An important aspect that must be taken into account when elevated temperature conditions are investigated is to consider a volume gain of specimens due to static oxidation of metal materials occurring in the contact. Thus, for tests performed at 300°C and higher temperatures, a correction resulting from the static oxidation of Jethete M152 and A-286 specimens was introduced (for lower temperatures it was unmeasurable or so small, below 3% of the total wear volume, that neglected). Hence, the determined wear volume of metal specimens was increased by the volume gain

(V_g) (converted from the mass loss, assuming an iron oxide density of 5.24 g/cm^3) obtained after static oxidation tests (specimens in the contact but without fretting action) in a time period corresponding to that of the conducted fretting tests. However, on account of considerable amount of fretting tests carried out at different number of cycles at 400°C (including tests at variable loading conditions, defined in Chapter 4) as well as limited number of specimens supplied for thesis realization, it was not possible to carry out all corresponding static oxidation tests. Hence, to provide data needed for accurate wear evaluation, oxidation curves of the Jethete M152/A-286 contact at 400°C (Figure 48), based on a few results obtained from static oxidation tests, were plotted and associated equations extracted. For both specimens static oxidation was found to proceed according to a parabolic law, where for the upper Jethete M152 and lower A-286 specimen it can be described by the relation 36 and 37, respectively.

$$V_{g\_upper} = -1.44 \cdot 10^{-8} \cdot t^2 + 1.97 \cdot 10^{-5} \cdot t \quad (36),$$

$$V_{g\_lower} = -4.87 \cdot 10^{-8} \cdot t^2 + 6.45 \cdot 10^{-5} \cdot t \quad (37),$$

with: V_{g_upper} and V_{g_lower} – the volume gain due to native oxide formation on the surfaces of the upper Jethete M152 and lower A-286 specimen, respectively; t – the time period corresponding to that of the performed fretting test.

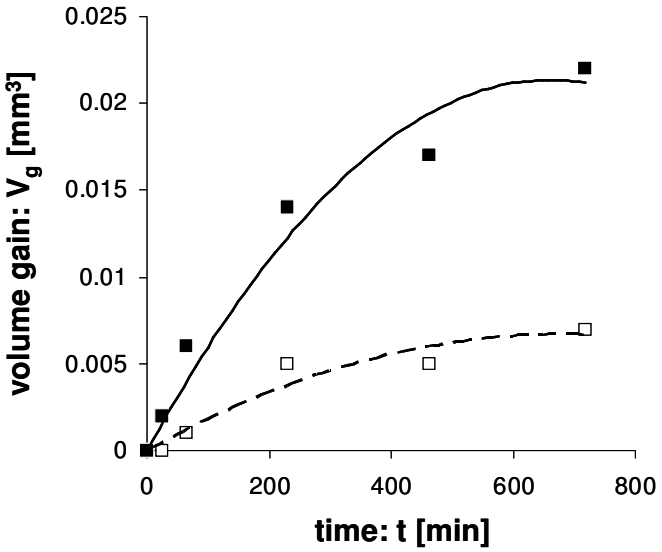

Figure 48: Static oxidation curves obtained at 400°C for the upper Jethete M152 (– –) and lower A-286 (——) specimen contacted as during fretting test.

Upper specimen from the contact (Jethete M152)			
Number of cycles / corresponding time period of static oxidation: N / t [min]	**Gain volume $V_{g\_upper\_JetheteM152}$ [mm^3] at temperature:**		
	300ºC	*350ºC*	*400 ºC*
20000 / 26	-	-	0
50000 / 64	-	-	0.001
100000 / 128	-	-	0.003^x
150000 / 192	-	-	0.004^x
180000 / 231	-	-	0.005
220000 / 282	-	-	0.006^x
360000 / 462	0.001	0.003	0.005
400000 / 513	0.001	-	0.007^x
560000 / 718	0.002	-	0.007
Lower specimen from the contact (A-286)			
Number of cycles / corresponding time period of static oxidation: N_{cyc} / t [min]	**Gain volume $V_{g\_lower\_A-286}$ [mm^3] at temperature:**		
	300ºC	*350ºC*	*400 ºC*
20000 / 26	-	-	0.002
50000 / 64	-	-	0.006
100000 / 128	-	-	0.007^x
150000 / 192	-	-	0.011^x
180000 / 231	-	-	0.014
220000 / 282	-	-	0.014^x
360000 / 462	0.007	0.011	0.017
400000 / 513	0.008	-	0.020^x
560000 / 718	0.010	-	0.022

Table V: Volume gains of the metal specimens from the Jethete M152/A-286 tribo-system obtained after static oxidation tests conducted at different temperatures in time periods corresponding to those of fretting experiments; Values marked with (^{x}) denotes corrections calculated using equation 36 and 37 for the upper Jethete M152 and lower A-286 specimen, respectively.

Using equation 36 and 37 the missing values of the volume gain of the metal specimens from the Jethete M152/A-286 contact were calculated, by assuming that time periods of the lacking static oxidation tests corresponds to those of conducted fretting experiments. For tests conducted under variable loading conditions (defined in Chapter 4) a time period of static oxidation was considered as a sum of the

individual time contributions at 400°C. For simplification, the correction for these tests was determined assuming continuous character of oxidation as that for experiments at constant temperature.

Detailed data concerning the correction values (i.e. volume gains) introduced to compensate for a static oxidation of the metal specimens are listed in Table V.

Summarizing, the total wear volume of the considered tribo-system (V) is here determined as a sum of the wear volumes of the upper Jethete M152 and lower A-286 specimen, increased by the corrections resulting from the static oxidation phenomenon (relation 38).

$$V = V_{upper} + V_{g\_upper} + V_{lower} + V_{g\_lower} \quad (38),$$

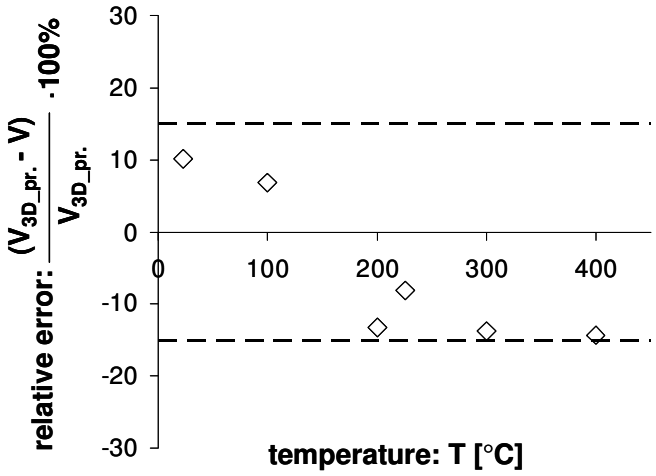

Figure 49: The relative error between the wear volume determined using mass loss method (V) and that measured by 3D profiler ($V_{3D\_pr.}$) for a few fretting scars generated on the A-286 specimens tested against Jethete M152 material at different temperatures under the mechanical key point loading conditions ($\delta^*=\pm 100$ μm, $p_m=25$ MPa (i.e. P=176 N), and N=360000 cycles).

In order to assess the reliability of results obtained using indirect mass loss method the wear volumes of a few fretting scars obtained under invariable test situations at different temperatures on to the A-286 plane specimens were also estimated by means of 3D VEECO-Wyko NT9300 interferometric profiler. The relative error between the wear volume determined using mass loss method (V) and that measured by 3D

profiler ($V_{3D\_pr.}$) was found to be low, less than 15% (Figure 49). Thus, considering such a good correlation as well as high operational costs of 3D profiler, use of mass loss method for wear evaluation is fully justified. Moreover, it provides an equivalent wear description of the upper axi-symetric pin type (for which wear evaluation using 3D profiler is difficult and time-consuming) and lower plane counter-bodies. Figure 50 shows 3D profiles of the fretting scars generated on the A-286 specimens at 23 and 400°C.

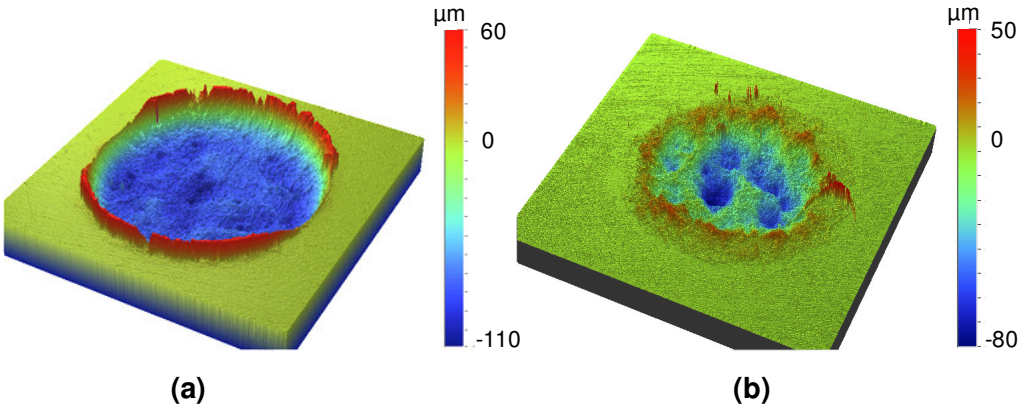

Figure 50: 3D profiles of the scars generated on the A-286 specimens tested against Jethete M152 material under the mechanical key point loading conditions at two temperatures:(a) 23°C and (b) 400°C.

CHAPTER 3

FRETTING BEHAVIOUR UNDER CONSTANT LOADING CONDITIONS

CHAPTER 3: FRETTING BEHAVIOUR UNDER CONSTANT LOADING CONDITIONS

In the present Chapter of the dissertation the influence of the temperature on the fretting wear behaviour and physico-chemical response of the associated interface of the Jethete M152/A-286 tribo-system under invariable loading conditions are being discussed.

1. LOADING CONDITIONS

The key point loading conditions with reference to the real situation occurring in the vane/bushing joint were defined as follows: p_m=25 MPa (i.e. P=176 N), δ^*=±100 µm, number of cycles N=360000 cycles and T=200ºC. The reference conditions produced the sliding amplitude δ_g=±77 ± 4 µm during the test. The corresponding fretting log showing the evolution of the fretting loops during the experiment performed under the key point conditions is illustrated in Figure 51.

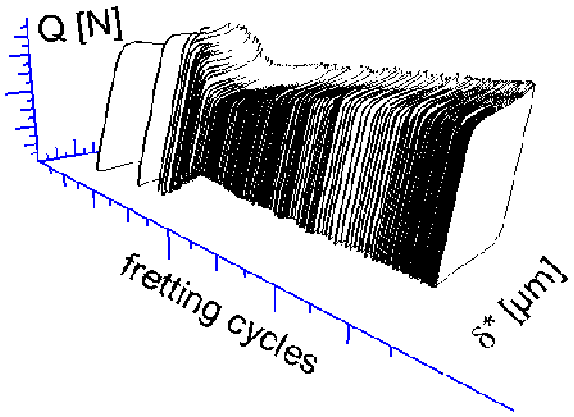

Figure 51: Illustration of the fretting log recorded for the test conducted under the key point loading conditions.

To evaluate the impact of temperature, the single mechanical key point loading conditions (i.e. p_m=25 MPa (P=176 N), δ^*=±100 µm and N=360000 fretting cycles) were studied at different temperatures from 23 to 400°C.

To quantify the wear response as a function of the pressure, displacement amplitude and test duration, a cross-experimental strategy centred on the mechanical key point

conditions was applied (Figure 52). Based on these reference loading conditions, the impact of pressure was evaluated by imposing the normal load from 88 to 352 N (i.e. from p_m=12.5 to p_m=50 MPa). The displacement amplitude ranging from ±50 to ±225 µm and the test duration ranging from 500 to 360000 fretting cycles were also studied. It must be noted that iso-sliding amplitude conditions corresponding to the key point value were maintained during the pressure effect analysis by monitoring the applied displacement amplitude in order to compensate for the tangential elastic accommodation. This complete investigation was carried out for the two temperatures: 200 and 400°C. The former is below while the latter above the severe to mild wear rate transition temperature.

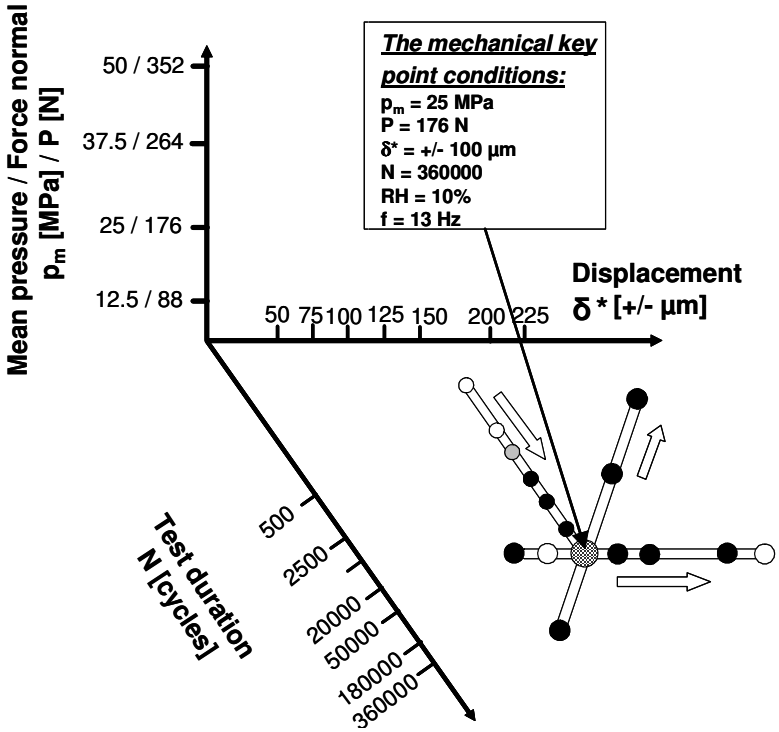

Figure 52: Illustration of the cross-experimental strategy studied at 200 and 400°C; Tests conducted at the both temperatures (●),only at 200°C (○)and only at 400°C (◌); Logarithmic scale was applied to depict test duration loadings.

Moreover, several dozen tests at certain values of the displacement amplitude in the range from ±50 to ±200 µm (at maintaining constant p_m=25 MPa (i.e. P=176 N) and N=360000 cycles) and pressure in the range from 5 to 50 MPa (i.e. from P=35 N to P=352 N) (at maintaining constant δ_g=±77 ± 4 µm and N=360000 cycles) at different

temperatures in the 150-400ºC range, but others than 200ºC, were carried out. The results obtained are being taken into consideration as the investigations under variable loading conditions are being discussed in the next Chapter.

Three experiments under the mechanical key point conditions (p_m=25 MPa (i.e. P=176 N), δ^*=±100 μm and N=360000 cycles) at 200 and 400°C were performed to verify test reproducibility. Then, mean values of all recorded variables and wear volumes were determined for use in further considerations. A high reproducibility of the tests was obtained as very low dispersions of the results were achieved (basically less than ±15%). For the rest loading conditions only a single fretting experiment was performed.

Matrix of all tests carried out at different temperatures, displacement amplitudes and pressures at constant number of cycles (N=360000) is shown in Table VI.

Temperature T [ºC]	**Displacement amplitude: δ^* [μm]** (p_m=25 MPa (i.e. P=176 N) and N=360000)							**Pressure: p_m [MPa]** (δ_g=±77 μm, N=360000)					
	50	*75*	*100*	*125*	*150*	*200*	*225*	*5*	*10*	*12.5*	*17.5*	*37.5*	*50*
23	-	-	x	-	-	-	-	-	-	-	-	-	-
100	-	-	x	-	-	-	-	-	-	-	-	-	-
150	-	-	x	-	-	-	-	x	-	-	-	-	-
200	x	-	x	x	x	x	x	-	x	x	-	x	x
215	-	-	x	-	-	-	-	-	-	-	-	-	-
225	x	-	x	-	x	-	-	-	x	-	x	-	x
250	x	-	x	-	x	-	-	-	-	-	-	x	-
275	-	-	x	-	-	-	-	-	-	-	-	-	-
300	-	-	x	-	-	x	-	-	-	-	-	-	-
350	-	-	x	-	-	-	-	-	-	-	-	-	-
400	x	x	x	x	x	x	-	-	-	x	-	x	x

Table VI: Matrix of all tests conducted at different temperatures, displacement amplitudes and pressures (at constant N=360000 cycles) for the Jethete M152/A-286 tribo-system; The cross 'x' in the cell denotes that test at the given parameters was carried out.

2. FRICTION BEHAVIOUR

2. 1. Development of the energy coefficient concept

Typical gross slip fretting loops were observed during the tests (Figure 53). A slight tangential force increase with displacement amplitude during the cycle observed under all studied conditions. This behaviour is probably related to continuous work hardening of contacted metal materials under fretting loadings. It is well known that especially steel materials having austenitic structure (A-286 superalloy) are susceptible to that type of strengthening mechanism [Peckner et al. (1977)]. Moreover, small tangential force peaks at the maximum displacement amplitude were noticed. This phenomenon, which is not observed for hard steel or hard coating contacts, is characteristic of ductile materials such as aluminium [Elleuch et al. (2002)] and titanium [Fouvry et al. (2004)] alloys. It may be associated to plastic draughts generated at the inlets contact borders which promotes surface interferences when the maximum displacement is reached [Fouvry et al. (2004)]. Such a ploughing effect might then explain the tangential force peaks observed on the fretting cycles.

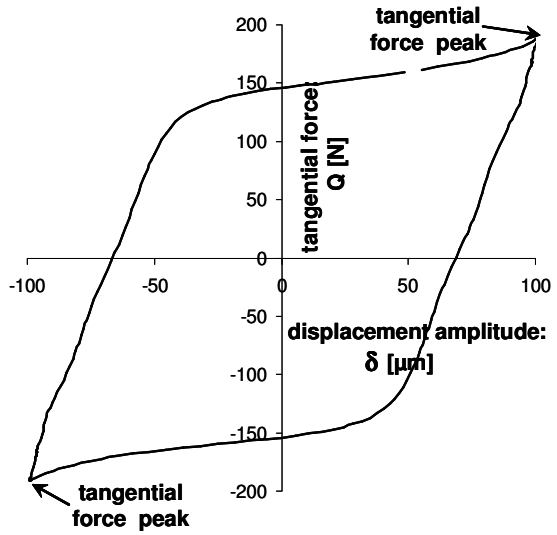

Figure 53: The characteristic fretting loop observed during all experiments.

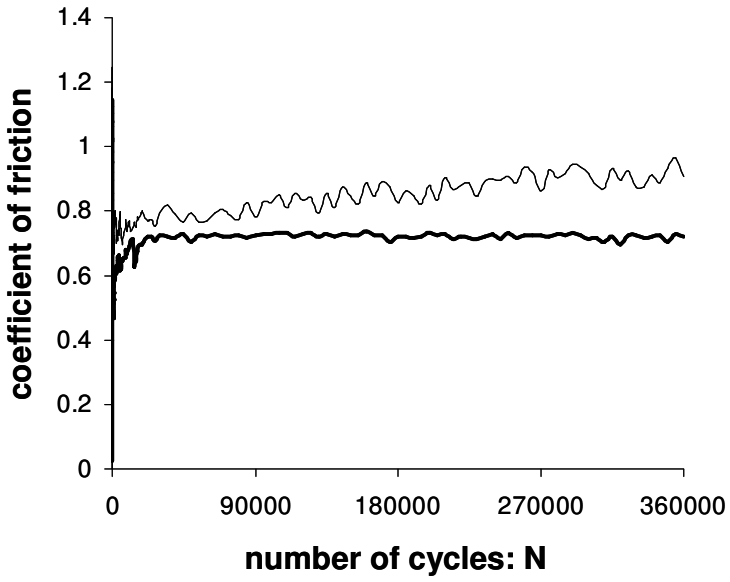

Figure 54: Comparison between evolution of the conventional (μ) (———) and energy (μ_e) (———) coefficient of friction for the key point loading conditions.

Hence, to characterize a friction law which is representative of the wear phenomena for the Jethete M152/A-286 tribo-system, the normalized or conventional tangential force ratio ($\mu = Q^*/P$) is therefore no longer appropriate, and an average value needs to be introduced. Based on an energy description, an energy coefficient of friction (μ_e) is considered (relation 39):

$$\mu_e = \frac{Ed}{4 \cdot P \cdot \delta_g} \qquad (39).$$

Figure 54 compares the evolution of the conventional and energy coefficient of friction under the key point loading conditions. As it can be observed the former continuously increases with time duration as Q^* grows as a result of above-mentioned phenomena, however the latter is characterized by stable evolution as the steady-state is reached.

2. 2. Impact of temperature

Figure 55 shows the evolution of the energy coefficient of friction for two temperatures (200 and 400°C) under the mechanical key point loading conditions (i.e.

p_m=25 MPa (P=176 N), δ*=±100 μm and N=360000 fretting cycles). For both the considered temperatures an initial stage (first a few hundreds cycles) of the friction evolution is similar. The difference in the friction behaviour can be observed, however, during next stages as tests are being proceeded for longer time duration. The evolution of the energy coefficient of friction depicted in Figure 55 for 200°C is characteristic of the experiments conducted at the temperatures lower than T_{ga}=220°C (temperature of 'glaze' layer activation), for 400°C of those carried out above T_{ga}.
In-depth analysis of the friction behaviour, where all essential friction-related parameters are defined is being discussed below.

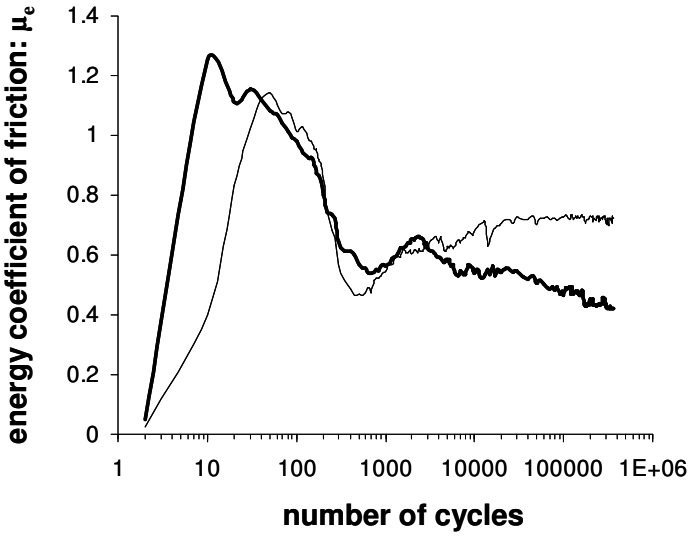

Figure 55: Evolution of the energy friction coefficient (μ_e) as a function of the test duration for two tests carried out under the mechanical key point conditions at 200 (——) and 400°C (——).

2. 2. 1. Analysis of the evolution of the energy coefficient of friction

The evolution of the energy coefficient of friction demonstrating a tendency characteristic of the experiments carried out under the mechanical key point loading conditions below and above T_{ga} is illustrated in the form of friction pattern in Figure 56 and 57, respectively.
Analyzing both graphs three stages in friction evolution can be distinguished, independently of test temperature. At the beginning of each test a running-in period

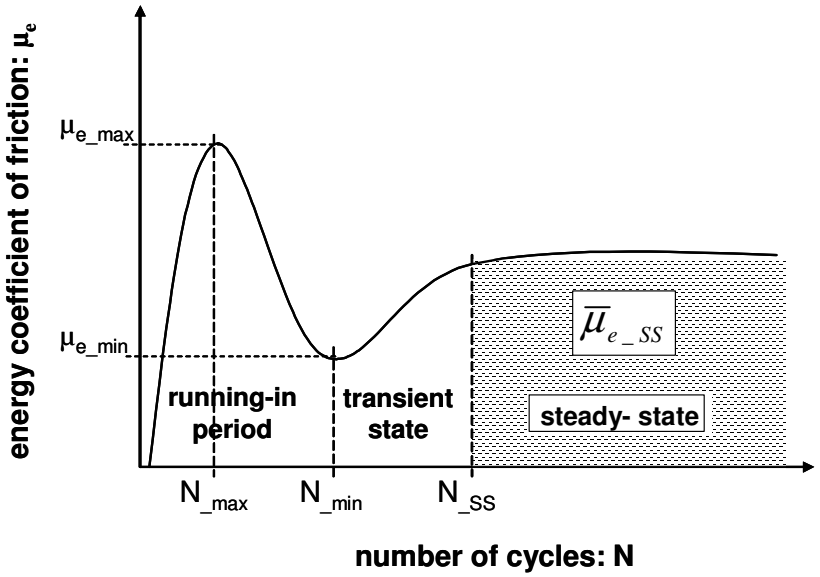

Figure 56: Friction pattern showing evolution of the energy coefficient of friction characteristic of tests carried out below transient temperature T_{ga}=220°C.

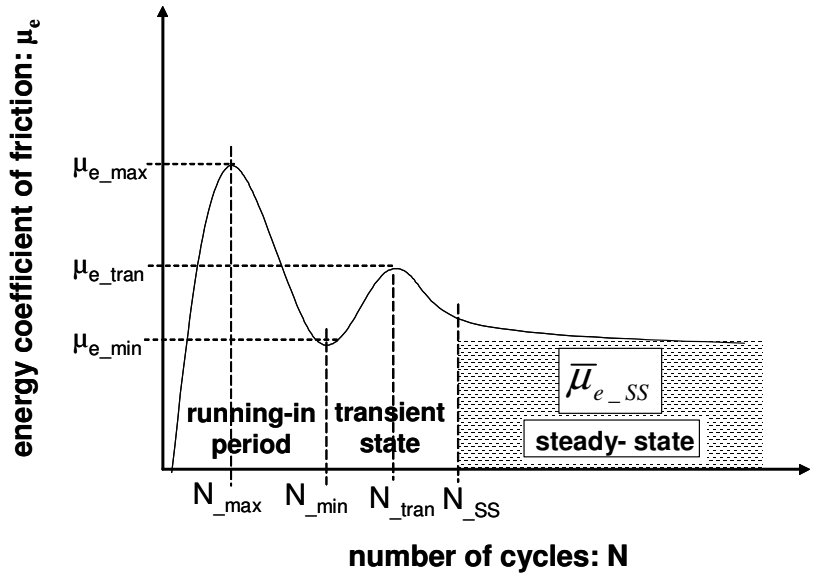

Figure 57: Friction pattern showing evolution of the energy coefficient of friction characteristic of tests carried out above transient temperature T_{ga}=220°C.

(initial short state taking up first a few hundreds cycles) characterized by a sharp increase of the energy coefficient of friction (where the highest energy friction coefficient (μ_{e_max}) within entire test duration at certain critical number of cycles ($N_{\_max}$) is achieved) followed by a drastic decrease in its evolution (down a

minimum friction value (μ_{e_min}) at $N_{\_min}$ number of cycles) can be observed. Subsequently, an intermediate transient state occurs. The evolution of the coefficient of friction within this stage characteristic of fretting tests carried out below T_{ga} proceeds as follows (Figure 56). The energy coefficient of friction increases asymmetrically from μ_{e_min} before stabilizes at a high steady-state friction value reached at $N_{\_SS}$ number of cycles. The transient period is different for experiments conducted at temperatures higher than T_{ga} (Figure 57). The monotonic increase observed below T_{ga} is here replaced by a heterogeneous evolution where the initial increase from μ_{e_min} up to some maximum μ_{e_tran} is followed by an asymptotic decrease down the more or less stabilized value achieved at $N_{\_SS}$. For all the considered temperatures the steady-state regime is determined by a mean steady-state energy coefficient of friction ($\overline{\mu}_{e\_SS}$).

2. 2. 1. 1. Running-in period characterization

A sharp increase in the evolution of the energy coefficient of friction (μ_e) observed for all the considered temperatures within the initial stage is related to strong adhesion and metal transfer phenomena as two similar metal materials are contacted [Hurricks (1972 and 1974), Kayaba et al. (1981-1982)]. Many researchers reported that even the seizure effect can then occur [Boas et al. (1977), Goto (1995), Maatta et al. (2001)]. The material transfer was confirmed by an energy dispersive X-ray spectroscopy (EDX) analysis of the fretting scar generated after short test (500 cycles) at 200°C. Figure 58 compares EDX spectrum obtained from outside the scar and that excited from the wear scar produced on the upper Jethete M152 specimen. An increase in nickel content after fretting experiment was found, thereby implying material transfer from the lower A-286 specimen on to the upper one (A-286 superalloy contains significantly higher amount of nickel in its composition compared to Jethete M152 stainless steel – see Table III). Moreover, oxygen was detected in the scar what signifies that fretting action activates processes that favours oxidation phenomenon. Figure 59a shows scanning electron microscope (SEM) picture of flake-like wear debris transferred on to the Jethete M152 counter-body what is in good agreement with literature where fretting wear is believed to be caused predominantly by the

formation of flake-like debris that is subsequently crushed into smaller spherical fragments (Figure 59b) [Kayaba et al. (1981)].

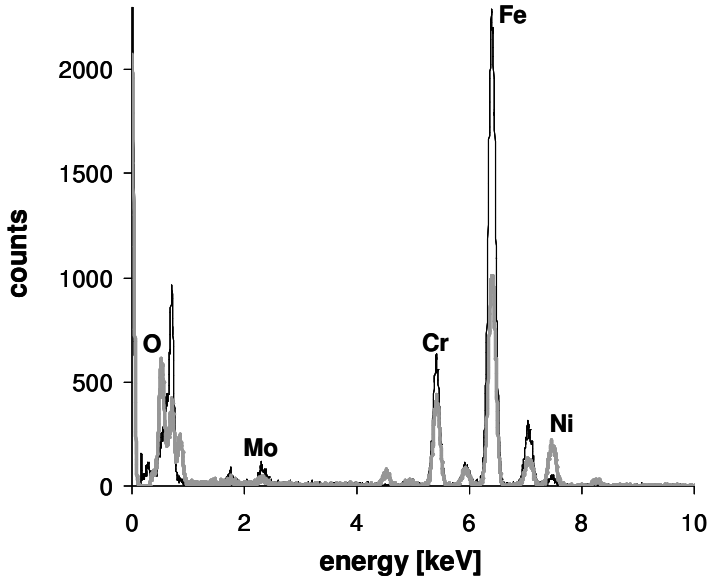

Figure 58: Comparison of EDX spectrum obtained from outside (——) and from the wear scar (——) generated on to the upper Jethete M152 specimen after short test (500 cycles) at 200°C.

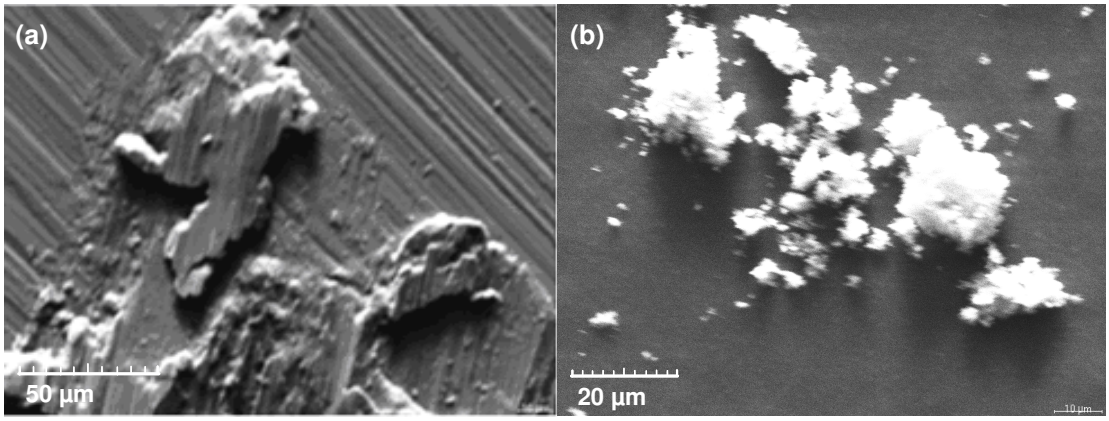

Figure 59: (a) Flake-like wear debris observed after the short (500 cycles) fretting experiment at 200°C; (b) Fine spherical wear debris particles observed after the long test (360000 cycles) at 200°C.

The impact of temperature on the adhesion during a running-in period is shown in Figure 60. As it can be observed there is no temperature influence and almost constant

value of maximum energy coefficient of friction (μ_{e_max}) is kept through a wide range of the studied temperatures (comprises between 1.10 and 1.30), even though it would be expected to decrease with temperature increase as higher temperature produces thicker layer of native oxides on to the mated surfaces that might prevent the formation of strongly adhesive metal-to-metal junctions [Glascott et al. (1985), Maatta et al. (2001)]. Hence, independence of the evolution of the maximum energy coefficient of friction (μ_{e_max}) on the applied temperature may be explained by the fact that not thick enough layer of oxides is formed on to the mated surfaces even at 400°C to protect against strong adhesion. As a result of the fretting action a native oxide layer is immediately damaged and removed, what in consequence leads to the metal-to-metal interface. A decrease in number of cycles needed to reach μ_{e_max} ($N_{\_max}$) with temperature increase was observed (Figure 60). This tendency is probably related to the susceptibility of the contacted materials to the plastic deformation, which increases with temperature. Thus, less amount of energy provided for the interface (less number of cycles) at the higher temperatures promotes similar adhesive behaviour as for lower ones.

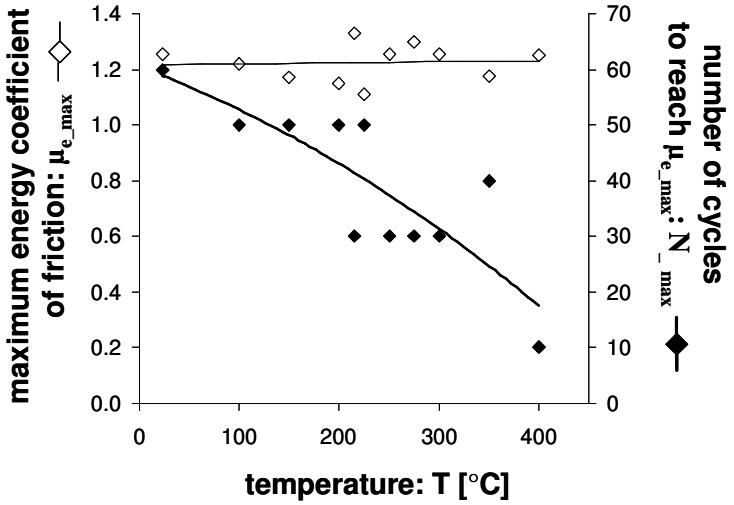

Figure 60: Maximum energy coefficient of friction (μ_{e_max}) and associated number of cycles ($N_{\_max}$) at which it is reached as a function of temperature under the mechanical key point loading conditions.

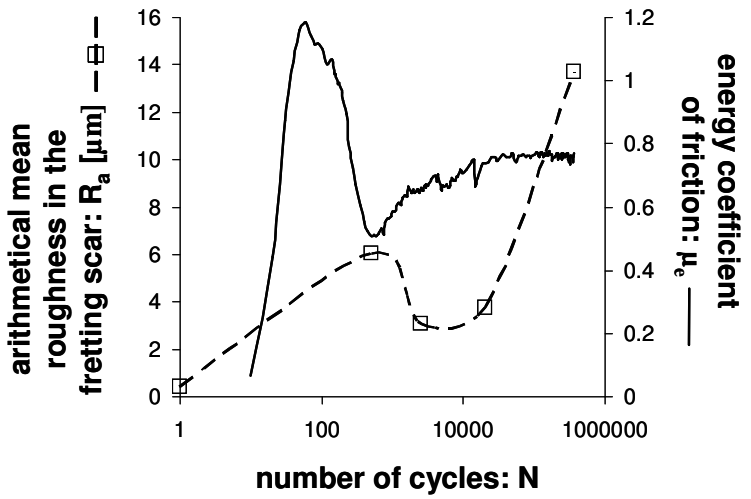

Figure 61: Arithmetical mean surface roughness (R_a) of the scars generated on to the lower A-286 specimens after interrupted tests with reference to the related friction evolution for the key point loading conditions (i.e. p_m=25 MPa (P=176 N), δ^*=±100 µm, N=360000 cycles and T=200ºC).

After a sharp increase a drastic drop down μ_{e_min} at $N_{\_min}$ in the friction evolution within a running-in period takes place. The abrupt decrease of the coefficient of friction observed for all temperatures can be related to the roughness evolution (Figure 61) of the contacted surfaces (determined by means of 3D VEECO-Wyko NT9300 interferometric profiler) that significantly increases at $N_{\_min}$ in relation to its initial value (before test R_a=0.4 µm) due to formation of post-adhesive prows and hollows. Indeed, two contradictory effects of roughness on adhesion exist. On the one hand for two surfaces stuck together the roughness increases the force needed to peel them apart, on the other hand for two solids placed in the contact roughness reduces a pull-off force [Singer et al. (1992)]. Though, it must be mentioned that roughness analysis was performed after ultrasonic cleaning of the contacted specimens. Thus, loose wear debris operating in the interface is not considered in the proposed hypothesis. This, however, was taken into account in the work of Merhej (2008) who studied dry self-mated 100 C6 steel contact at room temperature conditions and observed similar friction evolution (i.e. for $T<T_{ga}$). According to his observations, illustrated in Figure 62, after the peak value (μ_{e_max}) the surface layer of material,

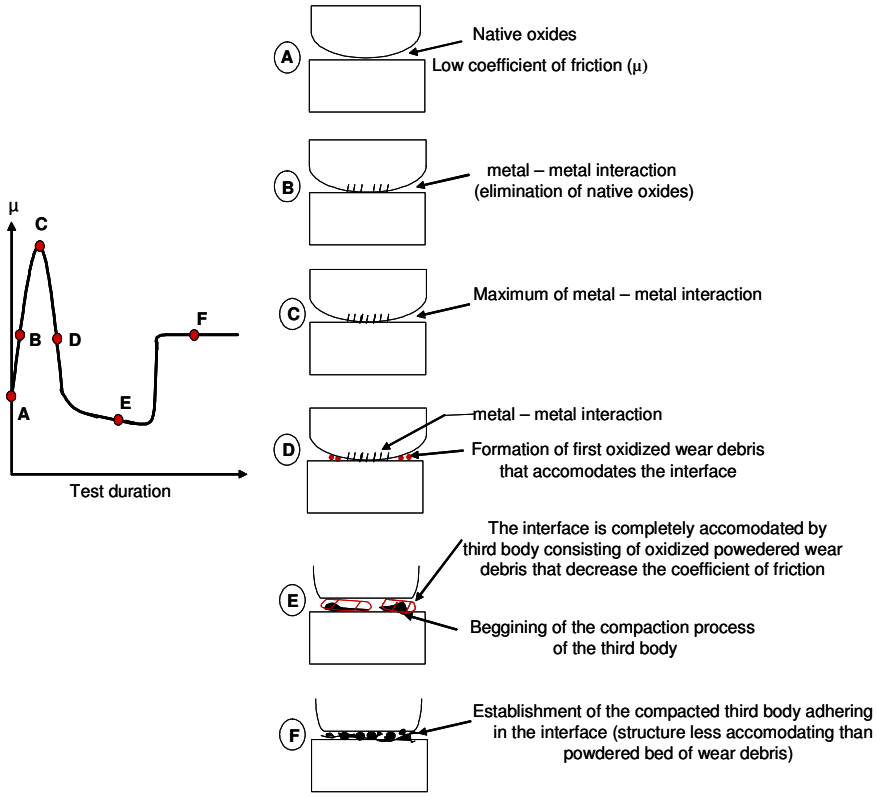

Figure 62: Schematic description of the interface evolution of the self-mated 100 C6 steel contact versus the test duration explaining the successive stages of the friction evolution (after [Merhej (2008)]).

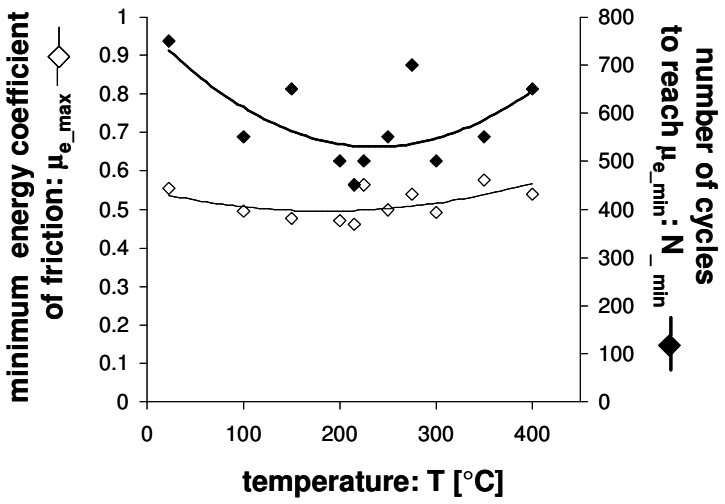

Figure 63: Minimum energy coefficient of friction (μ_{e_min}) and associated number of cycles ($N_{\_min}$)as a function of temperature under the mechanical key point loading conditions.

which supports severe plastic strain, starts to generate the first wear debris that are immediately oxidized. A consequence of the formation of this first debris within the interface is a separation of the adhering first bodies by limiting the metal-metal interactions, and consequently a sharp decrease of the coefficient of friction (Figure 62 D). The minimum of the coefficient of friction (μ_{e_min}) was found by him to be established thanks to the operating third body displaying powder structure. It may therefore be implied that probably synergetic effect of roughness increase and rheological properties of the formed third body contributes to the abrupt decrease of the coefficient of friction after a few hundred cycles of fretting test.

Like in the case of the μ_{e_max} the minimum energy coefficient of friction (μ_{e_min}) seems to keep more or less steady value (μ_{e_min}=0.52±0.05) independently of the temperature, while a conclusion as to the associated number of cycles needed to reach it ($N_{\_min}$) is not so obvious as it shows high scattering (Figure 63).

2. 2. 1. 2. Characterization of the transient and steady state

Transient state can be defined as an intermediate period occurring between a running-in period and steady-state. Within this stage a conditioning period characterized by a high work hardening as well as degradation and dispersal of the adhesion zones takes place. Debris is then generated, promoting the formation of a third body layer and the establishment of the steady-state regime. Comminution and dispersal of the adhesion zones is proved as roughness of the contacted surfaces decreases in the transient stage following its increase during adhesive stage (Figure 61). Afterwards, when a conditioning period comes to the end the roughness starts to grow as the crucial role plays then debris formation deciding which kind of wear regime will be promoted. On the other hand, the increase of the coefficient of friction within the transient state was reported by Merhej (2008) to be related to the formation of compacted third body (agglomerated structure), which was supposed to be less compliant than the powder structure observed as the minimum coefficient of friction was reached (Figure 62).

As it has already been mentioned above the evolution of the coefficient of friction within the transient state differs significantly for fretting experiments performed below and above T_{ga}. It suggests that the third body formed in the interface evolves differently within the transient stage and displays different properties below and

above T_{ga}. At temperatures higher than T_{ga} the energy coefficient of friction reaches some maximum (defined as a maximum transition energy coefficient of friction (μ_{e_tran})) at $N_{\_tran}$ number of cycles followed by its decrease down the stabilized value (μ_{e_SS}). The value of the μ_{e_tran} and associated number of cycles needed to achieve it ($N_{\_tran}$) generally decreases as the applied test temperature increases (Figure 64). Similar situation can be observed if we consider a time period that is taken up by transient stage before steady-state is established.

Figure 65 shows the evolution of the energy friction coefficients (μ_e) for two temperatures 250 and 400°C (both above T_{ga}) under the mechanical key point loading conditions. It is clearly seen that steady-state is reached at less number of cycles at higher temperature. It can also be concluded that the higher the temperature the lower the stabilized friction value (μ_{e_SS}) is.

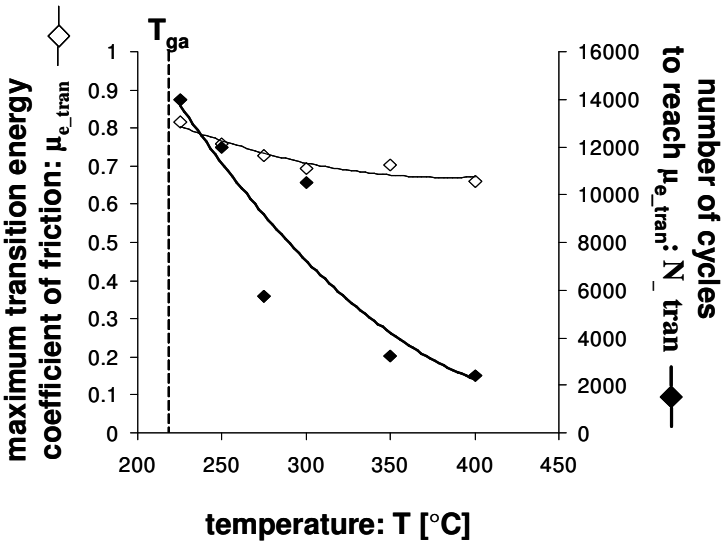

Figure 64: Maximum transition energy coefficient of friction (μ_{e_tran}) and associated number of cycles ($N_{\_tran}$) needed to reach it as a function of temperature under the mechanical key point loading conditions.

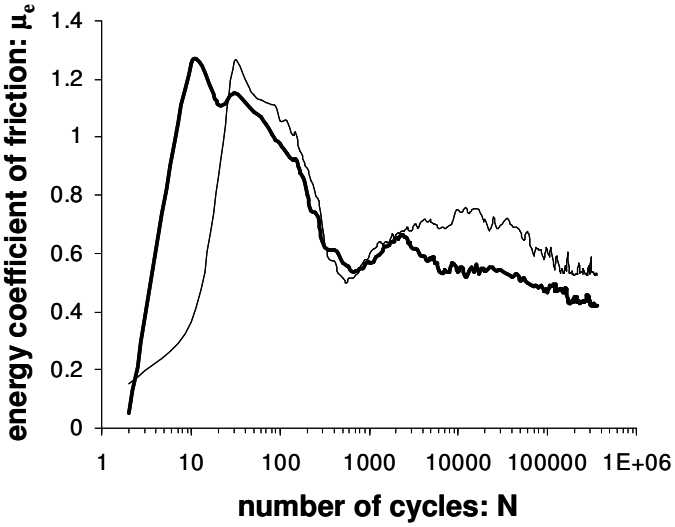

Figure 65: Evolution of the energy friction coefficient (μ_e) as a function of the test duration for two temperatures 250 (———) and 400°C (———) under the mechanical key point loading conditions.

The number of cycles needed to reach steady-state ($N_{\_SS}$) was determined based on the friction evolution and increment of the dissipated energy recorded during the tests. Figure 66 shows that for $T<T_{ga}$ and $T>_{ga}$ different tendencies can be observed. The number of cycles needed to establish steady-state below T_{ga} is practically independent of temperature ($N_{\_SS}$=20000 cycles), however above T_{ga} a decrease of $N_{\_SS}$ according the Arrhenius law as temperature increases is observed. Thus, it is clearly demonstrated that the third body formed below and above T_{ga} interacts in different manner. For the temperatures higher than T_{ga} thermal processes appear to be activated that lead to the modification of the third body structure.

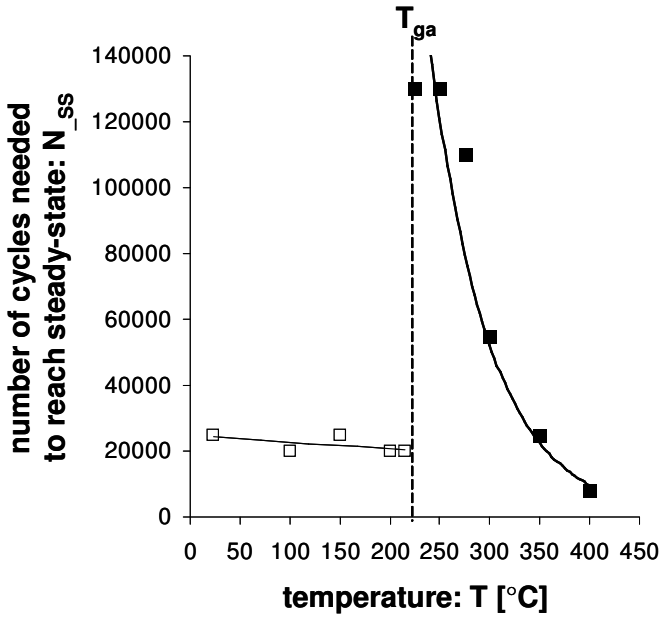

Figure 66: Number of cycles needed to reach steady-state energy coefficient of friction versus temperature below (—□—) and above (—■—) T_{ga}.

The average steady-state energy coefficient of friction ($\overline{\mu}_{e\_SS}$) is defined by averaging the friction value μ_e over the last (N-$N_{\_SS}$) cycles of the fretting tests when the stabilized friction response is systematically achieved (relation 40):

$$\overline{\mu}_{e\_SS} = \frac{1}{N - N_{\_SS}} \cdot \sum_{i=N_{\_SS}}^{N} \mu_{e(i)} \qquad (40),$$

with: N – the total number of cycles (360000), $N_{\_SS}$ – the number of cycles needed to reach a steady-state (Figure 66) and $\mu_{e(i)}$ - the energy coefficient of friction at i th number of cycles.

Figure 67 plots the evolution of the average steady-state energy coefficient of friction ($\overline{\mu}_{e\_SS}$) as a function of temperature. Three domains, indeed, can be identified. Below a threshold temperature established at T_{ga}=220°C (temperature of 'glaze' layer activation) a high friction regime, corresponding to the conventional steel/steel behaviour under ambient conditions, is observed. Above T_{ga} a decrease of the coefficient of friction is observed. Hence, it can be concluded that the higher the temperature, the more complete the formation of the lubricating third body layer. At this stage of the investigations, however, it is not possible to say if this evolution is related to the partial constitution of the 'glaze' layer (i.e. the interface displays a

composite structure including 'glaze' layer islands and non-lubricating domains) or if the interface consists of a continuous third body that has not reached lubricating properties yet. The coefficient of friction decreases in a quasi-linear manner down to a second threshold temperature T_{gs}= 240°C (temperature of 'glaze' layer stabilization). Above T_{gs} an effective 'glaze' layer is generated within the interface, promoting a low and practically stable coefficient of friction. The very long duration of the tests (360000 cycles) suggests that this trend is representative of the steady-state behaviour of the interface.

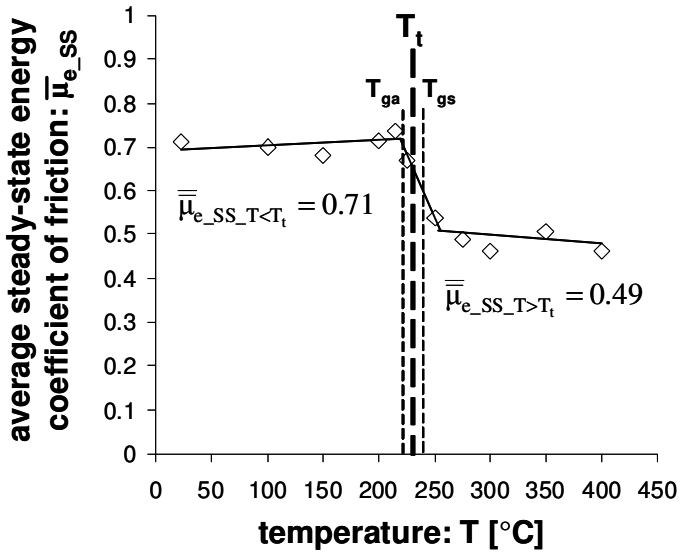

Figure 67: Evolution of the average steady-state energy friction coefficient ($\overline{\mu}_{e\_SS}$) as a function of the applied temperature for the key point conditions.

Furthermore, it must be noticed that at 225°C (just above T_{ga}) the value of the average steady-state energy coefficient of friction is close to the values characteristic of lower temperatures (i.e. below T_t). It is due to the fact that some disturbances in the friction evolution at 225°C within the steady-state characterized by sharp peaks are occurring (Figure 68). Thus, it appears that under the studied mechanical loadings at 225°C the formed 'glaze' layer, though activated, is yet unstable to be capable of bearing the load effectively. Found disturbances in the friction evolution imply that the activated 'glaze' layer is subjected to the destruction process straightaway after its formation.

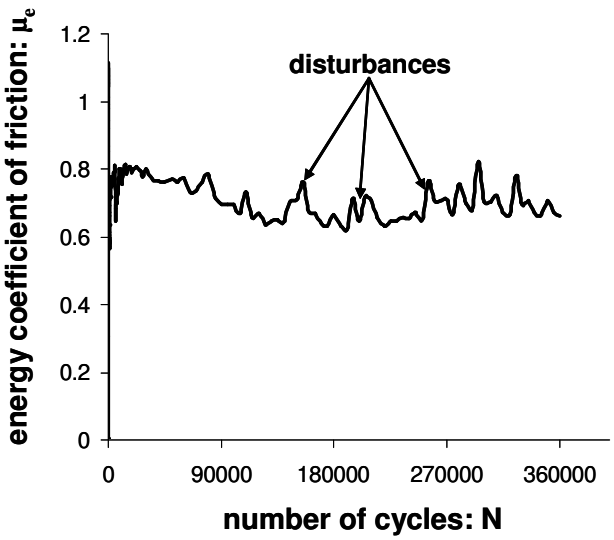

Figure 68: Evolution of the energy coefficient of friction at 225°C under the mechanical key point loading conditions.

Taking into account above discussion and the fact that the transition between high and low friction regime takes place in a narrow temperature range of 20°C ($T_{ga}<T<T_{gs}$) the transition temperature $T_t = \frac{(T_{ga} + T_{gs})}{2} = 230°C$ is defined to simplify our considerations. It is then assumed that only the two friction domains exist, where below T_t the interface with different than 'glaze' layer properties is predominantly developed, while above T_t a stable lubricating 'glaze' layer is formed. Quantifying (excluding the transition result at 225°C), the mean value of the average steady-state energy coefficient of friction ($\overline{\overline{\mu}}_{e\_SS}$) below and above the transition temperature T_t is $\overline{\overline{\mu}}_{e\_SS\_T<T_t} = 0.71$ and $\overline{\overline{\mu}}_{e\_SS\_T>T_t} = 0.49$, respectively.

It must be recalled that coefficient of friction is controlled by the generated interface, so by the third body and its structure. Taking into account a state of the art of tribological issues under elevated temperature conditions the observed difference in friction evolution as T_t=230°C is exceeded could be explained in two ways. On the one hand, it must be consider a tribo-chemical aspect as above T_t porous oxides (Fe_3O_4) are believed to act as a solid lubricants [Hurricks (1974)], on the other hand a tribo-sintering process [Jiang et al. (1998), Kato et al. (2007)] of wear particles as adhesion between them increases with temperature [Yamamoto et al. (1981)] leading to the formation of a load-bearing 'glaze' layer should be mentioned. Thus, high

coefficient of friction observed below T_t can be due to either brittle and hard oxides (Fe_2O_3) operating in the interface or poor adhesion between wear particles preventing the formation of the compact 'glaze' layer before they are ejected outside the contact. Furthermore, to explain the friction behaviour as a function of temperature a synergetic effect of tribo-chemical transformation and sintering process of the wear debris cannot be excluded. The response to the arising question: which of the above-mentioned phenomena plays a crucial role in the friction behaviour is being discussed extensively in the next paragraphs as wear behaviour and analytical investigations of the interface (providing its detailed physico-chemical characterization) are being analyzed.

2. 3. Impact of the mechanical loadings at 200 and 400˚C

Analysis of the friction behaviour for all tests performed at the different mean pressures and displacement amplitudes at 200 and 400˚C are being discussed in this section.

The evolutions of the maximum, minimum, maximum transition (only above T_t, i.e. at 400°C) and steady-state energy coefficients of friction as well as related number of cycles needed to reach them versus mean pressure and displacement amplitude for 200 and 400°C are shown in Figure 69, 70, 71 and 72, respectively. In general, each individual friction parameter and the associated value of the number of cycles considered appears to increase slightly as the mean pressure or displacement amplitude increases. The only exception is the evolution of the number of cycles needed to achieve the maximum and maximum transition energy coefficient of friction versus displacement amplitude where it tends to decrease as the parameter increases.

The increase of the maximum energy coefficient of friction (μ_{e_max}) as the displacement amplitude increases (Figure 69) can be explained qualitatively in terms of the probability of asperity collisions between the contacting surfaces. At the larger fretting amplitudes an asperity has a higher probability of interacting with many adjacent opposing asperities than it can be expected for smaller displacement. This, in consequence, may lead to higher adhesive contact as higher displacement amplitude is imposed [Aldham et al. (1985)]. The impact of the mean pressure (i.e. constant, corresponding to the normal force) can be similarly considered, namely area of the

real contact is directly proportional to the load [Singer et al. (1992)], thereby as the mean pressure increases the probability of asperities interactions grows.

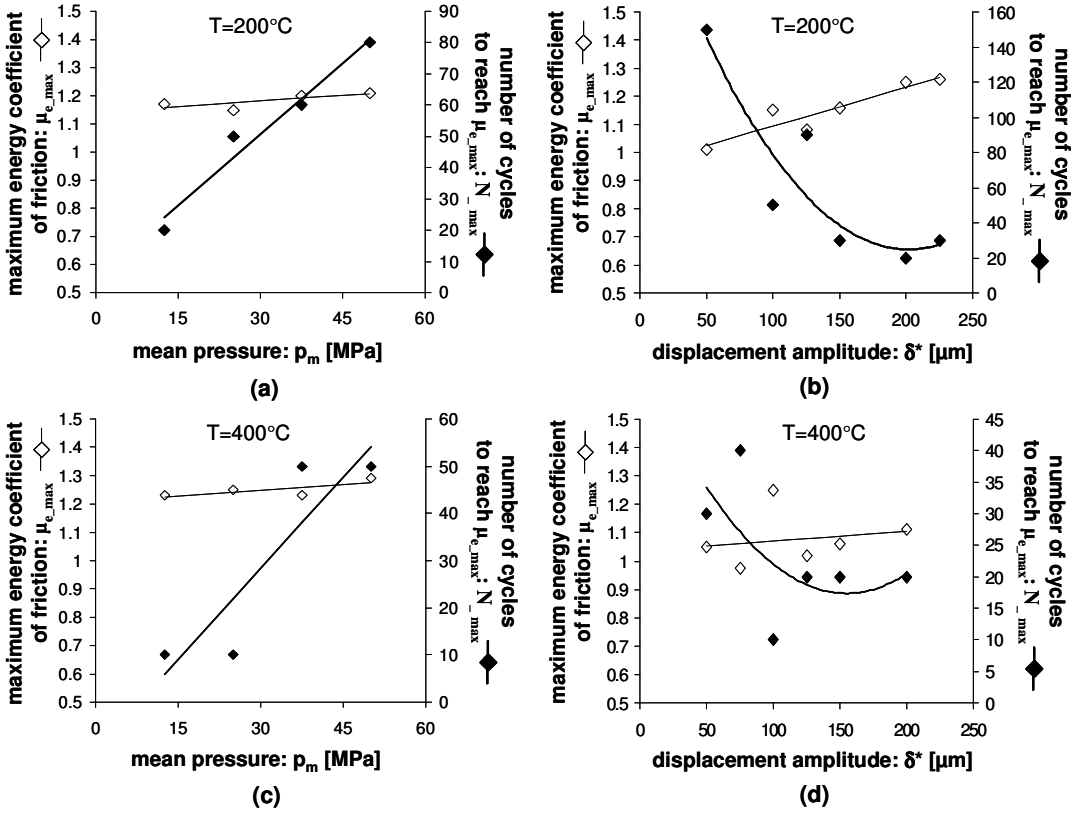

Figure 69: Maximum energy coefficient of friction (μ_{e_max}) and related number of cycles needed to reach it ($N_{\_max}$) as a function of the mean pressure at (a) 200°C and (c) 400°C and displacement amplitude at (b) 200°C and (d) 400°C.

The maximum of the energy coefficient of friction corresponds to the situation when there is a maximum metal-metal interaction. It can be observed that the number of cycles ($N_{\_max}$) to reach maximum energy coefficient of friction decreases as the imposed displacement amplitude increases. It infers that the faster the elimination of native oxides and spreading of the metal-metal interaction the faster the μ_{e_max} reaching. The larger the displacement the higher the amount of interlocking asperities, so faster elimination of native oxides and smaller $N_{\_max}$ at which maximum energy coefficient of friction is established. More difficult is to interpret the mean pressure effect, where the number of cycles to reach μ_{e_max} increases with the parameter. If it

is assumed that $N_{\_max}$ is a function of the total elimination of native oxides, then a following hypothesis should be verified. The greater the normal force (mean pressure) the larger the real contact area, so the longer the process of elimination of native oxides.

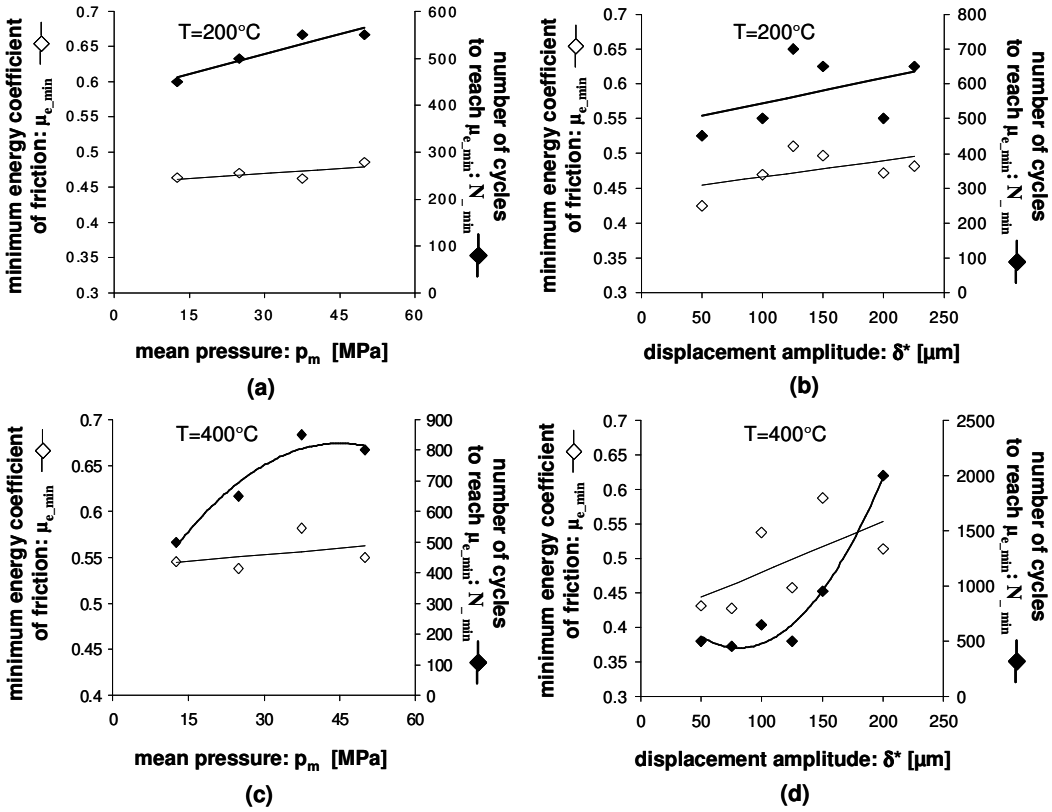

Figure 70: Minimum energy coefficient of friction (μ_{e_min}) and related number of cycles needed to reach it ($N_{\_min}$) as a function of the mean pressure at (a) 200°C and (c) 400°C and displacement amplitude at (b) 200°C and (d) 400°C.

As the steady-state is established the tribological behaviour is no longer controlled by the first bodies but by the third body occurring in the interface. The increase of the mean pressure or displacement amplitude causes generation of more severe working conditions, which produce higher coefficient of friction ($\overline{\mu}_{e\_SS}$) (Figure 72).

In case of the increased mean pressure and displacement amplitude the removal probability of the wear debris from the rubbing surfaces increases [Jiang et al.

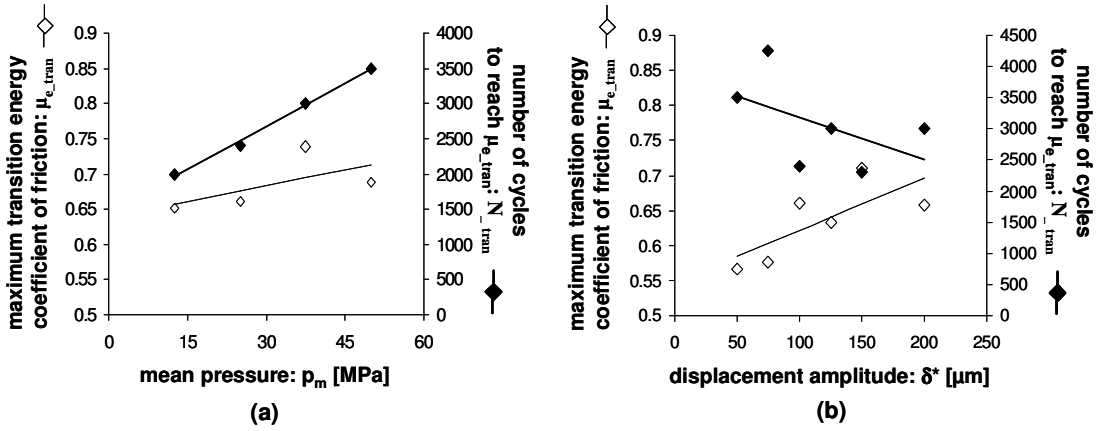

Figure 71: Maximum transition energy coefficient of friction (μ_{e_tran}) and related number of cycles needed to reach it ($N_{\_tran}$) at 400°C as a function of the (a) mean pressure and (b) displacement amplitude.

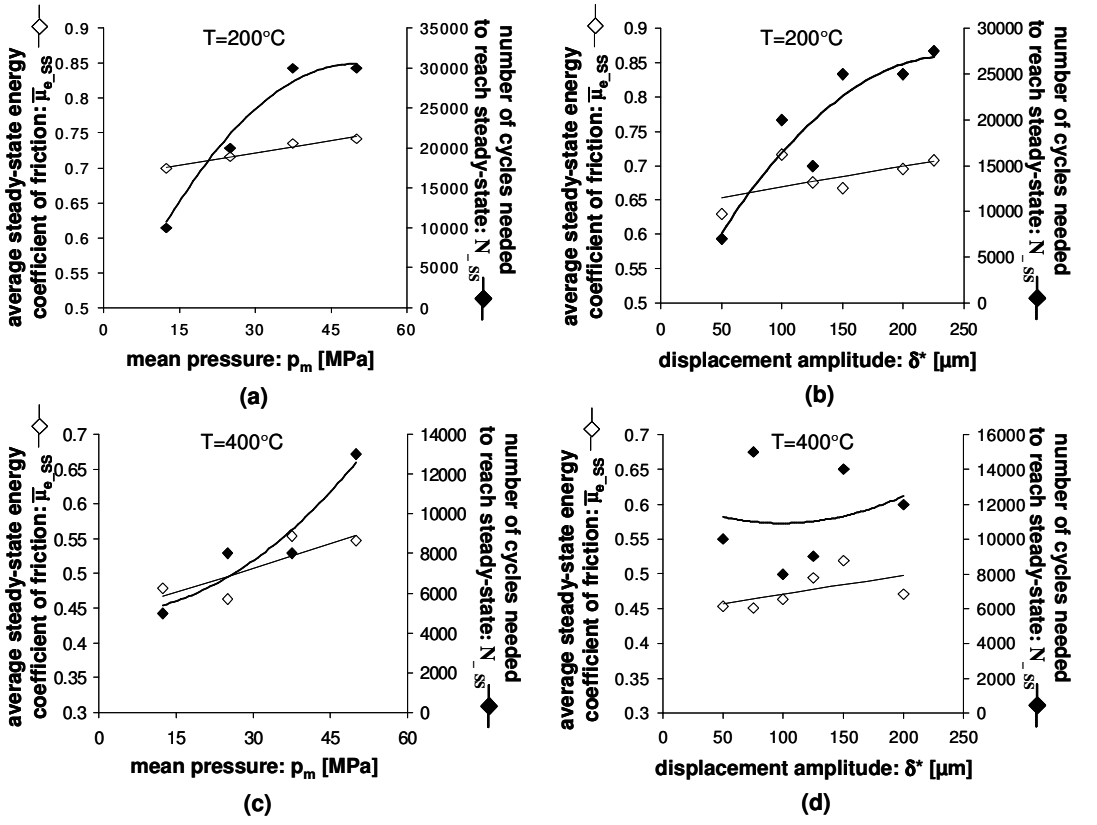

Figure 72: Average steady-state energy coefficient of friction ($\overline{\mu}_{e\_SS}$) and related number of cycles needed to reach it ($N_{\_SS}$) as a function of the mean pressure at (a) 200°C and (c) 400°C and displacement amplitude at (b) 200°C and (d) 400°C.

(1995)]. Moreover, it was reported that the depths of deformation layers on the wear surfaces increase with load, thus larger wear debris particles are produced [Soda et al. (1976)]. Bigger particles are more difficult to oxidize, thus the probability of their incorporation into the third body layer decreases. Hence, more time (higher number of cycles $N_{\_SS}$) is needed to establish the steady-state as more severe loadings are imposed (Figure 72).

3. WEAR BEHAVIOUR

3. 1. Criteria introduced for wear resistance analysis

In the present Chapter two wear criteria are considered to evaluate and compare the fretting wear resistance of the studied tribo-systems as a function of temperature.

3. 1. 1. Archard's wear criterion

Transposed to the studied gross slip fretting conditions the classical Archard's product ($P \cdot S$) previously discussed in Chapter 1 can be expressed by the following relationship:

$$P \cdot S = \sum_{i=1}^{N} 4 \cdot P_{(i)} \cdot \delta_{g(i)} \qquad (41),$$

with: N - the number of cycles, $P_{(i)}$ - the normal force and $\delta_{g(i)}$ - the sliding amplitude at the i th cycle.

Thus, the Archard's wear coefficient (K) where total wear volume (V) is compared to the Archard's product can be written as follows:

$$K = \frac{V}{P \cdot S} = \frac{V}{\sum_{i=0}^{N} 4 \cdot \delta_{g(i)} \cdot P_{(i)}} \qquad (42).$$

3. 1. 2. Energy wear approach

This approach permits a comparison of the total wear volume with the accumulated friction work dissipated through the interface (Chapter 1). The dissipated energy corresponds to the accumulated energy ($\sum Ed$) determined from the sum of the fretting cycle area:

$$\sum Ed = \sum_{i=1}^{N} Ed_{(i)} \quad (43),$$

with: N- the number of cycles and $Ed_{(i)}$ - the dissipated energy of the i th cycle.

Thus, the energy coefficient of friction (α) is defined as a ratio of the total wear volume to the accumulated energy dissipated in the interface (relation 10).

3. 2. Impact of temperature

Figure 73 shows the evolution of the total wear volume as a function of the temperature for the mechanical key point loading conditions (i.e. p_m=25 MPa (i.e. P=176 N), δ^*=±100 µm and N=360000 fretting cycles). The abrupt drop in the wear evolution can be observed as temperature exceeds the temperature T_{ga}=220°C. For 225°C (i.e. $T_{ga}<T<T_{gs}$) an intermediate value of the wear volume is observed. In the range of 20°C (i.e. between T_{ga} and T_{gs}) the wear response is therefore found to be reduced around 11 times above T_{gs} compared to the temperatures lower than T_{ga}. Simplifying our considerations above the threshold temperature T_t low wear response can be observed.

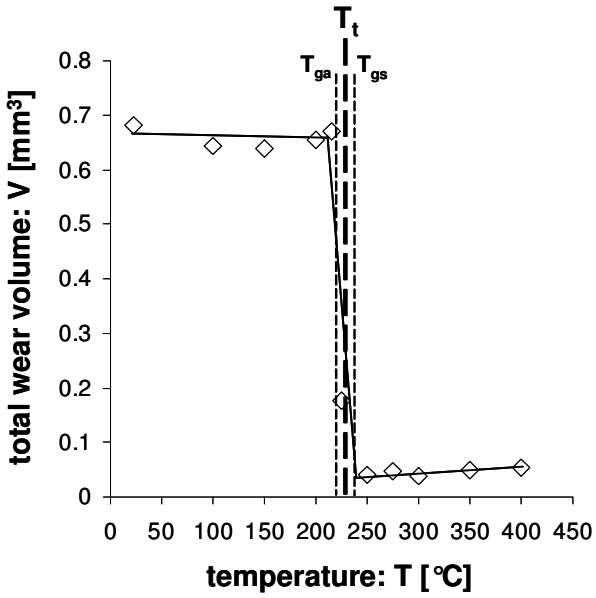

Figure 73: Evolution of the total wear volume obtained at the mechanical key point loading conditions as a function of temperature.

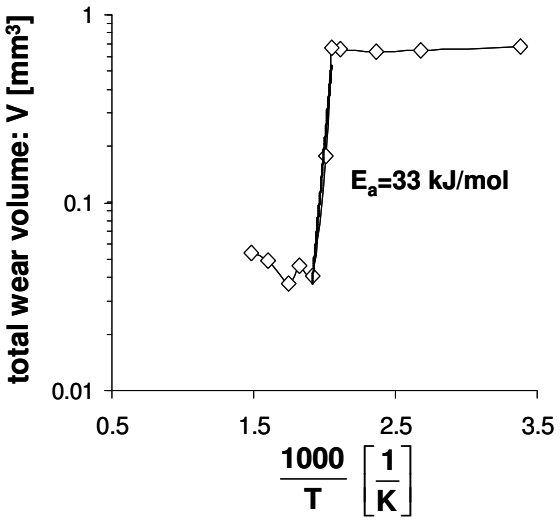

Figure 74: Replot of the evolution of the total wear volume obtained under the mechanical key point loading conditions as a function of temperature (Figure 73), according to Arrhenius relationship.

To explain the evolution of the total wear volume versus temperature the oxidational wear theory cannot be applied because, according to its assumption, wear should increase with temperature due to the increased oxidation rate (relation 31). On the other hand, the beneficial effect of the formation of a wear-protective 'glaze' layer promoted only by the increased temperature cannot also account for the obtained results. Attempting to find the response regarding the mechanism of a 'glaze' layer development, Figure 73 is replotted according to an Arrhenius relationship between wear and temperature (Figure 74). The activation energy for the wear process as the severe to mild wear rate transition takes place is here found to be approximately 33 kJ/mol. This value is of the same order of magnitude as the tribo-oxidation energy characteristic of the stainless steel [Hong et al. (1988)]. It is also consistent with the activation energy for the development of adhesion between contact asperities in the 'stick-slip' static friction process [Jiang et al. (1995)]. Hence, it signifies that either the tribo-oxidation or the tribo-sintering process cannot be excluded as that by which the development of the wear-protective 'glaze' layer is controlled. Moreover, perhaps a synergetic effect between tribo-oxidation and tribo-sintering should be considered. Such an assumption might be supported through the fact that both phenomena intensify with temperature. The beneficial effect of the higher oxidation rate is the faster wear particles oxidation as well as higher probability that larger debris would

be completely oxidized and incorporated into a 'glaze' layer. Hence, as temperature increases those both processes may favour the faster development of a 'glaze' layer of better lubricating properties.

Figure 75 plots the evolution of the energy wear coefficient defined from the mechanical key point loading conditions (α_{kp}) as a function of the applied temperature. Similarly to the friction behaviour (Figure 67) three domains can be identified. Below the temperature T_{ga}=220°C an almost constant high energy wear coefficient can be found, between T_{ga} and T_{gs} an intermediate value of α_{kp} can be observed, however above T_{gs}=240°C a quasi constant low energy wear coefficient is maintained. As the establishment of the low friction and wear interface takes place in a narrow range of temperature (20°C) the severe to mild wear rate transition temperature T_t=230°C is introduced in order to simply our considerations. It is then assumed that a change of the tribological response occurs at T_t. Below T_t high wear regime is predominant, while above T_t low wear regime is activated. Quantifying (excluding the result at 225°C), the average value of the energy wear coefficient ($\overline{\alpha}_{kp}$) below and above the transition temperature T_t is $\overline{\alpha}_{kp\_T<T_t} = 5.44 \cdot 10^{-5}$ and $\overline{\alpha}_{kp\_T>T_t} = 4.19 \cdot 10^{-6}$ $mm^3 \cdot J^{-1}$, respectively. Thus, the energy wear coefficient is reduced by a factor of 13 above T_t.

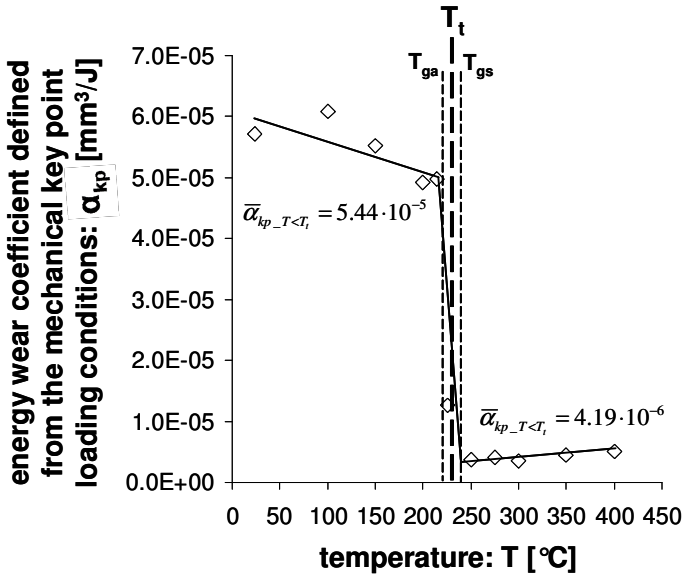

Figure 75: Evolution of the energy wear coefficient defined from the mechanical key point conditions (α_{kp}) as a function of temperature.

Though the friction analysis shows that at 225°C ($T_{ga}<T<T_{gs}$) the value of the coefficient of friction is close to those characteristic of lower temperatures (Figure 67), the energy wear response is characterized by a sharp decrease (Figure 75). It suggests that even if the lubricating properties of the 'glaze' layer are not fully developed within $T_{ga}<T<T_{gs}$, an immediate modification of wear response is activated. It therefore seems to be fully justified that only two wear regimes can be considered. Above T_t the dissipated energy at the interface is no longer consumed through a severe two body damage process, but involves the third body 'glaze' layer accommodation of shear work. Less energy is then available to produce debris and consequently the energy wear rate is reduced.

The above discussion on the effect of temperature on the wear evolution did not give the explicit answer regarding the process (tribo-chemical or tribo-sintering), which is responsible for friction and wear decrease as the transition temperature T_t is exceeded, but provided the clue that increasing adhesion interaction between particles with temperature enhanced by a tribo-oxidation process might be an essential factor for the development of the wear-protective 'glaze' layer. Results of the analytical analyses of the interface are being talked about in the next paragraph of the present dissertation in order to clarify the mechanism of 'glaze' layer formation.

Moreover, after the analysis of wear evolution versus temperature it arises a question: if the two found average energy wear coefficient are characteristic of the individual ranges of temperatures (below and above T_t), independently of the applied loading conditions? This aspect is being discussed extensively in the paragraph dedicated to fretting wear mapping of the 'glaze' layer activation.

3. 3. Impact of the mechanical loadings at 200 and 400°C

The wear behaviour at two different temperatures, this below (200°C) and that above (400°C) the severe to mild wear rate transition as a function of various loading conditions (defined in Figure 52) are being contemplated in this section. Figure 76, 77 and 78 shows the evolution of the total wear volume versus, respectively, the applied displacement amplitude, mean pressure and test duration for both the considered temperatures. As it can be observed for all cases the total wear volume increases with the value of the individual parameter. As a function of the displacement amplitude and mean pressure it appears to take a linear tendency, whereas a quasi-parabolic

trend characterizes the wear evolution versus number of cycles (during the running-in and conditioning period a higher wear rate can be observed).

Figure 79 depicts the evolution of the total wear volume as a function of the accumulated dissipated energy for the two considered temperatures. For each temperature a high linear correlation with the dissipated energy can be observed (coefficient of determination R^2 and standard deviation σ are $R^2_{200°C}$=0.96 and $\sigma_{200°C}$=0.034 mm^3 and $R^2_{400°C}$=0.90 and $\sigma_{400°C}$=0.003 mm^3 for 200°C and 400°C, respectively). Assuming a constant interface structure (i. e. a constant temperature condition), the energy variable appears as a single factor whatever the imposed mechanical conditions such as pressure, sliding amplitude and test duration. This correlation is verified for the studied loading range (Figure 52) and contact geometry. Linear approximations are therefore considered, allowing the energy wear coefficient (α) to be identified (according to relation 10). Quantifying the energy wear coefficient gives $\alpha_{200°C} = 6.50 \cdot 10^{-5}$ and $\alpha_{400°C} = 5.62 \cdot 10^{-6}$ $mm^3 \cdot J^{-1}$ at 200 and 400°C, respectively. Thus, the energy wear coefficient determined for all imposed mechanical loadings at the temperature 400°C (i.e. above the severe to mild wear rate transition temperature T_t=220°C) is reduced by a factor of about 12 compared to that established at 200°C (i.e. temperature below T_t). The value of the decrease found is practically the same as for the comparison of the average energy wear coefficients determined in the previous section. Relative error between the average energy wear coefficient below ($\overline{\alpha}_{kp\_T<T_t} = 5.44 \cdot 10^{-5}$ $mm^3 \cdot J^{-1}$) and above ($\overline{\alpha}_{kp\_T>T_t} = 4.19 \cdot 10^{-6}$ $mm^3 \cdot J^{-1}$) the severe to mild wear transition and the energy wear coefficient at 200 ($\alpha_{200°C} = 6.50 \cdot 10^{-5}$ $mm^3 \cdot J^{-1}$) and 400°C ($\alpha_{400°C} = 5.62 \cdot 10^{-6}$ $mm^3 \cdot J^{-1}$) determined for the wide range of the mechanical loadings is 15 and 25%, respectively. From the standpoint of tribological wear assessment such differences do not appear as very high, thus the assumption suggesting that the fretting wear behaviour of the studied tribo-couple as a function of temperature might be characterized by the two above-determined average energy wear coefficients in the studied range of loadings seems to be fully rationalized.

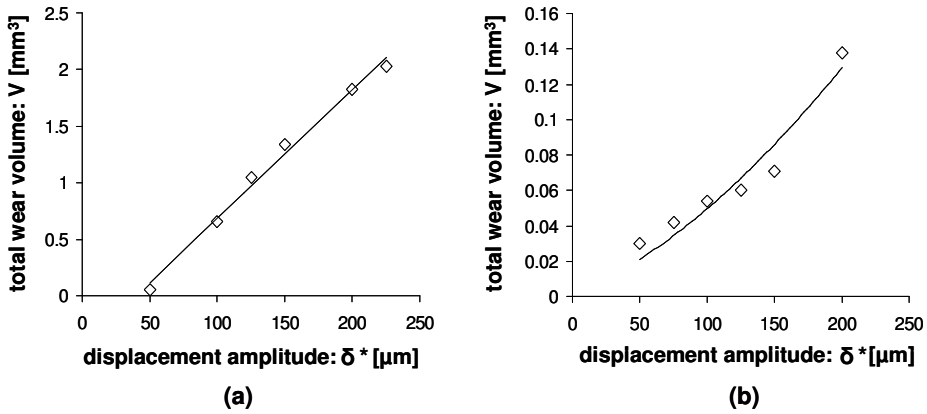

Figure 76: Evolution of the total wear volume versus the imposed displacement amplitude at (a) 200°C and (b) 400°C.

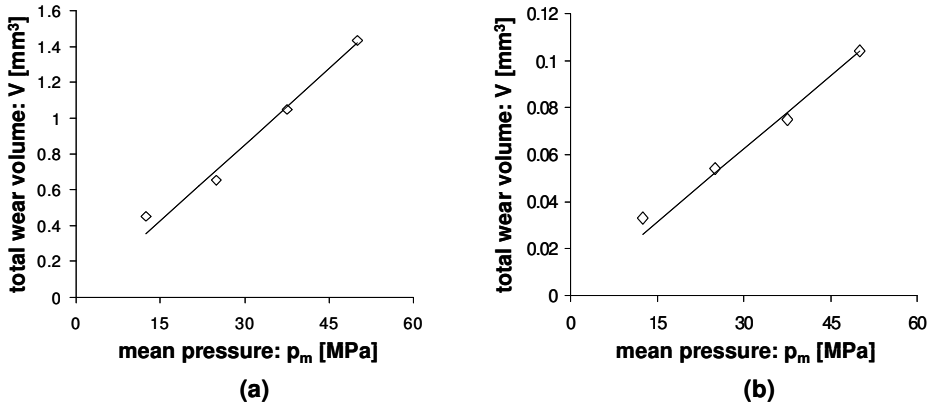

Figure 77: Evolution of the total wear volume versus the imposed mean pressure at (a) 200°C and (b) 400°C.

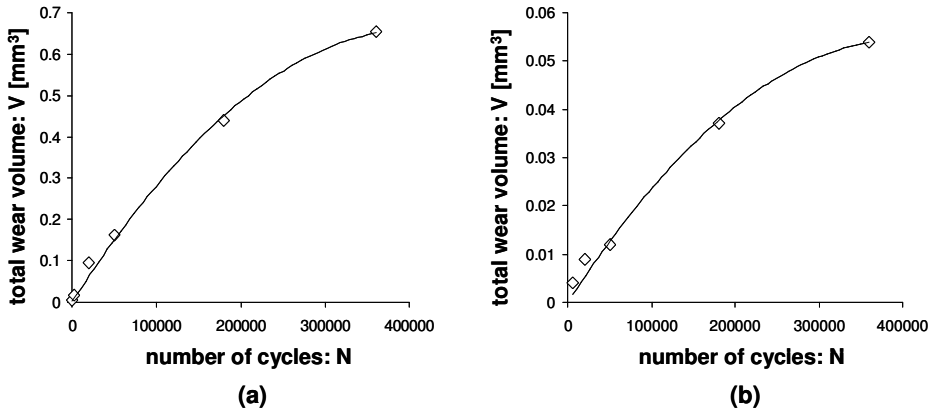

Figure 78: Evolution of the total wear volume versus the studied test duration (number of cycles) at (a) 200°C and (b) 400°C.

It must be emphasized that a comparison in terms of dissipated energy already integrates the friction reduction factor. A similar analysis based on the Archard's approach (Figure 80), which reflects the ratio of the total wear volume to the product of the normal force by the total sliding distance, produces a more abrupt reduction of the wear rate as threshold temperature T_t is exceeded ($\frac{K_{200°C}}{K_{400°C}} \approx 16$). Indeed, apart from decreasing the energy wear rate, the stabilized 'glaze' layer ($T>T_{gs}$) also decreases the amount of dissipated energy in the interface. Moreover, it is worth to notice that equally high linear correlation with the Archard's product (coefficient of determination R^2 and standard deviation σ are $R^2_{200°C}=0.98$ and $\sigma_{200°C}=0.023$ mm^3 and $R^2_{400°C}=0.93$ and $\sigma_{400°C}=0.003$ mm^3 for 200°C and 400°C, respectively) as with the above-discussed accumulated dissipated energy can be observed.

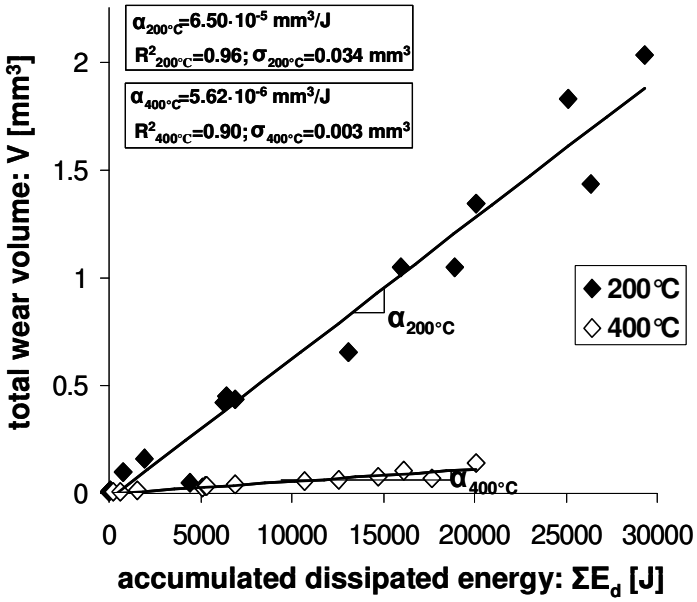

Figure 79: Total wear volume as a function of the accumulated dissipated energy at 200°C and 400°C for which the wide range of the mechanical loadings were investigated.

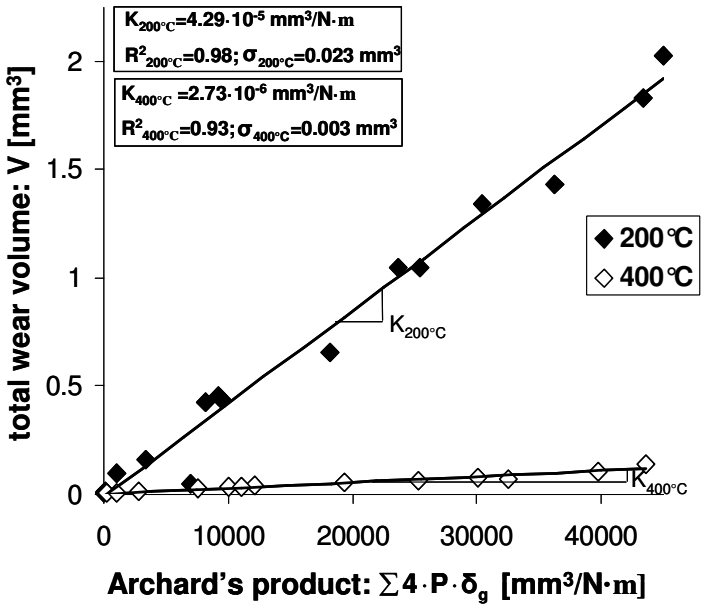

Figure 80: Total wear volume as a function of the Archard's product at 200°C and 400°C for which the wide range of the mechanical loadings were investigated.

4. ANALYTICAL CHARACTERIZATION OF THE INTERFACE

Different analytical techniques for characterization of the Jethete M152/A-286 interface were employed to complete the previous quantitative investigations and give the final answer regarding the process that controls the wear-protective layer development.

4. 1. Scanning electron microscope investigations

At first, scanning electron microscope observations combining energy dispersive X-ray spectrometry analyses of the fretting scars were carried out. All investigations were conducted under 15 keV of the accelerating voltage of the electron beam. Prior to the observations the specimens were cleaned in ultrasonic bath so that remove the loose wear debris. Figure 81 shows the morphology of the fretting scar generated on to the A-286 specimen under the mechanical key point loading conditions at 23°C (i.e. below T_t). The local adhesive wear mechanism characterized by tearing out of the material was found to be predominant (Figure 81a). The local metal transfer and surface seizure might have induced a higher wear rate. The particulate nature of the

wear surface was revealed (Figure 81b-c). Tilted secondary electron images allowed the measurements of the pilled up third body layers to be carried out. The thickness of the third body was found to be in the 2-6 μm range (Figure 81d). It appears, therefore, that the 2-6 μm thick wear debris layers were flaked off under fretting loadings as a result of delamination process [Waterhouse et al. (1974)]. The continuing fretting action caused that they were crushed into the fine spherical particles within the interface.

The morphology of the fretting scar obtained under the mechanical key point loading conditions at the high temperature (400°C) (Figure 82) showed the features different from those characteristic of the low temperature. The large smooth load-bearing areas ('glaze' layers) were formed at discrete locations on to the wear surface (Figure 82a). Higher magnification images (Figure 82b-c) revealed linear grooves on the 'glaze' layers aligned in the sliding direction, which mean that above T_t three body abrasive wear was dominant. Figure 82d depicts the image taken on the border of the scar where compacted particle regions can be observed. 'Glaze' layers were developed on the top of such areas as a result of burnishing of the agglomerations of particles adhered to each other during the test [Stott (1998)]. It is proved in high magnification picture (Figure 82c). It is apparent that the 'glaze' layers are very solidly compacted (characterized by a very high cohesion quality) on to the wear surface (Figure 82c) and elevate over the adjacent areas similar to those characteristic of adhesive wear mechanism observed at 23°C. These adjacent areas show, however, less particulate features than it was revealed at the lower temperature implying higher degree of particle compaction (i.e. higher cohesion). This seems to confirm that submission to the high local pressure and elevated temperature conditions favours the activation of the sintering process [Jiang et al. (1998), Kato et al. (2007)], promoting the formation of a compliant 'glaze' layer structure. The morphology of the wear scar generated at 200°C (Figure 83) revealed that most of its surface shows the features similar to those characteristic of the wear surface obtained at 23°C. Only somewhere the small 'glaze'-like patches could be noticed. The qualitative evaluation of the fretting scars produced at 200 and 400°C showed that it took up relatively smaller area at the former temperature than at the latter one. This therefore infers that T_t=230°C is not the threshold temperature below which a 'glaze' structure cannot be formed, but it is the temperature below which a 'glaze' layer is unstable mechanically.

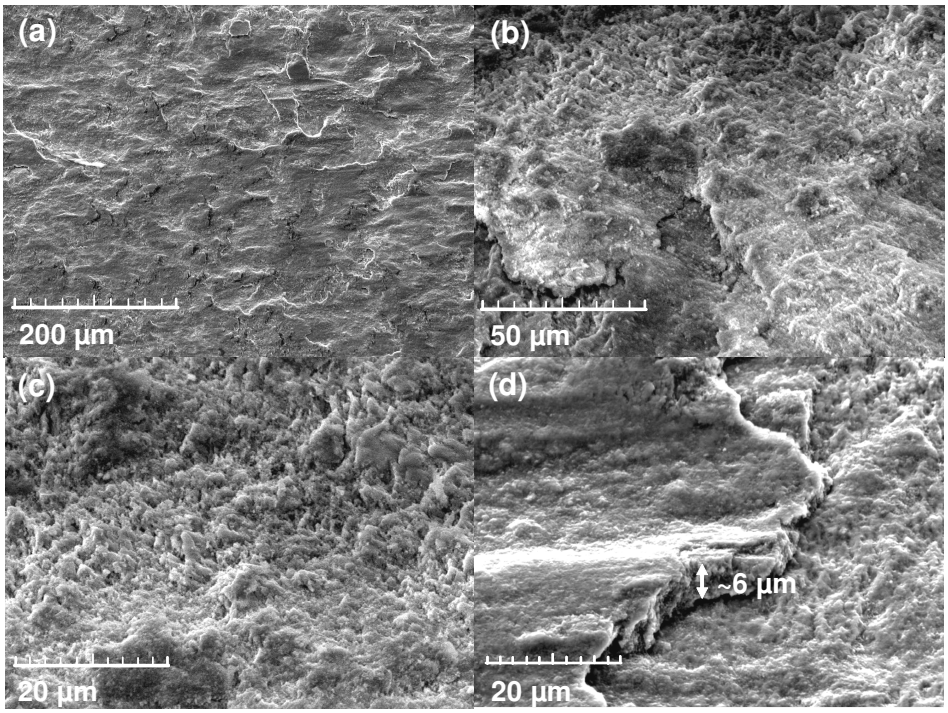

Figure 81: Characteristics of the wear surface formed on to the A-286 specimen at 23°C: (a) Low magnification image showing typical adhesive wear mechanism; (b) Tearing out of the material due to the local adhesive interactions; (c) High magnification image revealing the particulate nature of the third body; (d) Pilling up of third body layers.

The elevated temperature (i.e. above T_t) facilitates wear particles compaction (i.e. increase of adhesion forces between wear particles [Yamamoto et al. (1981)]), so the formation of a very coherent wear-resistant load-bearing layers is promoted. As soon as a stable 'glaze' layer is developed in the interface ($T>T_t$) the load-bearing capacity is fully modified and resistance to wear increases around order of magnitude compared to the lower temperatures ($\frac{\overline{\alpha}_{kp\_T<T_t}}{\overline{\alpha}_{kp\_T>T_t}} \approx 13$). A virtue of the formation of a 'glaze' layer is that, when breakdown occurs locally and material is lost, the fretting action repairs the damage by rapid recreating the 'glaze' as high amount of wear particles is retained within the interface due to the increased particle adhesion.

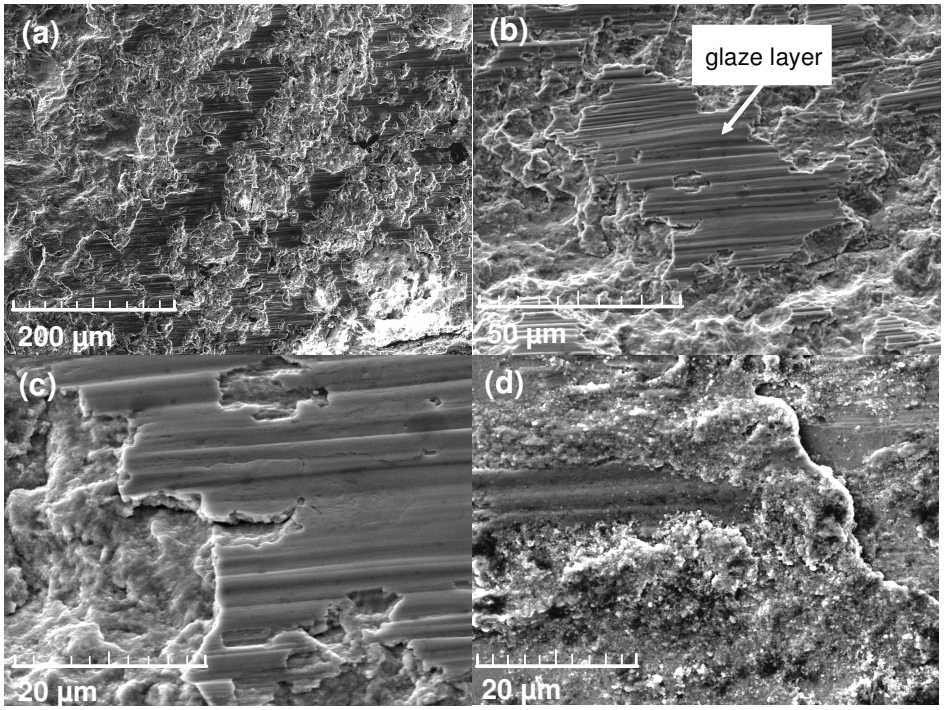

Figure 82: Characteristics of the wear surface formed on to the A-286 specimen at 400°C: (a) Large load-bearing glaze layers; (b) Linear grooves on the glaze layers aligned in the sliding direction; (c) High magnification image depicting very high cohesion of the glaze layer that is elevated over the adjacent granular areas; (d) Compacted particle region observed on the border of the scar.

Apart from the ordinary observations of the wear scars the cross-section investigations were carried out. The compacted third body layer overlying the substrate material was revealed in all cases. Figure 84 shows the cross-sectional view of the wear scar (Figure 84a) generated under the mechanical key point loading conditions at 400°C and associated EDX map of oxygen distribution (Figure 84b). The layered structure of the formed third body is clearly apparent as cracks parallel to the top surface can be observed. Some damaged areas apparent in the polished third body section show that the third body layer consists of the fine wear particles. The EDX map of oxygen distribution revealed a strong oxidation of the third body.

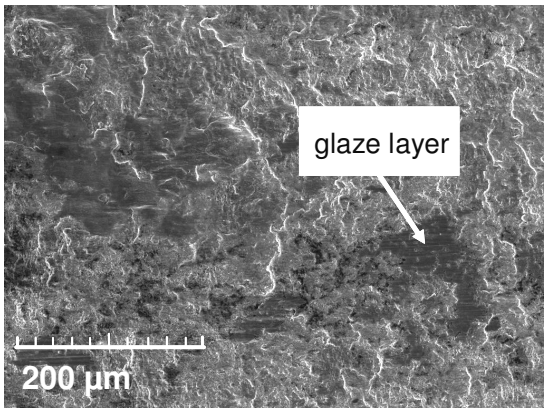

Figure 83: Morphology of the wear scar generated on to the A-286 specimen under the mechanical key point loadings at 200°C; Adhesive wear mechanism is predominant, even though some small areas of glaze layers can be observed.

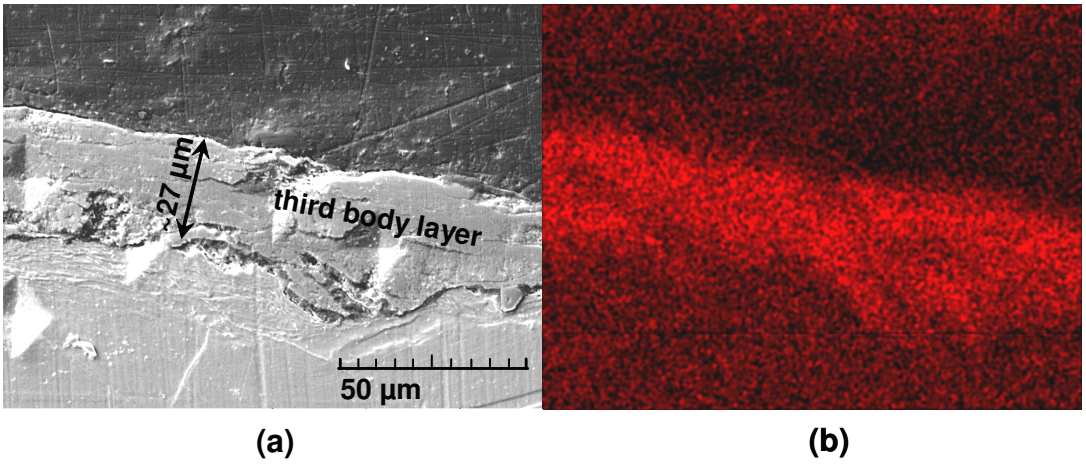

Figure 84: (a) Cross-sectional view of the wear scar generated at 400°C on to the A-286 revealing layered structure of the formed third body and (b) the associated EDX map of oxygen distribution showing its strong oxidation.

Figure 85 depicts a comparison between the EDX spectrum obtained from the third body layer formed under the mechanical key point loading conditions at 400°C on to the wear surface of the Jethete M152 counter body and that acquired from the substrate. A diminution in iron and chromium content due to a strong oxidation (i.e. high amount of oxygen detected) and an increase in nickel content in the third body composition in relation to the substrate was observed. This implies that transfer of particles from the lower A-286 specimen (having high nickel content – see Table III) that are subsequently mixed with the Jethete M52 counter body material (having low

nickel content – see Table III) and the environmental component (i.e. oxygen) takes place during the fretting experiments. The peaks from gold present on the spectra are a consequence of depositing this element on the resin-encapsulated metal specimens in order to ensure the conductivity of the electrons during the SEM observations. The quantitative EDX analyses of the third body layers (performed at the surface, in the centre and at the substrate) formed under the mechanical key point loading conditions at different temperatures (23, 200 and 400°C) showed that the chemical composition is homogenous across the third body thickness in the case of both counter-bodies at the given temperature. Similar chemical composition of the third body could be observed for all the considered temperatures for the individual counter bodies (Figure 86).

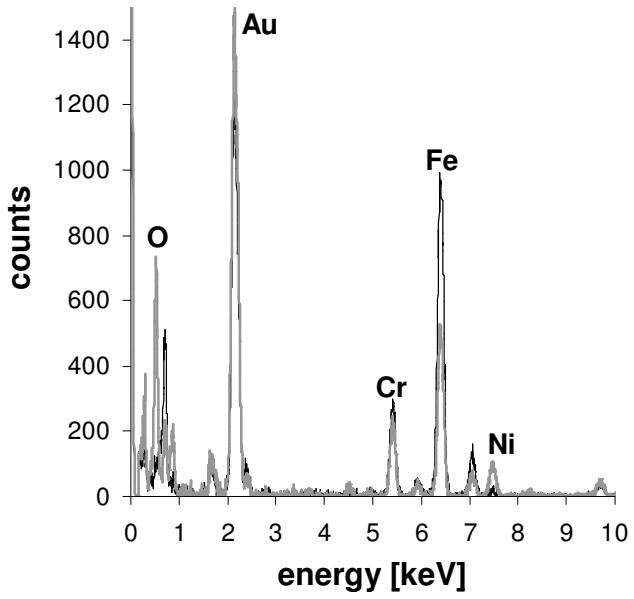

Figure 85: Comparison between EDX spectrum of the substrate (——) and the third body layer (——) formed on to the wear surface of the upper Jethete M152 specimen after test under the mechanical key point loadings at 400°C.

Figure 87 shows the evolution of the thickness of the third body formed under the mechanical key point loadings on to the wear surfaces of the Jethete M152 and A-286 counter body as a function of temperatures. As expected, it increases with temperature. This implies that greater amount of wear particles is retained in the interface what supports the hypothesis of the sintering process as a major factor controlling the 'glaze' layer development [Jiang et al. (1998), Kato et al. (2007)].

Moreover, it must be noticed that the thickness increases practically in linear manner. If a thickness controlled the development of a stable effective wear-protective 'glaze' layer there should be revealed the discontinuities in its evolution at T_t similar to those observed in friction and wear evolutions. It may therefore be implied that rather rheological properties of the interface, which change drastically with temperature variation, are in charge of effective 'glaze' layer development. At each the considered temperature the thickness of the third body developed on to the lower A-286 specimen was found to be greater than on to the Jethete M152 counter body. It is certainly due to gravity and a specificity of the studied contact geometry. Thus, the particles are easier retained within the wear scars of the lower specimens than on to the wear surfaces of the upper samples.

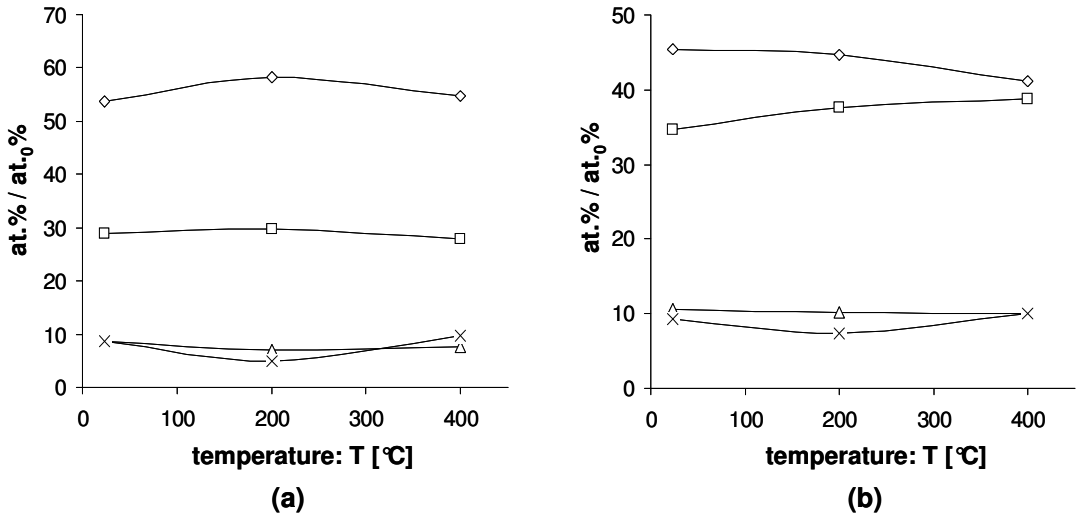

Figure 86: Evolution of oxygen (—◇—), iron (—□—), chromium (—△—) and nickel (—×—) content in the third body formed on to the (a) upper Jethete M152 and (b) lower A-286 specimen as a function of temperature.

Hardness distribution conducted on the cross-sections through the wear scars produced on the A-286 specimen at 200 and 400°C under the key point loading conditions is shown in Figure 88. For the both temperatures a relatively high hardness of the compacted third body compared to the substrate material was found. In Figure 84 indentation marks can be observed. The conducted hardness measurements can be considered only in the qualitative way since the measured third body hardness may be

affected by the hardness of the substrate and the adjacent resin, especially at the lower temperatures as the thickness of the formed third body is relatively small.

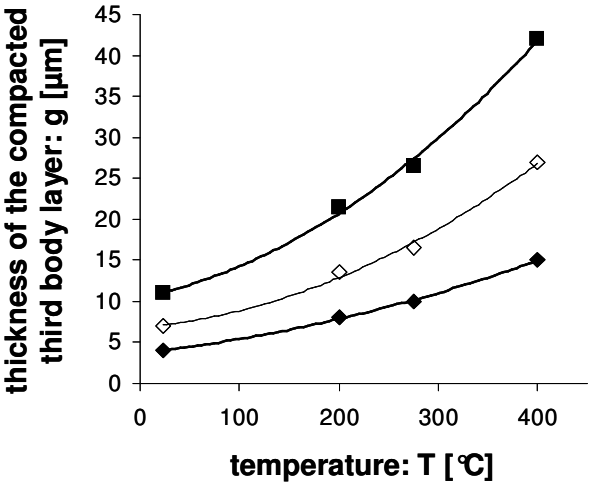

Figure 87: Evolution of the thickness of the compacted third body layer formed on to the wear surface of the upper Jethete M152 (—◆—) and lower A-286 (—◇—) specimen as a function of temperature; Total thickness of the third body (—■—)=(—◆—)+(—◇—).

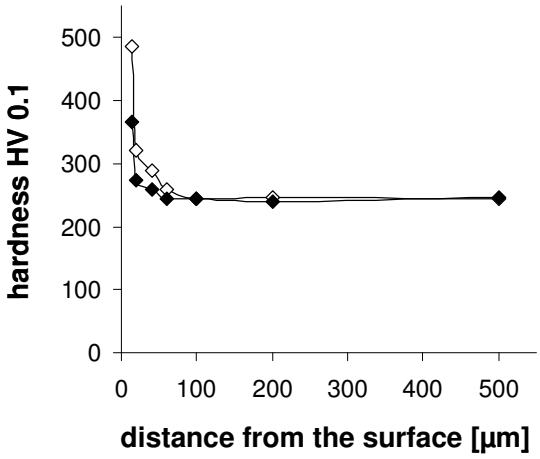

Figure 88: Hardness distribution performed on the cross-sections of the wear scars generated on the A-286 specimen at 200 (—◆—) and 400°C (—◇—) showing a high hardness of the third body layer in relation to the substrate.

Generalizing from the SEM studies undertaken, at lower temperatures ($T<T_t$) severe adhesive wear mechanisms dominates (characterized by the high energy wear

coefficient), whereas at higher ones ($T>T_t$) a third body abrasive process, involving the formation of a compliant 'glaze' layer structure takes place (characterized by the low energy wear coefficient). The compliant third body layer developed can be considered as compacted oxidized wear particles originating form the two steel surfaces. Where the 'glaze' areas have delaminated, the underlying material is of granular appearance, however in cross-section it has a layered structure. It is characterized by a high cohesion and elevated hardness, which enhances its load-bearing properties. It all supports the tribo-sintering approach of the 'glaze' development [Jiang et al. (1998), Kato et al. (2007)].

In order to provide explicit clarification as to process(es) involved in 'glaze' layer development, the structural analyses of the wear surfaces and wear debris were carried out.

4. 2. X-ray diffraction study

X-ray diffraction (XRD) analyses, using a cobalt (Co_α) lamp as a radiation source, of the wear scars on A-286 specimens did not reveal any oxide structures at 23 and 200°C. Similar XRD investigations performed for the fretting scar generated under the mechanical key point loadings at 400°C display small peaks, apart from high excitations from austenite, probably originating from Fe_2O_3 and/or Cr_2O_3 (Figure 89).

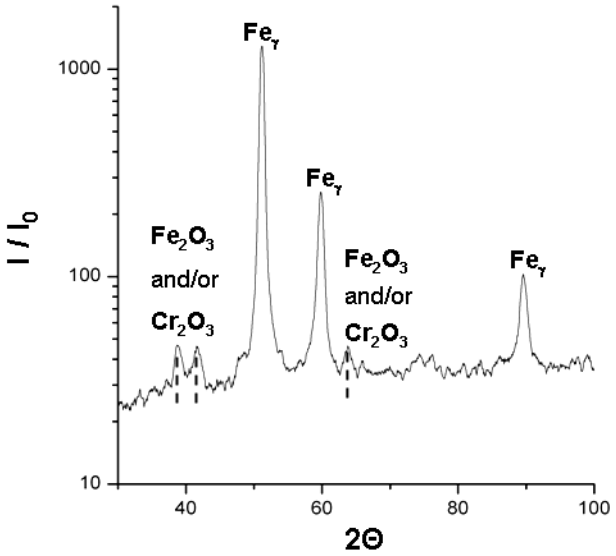

Figure 89: XRD pattern of the wear scar generated under the mechanical key point loading conditions at 400°C.

The obtained result is in agreement with thermodynamics (α-Fe_2O_3 structure is a The elevated temperature (i.e. above T_t) facilitates wear particles compaction (i.e. stable phase above 400°C), but contradicts the hypothesis proposed by Hurricks (1972 and 1974) that above 200°C the Fe_3O_4 spinel oxides operate in the interface contributing to the friction and wear rate decrease. Taking into account the specificity of a standard XRD technique (problem to get a reliable result from the small area (i.e. the wear scar) on to the sample as the output may be affected by the information from outside the chosen regions (i.e. reference surface)) the result obtained can be explained in two ways. Either the signal acquired originated from outside the wear scar (i.e. from native oxides) or there was no transformation in oxide structure due to fretting action and Fe_2O_3 and/or Cr_2O_3 formed on to the wear surface. Thus, at the current stage of investigations it cannot be stated if the activation of the lubricating 'glaze' layer is controlled only by a tribo-sintering process or perhaps by a change in oxide structures either. In order to clarify the possible correlation between the oxide structural transformation and the glaze layer development a specific surface Raman analysis was undertaken.

4. 3. Raman investigations

Raman spectroscopy analysis of the A-286 specimens previously subjected to the fretting tests under the mechanical key point loading conditions at 23 and 400°C was performed. The analysis was conducted at room temperature. To avoid a heating effect, the laser tuned at 785 nm was operated at 5 mW to excite the sample. The laser beam was focused on the sample with a spot size of 2 μm. A 5 sec exposure time and 10 acc was applied to collect the Raman spectra. Figure 90 shows the spectra obtained from the reference surfaces (i.e. from outside the wear scars). No characteristic peaks from any oxide structures were revealed for the specimen after the fretting test at 23°C. Hence, it may be concluded that the layer of native oxides formed on to the specimen's surface was very thin as the Raman spectrum was excited from the depth of 2 μm underneath the top surface. In the case of the higher temperature (400°C) thicker native oxides were formed on to the metal surface. Thus, several peaks on the Raman spectrum originating from the formed native oxides could be observed. The bands at 227, 294, 414, 502, 613 and 1320 cm^{-1} correspond to α-Fe_2O_3 (hematite) [De Faria et al. (1997)], while the feature at 671 cm^{-1} is characteristic of Fe_3O_4 (magnetite)

[De Faria et al. (1997)] and other spinel-like structures (e.g. $FeCr_2O_4$ [Wang et al. (2004)], $NiCr_2O_4$ [Wang et al. (2003)] or $NiFe_2O_4$ [Kim et al. (2005)] etc.) possible in terms of chemical composition of the tested materials. No peaks from Cr_2O_3 were found, although from the standpoint of thermodynamics formation of this compound would be highly probable (Figure 32). Thus, the native oxides formed at 400°C are mainly consisted of α-Fe_2O_3 with the some addition of spinel structures. The result obtained is according to the thermodynamics (relation 22).

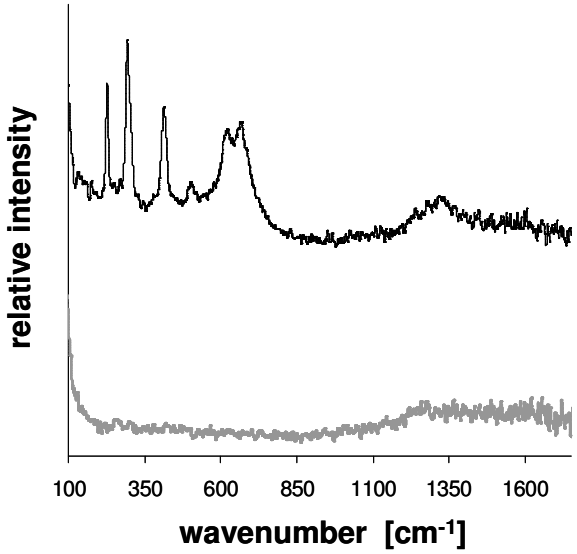

Figure 90: Comparison between Raman spectrum excited from outside the wear scar (i.e. native oxides) generated on to the lower A-286 specimen at 23°C (——) and 400°C (——).

Figure 91 shows the spectra excited from the generated fretting wear scars. For the both temperatures (i.e. 23 and 400°C) the similar features can be observed. The strong broad features excited at 660 cm^{-1} for 23°C and at 671 cm^{-1} for 400°C imply that spinel structures are mainly formed on to the wear surface independently of the test temperature. The shift between the peaks may be explained by differences in oxide stechiometries. The weak features appearing between 220 and 500 cm^{-1} as well as around 1320 cm^{-1} prove the presence of small quantities of α-Fe_2O_3 in the formed oxide structures as well. Moreover, it cannot be excluded the presence of Cr_2O_3 as its strongest line is excited at 550 cm^{-1}, which may be either superimposed (23°C) by, or a shoulder (400°C) of, the broad peak from spinel-like oxides. The small excitations

found at 810 and 779 cm^{-1}, respectively for 23 and 400°C were not characterized to origin from any common oxides of Fe, Cr or Ni or nitrides of Cr. Further in-depth investigations should be undertaken to clarify this issue.

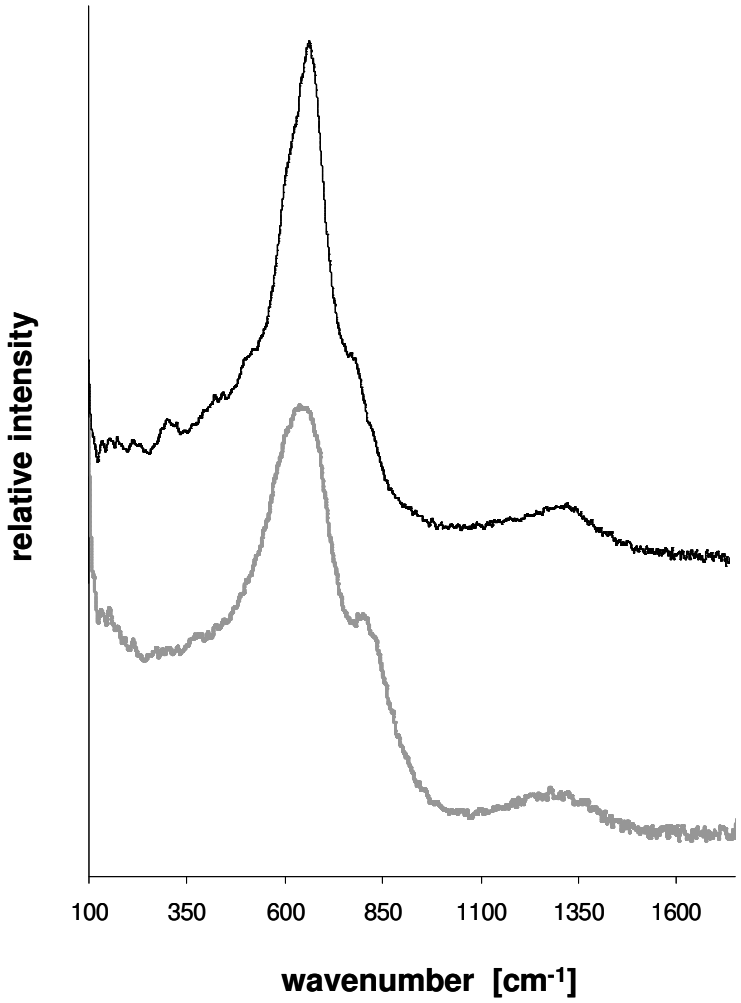

Figure 91: Comparison between Raman spectrum excited from the wear scar generated on to the lower A-286 specimen under the mechanical key point loading conditions at 23°C (——) and 400°C (——).

While the result obtained at 23°C is in accordance with thermodynamics of iron oxidation (i.e. below 200°C Fe_3O_4 is the most thermodynamically stable oxide – relation 22), the result acquired at 400°C contradicts it (i.e. at 400°C α-Fe_2O_3 should be expected to form mostly). This implies that fretting action (at least at elevated temperature conditions) induces the unique transformation in oxide structure (for pure iron it would be $\alpha - Fe_2O_3 \rightarrow Fe_3O_4$) due to a complex stress-strain response of the

interface under loadings. Of course, in the case when high-alloyed steels are investigated the transformation into more complex spinel-like compounds may be possible (e.g. $FeCr_2O_4$, $NiCr_2O_4$, $NiFe_2O_4$ etc.). The Raman analyses have also clarified the previously discussed XRD results indicating that the pattern obtained at 400°C was excited from outside the wear scar (i.e. native oxides were characterized).

Generalizing, the performed Raman spectroscopy analyses showed that both at the low (23°C) and high (400°C) temperature spinel-like oxides were main compounds formed on to the wear surfaces. The Raman technique is very sensitive to, and provides a clear identification of, the Fe_2O_3 and Cr_2O_3 oxides, but does not allow an unambiguous identification of spinels [Renusch et al. (1996)]. Thus, taking into account chemical compositions of the mated materials (Table III) it may be concluded that the formed products of tribo-oxidation are a mixture of different spinel oxides rather than consist of individual specific compound. The invariable with temperature interface in terms of structural composition implies that there is no correlation between the abrupt decrease in wear rate observed above T_t=230°C (Figure 75) and formed oxide structures as it was suggested by Hurricks (1972 and 1974). Thus, it can be stated that a modification of the rheological properties of the third body leading to the development of a lubricating 'glaze' layer is controlled mainly by a tribo-sintering process of oxidized wear particles.

In order to validate the Raman results transmission electron microscope (TEM) investigations of generated wear debris were undertaken.

4. 4. Transmission electron microscope investigations

The compacted oxidized third body layer has been found to be made up of wear debris generated during friction. Thus, chemical and phase composition of the former is constituted by the composition of the latter. High resolution (HRTEM) and conventional transmission electron microscope (TEM) observations combined with selected area electron diffraction (SAED) and electron spectroscopic imaging (ESI) analyses of numerous wear debris generated after fretting tests under the mechanical key point loading conditions (δ^*=± 100 μm, P=176 N and N=360000) at three temperatures: 23, 200 and 400°C were carried out. The samples were prepared from generated wear debris particles, which were collected straightaway after test on to the copper mesh grid with Lacey carbon support film. Just after this, the sample was

placed into the microscope and analyzed. Accelerating voltage in the case of the bright field imaging was 120 kV, however diffraction analyses were conducted at 100 kV excitation voltage.

High resolution observations showed that agglomerated wear debris was consisted of globular nano-particles of size from 10 to 20 nm, independently of fretting test temperature (Figure 92).

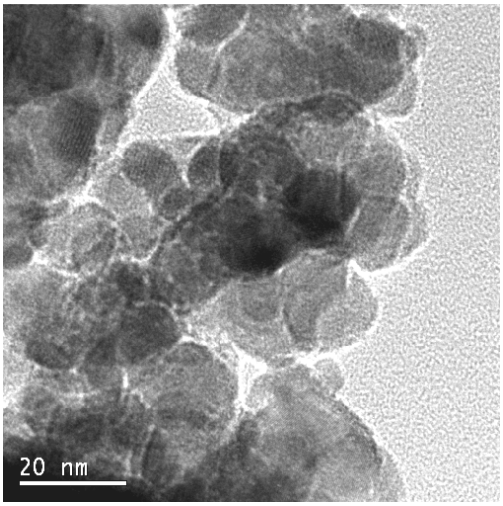

Figure 92: HRTEM bright filed image of wear debris revealing its nano-molecular structure.

Figure 93 shows the bright filed image, the associated diffraction pattern and elemental ESI distribution maps of wear debris produced during the fretting experiment at 400°C. ESI analysis proved the presence of oxygen, iron, chromium and nickel elements in all investigated wear debris generated at different temperatures. Conducted diffraction analysis showed that all produced diffraction patterns had the same features (i.e. the same interplane distances could be determined for the produced annuluses), independently of the test temperature. The representative diffraction pattern is depicted in Figure 93b. Annuluses observed on the patterns signify that formed compounds have polycrystalline structures. Having knowledge of the chemical composition of the studied wear debris the produced annuluses characteristic of all temperatures were identified to be corresponding to the (311), (440), (511), (220) and (400) planes (giving the peaks of the highest intensities in reference XRD analysis) of γ-Fe_2O_3 and/or Fe_3O_4 and/or $FeCr_2O_4$ and/or $NiCr_2O_4$

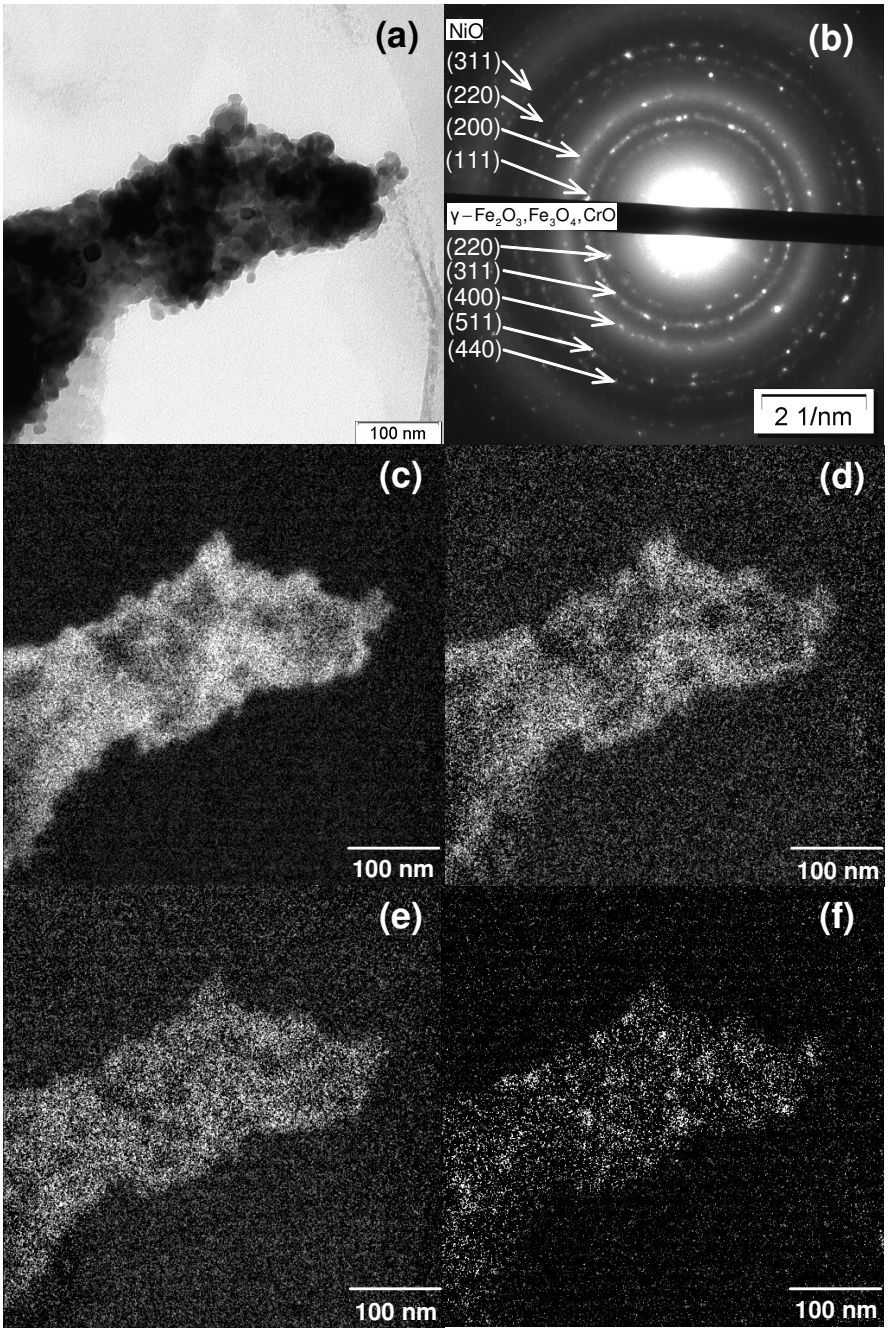

Figure 93: TEM bright field image of the wear debris generated during the fretting test under the mechanical key point loading conditions at 400°C (a); the associated diffraction pattern (b); the associated ESI map showing distribution of iron (c), oxygen (d), chromium (e) and nickel (f).

and/or $NiFe_2O_4$ and/or CrO compounds and to the (200), (111), (220) and (311) planes of NiO. Thus, many oxide compounds may be matched as they have the same cubic crystal structure with similar lattice constant (concerning the former group of possible oxides). In any case, the conducted XRD analysis proved the formation of spinel-like oxides. No evidence for the presence of α-Fe_2O_3 oxide in the wear debris generated at any temperature was shown, thereby, confirming previously obtained results of Raman analysis. While occurring the γ-Fe_2O_3 may be excluded based on the Raman analysis as it is a compound producing clearly distinguishable spectrum, the presence of the CrO and/or NiO oxides cannot be questioned since the Raman technique is insensitive to their identification [Renusch et al. (1996)].

Summarizing, from TEM investigations undertaken the following conclusion can be drawn. The generated wear debris was shown to be made up of globular nano-particles of size of 10-20 nm for all the considered temperatures. Spinel like-oxides (Fe_3O_4, and/or $FeCr_2O_4$ and/or $NiCr_2O_4$ and/or $NiFe_2O_4$) and/or CrO and/or NiO were found to be possible compounds formed as a result of tribo-oxidation process on to the wear surfaces, independently of the test temperature. This fact combined with the lack of evidence for the α-Fe_2O_3 presence once again casts doubt upon the hypothesis proposed by Hurricks (1972 and 1974), assuming oxides transformation as an essential factor explaining friction and wear decrease above around 200°C. Hence, it can be stated that the phenomenon that plays a crucial role for the development of the lubricating 'glaze' layer is a tribo-sintering process [Stott (1998), Kato et al. (2007)], whose the driving force is the increasing with temperature adhesion between oxidized wear particles. Summary of the performed analytical investigations of the interface is depicted in Figure 94.

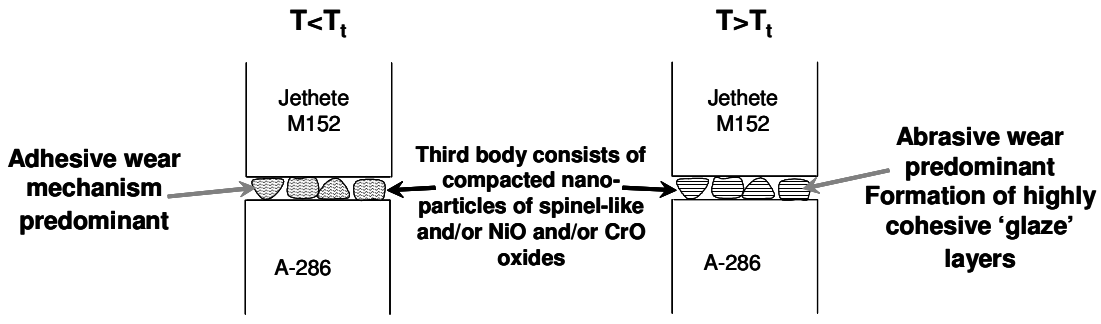

Figure 94: Schematic illustration summarizing the results of the undertaken analytical investigations of the interface at different temperatures.

5. EFFECT OF PRE-OXIDATION ON THE TRIBOLOGICAL BEHAVIOUR

In order to evaluate the effect of specimen pre-oxidation on the tribological behaviour of the Jethete M152/A-286 contact below the severe to mild wear rate transition temperature (T_t=220°C) three tests under the key point loading conditions (T=200°C, δ^*=± 100 μm, p_m=25 MPa (i.e. P=176 N) and N=360000), using specimens previously held in the set-up without fretting action for different time periods (1, 4.5 and 7.5 hours) at 400ºC, were carried out.

Figure 95 shows the evolutions of the energy coefficients of friction as a function of test duration for the reference experimental conditions (the key point loadings) and two fretting tests, in which pre-oxidized in the time period of 1 and 7.5 hours specimens were used. Similar friction tendency for all the considered cases can be noticed. It turns out that there is no influence of the applied specific pre-treatment of specimens on the maximum and steady-state energy coefficients of friction as their values are very close to those characteristic of reference test (Figure 96). No effect on the evolution of the maximum energy coefficient of friction implies that under applied loading conditions the formed native oxide layer is destroyed immediately as the fretting action is being run [Maatta et al. (2001)].

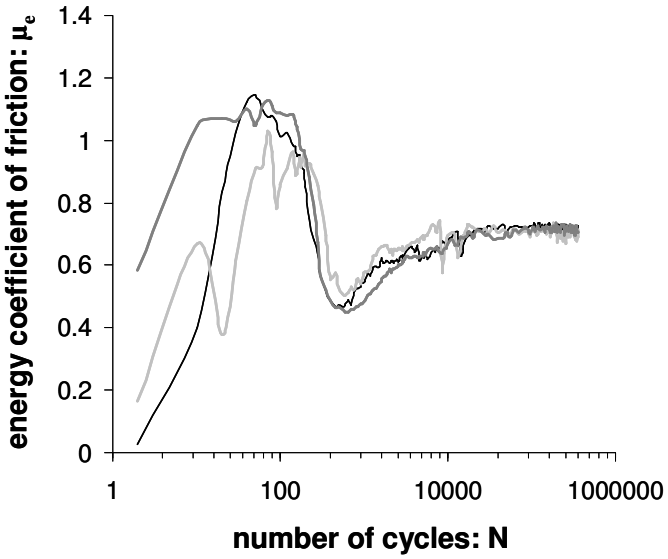

Figure 95: Evolution of the energy coefficient of friction (μ_e) as a function of the test duration for the reference test conditions (the key point) (——) and two fretting experiments, in which pre-oxidized in the time period of 1 (——) and 7.5 (——) hours specimens were used.

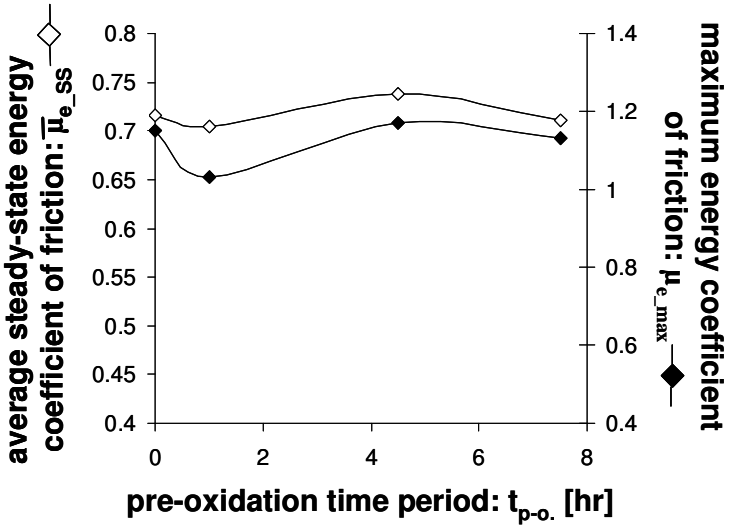

Figure 96: The evolution of the average steady-state and maximum energy coefficient of friction as a function of the time period of the applied pre-oxidation.

Also wear response of the studied tribo-system appears not to be affected by the applied pre-oxidation process since a low deviation from the reference wear volume ($V_{ref} = 0.654\,mm^3$) not higher than $\pm 0.060\ mm^3$ (it constitutes around 9% of the V_{ref}) could be observed. Figure 97 shows the evolution of the total wear volume versus the applied time period of the pre-oxidation treatment.

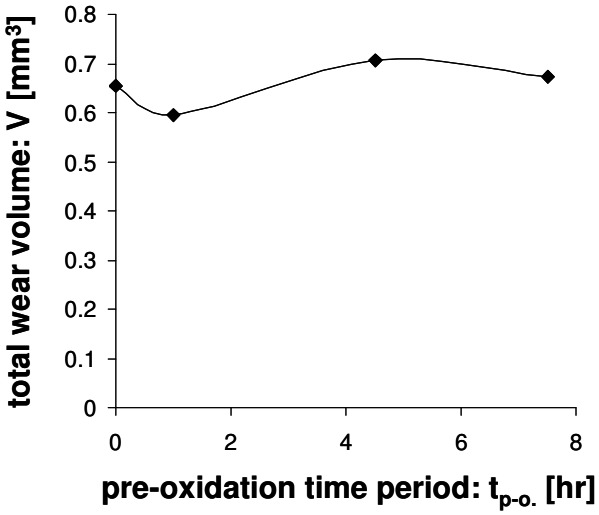

Figure 97: The evolution of the total wear volume as a function of the time period of the applied pre-oxidation.

The pre-oxidation was recognized, in this study, as a treatment that does not produce any effect on the tribological behaviour of the Jethete M152/A-286 tribo-system even on the initial period of friction evolution (Figure 95 and 96). It therefore confirms the idea that it is not a oxide structure that controls the development of a stable effective 'glaze' layer, but a tribo-sintering process, which is activated by a synergetic effect of temperature and mechanical fretting loadings. Hence, considering that the post-oxidation fretting experiments were carried out under the key point loadings at 200°C (temperature below the severe to mild wear rate transition temperature (T_t)) the inability of the interface to produce a stable effectively acting 'glaze' layer is fully understandable. Moreover, it was reported by Glascott et al. (1985) that formed steady-state oxide scale resulted in the development of a wear-protective oxide surface during subsequent normal sliding at certain elevated temperature but not at room one. It was shown that, by contrast with the elevated temperature conditions, the low ambient temperatures favoured detachment and break-up of the oxide during sliding, which prevent the particle compaction and load-bearing oxidized layer development. Hence, it seems to be interesting to investigate pre-oxidation effect more extensively by verifying the impact of the higher fretting test temperatures (above T_t).

6. SYNTHESIS OF THE CHAPTER

The profound analysis of the impact of temperature (23-400°C) on the tribological behaviour of the Jethete M152/A-286 tribo-system under the key point loading conditions (δ^*=± 100 µm, p_m=25 MPa (i.e. P=176 N) and N=360000) has been carried out. Friction and wear quantifications using a dissipated energy approach have been performed. It has been shown that the fretting wear of the Jethete M152/A-286 contact evolves in a series stages with one event initializing another. The initial short running-in period (similar for all the considered temperatures) of adhesion and material transfer is followed by the intermediate transient period (characterized by high work hardening and degradation of the adhesion zones), within which the formation of the third body layers on to the wear surfaces takes place before the steady-state is established. It has been proved that independently of the temperature the wear occurs by a delamination process of flake-like wear debris, which are subsequently crushed into the fine spherical particles within the interface. A threshold

temperature T_t=230°C has been established above which a stable lubricating 'glaze' layer is activated. Below and above T_t different friction behaviour has been observed:
1) for $T<T_t$: there is a high and practically stable friction value (a mean value of the average steady-state energy wear coefficient $\overline{\overline{\mu}}_{e\_SS\_T<T_t} = 0.71$);

2) for $T>T_t$: a compliant 'glaze' layer is stabilized within the interface, promoting the lower friction coefficient ($\overline{\overline{\mu}}_{e\_SS\_T>T_t} = 0.49$).

The dissipated energy approach has provided a good formulation of the wear kinetics whatever the spectrum of the studied loading conditions (pressure, sliding amplitude, test duration). However, different energy wear coefficients have been found depending on the nature of the interface (i.e. below and above T_t):
1) for $T<T_t$: there is a high and almost constant energy wear coefficient (an average value of the energy wear coefficient $\overline{\alpha}_{kp\_T<T_t} = 5.44 \cdot 10^{-5}$ $mm^3 \cdot J^{-1}$);

2) for $T>T_t$: a low constant energy wear rate is observed ($\overline{\alpha}_{kp\_T>T_t} = 4.19 \cdot 10^{-6}$ $mm^3 \cdot J^{-1}$).

This variation of the energy wear coefficient indicates that different tribological processes are activated below and above the transition temperature T_t. As soon as a stable 'glaze' layer is activated (in fact there is a negligible 20°C temperature range for the transition) the low wear mechanisms is favoured. The load-bearing capacity is then fully modified and resistance to wear decreases around 13 times compared to lower temperatures.
SEM observations showed that below T_t a typical severe adhesive wear dominates, whereas at higher ones ($T>T_t$) a third body abrasive process, involving the formation of a compliant 'glaze' layer structure, takes place. The compliant third body layers (the so-called lubricating glaze layers) developed can be considered as the compressed oxidized sub-microscopic wear particles originating from the two steel surfaces, which form solid compact layers, the tops of which are further burnished during the fretting action. The structural analyses of the wear surfaces using Raman and TEM techniques have shown that independently of the test temperature spinel-like (Fe_3O_4 and/or $FeCr_2O_4$ and/or $NiCr_2O_4$ and/or $NiFe_2O_4$) and possibly NiO and/or CrO oxides are main compounds formed. Hence, it is clear that the friction and wear rate decrease observed above T_t is not associated with the change in the type of oxide generated during fretting (as was suggested by Hurricks (1972 and 1974)), but is

closely related to a modification of the surface energy of oxidized nano-particles present in the interface that causes drastic increase of the adhesion work between them [Yamamoto et al. (1981)] and favours a sintering process of the third body [Stott (1998), Kato et al. (2007)] leading to development of a lubricating 'glaze' layer.

It has been found that the fretting time to develop the compact wear-protective 'glaze' layers decreases with increasing temperature above the transition temperature T_t. Presumably it is associated with the synergetic effect of the faster rate of oxide production and increased adhesion between the generated wear particles at the higher temperature.

No effect of specimen pre-oxidation treatment under subsequently investigated fretting loading conditions on the tribological behaviour of the considered tribo-couple has been found. It indirectly supports the hypothesis that a tribo-sintering process, which is activated by a synergetic effect of temperature and mechanical fretting loadings generates the formation of a stable wear-protective 'glaze' layer.

The following questions are being arisen after analyzing the results obtained under the invariable loading conditions:

- What would be the dynamics of the third body evolution under variable loading conditions?;
- How can an energy wear approach be transposed to capture the wear kinetics under variable loading conditions?;
- Can the fretting wear behaviour of the studied tribo-couple be characterized by the two average energy wear coefficients associated with the found wear mechanisms in the range of the studied loadings?.

The responses to these questions are being attempted to be found in the next Chapter in which results of the investigations conducted under variable loading conditions are brought up for discussion.

CHAPTER 4

FRETTING BEHAVIOUR UNDER VARIABLE LOADING CONDITIONS

CHAPTER 4: FRETTING BEHAVIOUR UNDER VARIABLE LOADING CONDITIONS

1. TRIBOLOGICAL BEHAVIOUR UNDER VARIABLE TEMPERATURE CONDITIONS

In practice, most mechanical systems operate under variable mechanical and environmental conditions. The investigated couple of materials is considered by Snecma to be applied to the vane/bushing joints of the third stage of the VSV system, where working temperature varies between 218 and 350°C (during cruise and take-off, respectively). The former temperature is below and the latter above the severe to mild wear rate transition temperature T_t found in the previous Chapter (Figure 75). Hence, to be adequately evaluated, for the tribological behaviour of the considered tribo-system should be taken into account variable environmental conditions. Thus, the friction and wear behaviour under the variable temperature conditions within a single fretting tests are being discussed below.

1. 1. Experimental methodology

A review of the literature shows that probably no attention has been paid to the tribological investigations under variable temperature conditions. Hence, a new methodology, taking into account the temperature variations within a test, was designed. A dozen experiments under variable temperature conditions (VT) during a single fretting test were carried out. They can be classified into two test configurations illustrated in Figure 98. The first type (the tests VT 1-7) consists of a different number of repeated blocks of 200°C-400°C, the second one (the tests VT 8-12) of 400°C-200°C. The other parameters were maintained as for the mechanical key point loading conditions (p_m=25 MPa (i.e. P=176 N) and $\delta^*=\pm$100 µm). The number of cycles within each step in the block in the given VT test was constant (the only exception is the test VT 7 – see Table VII). Between each temperature transition the fretting tests were suspended for a short time (less than 15 minutes) in order to adjust the new temperature value. During the treatment of cooling and heating the contact between specimens was always kept. In the case of the test VT 7, higher number of cycles was

imposed at the first step of the test in order to avoid the running-in and transient period and achieve well-stabilized steady-state conditions.

Details of all tests conducted under variable temperature conditions are provided in Table VII.

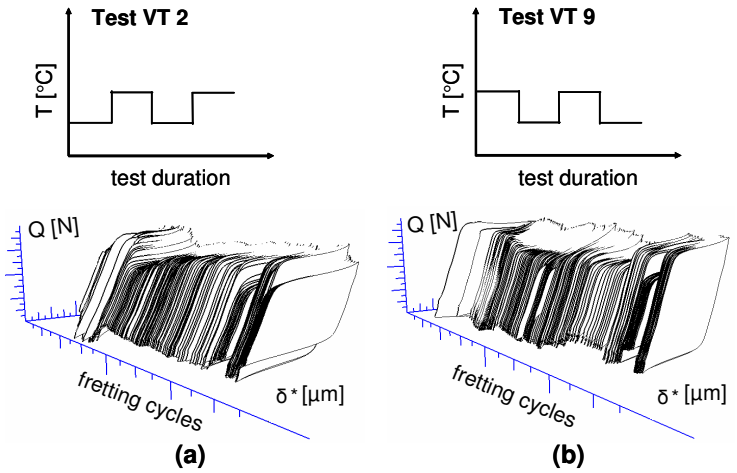

Figure 98: Pattern of the test under variable temperature conditions and the associated fretting log characteristic of experiments consisting of repeated blocks of: (a) 200 ℃-400 ℃ (test VT 2) and (b) 400 ℃-200 ℃ (VT 9).

Tests type VT	**N_i,** with: N - number of cycles for the given temperature, i – temperature value [ºC].								**Total No. of cycles**
Test No.	N_{200}	N_{400}	N_{200}	N_{400}	N_{200}	N_{400}	N_{200}	N_{400}	ΣN_i
1	50k	50k	50k	-	-	-	-	-	150k
2	75k	75k	75k	75k	-	-	-	-	300k
3	50k	50k	50k	50k	50k	50k	-	-	300k
4	110k	110k	110k	110k	-	-	-	-	440k
5	180k	180k	-	-	-	-	-	-	360k
6	37.5k	37.5k	37.5k	37.5k	37.5k	37.5k	37.5k	37.5k	300k
7	30k	5k	5k	5k	5k	5k	5k	5k	65k
Test No.	N_{400}	N_{200}	N_{400}	N_{200}	N_{400}	N_{200}	N_{400}	N_{200}	ΣN_i
8	50k	50k	50k	-	-	-	-	-	150k
9	75k	75k	75k	75k	-	-	-	-	300k
10	50k	50k	50k	50k	50k	50k	-	-	300k
11	110k	110k	110k	110k	-	-	-	-	440k
12	180k	180k	-	-	-	-	-	-	360k

Table VII: Detailed data concerning conditions of the tests carried out under variable temperature conditions (VT).

1. 2. Dynamics of third body evolution – friction behaviour

Figure 99 displays the evolution of the coefficient of friction for four fretting tests: VT 2, 3, 9 and 10. The experimental evolution is there compared with the theoretical response (the average steady-state energy coefficient of friction at the given temperature from Figure 67) obtained for the constant test situation. Quite a good correlation can be observed.

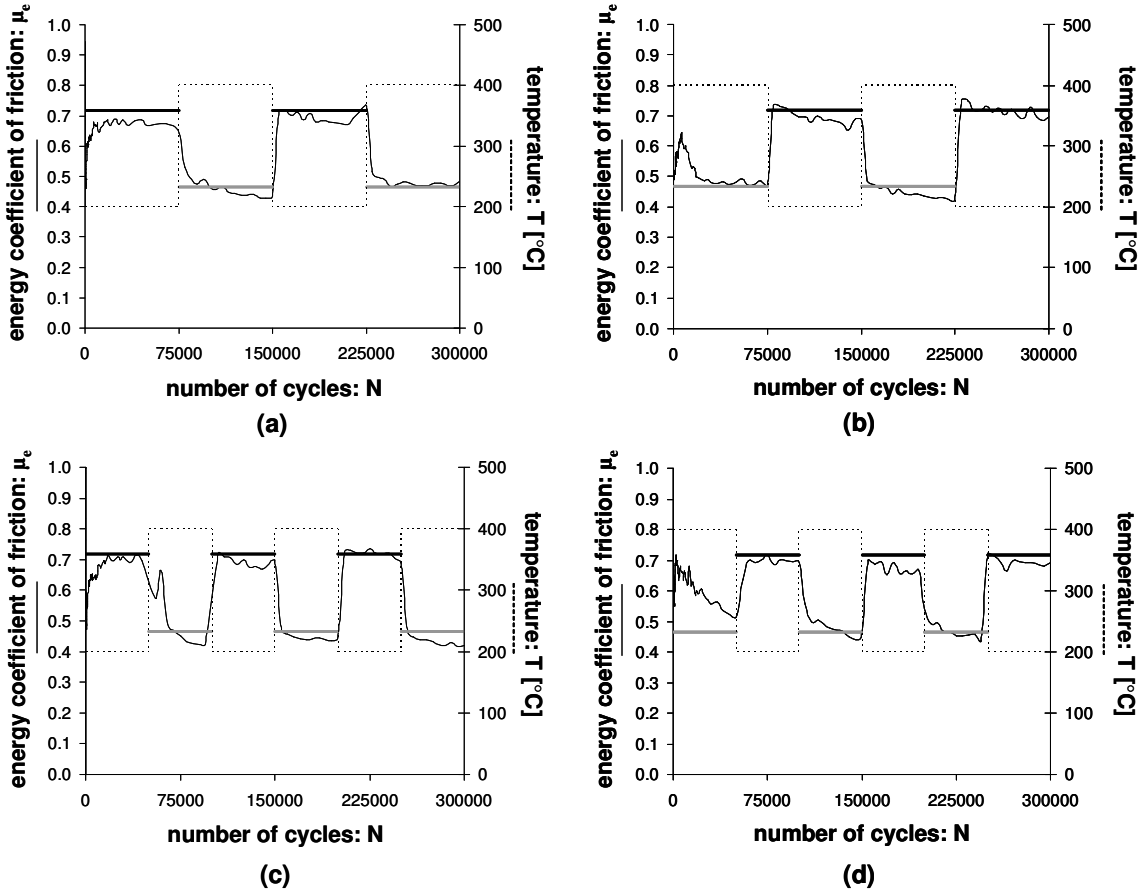

Figure 99: Evolution of the coefficient of friction versus the test duration for variable temperature conditions for the experiments: (a) VT 2, (b) VT 9, (c) VT 3 and (d) VT 10; Experimental evolution of the coefficient of friction under variable temperature conditions: ——; Evolution of the applied temperature: ------- ; Theoretical evolution of the coefficient of friction defined from the steady-state values obtained under 200 (——) ($\overline{\mu}_{e\_SS} = 0.72$) and 400°C (——) ($\overline{\mu}_{e\_SS} = 0.46$).

This suggests that the interface evolves from one tribological regime to another (adhesive to abrasive involving the 'glaze' layer formation) very fast as the temperature changes. Indeed, practically perfect discontinuous transitions can be noticed, which indicates that the friction memory effect after temperature change may be neglected. The 'glaze' layer (activated above T_t) would appear to form instantaneously from the third body previously generated below T_t. A similar evolution is observed when the contact passes from a lubricating high temperature (400°C) system to a high friction low temperature (200°C) interface. The lubricating glaze layer degrades very fast below T_t. However, it must be noticed that the test parameters during the fretting experiments VT 1-6 and 8-12 were read out only every 5000 cycles. In order to get reliable assessment of the dynamics of the third body evolution under temperature variation within a single fretting test the experiment with short steps (5000 cycles) between temperature transitions and dense data acquisition (every 50 cycles) was carried out. To verify test reproducibility the test was repeated twice. Similar friction response illustrated in Figure 100a was always achieved. Figure 100b shows details of the evolution of the friction transitions. The number of cycles needed to establish new friction regime was determined. And thus, it turns out that for the transitions from 400 to 200°C it was always around $N_{t\_400\text{-}200°C}$=500 cycles, from 200 to 400°C $N_{t\_400\text{-}200°C}$=600 cycles. However, it must be mentioned that data acquisition during the test VT 12 was limited by the software performance as after test suspensions during successive runs early acquisition points were lost. The given values of the number of cycles needed to change friction regime were the first acquisition points recorded after the transitions. Thus, it infers that the friction response may indeed change immediately after temperature transitions.

Summarizing, the transient periods to establish new friction regime were found to be shorter compared to the time required to generate the third body from a native interface (compare beginning of constant (Figure 55) and variable (Figure 100) fretting tests). In fact, for the invariable test at 200 and 400°C the number of cycles to establish steady-state is 20000 and 8000 fretting cycles, respectively (Figure 66). This infers that the friction evolution is not related to a progressive replacement of the third body by new one, but is controlled by the capability of the third body, which is already present in the interface, to reversible as a function of temperature change of its adhesive properties (elevated temperature conditions favours stronger adhesion between wear particles). No obvious influence of the order, number or duration of the

temperature sequences on the friction behaviour was found. Hence, it seems that rheological properties of the third body, which change drastically with temperature, play a vital role in the tribological behaviour as temperature variations below or above T_t are applied.

To fully clarify the tribological response of the studied tribo-system under variable temperature conditions interrupted tests, also considering the impact of the test detentions, combined with an evaluation of a rheological quality of the interface should be conducted.

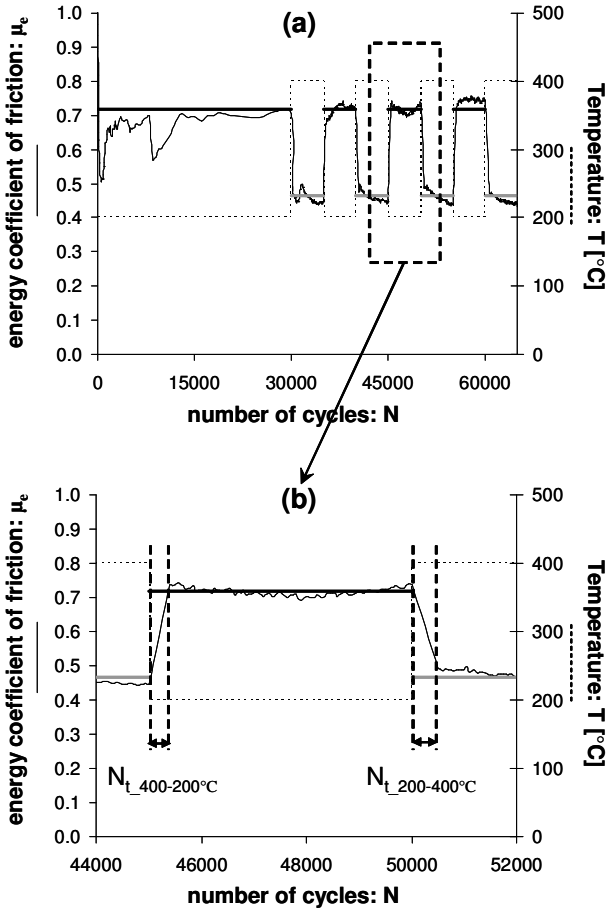

Figure 100: (a) Evolution of the coefficient of friction versus the test duration for the test VT 7; (b) zoom in of the evolution of the coefficient of friction showing details of the temperature transitions; Experimental evolution of the coefficient of friction under variable temperature conditions: ——; Evolution of the applied temperature: -------; Theoretical evolution of the coefficient of friction defined from the steady-state values obtained under 200 (——) and 400°C (——).

1. 3. Wear behaviour

In the present dissertation (Chapter 3) the capacity of the energy wear approach to quantify the wear response of the considered contact for the given interface structure (i.e. the given temperature domain – see Figure 75 and 79) has already been demonstrated. However, a crucial question concerns its ability to predict the wear kinetics under variable temperature situations. Previous investigations have shown that, assuming a constant interface structure (i.e. a given wear mechanism), the energy wear approach is able to predict the wear kinetics under variable loading conditions. This has been extensively demonstrated for variable gross slip conditions [Paulin et al. (2005), Liskiewicz et al. (2005a)]. In the situation that is being discussed, a variation of temperature can drastically modify the interface and consequently the energy wear rate. This has been highlighted by temperature analysis (Figure 75). Under the mechanical key point loading conditions (i.e. p_m=25 MPa (i.e. P=176 N), δ^*=±100 µm and N=360000 cycles) two wear kinetics (i.e. the average energy wear coefficients) are activated depending on whether the temperature is below or above a threshold value T_t=230°C (i.e. if a stable wear-protective 'glaze' layer is activated or not). The friction investigations have indicated that the studied interface is highly reactive, displaying negligible memory effect. Hence, it appears that by using these two determined energy wear coefficients characteristic of the individual temperature domain (i.e. below and above T_t) the wear kinetics under the variable temperature conditions might be captured. In order to quantify it a 'composite' wear law integrating the energy wear coefficient as a function of the applied temperature is being introduced.

1. 3. 1. Development of the 'composite' wear law

By considering the additive properties of the dissipated energy (i.e. energy is an extensive parameter), the 'composite' energy wear formulation is derived where the total wear response under variable temperature conditions (theoretical wear volume $V_{th.}$) is defined as a sum of the elementary wear contributions for each temperature sequence:

$$V_{th.} = \sum_{i=1}^{N} \alpha(T_{(i)}) \cdot Ed_{(i)} \qquad (44),$$

with: $\alpha(T_{(i)})$ - the energy wear coefficient at a given temperature $T_{(i)}$, $Ed_{(i)}$ - the accumulated dissipated energy corresponding to the appropriate $\alpha(T_{(i)})$ value.

According to the results obtained at constant temperature conditions where an abrupt decrease of the energy wear coefficient (α) has been found above T_t, the general formulation given above can be simplified by considering the following discontinuous evolution:

$$\text{if } T < T_t \text{, then } \alpha(T) = \overline{\alpha}_{kp\_T<T_t} = 5.44 \cdot 10^{-5} \text{ mm}^3 \cdot \text{J}^{-1}$$

$$\text{and if } T > T_t \text{, then } \alpha(T) = \overline{\alpha}_{kp\_T>T_t} = 4.19 \cdot 10^{-6} \text{ mm}^3 \cdot \text{J}^{-1}.$$

It leads to the formulation:

$$V_{th.} = \overline{\alpha}_{kp\_T<T_t} \cdot \sum_{j=1}^{N_{T<Tt}} Ed_{(j)} + \overline{\alpha}_{kp\_T>T_t} \cdot \sum_{k=1}^{N_{T>Tt}} Ed_{(k)} \quad (45),$$

$$V_{th.} = \overline{\alpha}_{kp\_T<T_t} \cdot \sum Ed_{T<T_t} + \overline{\alpha}_{kp\_T>T_t} \cdot \sum Ed_{T>T_t} \quad (46),$$

with: $\sum Ed_{T<T_t}$ and $\sum Ed_{T<T_t}$ – the accumulated dissipated energy obtained below and above T_t, respectively.

For the studied conditions the relation 46 can be written as follows:

$$V_{th.} = \overline{\alpha}_{kp\_T<T_t} \cdot \sum Ed_{200°C} + \overline{\alpha}_{kp\_T>T_t} \cdot \sum Ed_{400°C} \quad (47),$$

with: $\sum Ed_{200°C}$ and $\sum Ed_{400°C}$ - the accumulated dissipated energy obtained at 200 and 400°C, respectively.

1. 3. 2. ‘Composite’ wear law implementation

Figure 101 compares the experimental total wear volumes (V) obtained under variable temperature conditions, to the predicted wear volumes ($V_{th.}$) extrapolated from the proposed ‘composite’ wear formulation (equation 47). An optimal prediction is achieved when the theoretical wear volumes are identical to the experimental ones. As Figure 101 illustrates, a rather good correlation is observed (most of the results are aligned along the theoretical dashed line depicting the perfect prediction with the slope equal to 1). The points were fitted linearly using the sum of the least squares and the result compared with the assumed perfect predictions. It turns out that the introduced ‘composite’ wear law produces a rather high convergence (1.04) with the

experimental results. Such a linear regression also displays high stability with the coefficient of determination R^2=0.90. In order to take a measure of dispersion between experimental and theoretical results, a standard deviation analysis is applied:

$$\sigma = \sqrt{\frac{\sum_{i=1}^{N}(X_i - U_i)^2}{Z}} \qquad (48),$$

with: σ - the square root of the variance of the experimental data, X_i - the experimental wear data (V), U_i - the theoretical wear data ($V_{th.}$) according to equation 47, and Z - the number of samples (results) taken.

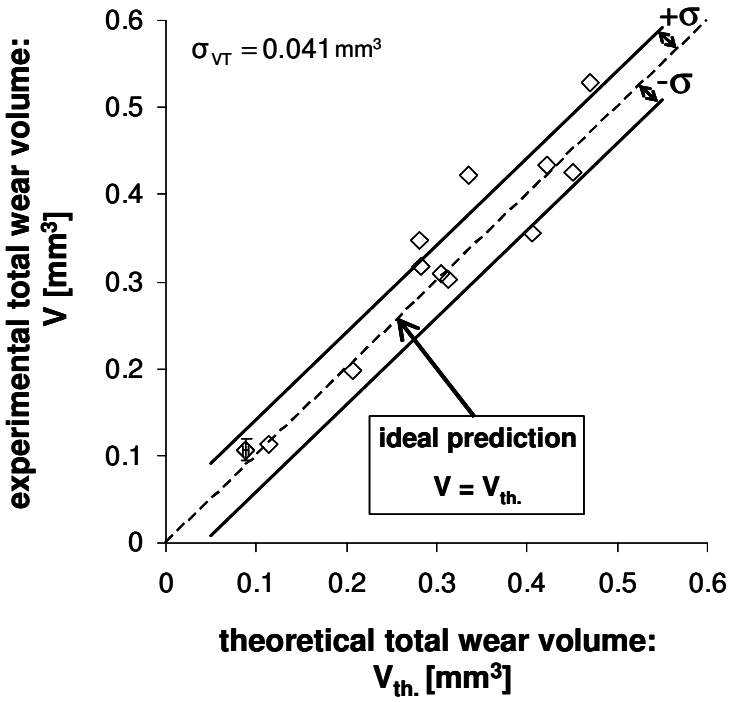

Figure 101: Wear extension under variable temperature conditions: comparison between experimental and theoretical (predicted from relation 47) wear volumes.

The analysis gave $\sigma_{VT} = 0.041\ mm^3$, which compared to the maximum experimental wear leads to a dispersion ($\frac{\sigma}{V_{max}} \cdot 100\%$) less than 8%. For the experiments performed at the same total test duration but different order and number of temperature increments (VT 2, 3, 6, 9 and 10 – see Table VIII) showed very similar wear response. Once again it is, therefore, proved that the interface memory effect can be considered to be negligible. It must also be noticed that high reproducibility of the

test with short temperature sequences (VT 7) was obtained as very low dispersions of the results were achieved (less than ±12 and ±4% from the experimental and theoretical wear volume, respectively).

Detailed data concerning the wear analysis under variable temperature conditions are given in Table VIII.

Test number	**Total accumulated dissipated energy: ΣEd [J]**	**The portion of dissipated accumulated energy at 200°C: $\Sigma Ed_{200°C}$ [J]**	**The portion of dissipated accumulated energy at 400°C: $\Sigma Ed_{400°C}$ [J]**	**Theoretical total wear volume: $V_{th.}$ [mm^3]**	**Experimental total wear volume: V [mm^3]**
VT 1	5186	3692	1494	0.207	0.197
VT 2	8434	4879	3555	0.280	0.348
VT 3	9119	5300	3819	0.304	0.309
VT 4	13450	7848	5602	0.450	0.425
VT 5	12660	7338	5322	0.421	0.433
VT 6	9433	5450	3983	0.313	0.303
VT 7	1943±78	1599±50	344±28	0.088±0.003	0.107±0.013
VT 8	4722	1874	2848	0.114	0.113
VT 9	8543	4923	3620	0.283	0.318
VT 10	10095	5834	4261	0.335	0.422
VT 11	14320	8176	6144	0.471	0.528
VT 12	12230	7057	5173	0.406	0.355

Table VIII: Values of the accumulated dissipated energies obtained at 200 and 400°C, the associated theoretical (predicted from relation 47) and experimental wear volumes for variable temperature conditions.

Summarizing, in spite of its simplicity, the proposed 'composite' energy wear formulation allows the wear kinetics under variable temperature conditions (i.e. variable interface structure) to be predicted. This can be explained by the extensive property of the energy variable, but above all by the very high reactivity of the interface. The interface memory effect was found to be negligible for the investigated tribo-system as the order, the number of increments as well as the length of the imposed temperature sequences, play little importance. Therefore, the introduced 'composite' wear law seems to be a promising tool to predict the wear response under

variable temperature conditions. However, by imposing the wider spectrum of investigated temperature levels (i.e. temperature values close to T_t), the impact of the transient period (i.e. interface memory) should be higher and consequently the given 'composite' formulation may be assumed to be less stable. Further investigations should be considered to probe this aspect and perhaps to propose a different formulation, which better integrates the interface memory effect in wear modelling.

2. FRETTING WEAR MAPPING OF 'GLAZE' LAYER ACTIVATION

The investigations undertaken within the framework of the previous Chapter have demonstrated that under the mechanical key point loading conditions (p_m=25 MPa (i.e. P=176 N), $\delta^*=\pm$100 µm and N=360000 cycles) below and above the transition temperature T_t=230°C different wear mechanism with the associated average energy wear coefficient (Figure 75) is predominant. Moreover, series of experiments carried out at 200 and 400°C (i.e. below and above T_t) have shown that regardless of the imposed mechanical loadings (displacement amplitude, normal force and test duration) in the studied range of the conditions the considered tribo-system can be characterized for the given temperature by the single energy wear coefficient (Figure 79) (i.e. the given interface structure), whose value is pretty close to that of the average energy wear coefficient determined for the temperatures lower and higher than T_t (Figure 75), respectively. Thus, in this place the following questions should be put:

- Does the change of predominant operating wear mechanism always take place at T_t=230°C, independently of the mechanical loadings?;
- If not, what is the influence of the displacement amplitude and mean pressure on the 'glaze' layer activation at different temperatures?.

These questions are being investigated in this paragraph as a new fretting wear mapping concept defining the 'glaze' layer activation conditions as a function of temperature, displacement amplitude and mean pressure is being discussed.

2. 1. Experimental methodology

An innovative test methodology where the considered parameter (displacement amplitude or mean pressure) was increasing stepwise (IS) within a single fretting experiment was designed. By using such a fast test procedure the fretting mapping of

'glaze' layer activation as a function of temperature, displacement amplitude and pressure might be plotted without necessity of carrying out numerous time-consuming invariable tests. In order to verify it the results obtained under variable conditions are compared to those under constant conditions defined in Table VI.

Experiments under parameters increasing stepwise within a single fretting test were performed at different temperatures in the 23-400ºC range, where for tests type DIS (displacement amplitude increasing stepwise) the displacement amplitude was increasing from ±50 to ±200 µm with the 50 µm step at maintaining constant mean pressure p_m=25 MPa (i.e. P=176 N), whereas in the case of tests type PIS (pressure increasing stepwise) the mean pressure was generally augmenting from 5 to 50 MPa (i.e. form P=35 N to P=352 N) in five steps at maintaining constant sliding amplitude δ_g=77±4 µm (i.e. that obtained at the key point loading conditions). For the tests type DIS the number of cycles within each step in the given test was constant: 100000 fretting cycles. The required value of the time-varying parameter (i.e. displacement amplitude and mean pressure, respectively) was automatically adjusted by a data acquisition platform.

Figure 102 shows a pattern of the test DIS 4 and the associated fretting log showing the evolution of the fretting loops.

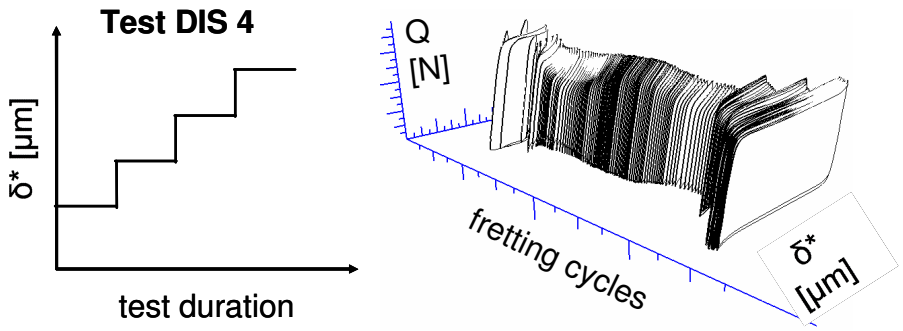

Figure 102: Pattern of the test DIS 4 (the fretting experiment under displacement amplitude increasing stepwise at 300°C) and the associated fretting log.

Detailed data concerning conditions of the test carried out under stepwise increasing displacement amplitude and pressure is given in Table IX.

Tests type DIS (displacement amplitude increasing stepwise)						
		N_i, with: N - number of cycles for the given displacement amplitude, i – displacement amplitude value [μm].				**Total No. of cycles**
Test No.	*Test temperature [ºC]*	N_{50}	N_{100}	N_{150}	N_{200}	ΣN_i
1	23	100k	100k	100k	100k	400k
2	200	100k	100k	100k	100k	400k
3	250	100k	100k	100k	100k	400k
4	300	100k	100k	100k	100k	400k
5	400	100k	100k	100k	100k	400k

Tests type PIS (pressure increasing stepwise)								
		N_i, with: N - number of cycles for the given mean pressure, I – mean pressure value [MPa].						**Total No. of cycles**
Test No.	*Test temperature [ºC]*	N_5	N_{10}	$N_{17.5}$	N_{25}	$N_{37.5}$	N_{50}	ΣN_i
1	23	60k	100k	100k	100k	100k	-	460k
2	200	135k	100k	100k	100k	-	-	435k
3	225	60k	100k	100k	100k	100k	100k	560k
4	250	50k	100k	100k	100k	100k	100k	550k
5	300	50k	100k	100k	100k	100k	100k	550k
6	400	60k	100k	100k	100k	100k	100k	560k

Table IX: Detailed data concerning conditions of the tests carried out under stepwise increasing displacement amplitude (DIS) and pressure (PIS).

2. 2. Definition of the threshold values of tribo-magnitudes for 'glaze layer activation

To make possible plotting the fretting wear mapping of 'glaze' layer activation, the threshold values of tribo-magnitudes (the average steady-state energy coefficient of friction and energy wear coefficient) for the formation of stable wear-protective 'glaze' layer must be defined. The analysis of the evolution of the average steady-state energy coefficient of friction and energy wear coefficient defined from the mechanical key point loadings (p_m=25 MPa (i.e. P=176 N), δ*=±100 μm and N=360000 cycles) versus temperature (Figure 67 and 75, respectively) has shown that a stable effective wear-protective 'glaze' layer (defined to occur above T_t=230°C) produces the mean value of the average steady-state energy coefficient of friction $\overline{\overline{\mu}}_{e\_SS\_T>T_t} = 0.49$ and the average energy wear coefficient

$\overline{\alpha}_{kp\_T>T_t} = 4.19 \cdot 10^{-6}$ mm$^3 \cdot$J^{-1}. However, it should also be taken into account the result obtained within the $T_{ga}<T<T_{gs}$ range of temperature (i.e. at 225°C) for which an unstable, in terms of effectiveness, 'glaze' layer has been found to form (Figure 68), characterized by $\overline{\mu}_{e\_SS\_225°C} = 0.67$ and $\alpha_{225°C} = 1.27 \cdot 10^{-5}$ mm$^3 \cdot$J^{-1}. Hence, because between 225°C and T_{gs} there may take place a formation of a stable 'glaze' layer the threshold value of the average steady-state energy coefficient of friction ($\overline{\mu}_{thr.\_e\_SS\_gs}$) and energy wear coefficient ($\alpha_{thr.\_gs}$) for a stable effective wear-protective 'glaze' layer formation is determined as follows:

$$\overline{\mu}_{thr.\_e\_SS\_gs} = \overline{\overline{\mu}}_{e\_SS\_T>T_t} + \frac{\overline{\mu}_{e\_SS\_225C} - \overline{\overline{\mu}}_{e\_SS\_T>T_t}}{2} = 0.58 \quad (49),$$

$$\alpha_{thr.\_gs} = \overline{\alpha}_{kp\_T>T_t} + \frac{\alpha_{225C} - \overline{\alpha}_{kp\_T>T_t}}{2} = 8.44 \cdot 10^{-6} \text{ mm}^3 \cdot \text{J}^{-1} \quad (50).$$

Thus, in further considerations it is assumed that $\overline{\mu}_{thr.\_e\_SS\_gs} = 0.58$ and $\alpha_{thr.\_gs} = 8.44 \cdot 10^{-6}$ mm$^3 \cdot$J^{-1} is the threshold value of the average steady-state energy coefficient of friction and energy wear coefficient, respectively, below which a stable effective 'glaze' layer is established in the interface.

2. 3. Evaluation of the dynamics of the third body evolution under variable loading conditions through analyzing the friction evolution

The evolution of the coefficient of friction for all fretting experiments carried out under displacement amplitude (tests type DIS) and mean pressure (tests type PIS) increasing stepwise at different temperatures is shown in Figure 103 and 104, respectively.

The experimental evolution is there compared with the theoretical response (an average steady-state energy coefficient of friction at the given conditions – see Table X) obtained for the certain adequate constant test situations. In general, rather a good correlation can be observed as the steady-state conditions are established.

For the test DIS 1 and 2 (Figure 103a and b) and PIS 1 (Figure 104a) the changes of the related parameter during the test do not affect the friction evolution, which is established practically at constant high level ($\mu_e \approx 0.70 \pm 0.05$ for tests type DIS,

$\mu_e \approx 0.75 \pm 0.05$ for the test type PIS), characteristic of adhesive wear regime for the whole test duration.

In the case of the test DIS 3 and 4 (Figure 103c and d) and PIS 2-4 (Figure 104b-d) the significant discontinuities in friction evolution (characterized by the abrupt increase of the coefficient of friction) at the displacement amplitude and pressure transitions can be observed. For these all tests the evolution of the coefficient of friction during the first sequence is similar to that characteristic of experiments conducted above T_{ga} (Figure 57), where after certain maximum within the transient stage the asymptotic decrease down the stabilized value, generally lower than $\overline{\mu}_{thr.\_e\_SS\_gs} = 0.58$ can be observed. It suggests that an effective 'glaze' layers are developed under such conditions. For the test DIS 3 the stabilization of the coefficient of friction ($\mu_e \approx 0.59$) takes place slightly above $\overline{\mu}_{thr.\_e\_SS\_gs}$, but the experiment performed under the adequate invariable conditions (Figure 105 and Table X) shows that also in this situation the low friction and wear regime is predominant. Of course, it is observed that the higher the temperature the less time is required to establish the low friction regime (25000 and 40000 cycles for the tests DIS 4 and 3; 20000 and 60000 cycles for the tests PIS 4 and 2, respectively). Such behaviour has already been discussed in Chapter 3. The stabilization of the coefficient of friction at the level characteristic of high wear adhesive regime occurs after longer time period (at later displacement amplitude or pressure transition) as test temperature increases. At the earlier transitions the abrupt increase of the coefficient of friction up to the high friction regime (generally up to $\mu_e \approx 0.70$; the only exception is test PIS 2) is followed by its progressive decrease below $\overline{\mu}_{thr.\_e\_SS\_gs} = 0.58$. The perfect discontinuous transitions observed suggest that the increase of the displacement amplitude or mean pressure causes an immediate degradation of the previously formed 'glaze' layer as more severe conditions are imposed. The 'glaze' re-forms later as μ_e progressively decreases after a time period shorter than observed for the adequate constant test situations. For example, it takes up about 60000 and 50000 cycles during the test DIS 3 (Figure 103c) and PIS 4 (Figure 104d) after the transition from 50 to 100 μm and from 17.5 to 25 MPa, respectively, in comparison to 130000 cycles during the adequate invariable test under $\delta^* = \pm 100$ μm and $p_m = 25$ MPa (i.e. P=176 N) at 250°C (Figure 105a). Thus, once again it is shown that during the tests

under the time-varying parameters after successive transitions the establishment of a 'glaze' layer that forms from already the present third body, which has partially accommodated the loads. Though it should be expected that with the increase of the investigated parameter (displacement amplitude or pressure) at the given temperature more time will be required to establish a stable effective 'glaze' layer (as has been observed at 200 and 400°C – Figure 72) it is not obvious after analyzing the friction evolution obtained under variable conditions. Also the other invariable experiments at different temperatures showed that the lower the loadings the faster the formation of a stable effective 'glaze' layer. It is demonstrated in Figure 105a and 106a as the evolution of the coefficient of friction versus test duration for different displacement amplitudes at 250°C and different mean pressures at 225°C is shown, respectively. The transitions to the high friction regime characteristic of adhesive wear mechanism are characterized by perfect discontinuities implying the high interface reactivity. Destruction of the 'glaze' layer takes place immediately and the imposed loadings are no longer favourable to a 'glaze' reconstruction as the coefficient of friction reaches values higher compared to $\overline{\mu}_{thr._e\_SS\_gs} = 0.58$ for the rest test duration (i.e. to the end of the experiment). Practically constant high friction level is maintained in the case of the test DIS 3 and 4 after the transition from 100 to 150 μm and from 150 to 200 μm, respectively. A slight increase in the friction evolution after the transition from 150 to 200 μm during the test DIS 3 being the response of the interface to more severe loading imposed can be observed. However, the coefficient of friction stabilizes very fast as new loading is accommodated. The invariable test performed under 150 μm of displacement amplitude at 250°C (Figure 105a) and under 200 μm at 300°C (Table X) confirms

that under such conditions adhesive high friction and wear regime is operating for whole test duration (tests at N=360000 cycles). Such long tests suggest that these results are representative of the applied conditions. In the case of the tests type PIS when after transition the adhesive high friction regime (higher than $\overline{\mu}_{thr._e\_SS\_gs} = 0.58$) is longer operated the coefficient of friction generally increases slightly with each consecutive transitions what is in good agreement with the results obtained under the adequate invariable test situations (e.g. 0.624 at 17.5 MPa and 0.763 at 50 MPa – Figure 106a and Table X). The value of the coefficient of friction within the individual sequence is practically stable.

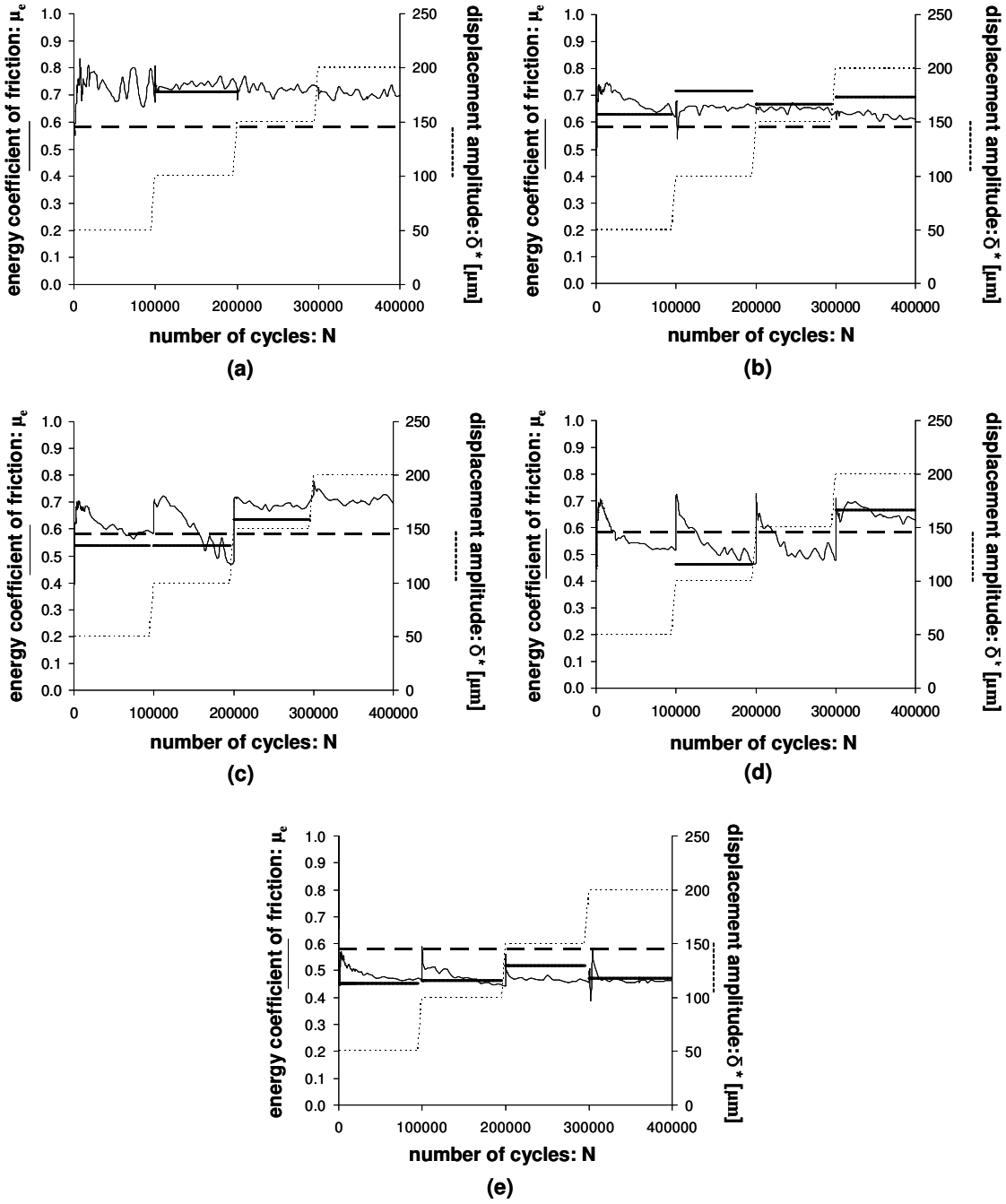

Figure 103: Evolution of the coefficient of friction versus the test duration for the experiments under displacement amplitude increasing stepwise (DIS): (a) DIS 1 at 23°C, (b) DIS 2 at 200°C, (c) DIS 3 at 250°C, (d) DIS 4 at 300°C, (e) DIS 5 at 400°C; Experimental evolution of the coefficient of friction under variable displacement amplitude conditions: ——; Evolution of the applied displacement amplitude: -------; Theoretical evolution of the coefficient of friction defined from the steady-state values obtained for certain the adequate constant test situations (——).

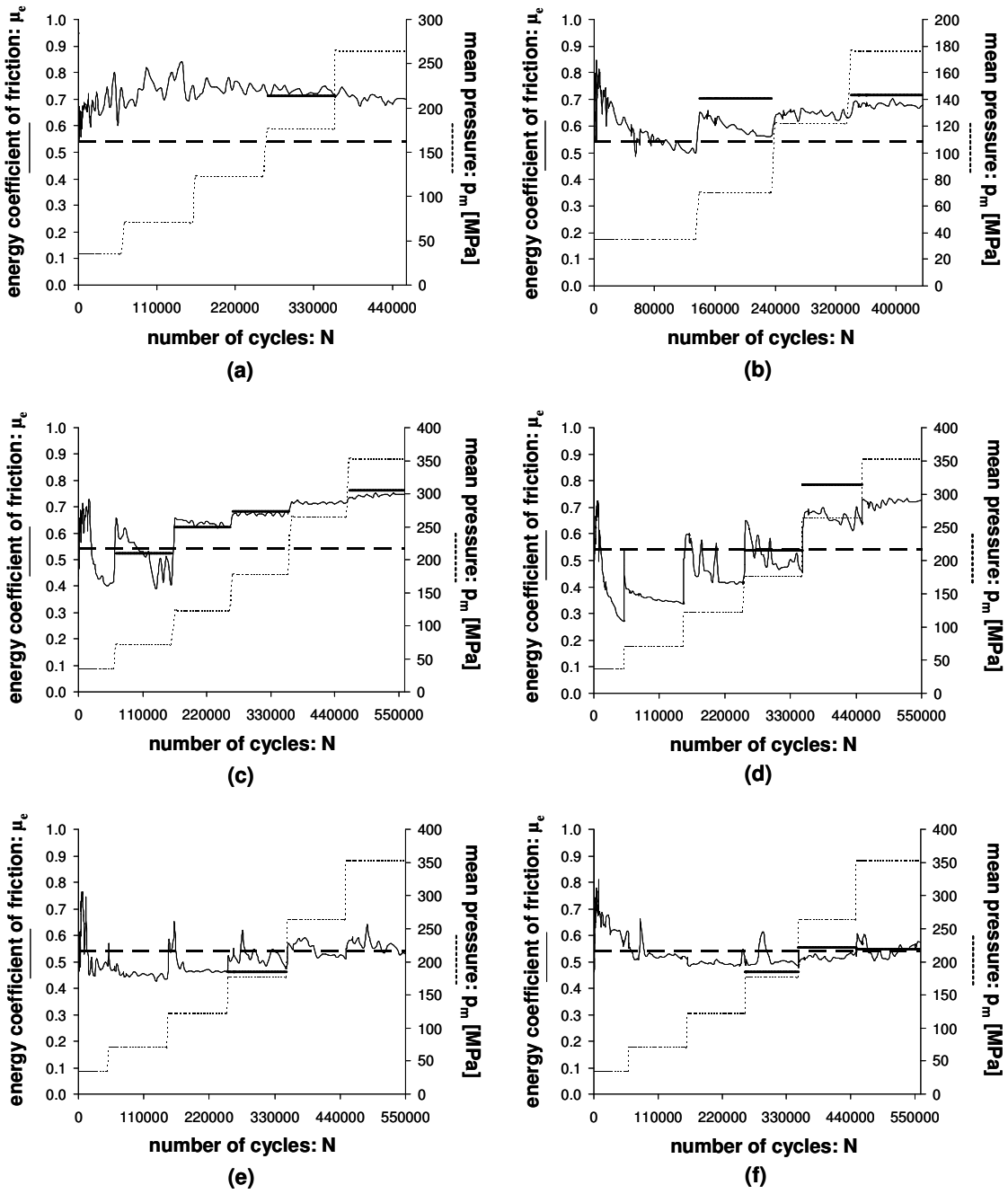

Figure 104: Evolution of the coefficient of friction versus the test duration for the experiments under pressure increasing stepwise (PIS): (a) PIS 1 at 23°C, (b) PIS 2 at 200°C, (c) PIS 3 at 225°C, (d) PIS 4 at 250°C, (e) PIS 5 at 300°C, (f) PIS 6 at 400°C; Experimental evolution of the coefficient of friction under variable pressure conditions: ——; Evolution of the applied mean pressure: ------- ; Theoretical evolution of the coefficient of friction defined from the steady-state values obtained for certain the adequate constant test situations (▬▬).

For the test DIS 5 (Figure 103e) and PIS 5 and 6 (Figure 104 e and f) after the transition period occurring at the beginning of each test the low coefficient of friction is established for whole test duration, in which evolution only small short disturbances can be observed at the parameter transitions. These disturbances are displayed by abrupt friction increase (generally slightly above $\overline{\mu}_{thr._e\_SS\_gs} = 0.58$), which practically immediately decreases after transitions. It therefore seems that though a stable 'glaze' layer is perturbed during transition it re-forms very quickly as high temperature conditions favour higher oxidation rate and higher adhesion forces between wear particles.

In order to clarify the aspect of the dynamics of the third body evolution after the consecutive parameter transitions during the tests under displacement amplitude and mean pressure increasing stepwise the interrupted experiments combined with post-mortem analytical investigations of the interface, involving rheological evaluation of its properties should be performed.

In order to complete the study on the wear mapping of glaze layer activation certain the complementary invariable tests must have been performed. The evolution of the energy coefficient of friction versus the test duration for the experiments under different displacement amplitudes (50, 100 and 150 μm) at 225°C (constant p_m=25 MPa (i.e. P=176 N) and N=360000 cycles) is shown in Figure 105b, under 5 MPa of mean pressure at 150°C (constant δ_g=77±4 μm and N=360000 cycles) in Figure 106b. As it can be observed, the tests at 100 and 150 μm are characterized by the higher energy coefficient of friction than $\overline{\mu}_{thr._e\_SS\_gs} = 0.58$. The analysis of the associated energy wear coefficients (Table X) confirmed that under such conditions the adhesive high friction and wear regime is predominant. In the case of the test under 50 μm of the displacement amplitude at 225°C the obtained average steady-state energy coefficient of friction was exactly as $\overline{\mu}_{thr._e\_SS\_gs} = 0.58$ and the associated energy wear coefficient α=3.78·10^{-6} mm^3·J^{-1} (lower than $\alpha_{thr._gs} = 8.44$ mm$^3 \cdot$ J^{-1}). Thus, the considered conditions favour the activation of the formation of a stable effective 'glaze' layer. The experiment under 5 MPa (i.e. P=35 N) of the mean pressure at 150°C was found to produce $\overline{\mu}_{e\_SS}$ lower then $\overline{\mu}_{thr._e\_SS\_gs} = 0.58$ (Table X). Hence, it

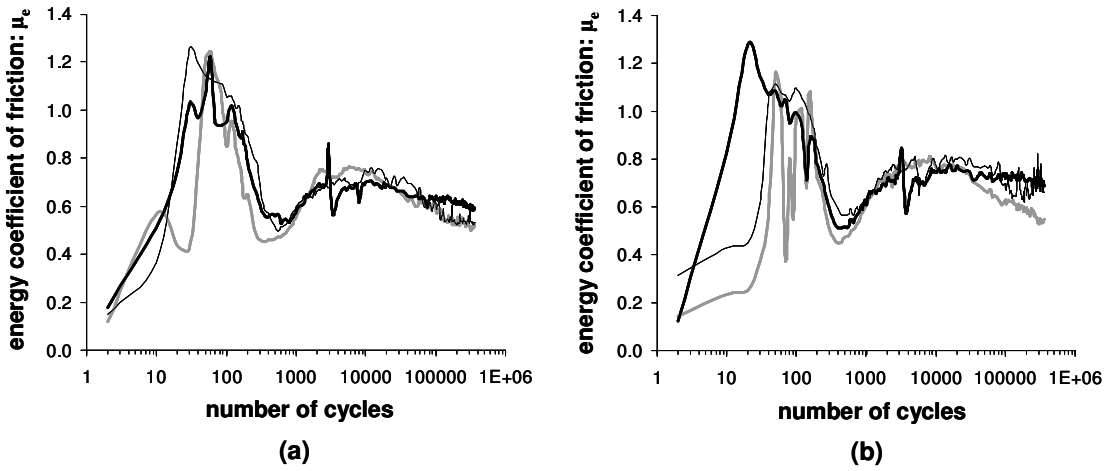

Figure 105: Evolution of the coefficient of friction versus the test duration for the invariable test under 50 (——), 100 (——) and 150 µm (——) of displacement amplitude (constant p_m=25 MPa (i.e. P=176 N) and N=360000 cycles) at (a) 250°C and (b) 225°C.

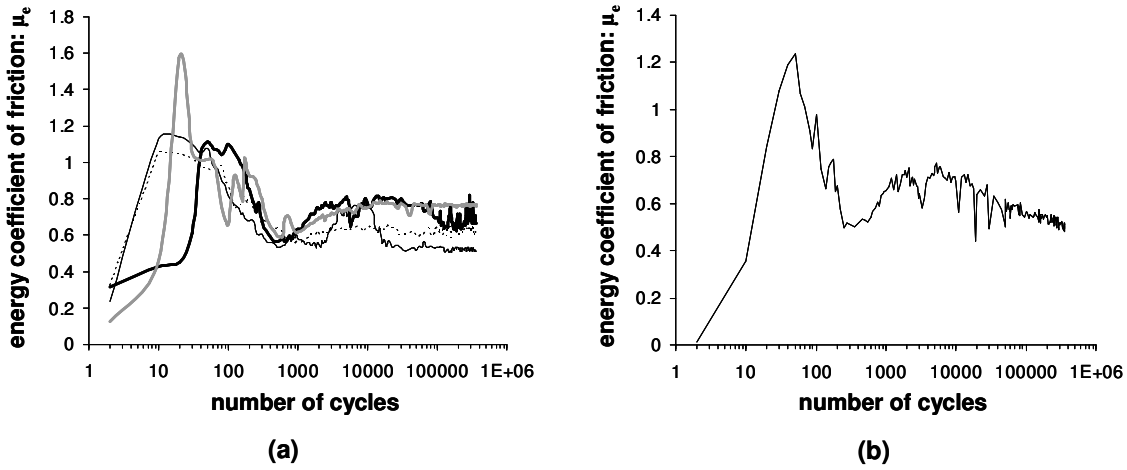

Figure 106: Evolution of the coefficient of friction versus the test duration for the invariable test performed at (a) 225°C under 10 (——), 17.5 (---------), 25 (——) and 50 MPa (——) of mean pressure and at (b) 150°C under 5 MPa of mean pressure; the rest loading conditions for all these tests were: constant δ_g=77±4 µm and N=360000 cycles.

Tribo-magnitudes	Temperature: T [°C]										
	23	*100*	*150*		*200*						
	δ* [μm]	δ* [μm]	δ* [μm]	p_m [MPa] (P [N])	δ* [μm]				p_m [MPa] (P [N])		
	100	*100*	*100*	*5 (35)*	*50*	*100*	*150*	*200*	*10 (70)*	*37.5 (264)*	*50 (352)*
$\overline{\mu}_{e\_SS}$	0.71	0.70	0.68	0.54	0.62	0.71	0.66	0.69	0.70	0.73	0.74
α *[10^5 mm^3/J]*	5.71	6.08	5.51	6.66	1.19	4.92	6.94	7.29	5.01	5.54	5.44
Tribo-magnitudes	**Temperature: T [°C]**										
	215	*225*						*250*			
	δ* [μm]	δ* [μm]			p_m [MPa] (P [N])			δ* [μm]			p_m [MPa] (P [N])
	100	*50*	*100*	*150*	*10 (70)*	*17.5 (122)*	*50 (352)*	*50*	*100*	*150*	*37.5 (264)*
$\overline{\mu}_{e\_SS}$	0.73	0.58	0.67	0.72	0.52	0.62	0.76	0.54	0.53	0.63	0.79
α *[10^5 mm^3/J]*	4.98	0.38	1.27	5.80	0.54	2.94	5.13	0.41	0.36	3.20	5.71
Tribo-magnitudes	**Temperature: T [°C]**										
	275	*300*		*350*	*400*						-
	δ* [μm]	δ* [μm]		δ* [μm]	δ* [μm]				p_m [MPa] (P [N])		-
	100	*100*	*200*	*100*	*50*	*100*	*150*	*200*	*37.5 (264)*	*50 (352)*	-
$\overline{\mu}_{e\_SS}$	0.49	0.46	0.66	0.51	0.45	0.46	0.51	0.47	0.55	0.55	-
α *[10^5 mm^3/J]*	0.42	0.36	4.15	0.46	0.58	0.50	0.34	0.69	0.68	0.79	-

Table X: Values of tribo-magnitudes (the average steady-steady energy coefficient of friction ($\overline{\mu}_{e\_SS}$) and energy wear coefficient (α)) obtained for invariable test situations under different displacement amplitudes (constant p_m=25 MPa (i.e. P=176 N) and N=360000 cycles) and mean pressures (constant δ_g=77±4 μm and N=360000 cycles) at different temperatures (in the 23-400°C range) used as a reference response of the interface as compared to the response under the adequate loading conditions for experiments under variable conditions (tests type DIS and PIS).

preliminarily could be assumed that the considered test conditions would support the activation of a stable effective 'glaze' layer. However, the associated energy wear coefficient (Table X) revealed the value much higher compared to $\alpha_{thr.\_gs}$, close to

that characteristic of adhesive wear regime $\overline{\alpha}_{kp\_T<T_t} = 5.44 \cdot 10^{-5}\ mm^3 \cdot J^{-1}$, explicitly indicating the predominant wear mechanism occurring under the considered conditions.

Summarizing from above discussion, as there is no friction memory effect found after the parameter transitions under variable test conditions the applied innovative experimental methodology can successfully be used to investigate the impact of the mechanical loadings at different temperatures on the tribological response of the considered tribo-system and find threshold conditions for the formation of a stable effective 'glaze' layer without necessity of performing numerous time-consuming invariable tests. Obviously, there is always a need to carry out certain complementary invariable experiments to resolve on unclear situations that may arise as the friction evolution under variable test conditions is considered. Then, throughout analyzing the energy wear coefficient an explicit verification on the predominant wear mechanism occurring under the given loading conditions can be done. It has been shown that the energy wear coefficient is more sensitive to the interface changes, thereby more reliable in determining the operating wear regime than the energy coefficient of friction.

2. 4. Displacement amplitude and pressure versus temperature maps of the 'glaze' layer activation

Based on the results obtained under variable and invariable conditions discussed above

the threshold value of the displacement amplitude (at constant p_m=25 MPa (i.e. P=176 N)) and mean pressure (at constant $\delta_g(\delta^*, P)= \pm 77$ μm) at the given temperature for adhesive high wear ($\delta^*_{thr.\_adh.}(T)$ and $p_{m\_thr.\_adh.}(T)$, respectively) and low wear ($\delta^*_{thr.\_gs}(T)$ and $p_{m\_thr.\_gs}(T)$, respectively), associated with the activation of 'glaze' layers, regime occurrence has been determined. It has been found that for $\delta^* \geq \delta^*_{thr.\_adh.}(T)$ and $p_m \geq p_{m\_thr.\_adh.}(T)$ the adhesive wear mechanism is predominant, however for $\delta^* \leq \delta^*_{thr.\_gs}(T)$ and $p \leq p_{m\_thr.\_gs}(T)$ the abrasive wear mechanism, involving activation of 'glaze' layers takes place. Thus, the fretting wear mapping of wear mechanisms can be plotted, illustrated in Figure 107. Displacement amplitude versus temperature map (under constant p_m=25 MPa (i.e. P=176N)) is

shown in Figure 107a, and mean pressure versus temperature (under $\delta_g(\delta^*, P)= \pm 77$ μm) in Figure 107b. As it can be observed the intermediate temperature domain between high friction and wear adhesive interface and low friction and wear 'glaze' layer interface as a function of pressure is quasi vertical (Figure 107b). It therefore infers that the pressure impact is rather inconsiderable and the activation of a stable 'glaze' layer is mainly controlled by temperature. The more influential parameter seems to be the displacement amplitude (Figure 107a). Figure 108 shows the width of the intermediate temperature domain (ΔT_{gs}) between high friction and wear adhesive interface and low friction and wear 'glaze' layer interface (determined from Figure 107) versus displacement amplitude and mean pressure. It is clearly seen that in the case of the pressure impact ΔT_{gs} is low (<30°C) and practically independent of the studied loading (Figure 108b). Situation is different when the displacement amplitude impact is considered. In this case, low ΔT_{gs} =25°C is maintained only below the critical value of the displacement amplitude $\delta^*_{cr.\_gs}=\pm 100$ μm. Above this critical displacement the intermediate temperature domain shows an abrupt increase and at 200 μm of displacement amplitude ΔT_{gs}=100°C (Figure 108a). It suggests that larger displacement amplitudes than $\delta^*_{cr.\_gs}=\pm 100$ μm may significantly interact on the stability of 'glaze' layers, retarding the formation of stable wear-protective structures. Further analysis of fretting wear maps shows that, as expected, the higher the temperature the greater the value of the displacement amplitude (Figure 107a) and mean pressure (Figure 107b) can be imposed at maintaining low friction and wear response of the interface (i.e. due to the activation of stable effective 'glaze' layers). It is certainly related to rheological properties of third body remaining in the interface. As high temperature increases adhesion forces between wear particles [Yamamoto et al. (1981)] a tribo-sintering process of the third body is favoured [Jiang et al. (1998), Kato et al. (2007)]. Thus, the rheology of the third body changes as the cohesion of the third body increases with temperature (it has been shown in Chapter 3). High cohesion quality of the third body makes it more effective in load-bearing action. Moreover, at high temperatures the debris ejection outside the contact may be limited as bigger particles are easier oxidized and incorporated in the third body. Then, due to the retention of greater amount of wear particles within the interface the thicker third body layer may be generated. That might bear the loads more effectively, even though a thickness of the third body layer does not seems to be an essential factor that controls the process of the development of a stable effective 'glaze' layer.

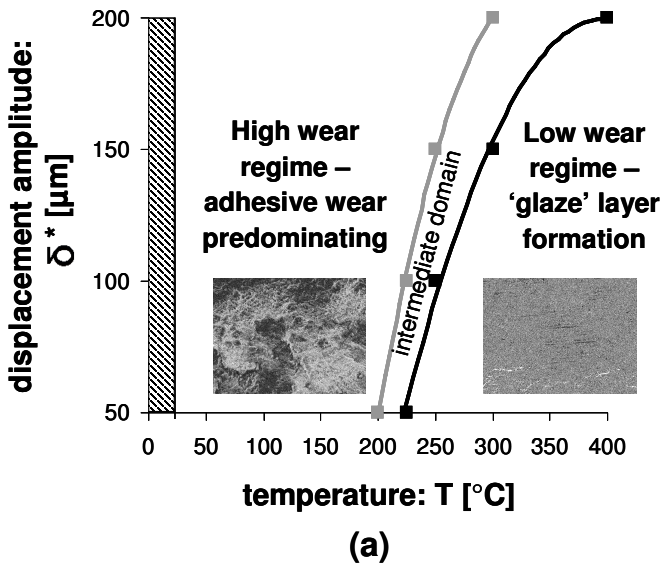

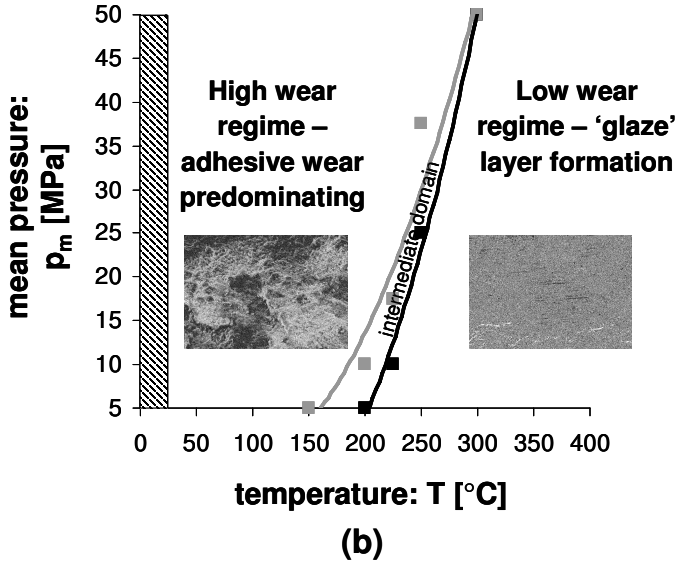

Figure 107: Displacement versus temperature (a) and mean pressure versus temperature (b) map of fretting wear regimes; Evolution of the $\delta^*_{thr.\_adh.}(T)$ *(a) and* $p_{m\_thr.\_adh.}(T)$ *(b) determining the threshold conditions for high wear regime occurrence in the studied range of loadings: (———); Evolution of the* $\delta^*_{thr.\_gs}(T)$ *(a) and* $p_{m\_thr.\_gs}(T)$ *(b) determining the threshold conditions for low wear regime occurrence in the studied range of loadings: (———).*

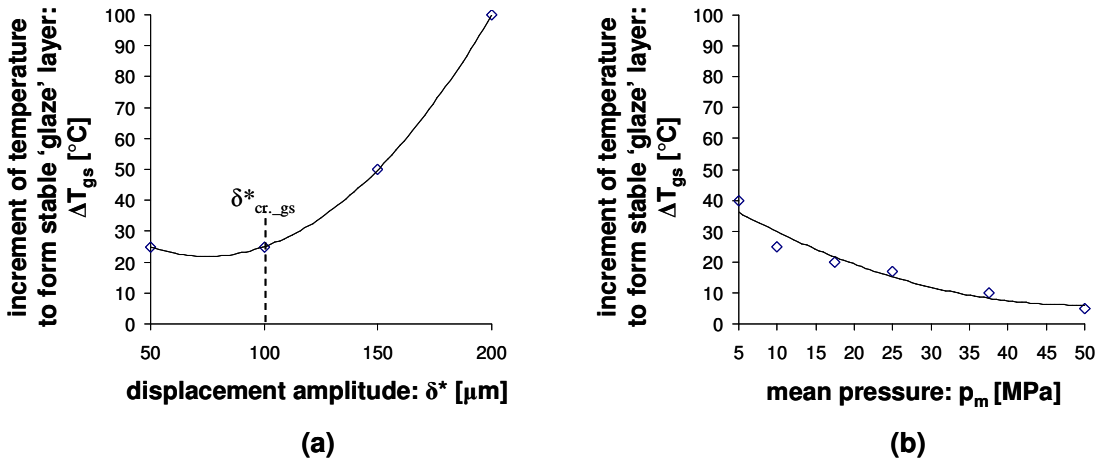

Figure 108: Width of the intermediate temperature domain between high friction and wear adhesive interface and low friction and wear 'glaze' layer interface (ΔT_{gs}=T(━) -T(═): from Figure 107) versus (a) displacement amplitude and (b) mean pressure.

2. 5. Wear prediction under variable displacement and mean pressure conditions

To predict wear volume under variable displacement amplitude and pressure conditions at different temperatures, already the introduced 'composite' wear law is employed. For the studied situation the formulation 44 can be written as follows:

$$V_{th.} = \sum_{i=1}^{N} \alpha((\delta^*, p_m, T)_{(i)}) \cdot Ed_{(i)} \qquad (51),$$

with: $\alpha((\delta^*, p_m, T)_{(i)})$ - the energy wear coefficient at a given displacement amplitude $\delta^*_{(i)}$, mean pressure $p_{m(i)}$ and temperature $T_{(i)}$, $Ed_{(i)}$ - the accumulated dissipated energy corresponding to the appropriate $\alpha((\delta^*, p_m, T)_{(i)})$ value.

By using the displacement amplitude versus temperature and the pressure versus temperature maps of the fretting wear regimes (Figure 107) and assuming that the individual wear regime is characterized by the associated single energy wear coefficient (defined in Chapter 3 – Figure 75) in the range of the studied loadings the general formulation (relation 51) can be simplified by considering the following discontinuities:

if $\delta^* \geq \delta^*_{thr.\_adh.}(T)$ (for tests type DIS – at constant p_m=25 MPa (i.e. P=176 N) and

$p_m \geq p_{m\_thr.\_adh.}(T)$ (for tests type PIS – at constant $\delta_g(\delta^*, P)= \pm 77$ μm),

$$\text{then } \alpha((\delta^*, p_m, T)_{(i)}) = \overline{\alpha}_{kp\_T<T_t}$$

and if $\delta^* \leq \delta^*_{thr.\_gs}(T)$ (for tests type DIS) and $p_m \leq p_{m\_thr.\_gs}(T)$ (for tests type PIS),

$$\text{then } \alpha((\delta^*, p_m, T)_{(i)}) = \overline{\alpha}_{kp\_T>T_t}.$$

It leads to the formulation:

$$V_{th.} = \overline{\alpha}_{kp\_T<T_t} \cdot \sum_{\substack{j=1 \\ p_m \geq p_{m\_thr.\_adh.}(T)}}^{N_{\delta^* \geq \delta^*_{thr.\_adh.}(T)}} Ed_{(j)} + \overline{\alpha}_{kp\_T>T_t} \cdot \sum_{\substack{k=1 \\ p_m \leq p_{m\_thr.\_gs}(T)}}^{N_{\delta^* \leq \delta^*_{thr.\_gs}(T)}} Ed_{(k)} \quad (52),$$

$$V_{th.} = \overline{\alpha}_{kp\_T<T_t} \cdot \sum_{\substack{\delta^* \geq \delta^*_{thr.\_adh.}(T) \\ p_m \geq p_{m\_thr.\_adh.}(T)}} Ed + \overline{\alpha}_{kp\_T>T_t} \cdot \sum_{\substack{\delta^* \leq \delta^*_{thr.\_gs}(T) \\ p_m \leq p_{m\_thr.\_gs}(T)}} Ed \quad (53),$$

with: $\sum_{\substack{\delta^* \geq \delta^*_{thr.\_adh.}(T) \\ p_m \geq p_{m\_thr.\_adh.}(T)}} Ed$ – the accumulated dissipated energy obtained at the given temperature for the displacement amplitudes δ* and mean pressure p_m superior or equal to $\delta^*_{thr.\_adh.}(T)$ and $p_{m\_thr.\_adh.}(T)$ for tests type DIS and PIS, respectively and $\sum_{\substack{\delta^* \leq \delta^*_{thr.\_gs}(T) \\ p_m \leq p_{m\_thr.\_gs}(T)}} Ed$ – the accumulated dissipated energy obtained at the given temperature for the displacement amplitudes δ* and mean pressure p_m inferior or equal to $\delta^*_{thr.\_gs}(T)$ and $p_{m\_thr.\_gs}(T)$ for tests type DIS and PIS, respectively.

Comparison of the experimental (V) and theoretical ($V_{th.}$) (i.e. determined from relation 53) wear volumes obtained under variable displacement amplitude (tests type DIS) and mean pressure (tests type PIS) conditions at different temperatures is shown in Figure 109a and 109b, respectively. The experimental results obtained under mean pressure increasing stepwise, in general, correspond well to those determined on the basis of the 'composite' wear formulation (the only exception is the test PIS 4). For the tests type DIS, however, higher dispersion with the 'composite' wear model can be observed. Very poor correlation for the test DIS 3 and 4 is found (the relative error ($\left(\frac{V - V_{th.}}{V}\right) \cdot 100\%$) is 125 and 60%, respectively). The greater dispersion observed as the impact of the displacement amplitude is investigated is related to the fact that the

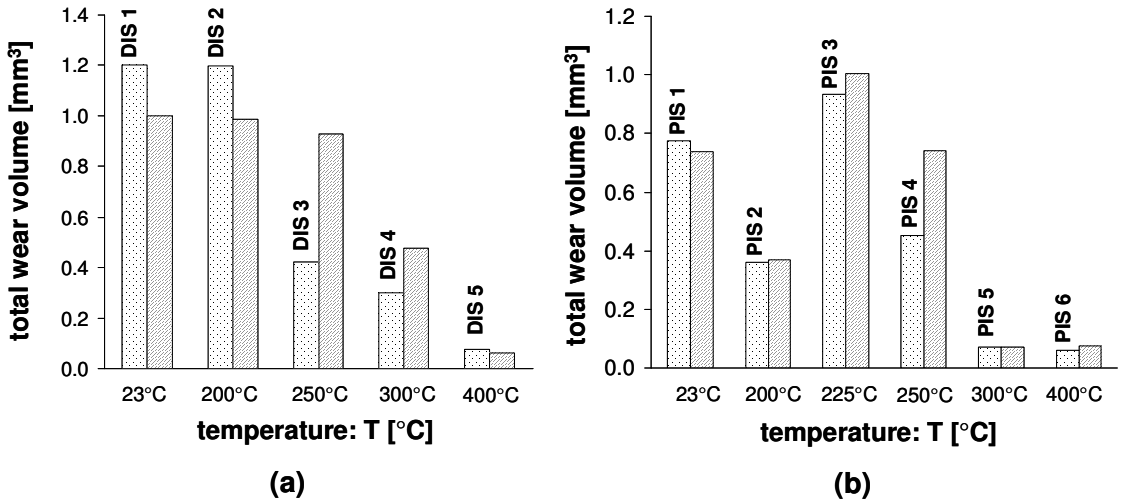

Figure 109: Comparison of the experimental ( ) and theoretical ( ) (predicted from relation 53) wear volumes obtained under variable: (a) displacement amplitude (tests type DIS) and (b) mean pressure (tests type PIS) conditions.

Test type and number	ΣEd **[J]**	$\Sigma Ed_{\delta^* \geq \delta^*_{thr.\_adh.}(T)\ p_m \geq p_{m\_thr.\_adh.}(T)}$ **[J]**	$\Sigma Ed_{\delta^* \leq \delta^*_{thr.\_gs}(T)\ p_m \leq p_{m\_thr.\_gs}(T)}$ **[J]**	$V_{th.}$ **[mm³]**	**V [mm³]**
DIS 1	18401	18401	-	1.001	1.201
DIS 2	18100	18100	-	0.985	1.197
DIS 3	21903	16670	5233	0.929	0.422
DIS 4	17284	8055	9229	0.477	0.299
DIS 5	14278	-	14278	0.060	0.089
PIS 1	13520	13520	-	0.735	0.774
PIS 2	7559	6736	823	0.370	0.363
PIS 3	19857	18384	1473	1.006	0.933
PIS 4	18735	13196	5539	0.741	0.451
PIS 5	17291	-	17291	0.072	0.073
PIS 6	17656	-	17656	0.074	0.059

Table XI: Values of the accumulated dissipated energies obtained under severe (adhesive wear mechanism is predominant) and mild (activation of load-bearing 'glaze' layers) fretting wear regime, the associated theoretical (predicted from relation 53) and experimental wear volumes for variable displacement amplitude (tests type DIS) and mean pressure (tests type PIS) conditions.

displacement amplitude affects the transition between high wear adhesive and low wear 'glaze' layer interface to a greater extent than pressure (Figure 108). Particularly for the displacement amplitudes larger than $\delta^*_{cr.\_gs}=\pm 100$ μm, larger the intermediate temperature domain (implying higher instability of a 'glaze' layer) will produce a higher dispersion with the 'composite' prediction. By contrast, in the case of the pressure impact the intermediate temperature domain is narrow, so the dispersion is lower and the correlation with the 'composite' model better for the tests type PIS. Moreover, it should be noticed that the comparison between experimental and predicted wear volumes for all tests do not display any tendencies (individual dispersion for the given test).

Detailed data concerning the wear analysis under variable displacement amplitude (tests type DIS) and mean pressure (tests type PIS) conditions are provided in Table XI.

3. GLOBAL USE OF THE 'COMPOSITE' WEAR LAW

The last part of the present dissertation is devoted to answering the question: can the fretting wear behaviour of the studied tribo-system be characterized by the two average energy wear coefficients (Figure 75) associated with the revealed wear mechanisms in the range of the studied loadings?. To answer this question the 'composite' wear law developed above (relation 53) on the basis of the fretting wear maps (Figure 107) is here employed in order to predict the wear volumes of all tests carried out within the framework of the present dissertation (i.e. under invariable and variable loading conditions).

The results can be observed in Figure 110 that compares the experimental total wear volumes (V) to the predicted wear volumes ($V_{th.}$) extrapolated from the proposed 'composite' wear formulation (relation 53). Tests of each group under variable conditions (VT, DIS and PIS) are differently marked. It turns out that the used 'composite' wear law produces a very high convergence (0.99) with the experimental results. Such a linear regression also displays fairly high stability with the coefficient of determination $R^2=0.89$. In order to take a measure of dispersion between experimental and theoretical results, a standard deviation analysis is applied (relation

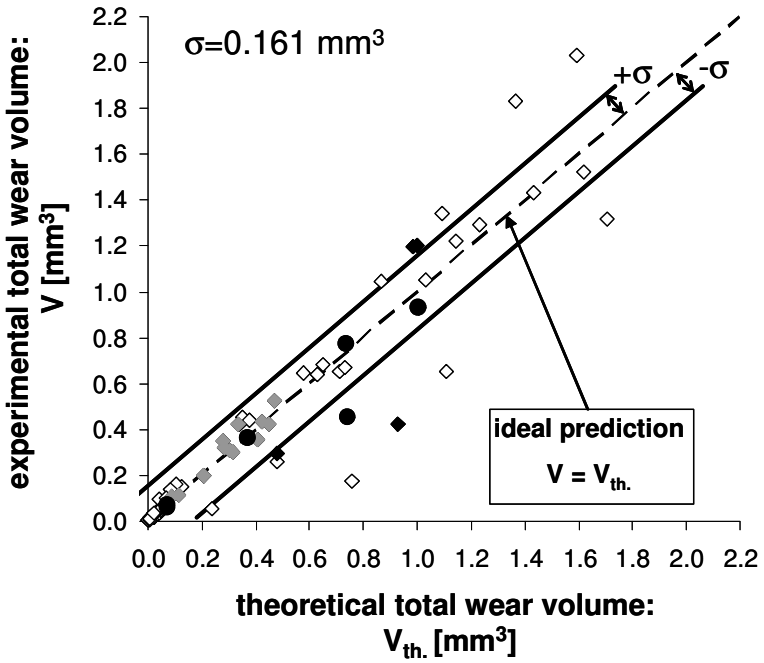

Figure 110: Global application of the developed 'composite' weal law: comparison between experimental and theoretical (predicted from relation 53) wear volumes for all experiments carried out within the framework of the present dissertation; Tests under invariable conditions: ◇; Tests under variable conditions type VT: ◆, DIS: ◆ and PIS: ●.

48). It gives $\sigma = 0.161$ mm^3, which compared to the maximum experimental wear leads to a dispersion in the range of studied loadings ($\frac{\sigma}{V_{max}} \cdot 100\%$) less than 9%. The worst fitting can be observed for the invariable experiments performed at high values of the displacement amplitude and intermediate temperatures (tests under constant p_m=25 MPa (i.e. P=176 N) and N=360000 cycles: δ*=±200, T=300°C; δ*=±200, T=200°C; δ*=±225, T=200°C; δ*=±150, T=250°C). It is therefore clearly shown that the stability of the developed 'composite' approach is degraded for higher displacement amplitudes. It is due to that above $\delta^*_{cr.\_gs}$=±100 μm the intermediate temperature domain between adhesive high wear regime and low wear 'glaze' layer interface is critically enlarged (Figure 108a). For the higher displacement amplitudes due to the activation of a rapid third body ejection process a 'glaze' layer becomes unstable. Thus, this once again implies that the studied interface is more sensitive to changes of the displacement amplitude (in terms of the produced wear kinetics) than

mean pressure, at least in the investigated range of loadings. This seems to be confirmed by investigations under variable conditions during a single fretting tests, as for the experiments type DIS higher differences between experimental and theoretical wear volumes have been found compared to the tests type PIS (Figure 109). Moreover, quite a poor fitting is seen for the variable test DIS 3 and PIS 4 at 250°C as well as for the invariable experiment under the mechanical key point loadings at 225°C. It is certainly due to the fact that at these intermediate temperatures a competing formation of the two different interfaces (adhesive and abrasive one, involving formation of 'glaze' layers) takes place as the main factor that controls the development of a stable 'glaze' layer is temperature. For the invariable experiment under the mechanical key point loadings at 225°C it has been clearly demonstrated in the previous Chapter (see Figure 67, 68 and 75).

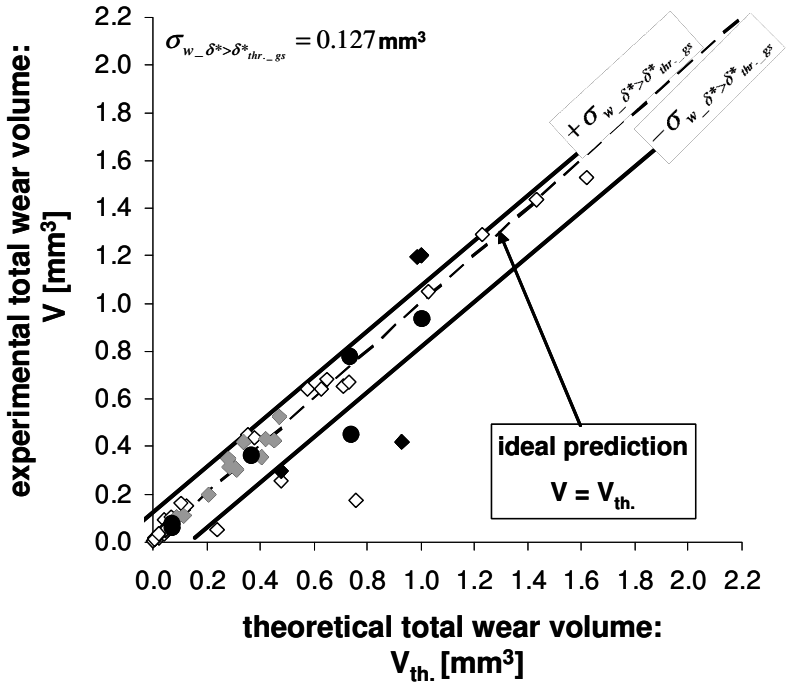

Figure 111: Replotted Figure 110 showing the comparison between experimental and theoretical (predicted from relation 53) wear volumes for all experiments carried out within the framework of the present dissertation except the results obtained under the displacement amplitudes higher than $\delta^*_{cr.\_gs}=\pm 100$ µm; Tests under invariable conditions: ◇; Tests under variable conditions type VT: ◆, DIS: ◆ and PIS: ●.

Figure 111 shows a replotted Figure 110 without the results obtained under the displacement amplitudes higher than $\delta^*_{cr._gs}=\pm 100$ μm, however Figure 112 a replotted Figure 110 without the results obtained under the displacement amplitudes higher than $\delta^*_{cr._gs}=\pm 100$ μm and for DIS 3, PIS 4 and the invariable experiment under the mechanical key point loadings at 225°C results (called intermediate temperature outliers). The standard deviation analysis gives $\sigma_{w\_\delta\_>\delta^*_{thr._gs}} = 0.127\ mm^3$ and $\sigma_{w\_T_{outl.}\_\delta^*>\delta^*_{thr._gs}} = 0.071$ for the situation in Figure 111 and Figure 112, respectively. Thus, it is observed that the dispersion is reduced around 20% in Figure 111 and 60% in Figure 112 in relation to the dispersion obtained in Figure 110.

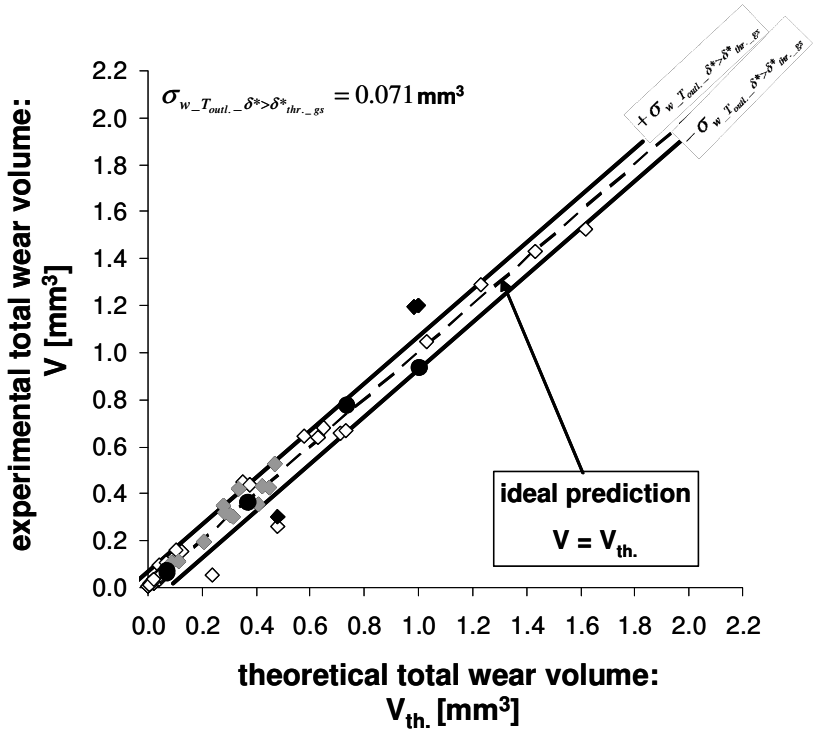

Figure 112: Replotted Figure 110 showing the comparison between experimental and theoretical (predicted from relation 53) wear volumes for all experiments carried out within the framework of the present dissertation except the results obtained under the displacement amplitudes higher than $\delta^*_{cr._gs}=\pm 100$ μm and for DIS 3, PIS 4 and the invariable experiment under the mechanical key point loadings at 225°C; Tests under invariable conditions: ◇; Tests under variable conditions type VT: ◆, DIS: ◆ and PIS: ●.

Generalizing from the study undertaken, the previously developed 'composite' energy wear formulation (relation 53), integrating the two average energy wear coefficients (determined in Chapter 3 – Figure 75) as a function of the loading conditions, allows a good prediction of the wear kinetics even under variable loading conditions. However, there is a limitation of its application for the displacement amplitudes larger than $\delta^*_{cr.\_gs}=\pm 100$ μm and for certain experiments performed in the intermediate 225-250°C temperature range. Such a high predictability presented by the 'composite' wear model implies that the investigated Jethete M152/A-286 tribo-system could be characterized by the two energy wear coefficients ($\overline{\alpha}_{kp\_T<T_t} = 5.44 \cdot 10^{-5}$ and ($\overline{\alpha}_{kp\_T>T_t} = 4.19 \cdot 10^{-6}$ $mm^3 \cdot J^{-1}$) each associated with the predominant wear mechanism (adhesive and abrasive, involving formation of effective 'glaze' layer, respectively).

4. SYNTHESIS OF THE CHAPTER

The experiments under variable temperature conditions adequate to those occurring in the Variable System Vanes have been performed. The interface memory effect has been found to be negligible for the investigated tribo-system as practically perfect transitions (implying high interface reactivity) from one wear regime to another have been observed. No obvious influence of the order, number or duration of the temperature sequences on the friction behaviour has been revealed. Hence, it seems that rheological properties of the third body, which change drastically with temperature, play a vital role in the tribological behaviour as temperature variations below or above T_t are applied.

The innovative experimental methodology consisting in conducting the experiments under displacement amplitude and mean pressure increasing stepwise conditions has been introduced. It has been demonstrated that this new experimental methodology allows a fast plotting of the fretting wear mapping of 'glaze' layer activation as a function of temperature, displacement amplitude and pressure merely by considering the friction evolution, practically without necessity of performing numerous time-consuming invariable experiments.

The plotted fretting wear mapping (displacement amplitude and normal force versus temperature map) of wear regimes has shown that the most determining factor for the

formation of a stable 'glaze' layer is temperature. Mechanical parameters (i.e. displacement amplitude and pressure) play a minor role. Pressure has a quasi negligible effect as the intermediate temperature domain between adhesive high wear and low wear 'glaze' layer interface as a function of pressure is practically vertical (Figure 107b). Moreover, the width of the intermediate temperature domain (ΔT_{gs}) is in the case of the pressure very low (<30°C) and practically independent of the studied loading (Figure 108b). The relatively low dispersion between the experimental results and those obtained from the proposed 'composite' wear model has been found. This all implies that pressure plays a minor impact on either the activation or the degradation of a 'glaze' layer. Displacement amplitude (i.e. sliding amplitude) is more influential parameter than pressure. Until the critical value of the displacement amplitude $\delta^*_{cr.\_gs}=\pm 100$ μm its impact is small (narrow the intermediate temperature domain – Figure 108a) as there is small effect of loading history. The relatively low dispersion between the experimental and the predicted wear volumes has then been observed (compare Figure 110 and 111). The larger displacement amplitudes (i.e. above $\delta^*_{cr.\_gs}=\pm 100$ μm) critically interact on the stability of a 'glaze' layer. Such more severe conditions tend to prevent the formation of a stable 'glaze' layer. This induces a wider intermediate temperature domain between established high wear and low regime. Under such conditions the impact of the loading history is more significant and, in consequence, the dispersion between experimental and predicted from the 'composite' wear model results is higher. Moreover, it has been observed that the higher the temperature the greater the value of the mechanical loadings can be imposed at maintaining low friction and wear response of the interface (i.e. due to the activation of stable effective 'glaze' layers). Such a tendency can be explained by rheological properties of the third body layer formed in the interface. Elevated temperature conditions intensify a tribo-sintering process of the third body. In that way a cohesion quality of the third body increases, so it can bear higher loadings.

The stability of the proposed 'composite' wear model to predict the wear volume even under variable loading conditions has been confirmed as a good forecast of the wear kinetics has been achieved. However, the developed formulation has represented certain limitations of its application. It has been demonstrated that the model is less stable as the displacement amplitudes larger than $\delta^*_{cr.\_gs}=\pm 100$ μm are studied and for certain experiments performed in the intermediate 225-250°C temperature range (i.e.

for the test DIS 3, PIS 4 and for the invariable experiment under the mechanical key point loadings at 225°C).

The results obtained from the study on the fretting wear mapping and the ‘composite’ wear model indirectly confirm the origin of a ‘glaze’ layer from a tribo-sintering process of the third body. It is outlined by the fact that above a threshold displacement amplitude the third body (‘glaze’ layer) is more easily ejected and then the interface displays an unstable response.

GENERAL CONCLUSIONS

Fretting wear behaviour of the Jethete M152/A-286 tribo-system under elevated temperature conditions has been investigated within the framework of the present dissertation.

The following conclusions can be drawn from the presented research work:

- Fretting wear mapping of wear regimes as a function of temperature, displacement amplitude and mean pressure in the contact has been elaborated. It has been demonstrated that depending on the loading combination different wear mechanism is predominant: high wear adhesive one or low wear abrasive, involving the formation of the lubricating 'glaze' layer.

- These two wear mechanism has been found to be associated to the specific evolution of the energy coefficient of friction.

- The temperature has been found to be the most determining factor for the formation of the stable wear-protective 'glaze' layer. The transition from the high to low wear interface is very sharp (i.e. in the narrow range of 20°C) (Figure 113a). Mechanical parameters (i.e. displacement amplitude and pressure) have been shown to play a minor role, where the displacement amplitude (i.e. sliding amplitude) has been found to be the more influential

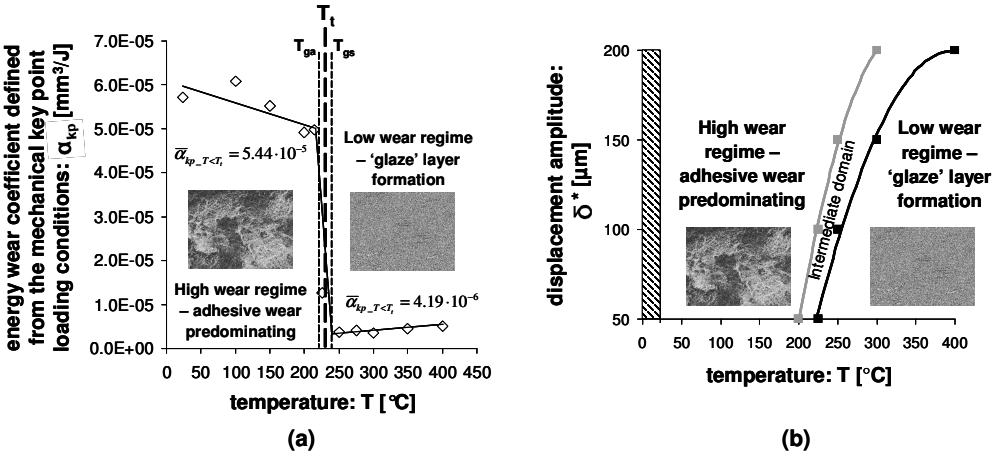

Figure 113: (a) The abrupt transition of the predominant wear regime as T_t is exceeded; (b) The influence of the displacement amplitude on the interface response.

parameter than the pressure. The critical displacement amplitude has been established ($\delta^*_{cr.\_gs}$=±100 µm) above which the interaction on the stability of the 'glaze' layer critically increases (Figure 113b).

- In-depth analytical investigations of the interface have shown that independently of the temperature conditions the third body layer developed on the wear surfaces can be considered as compacted oxidized wear nano-particles originating from the two alloy surfaces. It has also been revealed that spinel-like (Fe_3O_4 and/or $FeCr_2O_4$ and/or $NiCr_2O_4$ and/or $NiFe_2O_4$) and possibly CrO and NiO oxides are main compounds formed.

- The development of the wear-protective 'glaze' layer has been found to be closely associated with a tribo-sintering process of the third body. The load-bearing properties of the 'glaze' layer are a consequence of its high cohesion quality and elevated hardness.

- High temperature intensifies oxidation rate of wear particle and promotes a tribo-sintering process of the third body, which favour the development of the stable effective 'glaze' layer. The higher the temperature the faster the development of the wear-protective 'glaze' structures.

- It has been shown that the higher the temperature the greater the value of the mechanical loadings can be imposed at maintaining low wear response of the interface (i.e. due to the activation of stable effective 'glaze' layers).

- The pre-oxidation treatment has been found to have no effect on the tribological behaviour of the considered system. It therefore indirectly confirms the origin of the 'glaze' layer as the structure produced as a result of a tribo-sintering process, which is activated by a synergetic effect of the temperature and the mechanical fretting loadings.

- The innovative test methodology where the considered mechanical parameter is increasing stepwise during a single fretting experiment at different temperatures has been proposed. It has been demonstrated that it allows a considerably faster plotting of the fretting wear mapping of the wear regimes

without necessity of performing numerous time-consuming invariable experiments.

- Under the related variable mechanical loading test conditions after the parameter transitions the 'glaze' layer degradation takes place very fast followed by its subsequent re-formation if the imposed new loadings are still favourable to the development of a stable 'glaze' layer.

- The experiments under variable temperature conditions adequate to those occurring in the Variable Stator Vane system have been performed. The interface memory effect has been found to be negligible for the investigated tribo-system implying that rheological properties of the third body change drastically with the temperature transitions.

- Using the additive properties of the dissipated energy the 'composite' wear law integrating the energy wear coefficient as a function of the predominant interface (i.e. adhesive or 'glaze' layer) has been developed. The stability of the proposed 'composite' wear formulation to predict the wear volume even under variable loading conditions has been demonstrated as a good forecast of the wear kinetics has been achieved. It infers that the investigated tribo-system can be characterized by the two energy wear coefficients each associated with the different predominant wear mechanism. However, the model has been

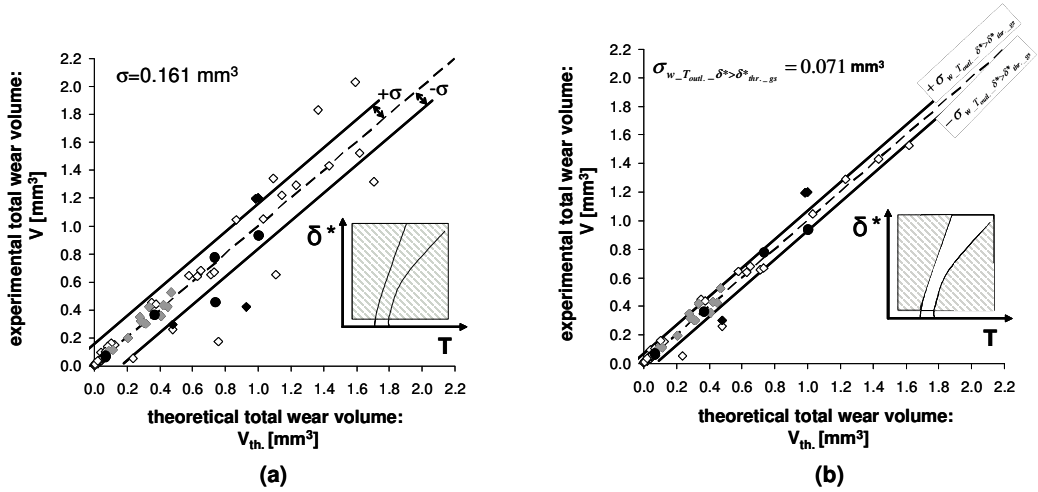

Figure 114: The 'composite' model applied to (a) all studied loading conditions and (b) all excluding the tests in the intermediate domains.

found to represent certain limitations of its application for the loading conditions in the intermediate domain (for the displacement amplitudes larger than $\delta^*_{cr.\_gs}=\pm 100$ μm and for the certain experiments performed in the intermediate 225-250°C temperature range) before the stable 'glaze' is formed (Figure 114a). The model has shown the high stability if it is applied to the loadings (temperature, displacement amplitude, pressure) from outside the intermediate domains (Figure 114b).

Though within the framework of the present dissertation the tribological behaviour of the considered tribo-system has profoundly been described both under invariable and variable loadings there are still some interesting aspects worth additional work. The further investigations should be undertaken to develop the following areas:

- Evaluation of the quantitative rheological properties of the third body (i.e. nano-hardness and Young modulus) under elevated temperature conditions in order to determine how its mechanical properties evolve with temperature;
- To fully clarify the tribological response of the studied tribo-system under variable loading conditions, interrupted tests after the parameter transitions combined with an evaluation of a rheological quality of the interface should be conducted;
- The developed 'composite' wear formulation seems to be a promising tool to predict the wear response under variable loading conditions. However, the model should be improved for the large displacement amplitude and the intermediate 225-250°C temperature domain conditions (i.e. for the intermediate transient domain). Further investigations should be undertaken to probe this aspect and perhaps to propose a different formulation which better integrates the transient response of the interface in wear modelling.

REFERENCES

Aldham D., Warburton J., *The unlubricated fretting wear of mild steel in air*, Wear 106 **(1985)**, p.177-201.

Alexandrov V. M., Romalis B. L., *Contact Problems in Mechanical Engineering*, Mashinostroenie **(1986)**.

Archard J. F., *Contact and rubbing of flat surfaces*, J. Appl. Phys. 24 **(1953)**, p. 981-988.

Archard J. F., Hirst W., *The wear of metals under unlubricated conditions*, Proc. Roy. Soc. A236 **(1956)**, p. 397-410.

Askeland D (Ed.), *The Science and Engineering of Materials*, Third Edition, Nelson Thornes Ltd., Cheltenham **(1998)**, p. 771.

ATI Allvac, Technical data sheet **(2001)** on www.allvac.com/allvac/pages/Steel/UNSS66286.htm.

Berthier Y., *Experimental evidence for friction and wear modelling*, Wear 139 **(1990)**, p. 77-92.

Berthier Y., Godet M., Brendle M., *Velocity Accommodation in Friction***,** Tribol. Trans. 32 **(1989)**, p. 490-496.

Bhushan B. (Ed.), *Modern Tribology Handbook, Vol. 1 – Principles of Tribology*, CRC Press, Boca Raton, Florida **(2001)**.

Blanchard P., Colombie C., Pellerin V., Fayeulle S., Vincent L., *Materials effects in fretting wear : Application to iron, titanium, and aluminium alloys*, Metallurgical Transaction A 22 **(1991)**, p. 1535-1544.

Blanpain B., Celis J. P., Roos J. R., Ebberink J., Smeets J., *A comparative study of the fretting wear of hard carbon coatings*, Thin Solid Films 223 **(1993)**, p. 65-71.

Blanpain B., Mohrbacher H., Liu E., Celis J. P., Roos J. R., *Hard coatings under vibrational contact conditions*, Surface and Coatings Technology 74-75 **(1995)**, p. 953-958.

Boas M., Rosen A., *Effect of load on the adhesive wear of steels*, Wear 44 **(1977)**, p. 213-222.

Bregliozzi G., Ahmed S. I.-U., Di Schino A., Kenny J. M., Haefke H., *Friction and wear behaviour of austenitic stainless steel: influence of atmospheric humidity, load range and grain size*, Tribol. Lett. 17 **(2004)**, p. 697-704.

Bregliozzi G., Di Schino A., Kenny J. M., Haefke H., *The influence of atmospheric humidity and grain size on the friction and wear of AISI 304 austenitic stainless steel*, Mater. Lett. 57 **(2003)**, p. 4505-4508.

Buckley D. H., *Surface Effects in Adhesion, Friction, Wear and Lubrication*, Elsevier, Amsterdam **(1981)**.

Burwell J. T., Strang C. D., *On the empirical law of adhesive wear*, J. Appl. Phys. 23 **(1952)**, p. 18-28.

Chen G. X., Zhou Z. R., *Study on transition between fretting and reciprocating sliding wear*, Wear 250 **(2001)**, p. 665-672.

Childs T. H. C., *The sliding wear mechanisms of metals, mainly steels*, Tribology International 13 **(1980)**, p. 285-293.

Collins J. A., *Failure of Materials in Mechanical Design*, New York, J. Wiley **(1981)**.

Colombie C., Berthier Y., Floquet A., Vincent L., Godet M., *Fretting: Load carrying capacity of wear debris*, Journal of Tribology 106 **(1984)**, p. 194-201.

Crossland B., *Effect of large hydrostatic pressures on the torsional fatigue strength of an alloy steel*, Proc. of Intr. Conf. on Fatigue of Metals, London **(1956)**, p. 138-149.

Dang Van K., *Macro-micro approach in high-cycle multiaxial fatigue*, Advances in Multiaxial Fatigue, ASTM STP 1191 **(1993)**, p. 120-130.

De Boer F. E, Selwood P. W., *The activation energy for the solid state reaction* γ-$Fe_2O_3 \rightarrow \alpha$-$Fe_2O_3$, J. Am. Chem. Soc. 76 **(1954)**, p. 3365-3367.

De Faria D. L. A., Venancio Silva S., De Oliveira M. T., *Raman microscopy of some iron oxides and oxyhydroxides*, Journal of Raman Spectroscopy 28 **(1997)**, p. 873-878.

Del Puglia A., Pratesi F., Zonfrillo G., *Experimental procedure and involved parameters in fretting-fatigue test*, ESIS 18, Edited by R.B. Waterhouse and T.C. Lindley, Mechanical Engineering Publication, London, **(1994)**, p. 219-238.

Descartes S., Berthier Y., Rheology *and flows of solid third bodies: background and application to an* $MoS_{1.6}$ *coating*, Wear 252 **(2002)**, p. 546-556.

Dobrzanski L. A., *Metaloznawstwo z podstawami nauki o materialach*, Wyd. Naukowo-Techniczne, Warszawa **(1999)**, p. 352-359.

Dowson D., *History of Tribology*, 2nd ed., PEP, London **(1998)**, p. 32-57.

Eden E. M., Rose W. N., Cunningham F. L, *The endurance of metals***,** Proc. Instn. Mech. Engrs. 4 **(1911)**, p. 875-883.

Elleuch K., Fouvry S., *Wear analysis of A357 aluminium alloy under fretting*, Wear 253 **(2002)**, p. 662-672.

Ellingham H. J. T., *Reducibility of Oxides and Sulphides in Metallurgical Processes*, J. Soc. Chem. Ind. 63 **(1944)**, p. 125-133.

Endo K., *Initiation and propagation of fretting-fatigue cracks*, Wear 38 **(1976)**, p. 311-324.

Forsyth P.J.E., *A two stage fatigue fracture mechanisms*, Proc. Cranfield Symposium on Fatigue, **(1961)**, p. 76.

Fouvry S., Duó P., Perruchaut Ph., A *quantitative approach of Ti-6al-4V fretting damage: friction, wear and crack nucleation*, Wear 257 **(2004)**, p. 916-929.

Fouvry S., Fridrici V., Langlade C., Kapsa Ph., Vincent L., *Palliatives in fretting : A dynamical approach*, Tribology International 39 **(2006)**, p. 1005-1015.

Fouvry S., Kapsa Ph., Vincent L., *Analysis of sliding behaviour for fretting loadings : determination of transition criteria*, Wear 185 **(1995a)**, p. 35-46.

Fouvry S., Kapsa Ph., Vincent L., *Quantification of fretting damage*, Wear 200 **(1996)**, p. 186-205.

Fouvry S., Kapsa Ph., Vincent L., Wear phenomena quantification of hard coating under fretting situation, proceeding of the International Tribology Conference, Yokohama **(1995b)**, p. 277-282.

Fouvry S., Kapsa Ph., Zahouani H., Vincent L., *Wear analysis in fretting of hard coatings through a dissipated energy concept*, Wear 203-204 **(1997)**, p. 393-403.

Fouvry S., Liskiewicz T., Kapsa Ph., Hannel S., Sauger E., *An energy description of wear mechanisms and its applications to oscillating sliding contacts*, Wear 255 **(2003)**, p. 287-298.

Fridrici V., Fouvry S., Kapsa Ph., *Effect of shot peening on the fretting wear of Ti-6Al-4V*, Wear 250 **(2001)**, p. 642-649.

Fu Y., Wei J., Batchelor A. W., *Some considerations on the mitigation of fretting damage by the application of surface-modification technologies*, Journal of Materials Processing Technology 99 **(2000)**, p. 231-245.

Glascott J., Stott F. H., Wood G. C., *The effectiveness of oxides in reducing sliding wear of alloys*, Oxidation of Metals 24 **(1985)**, p. 99-114.

Godet M., *The third-body approach: a mechanical view of wear*, Wear 100 **(1984)**, p. 437-452.

Godfrey D., Bailey J. M., Lubr. Eng. 10 **(1952)**, p. 155.

Gordelier S. C., Chivers T. C., *A literature review of palliatives for fretting fatigue*, Wear 56 **(1979)**, p. 177-190.

Goryacheva I. G., Rajeev P. T., Farris T. N., *Wear in partial slip contact*, Journal of Tribology 123 **(2001)**, p. 848-856.

Goto K., *The influence of surface induced voltage on the wear mode of stainless steel*, Wear 185 **(1995)**, p. 75-81.

Goto Y., *The Effect of squeezing on the phase transformation and magnetic properties of* γ*-*Fe_2O_3, Jpn. J. Appl. Phys. 3 **(1964)**, p. 739-744.

Guzowski S., *Effect of contact interaction in clamped joints on fretting wear development*, Tribologia 5 **(1998)**, p. 698-707.

Haavik C., Stolen S., Fjellvag H., Hanfland M., Hausermann D., *Equation of state of magnetite and its high-pressure modification: Thermodynamics of the Fe-O system at high pressure, Sample at P = 0*, American Mineralogist 85 **(2000)**, p.514-523.

Halliday J. S., Hirst W., *The fretting corrosion of mild steel*, Proc. Roy. Soc. A 236 **(1956)**, p. 411-425.

Harris S. J., Overs M. P., Gould A. J., *The use of coatings to control fretting wear at ambient and elevated temperatures*, Wear 106 **(1985)**, p. 35-52.

Hertz H. R., *On the contact of elastic solids*, In: Jones and Schott Editors **(1882)**, *Miscellaneous Papers by H. Hertz*, Macmillan **(1896)** London.

Hills D. A., Nowell D., O'Connor J. J., *On the mechanics of fretting fatigue*, Wear 125 **(1988)**, p. 129-146.

Hills D. A., Nowell D., Sackfield A., *Mechanics of Elastic Contacts*, Butterworth-Heinemann **(1993)**.

Hiratsuka K., Muramoto K., *Role of wear particles in severe-mild wear transition*, *Wear* 259 **(2005)**, p. 467-476.

Hirst W., in Proceedings of the Conference on Lubrication and Wear, IMechE 674, London **(1957)**.

Hokkirigawa K., Kato K., *An experimental and theoretical investigation of ploughing, cutting and wedge formation during abrasive wear*, Tribology International 21 **(1988)**, p. 51-57.

Hong H., Hochman R. F., Quinn T. F. J., *A new approach to the oxidational theory of mild wear*, STLE Trans. 31 **(1988)**, p. 71-75.

Hong H., *The role of atmospheres and lubricants in oxidational wear of metals*, Tribology International 35 **(2002)**, p. 725-729.

Huq M. Z., Celis J.-P., *Expressing wear rate in sliding contacts based on dissipated energy*, Wear 252 **(2002)**, p. 375-383.

Hurricks P. L., *The fretting wear of mild steel from 200° to 500°C*, Wear 30 **(1974)**, p. 189-212.

Hurricks P. L., *The fretting wear of mild steel from room temperature to 200°C*, Wear 19 **(1972)**, p. 207-229.

Hurricks P. L., *The mechanism of fretting – A review*, Wear 15 **(1970)**, p. 389-409.

Hutchings I. M., *Tribology: Friction and Wear of Engineering Materials*, CRC Press, Boca Raton **(1992)**.

Inman I. A., Datta P. K., Du H. L., J. S. Burnell-Gray, Pierzgalski S., Luo Q., *Studies of high temperature sliding wear of metallic dissimilar interfaces*, Tribology International 38 **(2005)**, p. 812-823.

Inman I. A., Rose S. R., Datta P. K., *Development of a simple 'temperature versus sliding speed' wear map for the sliding wear behaviour of dissimilar metallic interfaces*, Wear 260 **(2006)**, p. 919-932.

Iwabuchi A., *The role of oxide particles in the fretting wear of mild* steel, Wear 151 **(1991)**, p. 301-311.

Jiang J., Stott F. H., Stack M. M., *A generic model for dry sliding wear of metals at elevated temperatures*, Wear 256 (2004), p. 973-985.

Jiang J., Stott F. H., Stack M. M., *A mathematical model for sliding wear of metals at elevated temperatures*, Wear 181-183 **(1995)**, p. 20-31.

Jiang J., Stott F. H., Stack M. M., *The role of triboparticulates in dry sliding wear*, Tribology International 31 **(1998)**, p. 245-256.

Johansson L., *Model and numerical algorithm for sliding contact between two elastic half-phase with frictional heat generation and wear*, Wear 160 **(1993)**, p. 77-93.

Johnson K. L., *Contact Mechanics*, Cambridge, University Press **(1985)**.

Jost H. P., *Lubrication, education and research – A report on the present position and industry's needs*, Her Majesty's Stationery Office, London **(1966)**.

Kalin M., Vizintin J., *Comparison of different theoretical models for flash temperature calculation under fretting conditions*, Tribology International 34 **(2001)**, p. 831-839.

Kalin M., Vizintin J., Novak S., Drazic G., *Wear mechanisms in oil-lubricated and dry fretting of silicon nitride against bearing steel contacts*, Wear 210 **(1997)**, p. 27-38.

Kato H., Komai K., *Tribofilm formation and mild wear by tribo-sintering of nanometer-sized oxide particles on rubbing steel* surfaces, Wear 262 **(2007)**, p. 36-41.

Kato H., *Severe-mild wear transition by supply of oxide particles on sliding surface*, *Wear* 255 **(2003)**, p. 426-429.

Kayaba T., Iwabuchi A., *The fretting wear of 0.45% C steel and austenitic stainless steel from 20 to 650°C in air*, Wear 74 **(1981)**, p. 229-245.

Kennedy P. J., Stallings L., Petersen M. B., *A study of surface damage at low amplitude slip*, Proc. of Conf. "ASLE-ASME Lubrication Conf.", Hartford **(1983)**.

Kim J. H., Hwang I. S., *Development of an in situ Raman spectroscopic system for surface oxide films on metals and alloys in high temperature water*, Nuclear Engineering and Design 235 **(2005)**, p. 1029-1040.

Kitagawa H., Takahashi S., *Applicability of fracture mechanics to very small cracks or cracks in the early stage*, Proc. of Second Int. Conf. on Mech. Behaviour of Materials, American Society for Metals **(1976)**, p. 627-631.

Klaffke D., *Tribological behaviour of Me:CH coatings on steel against steel in the case of oscillating sliding motion at room temperature*, Diamond Films and Technology 3 **(1994)**, p. 149-165.

Kolodziejczyk T., S. Fouvry, G. Morales-Espejel, *Fretting generated by the vibrations in ball bearings in dry and oil-bath lubricated contact*, Proceedings from 1st International Conference on Artificial Intelligence for Industrial Applications **(2007)**, Ostravice, Czech Republic.

Krause H., *Tribochemical reactions in the friction and wearing process of iron*, Wear 18 **(1971)**, p. 403-412.

Kubiak K., Fouvry S., Marechal A. M., *A practical methodology to select fretting palliatives: Application to shot peening, hard chromium and WC-Co coatings*, Wear 259 **(1005)**, p. 367-376.

Labedz J., *Metal Treatments against Wear, Corrosion, Fretting Fatigue*, Oxford, Pergamon Press **(1988)**, p. 87-98.

Liew W. Y. H., *Effect of relative humidity on the unlubricated wear of metals*, Wear 260 **(2006)**, p. 720-727.

Liskiewicz T., Fouvry S., *Development of a friction energy capacity approach to predict the surface coating endurance under complex oscillating sliding conditions*, Tribology International 38 **(2005a)**, p. 69-79.

Liskiewicz T., Fouvry S., Wendler B., Development *of a Wöhler-like approach to quantify the Ti(CxNy) coatings durability under oscillating sliding conditions*, Wear 259 **(2005b)**, p. 835-841.

Liskiewicz T., Fouvry S., Wendler B., *Hard coatings durability under fretting wear*, Tribology and Interface Engineering Series 48 **(2005c)**, p. 657-665.

Liskiewicz T., Rybiak R., Fouvry S., Wendler B., *Fretting wear of Ti(C_X N_Y) PVD coatings under variable environmental conditions*, Journal of Engineering Tribology 220 J **(2006)**, p. 125-134.

Maatta A., Vuoristo P., Mantyla T., *Friction and adhesion of stainless steel strip against tool steels in unlubricated sliding with high contact load*, Tribology International 34 **(2001)**, p. 779-786.

Mary C., Fouvry S., *Numerical prediction of fretting contact durability using energy wear approach: Optimisation of finite-element model*, Wear 263 **(2007)**, p. 444-450.

Matveesky R. M., Trans. ASTM 87 **(1965)**, p. 754.

McDiarmid D.L., *A general criterion for high-cycle multiaxial fatigue failure*, Fatigue Fract. Engng Mater. Structs. 14 **(1991)**, p. 429-453.

McDowell O.J., *Fretting corrosion tendencies of several combinations of materials*, Symposium on fretting corrosion, ASTM, Philadelphia, USA, **(1953)**, p. 40-53.

Meng H. C., Ludema K. C., *Wear models and predictive equations: their form and content*, Wear 181-183 **(1995)**, p. 443-457.

Merhej R., *Impact de la taille du contact sur le comportement tribologique du contact 100C6/100C6 soumis a des solicitations de fretting*, Ph.D. thesis at Ecole Centrale de Lyon (Defence schelude on May 30th **2008**).

Mindlin R. D., *Compliance of elastic bodies in contact, Trans. ASME, Series E, Journal of Applied Mechanics* 16 **(1949)**, p. 259-268.

Mohrbacher H., Blanpain B., Celis J.-P., Roos J. R. Stals L., Van Stappen M., *Oxidational wear of TiN coatings on tool steel and nitrided tool steel in unlubricated fretting*, Wear 188 **(1995)**, p. 130-137.

Moore M. A., *Abrasive wear*, in: D. A. Rigney (Ed.), Fundamentals of friction and wear, American Society of Metals, Metals Park, OH **(1980)**, p. 73.

Muraca R. F., Whittick J. S., *Materials Data Handbook, Stainless steel alloy A-286*, Western Applied Research & Development, San Carlos, CA **(1972)**.

Nakazawa K., Sumita M., Maruyaman N., *Effect of contact pressure on fretting fatigue of high strength steel and titanium alloy*, Standardization of fretting fatigue test methods and equipment, ASTM STP 1159, M.H. Attia and R.B. Waterhouse Eds., ASTM, Philadelphia **(1992)**, p. 115-125.

Nosonovsky M., *Oil as a lubricant in the ancient Middle East*, Tribology Online 2 **(2007)**, p. 44-49.

Ohmae N., Tzukizoe T., *The effect of slip amplitude on fretting*, Wear 27 **(1974)**, p. 281-293.

Paulin C., Fouvry S., Deyber S., *Wear kinetics of Ti–6Al–4V under constant and variable fretting sliding conditions*, Wear 259 **(2005)**, p. 292-299.

Paulin C., Fouvry S., Meunier C., *Finite element modelling of fretting wear surface evolution : Aplication to a Ti-6Al-4V contact*, Wear 264 **(2008)**, p. 26-36.

Paulin Ch., *Etude de l'endommagement du contact multicouche aube/disque sous chargement de fretting : impact des sollicitations variables et de la dimension du contact*, Ph.D. thesis at Ecole Centrale de Lyon, No. 2006-01 **(2006)**.

Pauling L., Hendricks S. B., *Crystal structures of hematite and corundum*, Journal of the American Chemical Society 47 **(1925)**, p.781-790.

Peckner D., Bernstein I. M., *Handbook of Stainless Steels*, McGrow-Hill, New York **(1977)**.

Peckner D., Bernstein I.M., *Handbook of Stainless Steels*, McGraw-Hill, New York **(1977)**.

Plint M. A., in: Proceedings of the XI NCIT **(1995)**, p. 185.

Quinn T. F. J., *Review of oxidational wear, Part I: The origins of oxidational wear*, Tribology International 16 **(1983a)**, p. 257-271.

Quinn T. F. J., *Review of oxidational wear, Part II: Recent developments and future trends in oxidational wear research*, Tribology International 16 **(1983b)**, p. 305-315.

Quinn T. F. J., *The Classifications, Laws, Mechanisms and Theories of Wear, Part VII of Fundamentals of tribology*, Suh N. P and Saka N. (Eds.), The M. I. T. Press **(1980)**, p. 477-492.

Quinn T. F. J., *The effect of 'hot-spot' temperatures on the unlubricated wear of steel*, ASLE Trans. 10 **(1967)**, p. 158-168.

Quinn T. F. J., *The role of oxidation in the mild wear of steel*, Brit. J. Appl. Phys. 13 **(1962)**, p. 33-37.

Rabinowicz E., *Friction and wear materials*, Wiley, New York **(1965)**.

Rabinowicz E., *Wear coefficients – metals*, Wear Control Handbook, Peterson M. B. and Winer W. O. (Eds.), ASME 475 **(1980)**.

Renusch D., Veal B., Natesan K., Grimsditch M., *Transient oxidation in Fe-Cr-Ni alloys: a Raman-scattering study*, Oxidation of metals 46 **(1996)**, p. 365-381.

Rhee S. K., *Wear equation for polymers sliding against metal surfaces*, Wear 16 **(1970)**, p. 431-445.

Rigney D. A., Chen L. H., Naylor M. G. S., Rosenfield A. R., *Wear processes in sliding systems*, Wear 100 **(1984)**, p. 195-219.

Sato K., Stolarski T. A, Iida Y., *The effect of magnetic field on fretting wear*, Wear 241 **(2000)**, p. 99-108.

Sauger E., Fouvry S., Ponsonnet L., Kapsa Ph., Martin J.M., Vincent L., *Tribologically transformed structure in fretting*, Wear 245 **(2000)**, p. 39-52.

Shaw M. C., *Dimensional analysis for wear systems*, Wear 43 **(1977)**, p. 263-266.

Shima M., Suetake H., McColl I. R., Waterhouse R. B., Takeuchi M., On *the behaviour of an oil lubricated fretting contact*, Wear 210 **(1997)**, p. 304-310.

Singer I. L., Pollock H. M. (editors), *Fundamentals of friction: macroscopic and microscopic processes*, Kluwer Academic Publishers, Dordrecht, The Netherlands **(1992)**.

Smith K. N., Watson P., Topper T.H., *A stress-strain function for the fatigue of metals*, J. Mater. **(1970)**, 5(4), p. 767-778.

Soda N., Kimura Y., Tanaka A., *Wear of F.C.C. metals during unlubricated sliding Part III: A mechanical aspect of wear*, Wear 40 **(1976)**, p. 23-35.

Special Metals Corporation, Technical Bulletin **(2004)** on www.specialmetals.com/products/incoloyalloya286.php.

Stott F. H., *The role of oxidation in the wear of alloys*, Tribology International 31 **(1998)**, p. 61-71.

Tomlinson G. A., *The rusting of steel surfaces in contact*, Proc. of Royal Society A 115 **(1927)**, p. 427-483.

Tsuji E., Ando A., *Effects of air and temperature on speed dependency of sliding wear of steels*, JSLE-ASLE Int. Lubrication Conf., Tokyo **(1975)**, p. 101-109.

Vaessen G. H. G., Commissaris C. P. L., De Gee A. W. J., Proc. Inst. Mech. Eng. 183, London **(1968-1969)**, p. 125.

Varenberg M., Halperin G., Etsion I., *Different aspects of the role of wear debris in fretting wear*, Wear 252 **(2002)**, p. 902-910.

Vincent L., Berthier Y., Dubourg M. C., Godet M., *Mechanisms and materials in fretting*, Wear 153 **(1992)**, p. 135-148.

Vingsbo O., Soderberg S., *On fretting maps*, Wear 126 **(1988)**, p. 131-147.

Wang A., Kuebler K. E., Jolliff B. L., Haskin L. A., Am. Mineral. 89 **(2004)**, p. 665.

Wang Z., Saxena S. K., Lazor P., O'Neill H. S. C., *An in situ Raman spectroscopic study of pressure induced dissociation of spinel* $NiCr_2O_4$, Journal of Physics and Chemistry of Solids 64 **(2003)**, p. 425-431.

Waterhouse R. B., *Fretting Corrosion*, Oxford, Pergamon **(1972)**.

Waterhouse R. B., *Metal Treatments against Wear, Corrosion, Fretting Fatigue*, Oxford, Pergamon Press **(1988)**, p. 31-40.

Waterhouse R. B., Taylor D. E., *Fretting debris and the delamination theory of wear*, Wear 29 **(1974)**, p. 337-344.

Waterhouse R.B., *A historical introduction of fretting fatigue in Standardization of fretting fatigue test methods and equipment*, ASTM STP 1159 **(1992)**, p. 8-9.

Waterhouse R.B., *Fretting Fatigue*, London, Applied Science **(1981)**.

Wayson A. R., *A study of fretting on steel*, Wear 7 **(1964)**, p. 435-450.

Wei J., Fouvry S., Kapsa Ph., Vincent L., *Fretting behaviour of TiN coatings*, Surface Engineering 13 **(1997)**, p. 227-232.

Yamamoto M., Nakajima K., *A study of the physical adhesive state between solids*, Wear 70 **(1981)**, p. 321-327.

Zhou Y.-H., Harmelin M., Bigot J., *Sintering behaviour of ultra-fine Fe, Ni and Fe-25wt%Ni powders*, Scripta Metallurgica 23 **(1989)**, p. 1391-1396.

Zhou Z. R., Fayeulle S., Vincent L., *Cracking behaviour of various aluminium alloys during fretting wear*, Wear 155 **(1992)**, p. 317-330.

Zhou Z. R., Sauger E., Liu J. J., Vincent L., *Nucleation and early growth of tribologically transformed structure (TTS) induced by fretting*, Wear 212 **(1997)**, p. 50-58.

Zhou Z. R., Vincent L., *Lubrication in fretting – a review*, Wear 225-229 **(1999)**, p. 962-967.